

**DEVELOPMENT OF Ni-BASED CATALYSTS  
VIA MICROEMULSION SYNTHESIS APPROACH  
FOR METHANE DRY REFORMING**

**MUHAMMAD USMAN RASHID**

**THESIS SUBMITTED IN FULFILMENT  
OF THE REQUIRMENTS FOR THE DEGREE OF  
DOCTOR OF PHILOSOPHY**

**FACULTY OF ENGINEERING  
UNIVERSITY OF MALAYA  
KUALA LUMPUR**

**2017**

UNIVERSITI MALAYA

**ORIGINAL LITERARY WORK DECLARATION**

Name of Candidate: **Muhammad Usman Rashid** (Passport No:

Registration/Matric No: **KHA120105**

Name of Degree: **Doctor of Philosophy**

Title of Project Paper/Research Report/Dissertation/Thesis ("this work"):

**DEVELOPMENT OF Ni-BASED CATALYSTS VIA MICROEMULSION  
SYNTHESIS APPROACH FOR METHANE DRY REFORMING**

Field of Study: **Reaction Engineering**

I do solemnly and sincerely declare that:

- (1) I am the sole author/writer of this work;
- (2) This work is original;
- (3) Any use of any work in which copyright exists was done by way of fair dealing and for permitted purposes and any excerpt or extract from, or reference to or reproduction of any copyright work has been disclosed expressly and sufficiently and the title of the work and its authorship have been acknowledged in this work;
- (4) I do not have any actual knowledge nor do I ought reasonably to know that the making of this work constitutes an infringement of any copyright work;
- (5) I hereby assign all and every rights in the copyright to this work to the University of Malaya ("UM"), who henceforth shall be owner of the copyright in this work and that any reproduction or use in any form or by any means whatsoever is prohibited without the written consent of UM having been first had and obtained;
- (6) I am fully aware that if in the course of making this Work I have infringed any copyright whether intentionally or otherwise, I may be subject to legal action or any other action as may be determined by UM.

Candidate's Signature

Date

Subscribed and solemnly declared before,

Witness's Signature

Date

Name:

Designation:

## ABSTRACT

Dry reforming of methane has drawn increased attention as it utilizes inexpensive, local source of energy; landfill gas, containing considerable amounts of methane and carbon dioxide produced by anaerobic decomposition of municipal solid waste. In this study, microemulsion synthesis approach was adopted to synthesize Ni-based catalysts supported on MgO and CeO<sub>2</sub>. The investigation on the various synthesis parameters effecting Ni metal surface area such as: water-to-surfactant ratio (0.33, 0.5 and 0.66), aging time (0.5 to 24 h), calcination temperature (450 to 1000 °C) and Ni metal molar concentration (2 M to 7 M) exhibited that favourable parameters for the achievement of higher Ni surface area are the low calcination temperature (450 °C), moderate aging time (2 h) and lower Ni metal molar concentration (2 M). Furthermore, at constant water-to-surfactant ratio, an increase in water content leads to the decrease in surface area due to the higher micellar exchange rate favouring the growth of larger particles. 20%Ni/MgO catalyst exhibited higher methane (49.93 %) and carbon dioxide (54.80 %) conversion compared to pure Ni particles (18.72% CH<sub>4</sub> and 21.80% CO<sub>2</sub> conversion). Further study on the influence of calcination temperatures (450 °C, 600 °C and 800 °C) over 20%Ni/MgO catalysts indicated that the increase of calcination temperature (from 450 to 800 °C) leads to the decrease in surface area from 153.22 m<sup>2</sup>/g to 34.72 m<sup>2</sup>/g and also exhibits lower stability compared to the catalyst calcined at lower calcination temperature (450 °C). However, when the influence of calcination temperatures (450 °C, 600 °C and 800 °C) on the NiO-MgO solid solution formation was investigated with different Ni metal content (20, 40 and 80 wt%), it was observed that 80%Ni/MgO catalyst calcined at higher temperature (800 °C) exhibited better catalytic activity and stability at a very high weight hourly space velocity (WHSV = 1.68 x 10<sup>5</sup> ml h<sup>-1</sup> g<sup>-1</sup>). This was attributed to the presence of higher Ni<sup>0</sup> active sites due to higher Ni content and formation of strong NiO-MgO solid solution. The application of higher reduction temperature (800 °C) to

80%Ni/MgO exhibited severe deactivation compared to the catalyst reduced at lower temperature (550 °C). This was attributed to the fact that the catalyst reduced at lower temperature was less prone to sintering. Core-shell like structures (Ni@CeO<sub>2</sub>) were synthesized at different Ni content (20% Ni, 40% Ni, and 80%Ni) and investigated at reaction temperature of 800 °C and WHSV of  $1.2 \times 10^5 \text{ ml h}^{-1} \text{ g}^{-1}$ . 40% Ni@CeO<sub>2</sub> exhibited higher catalytic activity and better stability compared to 20% Ni@CeO<sub>2</sub> and 80% Ni@CeO<sub>2</sub>. This leads to the conclusion that proper balance between Ni active sites and CeO<sub>2</sub> content played a critical role in the achievement of higher stability and in the suppression of carbon deposition. Fresh and spent catalysts were characterized by BET, XRD, TPR-H<sub>2</sub>, TPD-CO<sub>2</sub>, FESEM and TEM.

## ABSTRAK

Pembaharuan kering metana telah mendapat perhatian berikutan kos yang diperlukan adalah rendah dan penggunaan sumber tenaga tempatan iaitu; gas di tapak pelupusan sampah, yang mengandungi sejumlah besar metana dan karbon dioksida yang terhasil daripada sisa pepejal perbandaran melalui penguraian secara anaerobik. Dalam kajian ini, pendekatan sintesis mikroemulsi telah digunakan untuk mensintesis pemangkin berasaskan Ni yang disokong pada MgO dan CeO<sub>2</sub>. Penyiasatan terhadap kepelbagaian parameter sintesis yang mempengaruhi permukaan logam Ni adalah seperti: nisbah air kepada surfaktan (0.33, 0.5 dan 0.66), masa penuaan (0.5-24 jam), suhu pengkalsinan (450-1000 °C) dan kepekatan larutan molar logam Ni (2 M hingga 7 M) telah menunjukkan bahawa parameter yang sesuai untuk pencapaian kawasan permukaan Ni yang lebih tinggi adalah pada suhu pengkalsinan yang rendah (450 °C), masa penuaan yang sederhana (2 j) dan kepekatan larutan molar logam Ni yang rendah (2 M). Tambahan pula, pada nisbah air kepada surfaktan yang malar, peningkatan dalam kandungan air menyasarkan kepada penurunan kawasan permukaan disebabkan oleh kadar pertukaran miceller yang lebih tinggi berpihak kepada pertumbuhan zarah yang lebih besar. Pemangkin 20% Ni/MgO telah menghasilkan penukaran metana (49.93%) dan karbon dioksida (54.80%) yang lebih tinggi berbanding zarah Ni tulen (penukaran 18.72% CH<sub>4</sub> dan 21.80% CO<sub>2</sub>). Kajian lanjut terhadap pengaruh suhu pengkalsinan (450 °C, 600 °C dan 800 °C) pada pemangkin 20% Ni/MgO telah menunjukkan bahawa peningkatan suhu pengkalsinan (daripada 450 kepada 800 °C) membawa kepada penurunan kawasan permukaan daripada 153.22 m<sup>2</sup>/g kepada 34.72 m<sup>2</sup>/g dan menyebabkan kestabilan yang lebih rendah berbanding pemangkin yang telah dikalsin pada suhu pengkalsinan yang lebih rendah (450 °C). Walau bagaimanapun, apabila pengaruh suhu pengkalsinan (450 °C, 600 °C dan 800 °C) pada pembentukan larutan pepejal NiO-MgO dikaji pada

perbezaan kandungan logam Ni (20, 40 dan 80% wt%), hasil kajian menunjukkan bahawa pemangkin 80% Ni/MgO yang telah dikalsin pada suhu yang lebih tinggi (800 °C) mempamerkan aktiviti pemangkinan yang lebih baik dan kestabilan yang tinggi pada berat setiap jam pada ruang halaju ( $WHSV = 1.68 \times 10^5 \text{ ml h}^{-1} \text{ g}^{-1}$ ). Hal ini disebabkan oleh kehadiran tapak aktif  $\text{Ni}^0$  yang lebih tinggi pada kandungan Ni yang lebih tinggi dan pembentukan larutan pepejal NiO-MgO yang kuat. Penggunaan suhu reduksi yang lebih tinggi (800 °C) pada pemangkin 80% Ni/MgO mempamerkan penyahaktifan yang serius berbanding pemangkin yang direduksi pada suhu yang lebih rendah (550 °C). Ini disebabkan oleh fakta bahawa pemangkin yang direduksi pada suhu yang lebih rendah adalah kurang terdedah kepada proses pensinteran. Struktur seperti kelompong teras ( $\text{Ni@CeO}_2$ ) telah disintesis pada kandungan Ni yang berbeza (20%  $\text{Ni@CeO}_2$ , 40%  $\text{Ni@CeO}_2$ , 80%  $\text{Ni@CeO}_2$ ) dan telah dikaji pada suhu tindak balas iaitu 800 °C dan pada WHSV iaitu  $1.2 \times 10^5 \text{ ml h}^{-1} \text{ g}^{-1}$ . 40%  $\text{Ni@CeO}_2$  menunjukkan aktiviti pemangkinan yang lebih tinggi dan lebih stabil berbanding dengan 20%  $\text{Ni@CeO}_2$  dan 80%  $\text{Ni@CeO}_2$ . Ini membawa kepada kesimpulan bahawa gabungan keseimbangan yang sesuai antara tapak aktif Ni dan kandungan  $\text{CeO}_2$  memainkan peranan yang penting dalam mencapai kestabilan yang lebih tinggi dan dalam penyingkiran pemendapan karbon. Pemangkin baru dan yang telah digunakan telah dianalisis menggunakan BET, XRD, TPR- $\text{H}_2$ , TPD- $\text{CO}_2$ , FESEM dan TEM.

## ACKNOWLEDGMENTS

I would like to sincerely thank and express my gratitude to Prof. Dr. Wan Mohd Ashri Wan Daud for serving as both my advisor and mentor. I appreciate the patience, guidance, criticism and encouragement during the research work.

I would like to thank all the supporting staff and technicians in the Department of Chemical Engineering: Cik Norhaya binti abdullah rahim, Cik Fazizah binti abdullah and Mr Zaharudin bin Md. Salleh and Mr. Jalaludin.

I would also like to thank my colleagues and fellow researchers in our group, who encouraged and supported me during my studies.

My gratitude goes to my parents, especially my lovely mother Naseem Akhtar for her unconditional love and continued support, without her moral support during whole period of my studies and research work, it would not have been possible to come that far in my career. She boosted my confidence in my hard times and advised me to stay humble in my happy times.

I would like to thanks Almighty Allah for giving me ability to undertake and complete my research work.

## TABLE OF CONTENTS

Title page	i
Original Literary Work Declaration Form	ii
Abstract	iii
Abstrak	v
Acknowledgements	vii
Table of Contents	viii
List of Figures	xiii
List of Tables	xix
List of Symbols and Abbreviations	xxi
List of Appendices	xxiv
<b>CHAPTER 1: INTRODUCTION</b>	<b>1</b>
1.1 Research background	1
1.2 Scope of work	5
1.3 Aim of study	5
1.4 Research objectives	6
1.5 Organization of the thesis	6
1.6 Summary	8
<b>CHAPTER 2: LITERATURE REVIEW</b>	<b>9</b>
2.1 Municipal solid waste and landfill gas	9
2.2 Dry reforming of methane	12
2.3 Reaction chemistry and carbon deposition	15
2.4 Design of catalyst	18
2.4.1 Setting goals for catalyst design	18
2.4.2 Target reaction	19
2.4.3 Stoichiometric analysis	20



2.4.4	Primary reactant reactions	20
2.4.5	Reactant self-interaction reactions	20
2.4.6	Reactant cross-interaction reactions	21
2.4.7	Reactant-product interaction	21
2.4.8	Product-product reactions	22
2.4.9	Network of reaction	22
2.5	Influence of parameters on catalytic activity	23
2.5.1	Influence of active metal on catalytic activity	24
2.5.2	Influence of support on catalytic activity	34
2.5.3	Influence of calcination temperature on catalytic activity	41
2.6	Catalyst preparation methods	51
2.6.1	Impregnation	53
2.6.2	Co-precipitation	53
2.6.3	Deposition	54
2.6.4	Ion-exchange	54
2.6.5	Microemulsion	54
2.7	Strategy for nanoparticles preparation by microemulsion synthesis	57
2.8	Influence of various factors on the synthesis of nanoparticles	58
2.8.1	Water content	58
2.8.2	Surfactant types	61
2.8.3	Compatibility of surfactant and oil	64
2.8.4	Effect of aging time	66
2.8.5	Effect of temperature	67
2.8.6	Metal salt concentration	68

2.9	Types of microemulsion	69
2.10	Mechanism	70
2.11	Preparation of catalysts via microemulsion synthesis	72
2.12	Summary	77
<b>CHAPTER 3: MATERIALS AND METHODS</b>		78
3.1	Introduction	78
3.2	<b>Part 1: Synthesis of Ni nanoparticles and 20%Ni/MgO at different preparation parameters (water/surfactant ratio, aging time, calcination temperature, molar concentration) and investigating their catalytic activity and characterization.</b>	79
3.2.1	Materials and chemicals	79
3.2.2	Preparation of Ni nanoparticles	79
3.2.3	Preparation of Ni/MgO catalyst	80
3.2.4	Catalyst characterization	82
	3.2.4.1 Surface area and pore volume	82
	3.2.4.2 X-Ray diffraction	83
	3.2.4.3 Temperature-programmed reduction	84
	3.2.4.4 Temperature-programmed desorption	85
	3.2.4.5 Transmission electron microscopy	85
	3.2.4.6 Scanning electron microscopy	86
3.3	Catalytic activity test	86
3.4	<b>Part 2: An investigation on the influence of catalyst composition, calcination and reduction temperatures on Ni/MgO catalyst for dry reforming of methane.</b>	88
3.4.1	Catalyst preparation	89
3.4.2	Experimental setup	90

3.5	<b>Part 3: Water-in-oil microemulsion synthesis of Ni@CeO<sub>2</sub> core-shell like structures for dry reforming of methane.</b>	90
3.5.1	Materials and chemicals	90
3.5.2	Catalyst preparation	90
3.5.3	Catalytic activity test	91
	<b>CHAPTER 4: RESULTS AND DISCUSSION</b>	93
	<b>Part 1: Synthesis of Ni nanoparticles and 20%Ni/MgO at different preparation parameters (water/surfactant ratio, aging time, calcination temperature, molar concentration) and investigating their catalytic activity and characterization.</b>	93
4.1	Characterization of fresh catalyst	93
4.1.1	Surface area and pore volume	93
4.1.2	X-ray diffraction	95
4.1.3	Temperature-programmed reduction	97
4.1.4	Temperature-programmed desorption	98
4.1.5	TEM and EDX analysis	100
4.2	Influence of different microemulsion parameters	100
4.2.1	Effect of surfactant, water and oil composition	100
4.2.2	Effect of aging time	104
4.2.3	Effect of calcination temperature	104
4.2.4	Effect of molar concentration	106
4.3	Activity and stability test	107
4.4	Characterization of spent catalyst	112
4.5	Summary	116

<b>Part 2: An investigation on the influence of catalyst composition, calcination and reduction temperatures on Ni/MgO catalyst for dry reforming of methane.</b>	116
4.6 Characterization of fresh catalyst	116
4.6.1 X-ray diffraction	116
4.6.2 Surface area and pore volume	117
4.6.3 Temperature-programmed reduction	119
4.6.4 Temperature-programmed desorption	121
4.6.5 TEM and EDX analysis	122
4.7 Activity and stability test	124
4.8 Characterization of spent catalyst	134
4.9 Summary	138
<b>Part 3: Water-in-oil microemulsion synthesis of Ni@CeO<sub>2</sub> core-shell like structures for dry reforming of methane.</b>	149
4.10 Characterization of fresh catalyst	139
4.10.1 X-ray diffraction	139
4.10.2 Surface area and pore volume	140
4.10.3 Temperature-programmed reduction	142
4.10.4 Transmission electron microscopy	143
4.11 Activity and stability test	145
4.12 Characterization of spent catalyst	151
4.13 Summary	157
<b>CHAPTER 5: CONCLUSIONS AND RECOMMENDATIONS FOR FUTURE WORK</b>	158
5.1 Introduction	158
5.2 Recommendations for future work	160
REFERENCES	162-189
APPENDICES A-G	190-195

## LIST OF FIGURES

Figure 2.1:	Municipal solid waste generation in Malaysia	9
Figure 2.2:	Composition of Malaysian Municipal solid waste	10
Figure 2.3:	Estimated methane and carbon dioxide emissions (thousand tonnes/year) by MSW.	11
Figure 2.4:	Simplified block diagram for dry reforming of methane	14
Figure 2.5:	(a) Equilibrium gas composition of $\text{CO}_2/\text{CH}_4$ (1:1) and 1 atm; (b) Effect of $\text{CO}_2/\text{CH}_4$ feed ratio on carbon deposition limit temperature at various pressures.	17
Figure 2.6:	TPH profiles for 3 mol% Ni/MgO catalyst at different contact times (2 min, 30 min and 60 min)	18
Figure 2.7:	Strategy of catalyst design	19
Figure 2.8:	(a) XRD profiles of the catalyst (1) before and (2) after activity test and (b) TEM image of the catalyst after the activity test	25
Figure 2.9:	XRD profiles of alumina support (a) and spent catalysts (b) 4Ni/ $\text{Al}_2\text{O}_3$ (c) 0.04Pt4Ni/ $\text{Al}_2\text{O}_3$ (d) 0.4Pt4Ni/ $\text{Al}_2\text{O}_3$ (e) 0. 4Pt/ $\text{Al}_2\text{O}_3$	27
Figure 2.10:	The influence of calcination duration on (a) $\text{Mo}_2\text{C}/\text{SiO}_2$ and (b) $\text{Mo}_2\text{C}/\text{Al}_2\text{O}_3$ (•) 4 and (°) 24 h	43
Figure 2.11:	XRD patterns of impNiO/MgO catalyst	47
Figure 2.12:	TPR profiles of fresh Ni-Ce/ $\text{SiO}_2$ catalyst	49
Figure 2.13:	Effect of calcination temperatures on $\text{H}_2$ yield	50
Figure 2.14:	The relationship between particle size and specific surface area for Ni ( $\rho = 8900 \text{ kg/m}^3$ )	52




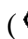

Figure 2.15:	Microemulsion schematics for water in oil and oil in water.	55
Figure 2.16:	Structure of reverse micelles	56
Figure 2.17:	Description of nanoparticles synthesis from the microemulsion route	58
Figure 2.18:	Influence of water content and oil type on copper particle diameter	61
Figure 2.19:	Types of surfactants based on their structure	61
Figure 2.20:	HLB values of different surfactants	64
Figure 2.21:	Phase diagram for water, cyclohexane and Igepal CO-520 system at 25 °C.	66
Figure 2.22:	Influence of reaction time on SiO <sub>2</sub> average diameter	66
Figure 2.23:	Maximum solubilisation of (a) Tween 85, (b) Igepal Co-520 (c) Triton X-114 in cyclohexane.	67
Figure 2.24:	The effect of temperature and composition of water and oil in the preparation of microemulsion.	68
Figure 2.25:	Schematics of dispersed and bicontinuous microemulsion a) water in oil dispersed b) water in oil bicontinuous c) oil in water bicontinuous d) oil in water dispersed.	69
Figure 2.26:	Micelle exchange mechanism	71
Figure 3.1:	(a,b) Microemulsion system containing Igepal CO-520, cyclohexane and Ni metal solution, (c) After addition of NH <sub>4</sub> OH in the microemulsion solution.	80
Figure 3.2:	Experimental methodology flow chart	81
Figure 3.3:	Adsorption/desorption isotherms for N <sub>2</sub> molecules	82
Figure 3.4:	X-ray diffraction principal	83

Figure 3.5:	Schematic diagram of experimental setup and dry reforming of methane unit.	87
Figure 4.1:	(a) N <sub>2</sub> adsorption-desorption isotherms (b) BJH pore width distribution of A2 and Cat1.	94
Figure 4.2:	(a) N <sub>2</sub> adsorption-desorption isotherms (b) BJH pore width distribution of NiO/MgO catalysts calcined at different temperatures.	95
Figure 4.3:	(a) XRD patterns for pure NiO particle, (b) XRD patterns of NiO/MgO catalysts prepared at different calcination temperatures. Where (✦) presents NiO-MgO solid solution, (◇) presents NiO crystallite peaks and (Δ) presents MgO crystallite peaks.	97
Figure 4.4:	(a) TPR profiles of pure Ni particles and (b) Ni/MgO catalyst calcined at different temperatures.	98
Figure 4.5:	TPD-CO <sub>2</sub> profiles of Ni/MgO catalyst calcined at different temperatures	99
Figure 4.6:	TEM images of the fresh Cat1	100
Figure 4.7:	EDX analysis of fresh A2 (a) and Cat1(b) before reduction.	100
Figure 4.8:	BET surface area for NiO particles at different aging time.	104
Figure 4.9:	BET surface area for NiO particles at different calcination temperature.	105
Figure 4.10:	BET surface area for NiO particles at different Ni molar concentration	107
Figure 4.11:	Methane and carbon dioxide conversion with respect to temperature for pure Ni and Ni/MgO catalyst.	107

Figure 4.12:	Methane and carbon dioxide conversion with respect to time at 750 °C for pure Ni and Ni/MgO catalysts calcined at different temperatures.	112
Figure 4.13:	XRD analysis of spent catalysts where (✦) presents NiO-MgO solid solution, (◇) presents Ni crystallite peaks and (☆) presents graphite crystallite peaks.	113
Figure 4.14:	TEM images of spent Cat1 (a,b,c) and FESEM images of Cat2 (d) after stability test.	115
Figure 4.15:	FESEM images of spent Cat3 (a,b) and pure Ni (c,d) after stability test.	115
Figure 4.16:	XRD patterns of calcined catalysts, where (✦), (◇), and (Δ) presents NiO-MgO solid solution peaks, NiO crystallite peaks and MgO crystallite peaks, respectively.	117
Figure 4.17:	(a) N <sub>2</sub> adsorption-desorption isotherms and (b) BJH pore width distribution of calcined catalysts.	118
Figure 4.18:	(a) N <sub>2</sub> adsorption-desorption isotherms and (b) BJH pore width distribution of calcined catalysts.	119
Figure 4.19:	TPR-H <sub>2</sub> profiles of (a) NiO and (b) Ni/MgO catalysts.	121
Figure 4.20:	TPD-CO <sub>2</sub> profiles for Ni/MgO catalysts.	122
Figure 4.21:	TEM images of freshly calcined catalysts (a,b) CS1 and (c,d) CS3.	123
Figure 4.22:	EDX analysis of (a) NiO, (b) CS1, (c) CS2 and (d) CS3 catalysts.	123
Figure 4.23:	Conversion-temperature relationship of different catalysts (Reaction conditions: CH <sub>4</sub> /CO <sub>2</sub> =1/1 and WHSV= 1.68 x 10 <sup>5</sup> ml g <sup>-1</sup> h <sup>-1</sup> ).	125



Figure 4.24:	Conversion-time relationship of different catalysts (Reaction conditions: 750 °C, CH <sub>4</sub> /CO <sub>2</sub> =1/1, WHSV= 1.68 x 10 <sup>5</sup> ml g <sup>-1</sup> h <sup>-1</sup> ).	128
Figure 4.25:	H <sub>2</sub> and CO yield of different catalysts (Reaction conditions: 750 °C, CH <sub>4</sub> /CO <sub>2</sub> =1/1, WHSV= 1.68 x 10 <sup>5</sup> ml g <sup>-1</sup> h <sup>-1</sup> ).	130
Figure 4.26:	XRD analysis of spent catalysts, where (✦), (◇) and (☆) presents NiO-MgO solid solution peaks, Ni crystallite peaks and graphite peaks, respectively.	135
Figure 4.27:	TEM and FESEM images of spent catalysts (a,b) CS1 and (c,d) CS2 after the dry reforming reaction at 750 °C.	137
Figure 4.28:	TEM images of spent catalysts (a,b) CS3, (c,d) CS5 and FESEM images of Ni (e,f) after the dry reforming reaction at 750 °C.	138
Figure 4.29:	XRD patterns of calcined catalysts, where (☆), and (Δ) presents CeO <sub>2</sub> peaks and NiO crystallite peaks, respectively.	140
Figure 4.30:	(a) N <sub>2</sub> adsorption-desorption isotherms and (b) BJH pore width distribution of calcined catalysts.	141
Figure 4.31:	TPR-H <sub>2</sub> profiles of (a) NiO and (b) Ni@CeO <sub>2</sub> catalysts.	142
Figure 4.32:	TEM images of freshly calcined catalysts (a,b,c) NC1 and (d,e,f) NC2, (g,h,k) NC3.	144
Figure 4.33:	Conversion-temperature relationship of different catalysts (Reaction conditions: CH <sub>4</sub> /CO <sub>2</sub> =1/1 and WHSV= 1.20 x 10 <sup>5</sup> ml g <sup>-1</sup> h <sup>-1</sup> ).	145
Figure 4.34:	Conversion-time relationship of different catalysts (Reaction conditions: 800 °C, CH <sub>4</sub> /CO <sub>2</sub> =1/1, WHSV= 1.20 x 10 <sup>5</sup> ml g <sup>-1</sup> h <sup>-1</sup> ).	147

Figure 4.35:	Oxygen transport mechanism reaction over Ni based ceria catalysts, where  indicates oxygen vacancy and  indicates occupied oxygen vacancy.	148
Figure 4.36:	H <sub>2</sub> /CO ratio of different catalysts (Reaction conditions: 800 °C, CH <sub>4</sub> /CO <sub>2</sub> = 1/1, WHSV= 1.20 x 10 <sup>5</sup> ml g <sup>-1</sup> h <sup>-1</sup> ).	150
Figure 4.37:	H <sub>2</sub> and CO yield of different catalysts (Reaction conditions: 800 °C, CH <sub>4</sub> /CO <sub>2</sub> = 1/1, WHSV= 1.20 x 10 <sup>5</sup> ml g <sup>-1</sup> h <sup>-1</sup> ).	151
Figure 4.38:	XRD analysis of spent catalysts, where (  ) , (  ) and (  ) presents graphite peaks, Ni crystallite peaks, CeO <sub>2</sub> peaks, respectively.	152
Figure 4.39:	TEM images of spent catalysts (a,b) NC1, (c,d) NC2 and (e,f) NC3 after stability test for 140 min at 800 °C.	154
Figure 4.40:	FESEM images of spent catalysts (a,b) NC1 and (c,d) NC2, (e,f) NC3 and (g) Ni catalysts after stability test.	156

## LIST OF TABLES

Table 2.1:	Primary reactant reactions in the dry reforming of methane.	20
Table 2.2:	Reactant self-interaction reactions.	21
Table 2.3:	Reactant cross-interaction reactions.	21
Table 2.4:	Reactant- product reactions.	21
Table 2.5:	Product-product reactions.	22
Table 2.6:	Influence of active metals on catalytic activity.	29
Table 2.7:	Influence of supports on catalytic activity.	37
Table 2.8:	Influence of calcination temperature on catalytic activity and stability.	45
Table 2.9:	Miscibility data of different surfactant with oil phases at 25 °C.	63
Table 2.10:	Miscibility data of different surfactant with oil phases at 60 °C.	63
Table 2.11:	Different catalysts prepared by microemulsion synthesis approach	76
Table 4.1:	Physical characteristics of NiO particles prepared at different microemulsion composition.	95
Table 4.2:	Physical characteristics of NiO particles, MgO and NiO/MgO catalysts prepared at different calcination temperatures.	95
Table 4.3:	Initial and final reactants conversion along with their carbon deposition at different calcination and reaction temperatures.	112
Table 4.4:	BET surface area, total pore volume and XRD crystallite size of calcined catalysts.	119

Table 4.5:	Reduction peaks temperatures and reducibility of Ni/MgO catalysts.	120
Table 4.6:	Activity and stability of Ni/MgO catalysts at $\text{CH}_4/\text{CO}_2 = 1/1$ and $\text{WHSV} = 1.68 \times 10^5 \text{ ml g}^{-1} \text{ h}^{-1}$ .	133
Table 4.7:	Comparison of catalytic activity of previous studies with Ni/MgO catalysts.	133
Table 4.8:	BET surface area, total pore volume and average XRD crystallite size of catalysts.	141
Table 4.9:	Activity and stability of Ni@CeO <sub>2</sub> catalysts at $\text{CH}_4/\text{CO}_2 = 1/1$ and $\text{WHSV} = 1.20 \times 10^5 \text{ ml g}^{-1} \text{ h}^{-1}$ .	146

## LIST OF SYMBOLS AND ABBREVIATIONS

$\Delta H_{298K}^{\circ}$	-	Change of enthalpy (kJ/mol)
$T_c$	-	Calcination temperature ( $^{\circ}\text{C}$ )
$\Delta G_{\text{rxn}}^{\circ}$	-	Gibbs free energy of reaction (kJ/mol)
M	-	Medium
$T_{\text{reac}}$	-	Reaction temperature ( $^{\circ}\text{C}$ )
$T_{\text{red}}$	-	Reduction temperature
t	-	time (h)
$F_{\text{feed}}$	-	Total feed flow rate (ml/h)
T	-	Temperature ( $^{\circ}\text{C}$ )
BET	-	Brunaur-Emmett-Teller
CNG	-	Compressed natural gas
CNT	-	Carbon nanotubes
CP	-	Co-precipitation
CM	-	Commercial
DBT	-	Dibenzothiophene
DHT	-	Direct hydrothermal synthesis
EO	-	Ethylene oxide
EDX	-	Energy- dispersive X-ray spectroscopy
FBR	-	Fixed bed reactor

FIBR	-	Fluidized bed reactor
FESEM	-	Field emission scanning electron microscopy
GHG	-	Green-house gases
HTM	-	Hard template method
HDS	-	Hydrodesulfurization
HLB	-	Hydrophile-lipophile balance
IMP	-	Impregnation
IMPCSG	-	Impregnation combined sol-gel
IPCC	-	Intergovernmental panel on climate change
IWIMP	-	Incipient wetness impregnation
LFG	-	Landfill gas
LNG	-	Liquefied natural gas
ME	-	Microemulsion
MVIMP	-	Multiplepore volume impregnation
MR	-	Microreactor
MSW	-	Municipal solid waste
NG	-	Natural gas
TB	-	Total blending
RWGS	-	Reverse water gas shift
RC	-	Reaction conditions

SG	-	Sol-gel
ST	-	Solvothermal approach
TPR-H <sub>2</sub>	-	Temperature-programmed reduction hydrogen
TPD-CO <sub>2</sub>	-	Temperature-programmed desorption carbon dioxide
TPH	-	Temperature programmed hydrogenation
TEM	-	Transmission electron microscopy
TCD	-	Thermal conductivity detector
WHSV	-	Weight hourly space velocity
XRD	-	X-ray diffraction
XPS	-	X-ray photoelectron microscopy

## LIST OF APPENDICES

Appendix A: N <sub>2</sub> Adsorption-desorption isotherms for the NiO nanoparticle prepared at different microemulsion compositions.	190
Appendix B: N <sub>2</sub> Adsorption-desorption isotherms for the NiO nanoparticle prepared at different aging times.	191
Appendix C: N <sub>2</sub> Adsorption-desorption isotherms for the NiO nanoparticle prepared at different calcination temperatures.	192
Appendix D: N <sub>2</sub> Adsorption-desorption isotherms for the NiO nanoparticle prepared at different molar concentrations.	192
Appendix E: Methane and carbon dioxide conversions of Ni/MgO catalyst at 800 °C with respect to time.	193
Appendix F: Methane and carbon dioxide conversions of Ni/MgO catalyst at 850 °C with respect to time.	193
Appendix G: Calculation of Gibbs free energy and enthalpy of reaction.	194



## CHAPTER 1: INTRODUCTION

### 1.1 Research background

Malaysia has a total land area of 328,550 km<sup>2</sup> and a population of approximately 27 million. The increase in population, industrialization and urbanization has led to the increase in municipal solid waste (MSW) considerably during the years. An increase of 2.4 million tons was reported in 2010 (8 Million ton) from the previously recorded 5.6 million tons in 1997 and it was estimated that it will increase to 9 million tons of MSW in 2020 (Noor et al., 2013). The analysis of the Malaysian MSW composition indicates that it contained huge amount (37.43%) of biodegradable components (food waste and paper), which creates a favourable environment for the generation of biogas or landfill gas (Johari et al., 2012).

Anaerobic decomposition of organic content in MSW leads to the generation of landfill gas consisting of methane (50-55%) and carbon dioxide (40-45%) (Johari et al., 2012). Methane and carbon dioxide constitute a major part of greenhouse gases (GHG) and are considered to have the key contribution in climate-change. In this present scenario, methane and carbon dioxide (GHG) produced by the decomposition of MSW can be utilized in a process known as dry reforming of methane (equation 1.1).



Dry reforming of methane leads to the generation of synthesis gas (H<sub>2</sub>/CO), which is a major building block for many hydrocarbons, liquid fuels and oxygenated chemicals. Moreover, hydrogen (H<sub>2</sub>) can separated from syn-gas and utilized in the fuel cells to produce energy (Usman et al., 2015). The major challenge in the industrial application of this environmentally beneficial reaction is the occurrence of coke formation by routes of Boudouard reaction or methane decomposition (Al-Fatish et al., 2009; Gucci et al., 2010; Long Xu et al., 2014; M. Yu et al., 2014).

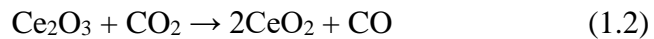
Dry reforming of methane has been investigated with noble (Rh, Ru, Pd and Pt) and non-noble metal (Ni, Co and Fe) catalysts (Y. J. Asencios et al., 2011; D. Liu, Quek, et al., 2009). Noble metal catalysts have drawn attention for their superior coking resistance, higher stability and activity especially for higher temperature applications ( $> 750\text{ }^{\circ}\text{C}$ ) (Djinović et al., 2011). However, noble metals with their superior carbon deposition resistance cannot be applied at the industrial scale due to their high-cost (Crisafulli et al., 2002). In this scenario, non-noble metal (Ni, Co, Fe) catalysts become a suitable alternative for industrial application due to low cost, however, these catalysts are more prone to carbon deposition due to the higher affinity of carbon to catalyst surface (Y. J. O. Asencios & Assaf, 2013; Helveg et al., 2011; D. Liu, Quek, et al., 2009).

Therefore, number of studies were conducted to optimize the process and also to search for new catalysts with improved catalyst performance in order to eliminate or attenuate carbon deposition. The research is mainly focused on the nature of support, preparation methods, conditions of pretreatment and also the application of different promoters in the catalyst to have better catalytic activities with lower carbon deposition (Castro Luna & Iriarte, 2008; Zhu et al., 2012). The literature suggests that the structure and surface properties of the support play an important role in the enhancement of catalytic activity (Santos et al., 2005). Previous study suggested that the issue of carbon deposition can be tackled by the application of basic metal oxides (MgO, CaO, and BaO) as support materials, because the application of acidic supports ( $\text{Al}_2\text{O}_3$ ) (Tsipouriari et al., 1996) favor the occurrence of carbon deposition (Hu & Ruckenstein, 2002).

The basic nature of MgO employed for dry reforming assisted in the gasification of carbon species by enhancing  $\text{CO}_2$  chemisorption due to its acidic nature, which resulted in the suppression of carbon deposition without adding extra cost (Hu & Ruckenstein, 2002; Lucrédio et al., 2011; Özdemir, Öksüzömer, & Ali Gürkaynak, 2010; Zanganeh et al., 2013). Moreover, MgO has been considered a suitable support material due to its low

cost, high stability and high basicity (Hu & Ruckenstein, 2002). Among all these basic metal oxides (MgO, CaO, and BaO), only MgO has the same lattice parameters as NiO, therefore, both of these metal oxides will form solid solution at any molar ratio, however, the formation of solid solution strongly depends on the calcination temperature, preparation history and weight percentage of Ni. The formation of NiO-MgO solid solution has a considerable influence over the size control and on the formation of Ni<sup>0</sup> particles (Hu & Ruckenstein, 2002; Y. Li et al., 2014).

Furthermore, bifunctionality of ceria (CeO<sub>2</sub>) was reported for metal nanocrystalline doped CeZrO<sub>2</sub> oxides (Bobin et al., 2013). The study suggested that the dissociation of CO<sub>2</sub> occur on reduce oxide support and methane activation occurs on metal active sites. The main attraction in the application of ceria as support material is its higher oxygen storage capacity, which assists in the oxidation of coke (Abasaeed et al., 2015; A Kambolis et al., 2010). The unique redox properties of CeO<sub>2</sub> imparted by quick reduction creates oxygen vacancies on CeO<sub>2</sub> metal oxide, which provides additional driving force for conversion of CO<sub>2</sub> to CO under reducing atmosphere (Ay & Üner, 2015; de Leitenburg et al., 1997). The basic nature of CeO<sub>2</sub> will assist in the enhancement of CO<sub>2</sub> adsorption, thus CO<sub>2</sub> can be reduced easily due to the oxygen vacancies on CeO<sub>2</sub> support (Tada et al., 2012). Previous studies suggested that the following reactions are possible between reactants and support as described in equation 1.2 (Abasaeed et al., 2015; Khajenoori et al., 2014; M. Rezaei et al., 2009)



Moreover, the coke formed via the route of methane decomposition can be oxidize by CeO<sub>2</sub> as it provides lattice oxygen during the reforming reaction described below in equation 1.3 (Khajenoori et al., 2014):



Thus, it would be interesting to develop Ni-based catalysts encapsulated in a non-silica metal oxide such as CeO<sub>2</sub> to exhibit bifunctional mechanism, as previous studies were mostly on the synthesis of Ni nanoparticles encapsulation in SiO<sub>2</sub> having monofunctional mechanism (both methane and carbon dioxide activated by metal alone) (Theofanidis et al., 2015). Another important feature of CeO<sub>2</sub> is its high stability, low cost and its ability to provide active oxygen due to its unique electronic configuration (S. Song et al., 2015). However, the role and behavior of widely discussed NiO-MgO solid solution and also the synthesis of Ni@CeO<sub>2</sub> catalyst is not yet investigated for the catalyst prepared by microemulsion synthesis approach.

Water-in-oil (W/O) microemulsion is considered as a system in which nanosize water droplets (dispersed phase) are present in continuous phase (oil) and stabilized by surfactant molecules. Transparent nature and thermodynamic stability are salient features of microemulsion system, a microenvironment is created by this unique type of surfactant covered water droplets, which inhibit the agglomeration of synthesized nanoparticles (D.-H. Chen & Wu, 2000; Eriksson et al., 2004). The advantages of microemulsion synthesis approach over precipitation method, sol-gel process, hydrothermal method are its superior control over the morphology of the nanoparticles (Chandradass & Bae, 2008; Shiraz et al., 2016) and also the synthesis of nanoparticles at room temperature is a very attractive feature of this approach (Eriksson et al., 2004). Furthermore, the application of precipitation method for the synthesis of metal oxides suffer from its complexity and also requires longer aging time, sol-gel process uses metal alkoxides as raw materials, which are expensive and also demands long gelation time, while, hydrothermal method requires high temperature and pressure (Chandradass & Bae, 2008).

To the best of my knowledge, none of the previous studies reported the preparation of Ni/MgO and Ni@CeO<sub>2</sub> catalyst by microemulsion system (water/IgepalCO-520/cyclohexane) and specifically applied for dry reforming of methane. The

main purpose of this study is to investigate Ni-based catalysts supported on basic metal oxide (MgO) and oxygen storage capacity metal oxide (CeO<sub>2</sub>) for dry reforming reaction synthesized by microemulsion synthesis approach. Therefore, in this study, we will investigate in detail the influence of water/surfactant ratio, aging time, calcination temperature and Ni metal concentration on the preparation of pure NiO nanoparticles by microemulsion synthesis approach. Thereafter, the study focuses on the synthesis of Ni/MgO and Ni@CeO<sub>2</sub> catalysts in the non-anionic W/O microemulsion system of water/IgepalCO-520/cyclohexane at different Ni metal content, calcination temperature and reduction temperature.

## **1.2 Scope of work**

Dry reforming of methane has been considered a suitable option for the utilization of landfill gas. However, the catalytic activity of dry reforming of methane is hampered by the catalytic deactivation raised from the coke deposition. In this study, Ni-based catalysts supported on MgO and CeO<sub>2</sub> are synthesized by water-in-oil microemulsion approach and applied to dry reforming of methane. The activity of catalysts with respect to temperature were investigated in the range of 550 to 850 °C. The long-term stability of catalysts was also investigated at three different temperatures (750, 800 and 850 °C). In this study, fresh and spent catalysts were characterized by various characterization techniques and also the influence of different Ni metal content on activity was also investigated. Furthermore, the influence of water/surfactant ratio, aging time, calcination temperature, Ni metal concentration was investigated to optimize Ni metal surface area.

## **1.3 Aim of study**

Synthesis of Ni-based catalysts supported on MgO and CeO<sub>2</sub> by microemulsion synthesis approach with the aim of attenuating carbon deposition.

## 1.4 Research objectives

The objectives of this project are to first optimize the synthesis parameters for the preparation of Ni nanoparticles and later on the preparation of Ni/MgO and Ni@CeO<sub>2</sub> catalysts. The major objectives of this project are listed down:

- ❖ To synthesize pure Ni nanoparticles by microemulsion synthesis approach at different composition of microemulsion system (water, oil and surfactant), aging time (0.5 to 24 h), calcination temperature (450 to 1000 °C) and Ni metal molar concentration (2M, 3M, 5M and 7M).
- ❖ To synthesize Ni/MgO catalyst at different weight percentage of Ni (20%, 40%, and 80 wt%), and investigate the influence of calcination temperature (450 °C, 600 °C and 800 °C) and reduction temperature (550 °C and 800 °C) on catalyst structure and also characterization of fresh Ni/MgO catalyst by various techniques.
- ❖ To investigate the synthesis of Ni@CeO<sub>2</sub> catalyst at different weight percentage of Ni content (20%, 40%, and 80 wt%) and their characterization studies by various techniques.
- ❖ Inspecting the catalyst performance of pure Ni, Ni/MgO and Ni@CeO<sub>2</sub> catalysts at different reaction temperatures (550 °C to 850 °C) and also investigating the catalyst stability in the temperature range of 750 °C to 850 °C.

## 1.5 Organization of the thesis

1. **Introduction** introduces the current status of municipal solid waste (MSW), methane and carbon dioxide emissions and the application of dry reforming of methane to utilize these gases. This chapter also briefly discusses the microemulsion synthesis approach and also the application of basic metal

oxides as support materials. Moreover, research objectives, scope of work and aim of study are also described in this chapter.

2. **Literature review** This chapter reviews and summarizes the landfill sites, MSW generation, estimated methane emission, significance of dry reforming of methane and also describes the microemulsion synthesis approach in details. Furthermore, reaction chemistry, types of deposited carbon, design of catalysts and influence of different parameters on catalytic activity were discussed.
3. **Materials and methods** list down all the reagents, solvents and gases used during the catalyst preparation and catalytic activity experiments. Moreover, details of the characterization techniques employed, procedure and equipment being used are discussed in detail.
4. **Results and discussion** This chapter represents all the characterization results regarding the synthesis of Ni nanoparticles and also the supported catalysts. Furthermore, catalytic activity and stability of the synthesized catalysts are discussed in detail along with the description of the deposited carbon.
5. **Conclusions and recommendations for future work** This chapter includes conclusion and future recommendations based on the findings during the study.

## 1.6 Summary

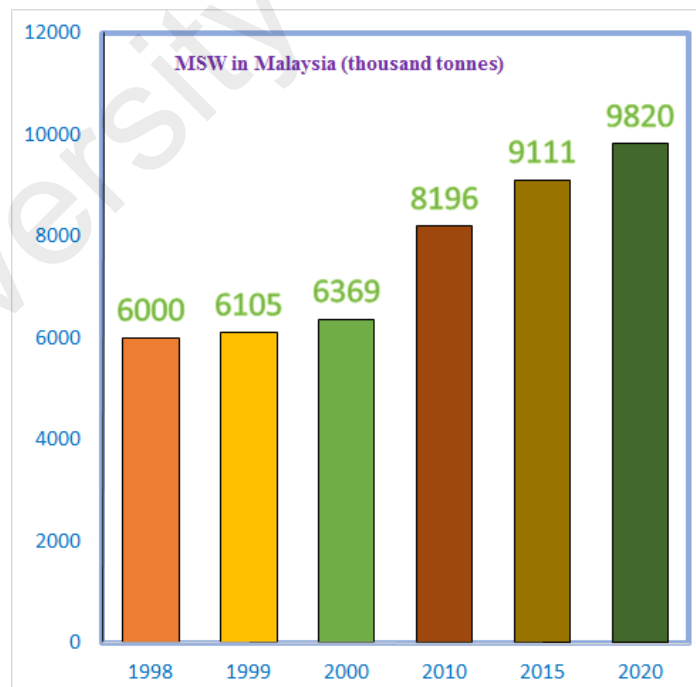
This study focuses on the utilization of two major greenhouse gases (methane and carbon dioxide) produced by the anaerobic decomposition of MSW in the landfill sites. The utilization of landfill gas via dry reforming of methane attains a great attention of researchers as it has the potential to utilize these gases to produce valuable syn-gas ( $H_2/CO$ ). The preparation of Ni/MgO and Ni@CeO<sub>2</sub> catalysts via microemulsion synthesis approach will also enhance the understanding of the structural behaviour of these catalysts at different synthesis parameters.



## CHAPTER 2: LITERATURE REVIEW

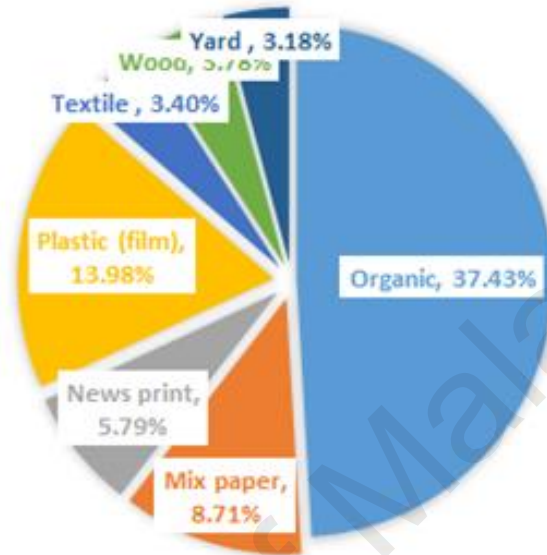
### 2.1 Municipal solid waste and landfill gas

Rapid population growth has resulted in the increased rate of waste generation and improper handling of waste created environmental issues. Municipal solid waste (MSW) has been a major challenge for Malaysia (Saeed et al., 2009) with an enormous increasing rate of 0.5-0.8 to 1.7 kg/person/day and generated around 17,000 tonnes per day of MSW in 2002 (6.2 million tonnes/year) (Hussain et al., 2006; Manaf et al., 2009). Bases on the previous data available between 1998 and 2000, it was estimated that in 2010, 2015 and 2020 peninsular Malaysia will generate around 8,196,000 tonnes, 9,111,000 and 9,820,000 tonnes, respectively. Figure 2.1 shows the detailed trend of estimated MSW generation until 2020 based on average generation rate of 2.14% recorded between 1998 and 2000. (Johari et al., 2012).



**Figure 2.1:** Municipal solid waste generation in Malaysia

The interesting feature of Malaysian MSW is the higher organic content (37.43%) present in the MSW as shown in Figure 2.2, which is deemed suitable for anaerobic digestion (Abd Kadir et al., 2013; Johari et al., 2012; Kathirvale et al., 2004; Noor et al., 2013).



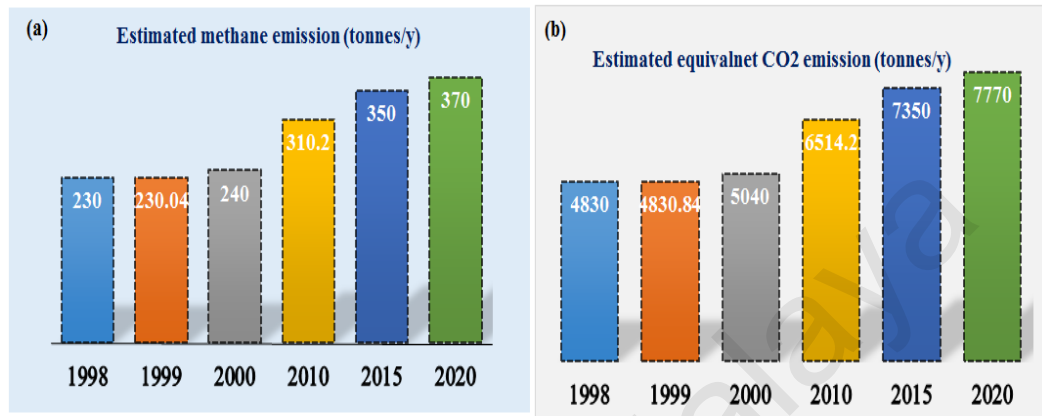
**Figure 2.2:** Composition of Malaysian municipal solid waste.

Disposal of MSW in the landfill sites leads to the generation of landfill gas (methane and carbon dioxide) by anaerobic degradation of the organic content in the waste as shown in equation 2.1 (Abushammala et al., 2011).



Landfill gas consists of 40-45% methane and 55-60% carbon dioxide by volume (Raco et al., 2010), while some predicted 50-60% and 30-40% by volume of methane and carbon dioxide, respectively (Wang-Yao et al., 2006). The methane emission based on MSW landfill in peninsular Malaysia was calculated by using the Intergovernmental Panel on Climate Change (IPCC) methodology. MSW generation as expressed in Figure 2.1 were used to estimate the methane emission for the respective years. Furthermore, to calculate the equivalent  $\text{CO}_2$  emissions, methane emission was multiplied by 21 as the methane has 21 times more global warming potential than  $\text{CO}_2$  (Shin et al., 2005). For

example, in 2010, 8,196,000 tonnes of MSW generated will produce around 310,220 tonnes per year of methane emission with equivalent CO<sub>2</sub> emission of 6514.2 tonnes per year. Both methane and carbon dioxide emissions for respective years are shown in Figure 2.3 (Johari et al., 2012).



**Figure 2.3:** Estimated methane and carbon dioxide emissions (thousand tonnes/year) by MSW.

Methane and carbon dioxide constitute a major part of GHG and have key contributions in climate-change (Noor et al., 2013), forecasted in terms of greater incidence and magnitude of hurricanes, floods, and droughts (McCarthy et al., 2001), affecting productivity, natural ecosystems, agriculture, rangelands, forestry and society (Montagnini & Nair, 2004; Parry, 2007). An increase of 0.8 °C in global surface temperature occurred in the 20th century and further increase (1.4-5.8 °C) has been anticipated in twenty-first century (McCarthy et al., 2001; Parry, 2007).

There are different opinions to utilize this valuable local source of renewable energy and one of them is the energy production by incineration of MSW, despite of its advantages it is not yet to be considered as a carbon neutral process. It is estimated that 1 ton of MSW incineration leads to the generation of 1 ton of CO<sub>2</sub> (Abd Kadir et al., 2013), moreover; the higher moisture content in the Malaysian MSW leads to the disruption of the incineration operation and requires additional costs to pretreat the feedstock to remove moisture. Furthermore, the higher CO<sub>2</sub> content in landfill gas limits its use for energy

generation as it decreases the heating value and flame stability of the gas mixture. Due to the aforementioned issues, the combustion of landfill gas in an engine, turbine or boiler leads to the increase in concentrations of CO, NO<sub>x</sub> and unburned hydrocarbons compared to pure CH<sub>4</sub> or natural gas (Kohn et al., 2011). Another option is to separate CO<sub>2</sub> from landfill gas stream to produce pure CH<sub>4</sub> and use it as a natural gas replacement or further process it to compressed natural gas (CNG) or liquefied natural gas (LNG), which can be used as a transportation fuel. The separation of CO<sub>2</sub> is executed by membrane separation, pressure swing absorption (PSA) or amine scrubbing. To obtain CNG and LNG, methane is then compressed to 3000 Psi to produce CNG and then cooled further until methane liquefies to produce LNG. However, the process is expensive due to the higher compression and cryogenic temperature requirements and only economical feasible for the higher CH<sub>4</sub>/CO<sub>2</sub> flows (Tchobanoglous et al., 1993). Therefore, for these reasons landfill gas is often burned or flared on site and leads to the emissions of CO<sub>2</sub> and H<sub>2</sub>O without utilizing the latent chemical energy of landfill gas. Landfill gas is a significant source of renewable energy to be utilized, and the development and commercialization of a reforming technology would serve to vastly improve the efficiency of landfill gas utilization. Therefore, it will be beneficial to utilize these problematic GHGs (CH<sub>4</sub> and CO<sub>2</sub>) in an efficient manner to attenuate their effects and also combat with the issues of energy shortage. In this scenario, catalytic reforming of landfill gas is an attractive option that has the potential of fully utilizing the latent chemical energy in the landfill gas.

## **2.2 Dry reforming of methane**

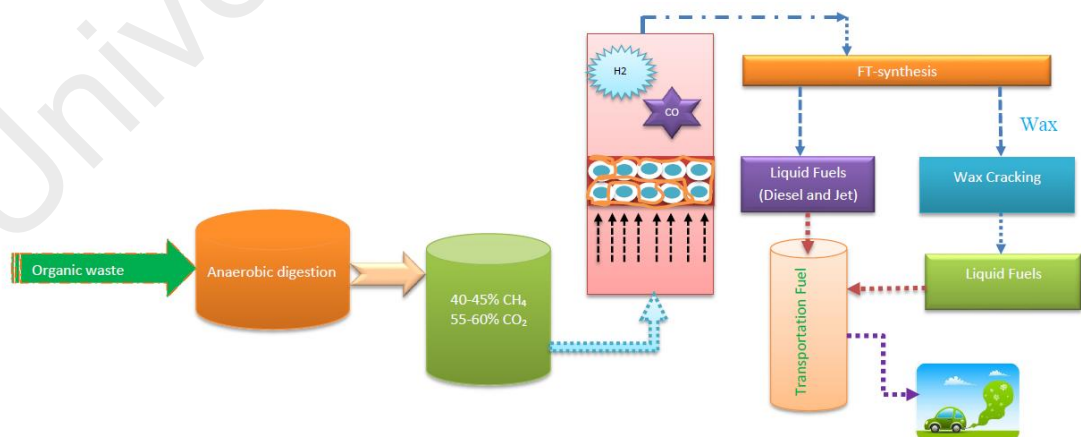
Various technologies are available to produce synthesis gas (syn-gas) from the sources having high content of methane (D. Li et al., 2011), as syn-gas is a building block for valuable liquid fuels and chemicals such as Fischer-Tropsch oil, methanol and dimethyl ether (Lunsford, 2000; Pena et al., 1996; Rostrup-Nielsen, 1993). The three

processes that draw industrial attention are steam reforming of methane (equation 2.2), partial oxidation of methane with oxygen or air (equation 2.3) and dry reforming of methane with carbon dioxide (equation 2.4) (Y. J. O. Asencios & Assaf, 2013).



Reforming of methane through steam or partial oxidation of methane with oxygen or air are well-established technologies with the advantages and disadvantages (Djinović, Osojnik Črnivec, et al., 2012; Wilhelm et al., 2001). Steam reforming of methane produces a higher ratio of syn-gas ( $\text{H}_2/\text{CO} = 3$ ) (Gangadharan et al., 2012) compared to that required for Fischer-Tropsch or methanol synthesis ( $\text{H}_2/\text{CO} = 2$ ) (Olah et al., 2012; Oyama et al., 2012). The process is energy intensive due to the endothermic nature and requires high investments of capital (Nieva et al., 2014). A higher  $\text{H}_2\text{O}/\text{CH}_4$  ratio is required to produce higher yields of hydrogen, which makes steam reforming of methane energetically unfavourable leading to the deactivation of the catalyst (Carvalho et al., 2009). Moreover, steam reforming faces corrosion issues and requires a desulphurization unit (Djinović, Osojnik Črnivec, et al., 2012; Wilhelm et al., 2001). Partial oxidation of methane is suitable for the production of heavier hydrocarbons and naphtha (Djinović, Osojnik Črnivec, et al., 2012; Larimi & Alavi, 2012). The advantages of this process are high conversion rates, high selectivity and very short residence time (Eli Ruckenstein & Hang Hu, 1999). The exothermic nature of reaction induces hot spots on catalyst arising from poor heat removal rate and makes operation difficult to control (Y. J. O. Asencios & Assaf, 2013; Wilhelm et al., 2001). Desulphurization unit is not required in the partial oxidation of methane (Wilhelm et al., 2001), but a cryogenic unit is necessary for the separation of oxygen from air (Djinović, Osojnik Črnivec, et al., 2012).

The utilization of landfill gas in dry reforming of methane will result in the efficient utilization of the energy content of methane trapped inside organic matter and efficient management of MSW resulting in reduced greenhouse emission. Dry reforming of methane offers valuable environmental benefits such as: landfill gas utilization (Kohn et al., 2014; Lucredio et al., 2012), removal of GHG (methane and carbon dioxide) and conversion of NG with a high carbon dioxide content to valuable syn-gas (M. C. J. Bradford & Vannice, 1999; Lunsford, 2000). Simplified block diagram for the dry reforming process is shown in Figure 2.4. Dry reforming of methane yielded a lower syn-gas ratio ( $H_2/CO = 1$ ), which is suitable for the synthesis of oxygenated chemicals (Wurzel et al., 2000) and hydrocarbons from Fischer-Tropsch synthesis (Oyama et al., 2012). Syn-gas from dry reforming has also been considered for storage of solar or nuclear energy (Chubb, 1980; Fraenkel et al., 1986; Levy et al., 1992) through the chemical energy transmission system (CETS). Solar energy can convert feed gases (methane and carbon dioxide) to syn-gas that can be exported to places where energy sources are scarce. The energy stored in syn-gas is liberated by the backward reaction and utilized as an energy source (Fraenkel et al., 1986).



**Figure 2.4:** Simplified block diagram for dry reforming of methane.

### 2.3 Reaction chemistry and carbon deposition

The major obstacle in the industrial application of this environmentally beneficial reaction is the occurrence of coke formation by routes of methane decomposition (equation 2.5) and Boudouard reaction (equation 2.6) (Al-Fatish et al., 2009; Guczi et al., 2010; Long Xu et al., 2014). Moreover, it has been suggested that dry reforming of methane has more tendency to form carbon deposits due to the absence of H<sub>2</sub>O and lower H/C ratio in the reactant feed (D. Liu, Lau, et al., 2009).



The tendency towards carbon deposition can be estimated by the ratio of O/C and H/C in the feed gas. The higher tendency towards carbon deposition will be observed in lower O/C and H/C ratio (D. Li et al., 2011), which is the case in dry reforming of methane (CH<sub>4</sub>/CO<sub>2</sub> = 1/1) having O/C = 1 and H/C = 2. Reverse case was observed for steam reforming of methane (CH<sub>4</sub>/H<sub>2</sub>O = 1/1) having high O/C = 1 and H/C = 6 (Pena et al., 1996). Similarly, partial oxidation of methane (CH<sub>4</sub>/0.5O<sub>2</sub>) showed a quite higher ratio, O/C = 1 and H/C = 4. Considering the aforementioned ratios, it was clear that dry reforming of methane has a higher tendency towards carbon deposition compared to steam reforming and partial oxidation of methane (J. Edwards & A. Maitra, 1995). The production of syn-gas from dry reforming of methane is influenced by the simultaneous occurrence of reverse water gas shift (RWGS) reaction (equation 2.7) resulting in a syn-gas ratio less than unity (M. C. J. Bradford & Vannice, 1999).



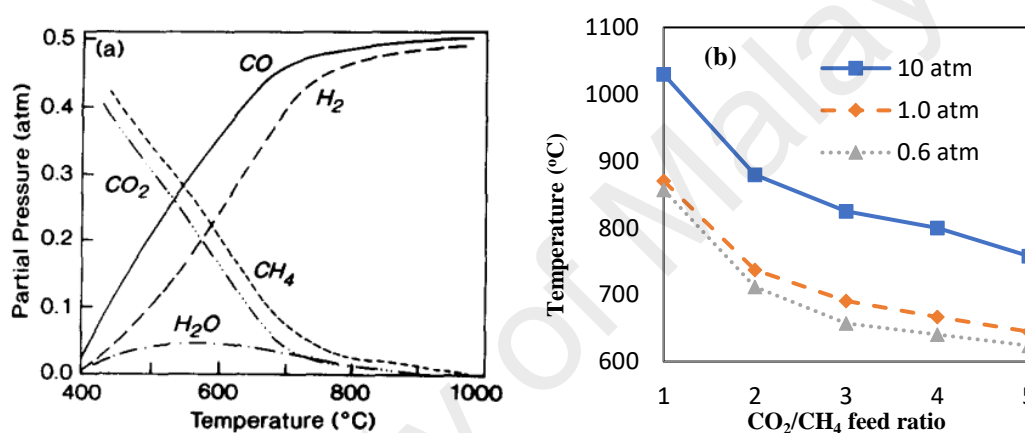
Moreover, it has been suggested that deposited coke may have different structure order, morphologies and reactivity depending upon the reaction conditions and catalyst structure (Guo et al., 2007). It is suggested that the reforming of hydrocarbon on Ni catalysts leads to the production of filamentous carbon and encapsulating carbon species.

In terms of degree of toxicity, the former is considered to be the less toxic form the point of view of deactivation process (D. Chen et al., 2001; Frusteri et al., 2002; Tsang et al., 1995). Encapsulating (shell-like) carbon causes the deactivation of the catalysts by decreasing the total number of active sites. The challenge lies in the synthesis of highly stable nanoparticles to prevent from rapid sintering and also the minimization of the coke formation or produce active type of carbon that does have little effect on catalyst stability and have little toxicity.

Thermodynamic studies on dry reforming reaction revealed that spontaneous reaction cannot be achieved below 640 °C (Tsang et al., 1995) and the side reactions (equation 2.5) and (equation 2.6) took place at a significant rate between 633 and 700 °C. Therefore, a higher temperature ( $T \geq 700$  °C) was employed to minimize the effect of side reactions, which lead to reactor blockages and reduction in activity (San José-Alonso et al., 2013; J. Zhang et al., 2007). Another study reported little higher temperature than the previously mentioned (Djinović, Osojnik Črnivec, et al., 2012). They proposed that to minimize the effect of RWGS (equation 2.7) and increase  $H_2$  yield, a higher temperature ( $> 750$  °C) or a higher ratio of  $CH_4/CO_2$  ( $> 1$ ) should be used (Djinović, Osojnik Črnivec, et al., 2012). However, a higher ratio of  $CH_4/CO_2$  created operational complexities such as an increased amount of carbon deposition (M. C. J. Bradford & Vannice, 1999), and the need for a separation system downstream to collect and recycle the surplus methane (Djinović, Osojnik Črnivec, et al., 2012). The reforming of methane at 1 atm and  $CO_2/CH_4 = 1$  (Figure 2.5a) assumed that reacting mixture was in equilibrium regarding the reactions from equation 2.5 to equation 2.7. The formation of water ( $< 900$  °C) from the reaction (equation 2.7) resulted in lower  $H_2$  yield compared with CO, while at 900 °C, methane conversion reached 97% and production of water becomes negligible after 900 °C (Fraenkel et al., 1986). The temperature limits for carbon deposition were also investigated (Figure 2.5b) with respect to pressure (0.6, 1, 10 atm) and feed gas ratios



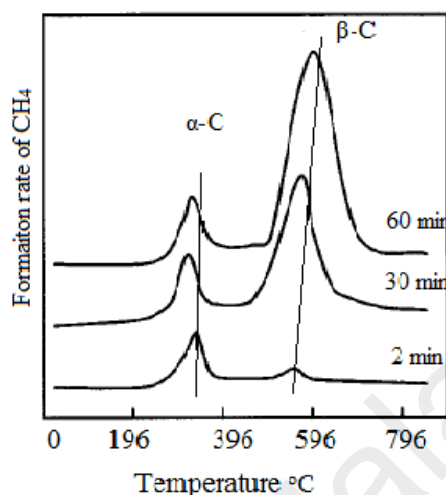
( $\text{CO}_2/\text{CH}_4$ ) (Gadalla & Bower, 1988). When the reforming reaction was performed at 1 atm and  $\text{CO}_2/\text{CH}_4 = 1$ , carbon deposition was unavoidable at temperatures lower than 870 °C. The rise of pressure from 1 atm to 10 atm lead to the increased carbon deposition limit from 870 °C to 1030 °C, which confirmed that for the same feed ratio, an increase in pressure will increase the temperature limit for carbon deposition. Moreover, decreasing  $\text{CO}_2/\text{CH}_4$  ratios at a constant pressure also increased the temperature limit for carbon deposition (Figure 2.5b) (Gadalla & Bower, 1988).



**Figure 2.5:** (a) Equilibrium gas composition of  $\text{CO}_2/\text{CH}_4$  (1:1) and 1 atm (Fraenkel et al., 1986); (b) Effect of  $\text{CO}_2/\text{CH}_4$  feed ratio on carbon deposition limit temperature at various pressures (Gadalla & Bower, 1988).

Different types of carbon were produced during the dry reforming of methane.  $\text{Ni}/\text{Al}_2\text{O}_3$  exhibited three types of carbonaceous species denoted as  $\alpha$ -C,  $\beta$ -C, and  $\gamma$ -C. It was suggested that  $\alpha$ -C assisted in the formation of CO, while less active carbon types ( $\beta$ -C and  $\gamma$ -C) leads to the deactivation of the catalyst (Z. L. Zhang & Verykios, 1994). Temperature programmed hydrogenation (TPH) of  $\text{Ni}/\text{MgO}$  (Figure 2.6) exhibited two peaks: first peak in the range of 300 to 310 °C was labelled as  $\alpha$ -C, while the second peak at slightly higher temperature (580 to 600 °C) was denoted as  $\beta$ -C, which exhibited less reactivity towards hydrogenation and oxidation than  $\alpha$ -C. It was concluded that different types of carbonaceous species played different roles in the dry reforming of methane.  $\beta$ -C being less reactive was referred to as a major contributor in the deactivation of the

catalyst. However,  $\alpha$ -C was increased with the proceeding of dry reforming reaction. This linear relation leads to the conclusion that  $\alpha$ -C may serve as reaction intermediate (Y.-G. Chen et al., 1997).

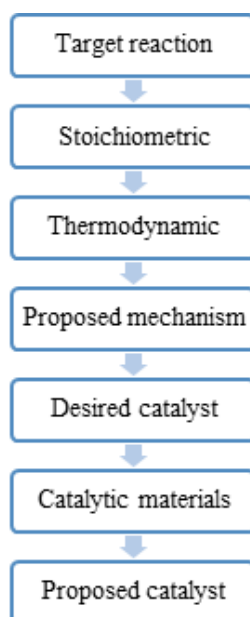


**Figure 2.6:** TPH profiles for 3 mol% Ni/MgO catalyst at different contact times (2 min, 30 min and 60 min) (Y.-G. Chen et al., 1997).

## 2.4 Design of catalyst

### 2.4.1 Setting goals for catalyst design

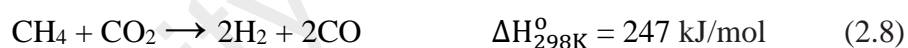
In order to prepare a suitable catalyst for dry reforming of methane an effective strategy for design of catalyst was proposed (Dowden et al., 1968). The major components of that strategy which should be followed are mentioned in Figure 2.7. The key points in the catalyst design are (1) to identify the desired catalyst functions; (2) suitable catalyst composition; and 3) the selection of active metal and support. In the following section, the key reactions in the dry reforming of methane were presented and also the influence of different active metal and support materials will be discussed in detail.



**Figure 2.7:** Strategy of catalyst design (Dowden et al., 1968)

#### 2.4.2 Target reaction

The basic reaction in the dry reforming of methane to produce syn-gas ( $H_2/CO = 1$ ) is shown in equation 2.8



Previous studies indicate that favourable temperature for the occurrence of dry reforming reaction is around 750 °C to decrease the influence of side reaction, which leads to the lower syn-gas ratio (Djinović, Osojnik Črnivec, et al., 2012). Therefore, reactions involved in dry reforming of methane were studied at 750 °C because this is most commonly studied temperature found in the literature (M. C. J. Bradford & Vannice, 1999). The reaction will be taken under consideration in this study are the one, which can proceed spontaneously using simple thermodynamic principle, i.e., reaction with negative Gibbs free energy change.

### 2.4.3 Stoichiometric analysis

Based on stoichiometry, the reaction which are possible to occur are: i) primary reactant reactions, ii) reactant self-interactions, iii) reactant cross-interactions, and iv) reactant-product reactions and v) product-product reactions (Richardson, 1989). However, the above explained thermodynamic principle will be applied to rule out or include reaction at 750 °C (1023 K). The calculation of Gibbs free energy at certain reaction temperature (750 °C) is explained in Appendix G.

### 2.4.4 Primary reactant reaction:

In this category, the reaction of main reactants (CO<sub>2</sub> and CH<sub>4</sub>) are considered and Gibbs free energy change was calculated (Table 2.1). It can be concluded that CH<sub>4</sub> decomposition is the only primary reactant reaction in dry reforming of methane, while CO<sub>2</sub> molecule does not react at 750 °C.

**Table 2.1:** Primary reactant reaction in the dry reforming of methane

Reaction	$\Delta G_{\text{rxn}, 1023 \text{ K}}^{\circ}$ (kJ)
CH <sub>4</sub> ↔ 2 H <sub>2</sub> + C	-22
CO <sub>2</sub> showed stability at 750 °C.	Not applicable at this temperature range.

### 2.4.5 Reactant self-interaction reactions

In this category, the self-interaction of two reactant molecules is considered and simple principle discussed above was applied to investigate the significance of the reactions. As can be seen in Table 2.2, carbon dioxide molecules did not show any interaction and for methane self-interaction reactions, it was observed that their existence was not possible at 750 °C due to positive Gibbs free energy change.

**Table 2.2:** Reactant self-interaction reactions

Reaction	$\Delta G_{\text{rxn},1023\text{ K}}^{\circ}$ (kJ)
$2\text{CH}_4 \leftrightarrow \text{H}_2 + \text{C}_2\text{H}_6$	71
$2\text{CH}_4 \leftrightarrow 2\text{H}_2 + \text{C}_2\text{H}_4$	77
$2\text{CH}_4 \leftrightarrow 3\text{H}_2 + \text{C}_2\text{H}_2$	126
No interaction between two $\text{CO}_2$ molecules at 750 °C.	Not applicable at this temperature range.

#### 2.4.6 Reactant cross-interaction reactions

In this category, the interaction of two different reactants among themselves is considered and values are tabulated in Table 2.3. Interestingly, all the reactions in this category are thermodynamically favourable (-ve values for Gibbs free energy).

**Table 2.3:** Reactant cross-interaction reactions

Reaction	$\Delta G_{\text{rxn},1023\text{ K}}^{\circ}$ (kJ)
$2\text{CH}_4 + 3\text{CO}_2 \leftrightarrow 4\text{CO} + 2\text{H}_2\text{O}$	-27
$\text{CH}_4 + \text{CO}_2 \leftrightarrow 2\text{CO} + 2\text{H}_2$	-31
$\text{CH}_4 + 2\text{CO}_2 \leftrightarrow 3\text{CO} + \text{H}_2\text{O} + \text{H}_2$	-31

#### 2.4.7 Reactant-product interaction:

There are some types of side reaction which are taking place between reactant and products. These types of reaction are important in dry reforming of methane. The most famous reaction of this type is RWGS reaction resulting in the utilization of  $\text{H}_2$  and produces  $\text{H}_2\text{O}$ . Instead of its slightly positive Gibbs free energy, this reaction is considered for further investigation (Table 2.4 ).

**Table 2.4:** Reactant- product reactions

Reaction	$\Delta G_{\text{rxn},1023\text{ K}}^{\circ}$ (kJ)
$\text{CO}_2 + \text{C} \leftrightarrow 2\text{CO}$	-9
$\text{CH}_4 + 2\text{H}_2\text{O} \leftrightarrow \text{CO}_2 + 4\text{H}_2$	-35
$\text{CH}_4 + \text{H}_2\text{O} \leftrightarrow \text{CO} + 3\text{H}_2$	-33
$\text{CO}_2 + \text{H}_2 \leftrightarrow \text{CO} + \text{H}_2\text{O}$	2

#### 2.4.8 Product-product reactions

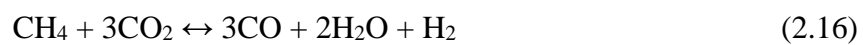
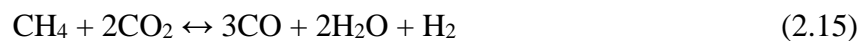
In this category, the interaction of products molecules is taken under consideration as seen in Table 2.5. The reaction of water and carbon has potential to occur while other reactions between CO and H<sub>2</sub> are not considered in this study.

**Table 2.5:** Product-product reactions

Reaction	$\Delta G_{\text{rxn},1023\text{ K}}^{\circ}$ (kJ)
$\text{CO} + \text{H}_2 \leftrightarrow \text{HCHO}$	122
$\text{H}_2\text{O} + \text{C} \leftrightarrow \text{CO} + \text{H}_2$	-11
$\text{CO} + 2\text{H}_2 \leftrightarrow \text{CH}_3\text{OH}$	150

#### 2.4.9 Network of reaction

Based on the above studied reaction and their occurrence at 750 °C, one can easily point out the reactions which will be thermodynamically favourable and have significant influence over the dry reforming of methane. The reactions selected from the above discussion are steam reforming of methane and RWGS reaction (Table 2.4), CH<sub>4</sub> decomposition (Table 2.1), reactant cross reactions (Table 2.3), and carbon removal reactions (Table 2.4 and 2.5). The similar network of reaction can be found in (Mark et al., 1997) study.



From the above independent reactions, which are sufficient to describe the reaction system are describe above. However, to narrow down our study to those reactions which will be enough to exhibit the influence of reaction, it is necessary to determine the rank of stoichiometric coefficient matrix (Fogler, 1986). The stoichiometric coefficient matrix is expressed in equation 2.17, with the conventional style (–ve sign for reactants and +ve sign for products) and the reduced matrix is shown in equation 2.18. The rank of matrix (in this case 3) shows that only 3 reactions will be sufficient to describe the whole reaction system. However, in the selection process of three independent reactions (Equation 2.9, Equation 2.12 and Equation 2.13), it is important to note that one carbon formation or removal reaction should be included.

	CH <sub>4</sub>	CO <sub>2</sub>	CO	H <sub>2</sub>	H <sub>2</sub> O	C
Eq 2.9	-1	-1	2	2	0	0
Eq 2.10	0	-1	1	-1	1	0
Eq 2.11	-1	0	1	3	-1	0
Eq 2.12	-1	0	0	2	0	1
Eq 2.13	0	-1	2	0	0	-1
Eq 2.14	0	0	1	1	-1	-1
Eq 2.15	-1	-2	3	1	1	0
Eq 2.16	-1	-3	4	0	2	0

(2.17)

	CH <sub>4</sub>	CO <sub>2</sub>	CO	H <sub>2</sub>	H <sub>2</sub> O	C
Eq 2.9	-1	-1	2	2	0	0
Eq 2.10	0	-1	1	-1	1	0
Eq 2.11	0	0	0	0	0	0
Eq 2.12	-1	0	0	2	0	1
Eq 2.13	0	0	0	0	0	0
Eq 2.14	0	0	0	0	0	0
Eq 2.15	0	0	0	0	0	0
Eq 2.16	0	0	0	0	0	0

(2.18)

## 2.5 Influence of parameters on catalytic activity

Numerous variables, such as active metal, support and calcination temperature, affected the catalytic activity and carbon deposition. The following section will

investigate the influence of these variables over catalytic activity, stability and morphology of deposited carbon.

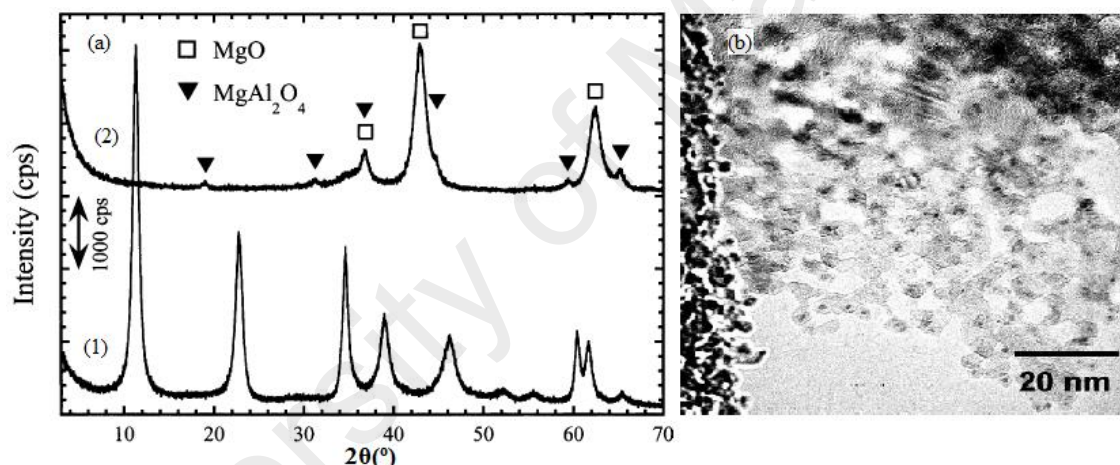
### 2.5.1 Influence of active metal on catalytic activity

Dry reforming of methane has been investigated with noble (Rh, Ru, Pd and Pt) and non-noble metal (Ni, Co and Fe) based catalysts (D. Liu, Quek, et al., 2009). Noble metal catalysts have drawn attention for their superior coking resistance, higher stability and activity especially for higher temperature applications ( $> 750\text{ }^{\circ}\text{C}$ ) (Djinović et al., 2011). A study investigated the effect of different noble metals (Rh, Ru, Pt, Pd and Ir) supported over alumina and concluded that noble metal (5 wt%) supported catalysts lead to higher coking resistance and stability (Hou et al., 2006). The catalytic activity and stability trend of the catalysts was  $\text{Rh}/\alpha\text{-Al}_2\text{O}_3 > \text{Ru}/\alpha\text{-Al}_2\text{O}_3 > \text{Ir}/\alpha\text{-Al}_2\text{O}_3 > \text{Pd}/\alpha\text{-Al}_2\text{O}_3 > \text{Pt}/\alpha\text{-Al}_2\text{O}_3$ . The amount of carbon deposited (mg cat/g cat h) over these catalysts was 4.9 for  $\text{Pd}/\alpha\text{-Al}_2\text{O}_3$ , and rest of them showed no carbon deposition  $\text{Ru}/\alpha\text{-Al}_2\text{O}_3$ ,  $\text{Rh}/\alpha\text{-Al}_2\text{O}_3$ ,  $\text{Ir}/\alpha\text{-Al}_2\text{O}_3$  and  $\text{Pt}/\alpha\text{-Al}_2\text{O}_3$ . The lower stability of Pt and Pd supported catalysts can be ascribed to the sintering of the metal particles at higher reaction temperatures.

Another study investigated the effect of incorporation of noble metals (Ru, Rh, Pt, Pd, Ir and Au) over Mg-Al layered double hydroxides and reported higher catalytic activity and stability for  $\text{Ru}/\text{MgAlO}_x$ ,  $\text{Rh}/\text{MgAlO}_x$  and  $\text{Ir}/\text{MgAlO}_x$ . (Tsyganok et al., 2003) However, the catalytic activity and stability for Pd, Pt and Au catalysts were such as:  $\text{Pd}/\text{MgAlO}_x > \text{Pt}/\text{MgAlO}_x > \text{Au}/\text{MgAlO}_x$ . The coke deposition (wt%) in the decreasing trend over these catalysts was  $\text{Pd}/\text{MgAlO}_x$  (102.9)  $> \text{Au}/\text{MgAlO}_x$  (41.4)  $> \text{Pt}/\text{MgAlO}_x$  (5.5)  $> \text{Ir}/\text{MgAlO}_x$  (4.9)  $> \text{Rh}/\text{MgAlO}_x$  (1.9)  $> \text{Ru}/\text{MgAlO}_x$  (1.3). The catalytic activity and stability of the catalysts matched with the coke deposition trend. The higher catalytic activity and lower carbon deposition by Ru supported catalysts can be explained on the basis of X-ray diffraction (XRD) and transmission electron microscopy (TEM). XRD



profiles (Figure 2.8a) depicting the structure of catalyst before (1) and after (2) dry reforming of methane at 800 °C for 50h. The spent catalyst indicates the presence of MgO and MgAl<sub>2</sub>O<sub>4</sub> and the absence of metallic Ru was noticed, which indicates that Ru was present in a small particle size on the support. This conclusion was verified by TEM image (Figure 2.8b) that showed the presence of highly dispersed and smaller metal particles around 1.5 nm. The presence of highly dispersed and smaller particle size assisted in the reduction of carbon deposits, agglomeration and sintering. The ability of Ru to completely eliminate or reduce carbon deposition to a minimal level also matched with the above discussed study (Hou et al., 2006).

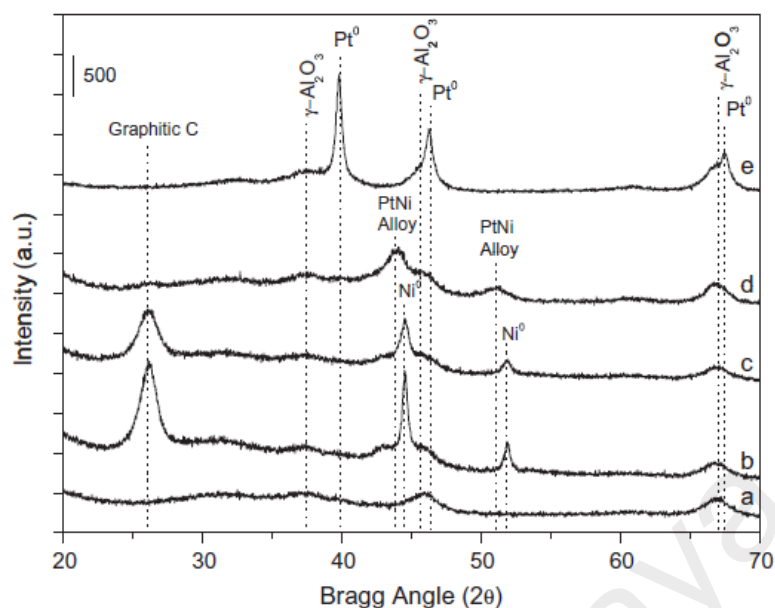


**Figure 2.8:** (a) XRD profiles of the catalyst (1) before and (2) after activity test and (b) TEM image of the catalyst after the activity test (Tsyganok et al., 2003).

However, noble metals exhibiting superior carbon deposition resistance and in certain studies displayed higher catalytic activities, cannot be applied on the industrial scale due to their high-cost (Crisafulli et al., 2002). In this scenario, non-noble metals (Ni, Co, Fe) become a suitable alternative for the industrial application due to low cost (Y. J. O. Asencios & Assaf, 2013; D. Liu, Quek, et al., 2009). The comparison of noble (Rh, Ru, Pd, Ir and Pt) and non-noble (Ni and Co) metal catalysts showed higher catalytic activities of Ni and Co catalysts compared to the noble metal supported catalysts. However, the higher coke deposition for Ni (24.0 mg cat/g cat h) and Co (49.4 mg cat/g

cat h) catalysts indicate their poor coke resistance ability compared to noble metal catalysts. Moreover, the addition (small amounts) of noble metals (Rh, Ru, Pd, and Pt) to Ni produced catalysts with affordable cost having good catalytic properties and lower sensitivity to carbon deposition (Ocsachoque et al., 2011).

The modification effect of Rh over Ni catalyst supported over mesoporous alumina indicated that Ni catalyst without Ru addition exhibited higher coke formation rates (17.2 mg coke/mg cat h) and lower methane (62.0%) and carbon dioxide (68.0%) conversions (Hou et al., 2006). However, with the addition of small amount of Rh, Rh-Ni catalyst exhibited higher catalytic and no coke deposition was detected. This higher stability and activity was attributed to the synergic effect of Rh and Ni, which lead to the formation of Rh-Ni cluster. Moreover, another study reported that bimetallic catalyst (0.4Pt-Ni/ $\gamma$ -Al<sub>2</sub>O<sub>3</sub>) exhibited the highest activity (69% methane conversion) compared to monometallic 4Ni/ $\gamma$ -Al<sub>2</sub>O<sub>3</sub> (60%) and 0.4Pt/ $\gamma$ -Al<sub>2</sub>O<sub>3</sub> (65%) catalysts (García-Diéguez et al., 2010). The highest catalytic activity was associated with the formation of Pt-Ni alloy, which has higher Pt content on its surface and leads to the production of smaller metal particle size (10 nm) than monometallic Ni catalysts (25 nm). The graphitic carbon peak in Figure 2.9 has been noticed to decrease with the increase of Pt content (0.04 to 0.4) in Ni/ $\gamma$ -Al<sub>2</sub>O<sub>3</sub> catalyst, moreover, the study indicated the lower carbon deposition (6wt%) for bimetallic catalyst (0.4Pt-Ni/ $\gamma$ -Al<sub>2</sub>O<sub>3</sub>) compared to monometallic (Ni/ $\gamma$ -Al<sub>2</sub>O<sub>3</sub>) catalyst (45 wt%).



**Figure 2.9:** XRD profiles for alumina support (a) and spent catalysts: (b) 4Ni/Al<sub>2</sub>O<sub>3</sub>, (c) 0.04Pt4Ni/Al<sub>2</sub>O<sub>3</sub>, (d) 0.4Pt4Ni/Al<sub>2</sub>O<sub>3</sub>, and (e) 0.4Pt/Al<sub>2</sub>O<sub>3</sub> (García-Diéguez et al., 2010).

The highest catalytic activity of bimetallic catalyst was also proved by another study (M.-S. Fan et al., 2010), which reported higher methane conversion (80%) for Ni-Co/MgO-ZrO<sub>2</sub> compared to monometallic Ni (70%) and Co (71%). It was attributed to the better metal dispersion, smaller particle size and the synergic effect between Ni and Co. Similarly, an addition of Rh (Jóźwiak et al., 2005) and Pt (Pawelec et al., 2007) to Ni supported on SiO<sub>2</sub> (Jóźwiak et al., 2005) and ZSM-5 (Pawelec et al., 2007) indicated higher methane conversions 84% and 28%, respectively, compared to monometallic Ni/SiO<sub>2</sub> (72%) and Ni/ZSM-5 (25.8%).

Another study reported that a combination of Ni and Pd exhibited better catalytic activities compared to Ni or Pd alone (Steinhauer et al., 2009). A study investigated Ni, Ni-Rh and Ni-Co supported on CeZr and reported that bimetallic catalysts (Ni-Rh/CeZr and Ni-Co/CeZr) showed stable catalytic activities compared to Ni/CeZr (Horváth et al., 2011). The addition of Mo (T. Huang et al., 2011) and Pt (D. Liu et al., 2010) to Ni supported on mesoporous materials SBA-15 (T. Huang et al., 2011) and MCM-41 (D.

Liu et al., 2010) showed higher activities compared to Ni/SBA-15 and Ni/MCM-41. The role of active metals in the enhancement of catalytic activity is listed in Table 2.6.

University of Malaya

**Table 2.6:** Influence of active metals on catalytic activity.

Metals	Support	W	P	RC		Reactor	Conversion <sup>a</sup>		Ref.
				T	t		CH <sub>4</sub>	CO <sub>2</sub>	
Ni	Al <sub>2</sub> O <sub>3</sub>	10	IMP	800	30	FBR	63.0	69.0	(Hao et al., 2009)
Co	$\gamma$ -Al <sub>2</sub> O <sub>3</sub>	20	SG	700	48	FIBR	94.0	93.0	(Hao, Zhu, Jiang, et al., 2008)
			SG		20	FIBR	66.0	71.0	
					IWIMP	550	7	FBR	
Ni	ZrO <sub>2</sub>	5	IWIMP	750	10	FBR	65.0	-	(Chang et al., 2006)
Ni-CeO <sub>2</sub>	ZrO <sub>2</sub>	5	IWIMP	700	50	FBR	59.0	-	(M. Rezaei et al., 2009)
Pt	ZrO <sub>2</sub>	1	IMP	700	4	FBR	79.0	86.0	(Özkara-Aydinoğlu et al., 2009)
Rh	CeO <sub>2</sub>	0.5	IMP	800	50	FBR	50.7	63.2	(H. Y. Wang & Ruckenstein, 2000)
	ZrO <sub>2</sub>						65.9	74.2	
Pt	Al <sub>2</sub> O <sub>3</sub>	1	IMP	800	97	FBR	46.0	62.0	(Ballarini et al., 2005)
	ZrO <sub>2</sub>						83.0	94.0	
Ru	Al <sub>2</sub> O <sub>3</sub>	3	IMP	750	20	FBR	46.0	48.0	(Djinović et al., 2011)
	CeO <sub>2</sub>	2					52.0	60.0	
NiO	MgO	13.1	IMP	800	5	FBR	93.0	95.0	(Feng et al., 2012)

**Table 2.6: Continued**

Co	MgO	12	IMP	900	0.5	FBR	91.9	93.9	(H. Y. Wang & Ruckenstein, 2001)
Ni	MgO-SiO <sub>2</sub>	5	IMP	700	--	FBR	58.3	-	(Jing et al., 2004)
Pt-Ni		0.01-5					80.7	-	
Ni	SiO <sub>2</sub>	5					55.0	-	
Pt-CeO <sub>2</sub> -ZrO <sub>2</sub>	MgO	0.8-3.0-3.0	IMP	800	24	FBR	69.0	80.0	(M. Yang et al., 2012)
Ni	CeZr	5	IMP	750	70	FBR	41.0	-	(Pietraszek et al., 2011)
Ni	Ce <sub>0.75</sub> Zr <sub>0.25</sub> O <sub>2</sub>	14	IMP	750	17	FBR	5.8	8.3	(Makhum, 2006)
Ni-Rh		14-0.7					6.9	11.8	
Ni	Ce <sub>0.75</sub> Zr <sub>0.25</sub> O <sub>2</sub>	2.1	CP	850	9	FBR	92	95	(J. Chen et al., 2008)
Ni	Ce <sub>0.8</sub> Zr <sub>0.2</sub> O <sub>2</sub>	15	CP	800	42	FBR	78.0	77.0	(Jang et al., 2013)
Ni-MgO		15-10			200		95.0	96.0	
Ru	Al <sub>2</sub> O <sub>3</sub>	5	IMP	750	--	FBR	91.0	90.0	(Safariamin et al., 2009)
	CeO <sub>2</sub>	5			--		90.0	96.0	
Ru-Ce	Al <sub>2</sub> O <sub>3</sub>	5 & 3			--		97.0	97.0	
Ni	MCM-41	1.2	DHT	750	30	FBR	70.0	-	(D. Liu, Lau, et al., 2009)
		Ni/Si= 0.04							

**Table 2.6: Continued**

Ni	MCM-41	Ni/Si= 0.19	DHT	600	4	FBR	20.0	38.0	(Arbag et al., 2010)
Ni-Rh					14		29.0	39.0	
Ni	MCM-41	0.22	DHT	600	4	FBR	28.0	39.0	(Yasyerli et al.,
Rh@Ni		1.0			1		31.0	41.0	2011)
Mg@Rh@Ni		1.0-1.0			1		38.0	40.0	
Ni	SBA-15	12.5	IMP	800	720	FBR	43	70	(M. Zhang et al., 2006)
Ni-Mo	SBA-15	5-25	IWIMP	800	120	FBMR	84.0	96.0	(J. Huang et al., 2011)
Ni	SiO <sub>2</sub>	4.5	IWIMP	750	11	FBMR	47.0	60.0	(Effendi et al., 2003)
Ni-Ce	SiO <sub>2</sub>	10-5	IWIMP	800	30	FBR	81.4	87.5	(Zhu et al., 2013)
Rh	SiO <sub>2</sub>	0.5	IMP	800	50	FBR	71.9	77.2	(H. Y. Wang & Ruckenstein, 2000)

a: %; -: data not available in the original work; --: initial conversion at time (0 h); W: metal weight percentage; P: preparation method; RC: reaction condition; T: temperature (°C); t: time (h); IMP: impregnation; CP: co-precipitation; SG: sol-gel; IWIMP: incipient wetness impregnation; DHT: Direct hydrothermal synthesis; CM: commercial; FBR: fixed bed reactor; FIBR: fluidized bed reactor; MR: microreactor; FBMR: fixed bed quartz micro-reactor.

The comparison of Ni and Co catalysts supported on Al<sub>2</sub>O<sub>3</sub> having similar preparation method (sol-gel) and reactor type (fluidized bed) exhibited higher catalytic activities for Ni/Al<sub>2</sub>O<sub>3</sub> compared to Co/Al<sub>2</sub>O<sub>3</sub> (Hao et al., 2009; Hao, Zhu, Jiang, et al., 2008). The higher catalytic activity and stability can be attributed to the higher surface area (216 m<sup>2</sup>/g), smaller particle size (10.5 nm) and higher dispersion (9.5%) of Ni-based catalyst; however, the role of slightly higher reaction temperature (800 °C) cannot be neglected. The study of the monometallic (Ni) (Chang et al., 2006), bimetallic catalyst (Ni-CeO<sub>2</sub>) (M. Rezaei et al., 2009) and noble metal (Pt) supported on ZrO<sub>2</sub> (Özkara-Aydinoğlu et al., 2009) exhibited higher catalytic activities for the Pt/ZrO<sub>2</sub> (Özkara-Aydinoğlu et al., 2009) catalyst. The investigation on catalysts Rh (H. Y. Wang & Ruckenstein, 2000) and Pt (Ballarini et al., 2005) supported on ZrO<sub>2</sub> at same reaction and preparation conditions showed higher methane conversion (83%) for Pt/ZrO<sub>2</sub> compared to Rh/ZrO<sub>2</sub> (65.9%).

NiO/MgO (Feng et al., 2012), Co/MgO (H. Y. Wang & Ruckenstein, 2001) and Pt-CeO<sub>2</sub>-ZrO<sub>2</sub>/MgO (M. Yang et al., 2012) exhibited higher catalytic activity for NiO/MgO compared to other catalysts although its stability was not high as in the case of Pt-CeO<sub>2</sub>-ZrO<sub>2</sub>/MgO but it was fair enough to be regarded as a suitable catalyst due to its low cost. The comparison of monometallic (Ni) and bimetallic (Pt-Ni) catalysts supported on MgO-SiO<sub>2</sub> exhibited the higher catalytic activity for the bimetallic catalyst (Jing et al., 2004). The incorporation of different active metals on the ceria-zirconia mixture revealed that Ni/CeZr (Pietraszek et al., 2011) produced better catalytic activities compared to Ni/Ce<sub>0.75</sub>Zr<sub>0.25</sub>O<sub>2</sub> and Ni-Rh/Ce<sub>0.75</sub>Zr<sub>0.25</sub>O<sub>2</sub> (Makhum, 2006). Similarly, Ni (J. Chen et al., 2008; Jang et al., 2013) and Ni-MgO (Jang et al., 2013) supported on Ce<sub>0.75</sub>Zr<sub>0.25</sub>O<sub>2</sub> (J. Chen et al., 2008) and Ce<sub>0.8</sub>Zr<sub>0.2</sub>O<sub>2</sub> (Jang et al., 2013) exhibited higher catalytic activities and enhanced stability for Ni-MgO/Ce<sub>0.8</sub>Zr<sub>0.2</sub>O<sub>2</sub>. The catalytic activity of Ni/Ce<sub>0.75</sub>Zr<sub>0.25</sub>O<sub>2</sub> was almost equal to Ni-MgO/Ce<sub>0.8</sub>Zr<sub>0.2</sub>O<sub>2</sub>, however the addition of



MgO to Ni lead to the increased stabilities (200 h). The incorporation of different monometallic (Arbag et al., 2010; Yasyerli et al., 2011) and bimetallic catalysts (Arbag et al., 2010; Yasyerli et al., 2011) in mesoporous support (MCM-41) leads to the conclusion that bimetallic catalysts produced better catalytic activities and stability compared to monometallic. However, another study proves otherwise and the catalytic activity of Ni/MCM-41 was higher than the above discussed articles, whereas, it can be attributed to the higher reaction temperature (750 °C) (D. Liu, Lau, et al., 2009). The comparison of various studies for monometallic (Ni) (M. Zhang et al., 2006) and bimetallic (Ni-Mo) (J. Huang et al., 2011) catalysts supported by mesoporous support (SBA-15) exhibited higher catalytic activities for the bimetallic catalyst Ni-Mo/SBA-15. This was attributed to the smaller particle size, higher specific surface area, strong metal support interaction and it was concluded that Mo has significant influence in effectively reducing the carbon deposition (J. Huang et al., 2011; T. Huang et al., 2011).

The incorporation of the various active metals (Ni (Effendi et al., 2003; Jing et al., 2004), Rh (H. Y. Wang & Ruckenstein, 2000)) and their combinations (Ni-Ce) (Zhu et al., 2013) on SiO<sub>2</sub> exhibited higher catalytic activity and stability for the bimetallic catalyst (Ni-Ce/SiO<sub>2</sub>). The investigation of various active metals (Ni (Barroso-Quiroga & Castro-Luna, 2010), Rh (H. Y. Wang & Ruckenstein, 2000) and Ru (Djinović et al., 2011; Safariamin et al., 2009)) supported on CeO<sub>2</sub> exhibited higher catalytic activity (90% methane conversion) for Ru/CeO<sub>2</sub>, however stability data for this study is missing. Even the higher reaction temperature in case of Rh/CeO<sub>2</sub> did not improve the catalytic activity compared to Ru/CeO<sub>2</sub> (lower reaction temperature). The addition of Ru (Crisafulli et al., 2002) and Pt (Pompeo et al., 2007) to Ni supported on silica, H-ZSM-5 (Crisafulli et al., 2002),  $\alpha$ -Al<sub>2</sub>O<sub>3</sub>,  $\alpha$ -Al<sub>2</sub>O<sub>3</sub>-ZrO<sub>2</sub> and ZrO<sub>2</sub> (Pompeo et al., 2007) lead to the superior catalytic activities compared to the monometallic catalyst (Ni), which was attributed to the higher dispersion and synergy between the metals. Similar results were reported by

various authors, which concluded that the Ni-Co catalyst supported on  $\text{TiO}_2$  and  $\gamma\text{-Al}_2\text{O}_3$  exhibited highest catalytic activities compared to monometallic (Ni, Co) catalysts (Takanabe et al., 2005b; J. Xu et al., 2009). Similarly, Rh-Ni catalyst supported on  $\text{CeO}_2\text{-Al}_2\text{O}_3$  (Ocsachoque et al., 2011), BEA zeolite (P. Frontera et al., 2010) and boron nitride (BN) (J. C. S. Wu & Chou, 2009) resulted in higher catalytic activity (85%, 73% and 72% methane conversion, respectively) compared to monometallic (Ni) catalysts.

From Table 2.6, it was established that addition of various non-noble metals (Ce, Mo) and noble metals (Rh, Pt) to Ni showed significantly higher catalytic activities and better stability compared to monometallic Ni-based catalysts (Arbag et al., 2010; Crisafulli et al., 2002; J. Huang et al., 2011; Jing et al., 2004; Makhum, 2006; Pompeo et al., 2007; Yasyerli et al., 2011; Zhu et al., 2013). However, it was encountered in some studies that monometallic catalyst showed higher catalytic activity compared to noble metals but showed higher carbon deposition (Hou et al., 2006). This study leads to the conclusion that even though the superior ability of noble metals for carbon deposition resistance is established throughout the study, however, keeping in mind the high cost and its application on a larger scale, it is advisable to apply monometallic catalysts. The proper selection of active metals for dry reforming of methane is a first step towards the achievement of better catalytic activity and stability. Therefore, various parameters (selection of support and pretreatment conditions), which have strong potential to affect the catalytic activity will be discussed in the following sub-sections.

### **2.5.2 Influence of support on catalytic activity**

Smaller metal particles produced in the nanometer range (1-10 nm) resulted in the difficulty of their application in the reactor; therefore, support bodies are required (Mul & Moulijn, 2005). It is suggested that supports has important role in the enhancement of

catalytic activity and suppression of carbon deposition produced during dry reforming reaction (M. C. J. Bradford & Vannice, 1999). The basic supports employed for dry reforming assisted in the gasification of carbon species, which resulted in the suppression of carbon deposition (Lucrédio et al., 2011; Özdemir, Öksüzömer, & Ali Gürkaynak, 2010). Ni (3.4-45 wt%) supported on the basic metal oxide (MgO) was investigated for dry reforming of methane (Y.-H. Wang et al., 2009) and among various catalysts prepared, Ni8Mg-6 (8 wt% Ni and calcination temperature of 600 °C) showed the highest methane conversion (84%). Previous studies showed that the formation of NiO/MgO solid solution significantly increased the stability of the catalyst (Hu & Ruckenstein, 2002). XRD studies revealed that free NiO or NiO-based MgO-NiO was present in the catalyst, leading to the conclusion that all reduced  $\text{Ni}^{2+}$  was incorporated into the MgO support lattice forming NiO-MgO, which exhibited stable activity (Y.-H. Wang et al., 2009). Metal oxide supports such as  $\text{CeO}_2$ ,  $\text{CeO}_2\text{-ZrO}_2$ , YSZ, and  $\text{TiO}_2$  supports were used extensively due to their good redox properties and oxygen mobility (A. Kambolis et al., 2010). Several authors (W. Chen et al., 2013; Djinović et al., 2011; Odedairo et al., 2013) reported that  $\text{CeO}_2$  improved metal dispersion and resisted sintering. Improvements in catalytic activity were attributed to strong metal-support interaction, high oxygen storage capacity and the  $\text{Ce}^{4+}/\text{Ce}^{3+}$  redox potential. The modification of  $\text{CeO}_2$  by the addition of  $\text{ZrO}_2$  resulted in good thermal stability and superior oxygen mobility compared to  $\text{CeO}_2$  alone (Horváth et al., 2011; M Rezaei et al., 2008). Similarly, higher catalytic activity (90% methane conversion) and stability (10 h) was reported for Ni/ $\text{CeO}_2\text{-ZrO}_2$  (Akpan et al., 2007), which confirmed the influence of  $\text{CeO}_2$  addition over  $\text{ZrO}_2$  to enhance catalytic activity. Supports providing oxygen to metals, such as  $\text{ZrO}_2$  were more beneficial compared to irreducible oxide ( $\text{Al}_2\text{O}_3$  or  $\text{SiO}_2$ ) (Nagaoka et al., 2001; H. Y. Wang & Ruckenstein, 2000). Pt supported on  $\text{ZrO}_2$  for dry reforming of methane exhibited highest stability and catalytic activity (86% methane conversion)

(Özkara-Aydinoğlu et al., 2009). The catalytic activity of Ni supported on MgO-ZrO<sub>2</sub> (MZ) showed highest methane (61%) and carbon dioxide (72%) conversions for 20Ni20MZ (20 wt% Ni and 20 mol% MZ) and attributed to a balance between Ni sites and oxygen vacancies produced by the MZ. The smaller particle size (22 nm) of 20Ni20MZ reduced coke formation and significantly improved catalytic activity compared to the other catalysts (Y. J. O. Asencios & Assaf, 2013). The reactant conversions for different catalysts are listed in Table 2.7.

University of Malaya

**Table 2.7:** Influence of supports on catalytic activity.

Metal	Support	P	W	RC		Reactor	Conversion <sup>a</sup>		Carbon	Ref.
				T	T		CH <sub>4</sub>	CO <sub>2</sub>		
Ni	Al <sub>2</sub> O <sub>3</sub>	IMP	15	700	--	FBR	63.0	57.3	-	(Therdthianwong et al., 2008)
NiO	Al <sub>2</sub> O <sub>3</sub>	IMP	10.5	800	5	FBR	52.5	-	-	(X. Chen et al., 2005b)
Ni	MgO	IWIMP	10	700	4	FBR	20.0	30.0	-	(Hua et al., 2010)
NiO	MgO	IMP	13.1	800	5	FBR	82.0	90.0	-	(Feng et al., 2012)
Ni	CeO <sub>2</sub>	IMP	10	550	7	FBR	11.7	29.7	-	(Barroso-Quiroga & Castro-Luna, 2010)
Ni	SiO <sub>2</sub>	MVIMP	4.5	750	11	FBR	47.0	60.0	4.40 <sup>c</sup>	(Effendi et al., 2003)
Ni	Al <sub>2</sub> O <sub>3</sub> -ZrO <sub>2</sub>	IMP	10	850	24	FBR	80.0	81.0	-	(Rahemi et al., 2013)
Ru	Al <sub>2</sub> O <sub>3</sub>	IMP	3	750	20	FBR	46.0	48.0	-	(Djinović et al., 2011)
Rh	CeO <sub>2</sub>	IMP	2				52.0	60.0	-	
Rh	CeO <sub>2</sub>	HTM	2	750	70	FBR	44.1	50.1	0.67 <sup>c</sup>	(Djinović, Batista, et al., 2012)
Rh	γ-Al <sub>2</sub> O <sub>3</sub>	IMP	0.5	800	50	FBR	82.1	87.4	-	(H. Y. Wang & Ruckenstein, 2000)
	La <sub>2</sub> O <sub>3</sub>						68.2	77.5	-	
	MgO						80.3	85.8	-	
	SiO <sub>2</sub>						71.9	77.2	-	
	Y <sub>2</sub> O <sub>3</sub>						73.0	82.1	-	
	CeO <sub>2</sub>						50.7	63.2	-	
	Nb <sub>2</sub> O <sub>5</sub>						15.3	26.6	-	
	Ta <sub>2</sub> O <sub>5</sub>						63.4	69.7	-	
	TiO <sub>2</sub>						33.1	46.5	-	
	ZrO <sub>2</sub>						65.9	74.2	-	

**Table 2.7: Continued**

Ni	Ce <sub>0.8</sub> Zr <sub>0.2</sub> O <sub>2</sub>	CP	15	800	42	FBR	78.0	77.0	-	(Jang et al., 2013)
	MgO-		15-10		200		96.0	97.0		
	Ce <sub>0.8</sub> Zr <sub>0.2</sub> O <sub>2</sub>									
Ni	CaO	SG	10	700	34	FBR	33.0	35.0	44 <sup>c</sup>	(W. D. Zhang et al., 2007)
	Sm <sub>2</sub> O <sub>3</sub>				5		42.0	47.0	-	
	CaO-Sm <sub>2</sub> O <sub>3</sub>				34		54.0	58.0	20 <sup>c</sup>	
3Ni-Co	CeO <sub>2</sub> -ZrO <sub>2</sub>	ST	3-3	800	20	FBR	30.0	37.0	2.54 <sup>c</sup>	(Osojnik Črnivec et al., 2012)
6 Ni-Co			6-6				30.0	45.0	2.55 <sup>c</sup>	
Ni	MgO-ZrO <sub>2</sub>	IMP	10	750	14	FBR	80.0	-	-	(Nagaraja et al., 2011)

a: % ; b: % weight loss ; c: wt% ; -: data not available in the original work; --: initial conversion at time (0 h); P: Preparation method; W: Metal weight percentage; RC: reaction condition; T: temperature (°C); t: time (h); IMP: impregnation; CP: Co-precipitation; SG: sol-gel; ST: solvothermal approach and aging in ethylene glycol medium; MVIMP: multipore volume impregnation; HTM: hard template method; FBR: fixed bed reactor.

The comparison of the catalytic activities of Ni (Hua et al., 2010; Therdthianwong et al., 2008) supported on  $\text{Al}_2\text{O}_3$  and MgO showed higher catalytic activity for Ni/ $\text{Al}_2\text{O}_3$  catalyst compared to Ni/MgO. However, opposite trend was observed for nickel oxide (NiO) (X. Chen et al., 2005a; Feng et al., 2012) supported on  $\text{Al}_2\text{O}_3$  and MgO, which showed higher catalytic activity and stability for NiO/MgO catalyst. While Rh supported on MgO and  $\gamma\text{-Al}_2\text{O}_3$  showed somewhat similar reactant conversions (Table 2.7) (H. Y. Wang & Ruckenstein, 2000). However, the basic supports are considered to reduce carbon deposition due to enhanced  $\text{CO}_2$  chemisorption and in this view MgO appears to be a suitable support which can reduce carbon deposition without adding extra cost (Zanganeh et al., 2013).

Ranjbar and Rezaei (2012) reported 60% methane conversion for Ni/CaO- $\text{Al}_2\text{O}_3$  catalysts and lower coke deposition was observed due to addition of basic metal oxide (CaO) to alumina. Similarly, the addition of cations ( $\text{Y}^{3+}$ ,  $\text{Mg}^{2+}$ ,  $\text{Ca}^{2+}$  and  $\text{La}^{2+}$ ) to  $\text{ZrO}_2$  enhanced catalytic activity by producing oxygen species ( $\text{O}^{2-}$  or  $\text{O}^-$ ) and assisted in the oxidation of hydrocarbon (S. Wang et al., 2001). Furthermore, Ni supported on CaO- $\text{ZrO}_2$  exhibited 86% methane conversion, which was dedicated to the high basicity of  $\text{Ca}^{2+}$  ions and  $\text{ZrO}_2$  (acidic-basic character). Higher hydrothermal stability of the catalyst suppressed water generation produced by the RWGS reaction (S. Liu et al., 2008). Another study also reported the influence of MgO addition to  $\text{ZrO}_2$  over Ni and reported higher methane conversion(80%) and was stable up to 14 h (Nagaraja et al., 2011). Several authors reported that the addition of MgO to  $\text{ZrO}_2$  will lead to enhanced resistance to coke deposition and lead to higher surface areas (García et al., 2009; Trakarnpruk & Sukkaew, 2008).

Rh supported on  $\text{SiO}_2$ ,  $\text{TiO}_2$ ,  $\text{Nb}_2\text{O}_5$  and  $\text{Y}_2\text{O}_3$  showed 71.9%, 33.1%, 15.3% and 73.0% methane conversion, respectively (H. Y. Wang & Ruckenstein, 2000). There are various studies reporting the influence of  $\text{CeO}_2$  supported over Rh and all studies reported

somewhat similar catalytic activities in the range of 44-53% methane conversion (Djinović, Batista, et al., 2012; Djinović et al., 2011; H. Y. Wang & Ruckenstein, 2000).  $\text{TiO}_2$  and  $\text{SiO}_2$  were investigated as a support for different metals (Cu, Co, Fe, Ni, Ru, Rh, Pd, Pt, Ir) and reported higher methane conversion (0.05-7.1%) for  $\text{TiO}_2$  compared to  $\text{SiO}_2$  (0.05-2.9%) (Michael C. J. Bradford & Albert Vannice, 1999). The highest activity exhibited by  $\text{TiO}_2$  was attributed to  $\text{TiO}_x$  species formed during reduction, which reduced the large ensemble sizes and the metal-support interaction enhanced catalytic activity. Another study investigated the different types of supports ( $\text{Al}_2\text{O}_3$ ,  $\text{TiO}_2$ ,  $\text{SiO}_2$ ,  $\text{ZrO}_2$ ) for molybdenum carbide ( $\text{Mo}_2\text{C}$ ) and reported that higher activity and stability was observed for  $\text{Mo}_2\text{C}/\text{Al}_2\text{O}_3$  (Brungs et al., 2000). The stability trend for the catalysts was  $\text{Mo}_2\text{C}/\text{Al}_2\text{O}_3 > \text{Mo}_2\text{C}/\text{ZrO}_2 > \text{Mo}_2\text{C}/\text{SiO}_2 > \text{Mo}_2\text{C}/\text{TiO}_2$ . The higher stability for alumina supported catalyst was due to the enhanced metal-support interaction during the preparation (between  $\text{Mo}_2\text{C}$  precursor and support). Moreover, it was concluded that the oxidation of active metal was the major reason for the deactivation of the catalyst. The oxidation of molybdenum carbide to molybdenum oxide leads to the deactivation because  $\text{MoO}_3$  is inactive during the reaction period. The study indicated that supports played a prominent role in the enhancement of catalytic activity and reduction in the carbon deposition. The information previously discussed (Table 2.7) indicated that supports such as:  $\text{ZrO}_2$ , metal oxides ( $\text{Mg}^{2+}$ ,  $\text{Y}^{2+}$ ,  $\text{Ca}^{2+}$ ) addition on  $\text{ZrO}_2$ ,  $\text{MgO}$ ,  $\text{CeO}_2$  and ceria-zirconia mixtures showed higher catalytic activities and their basic character enhanced the stability by reducing coke deposition. The study emphasized the importance of proper support selection, suitable molar or weight ratios of the support materials and the proper combination of various metal oxides to enhance catalytic activity.

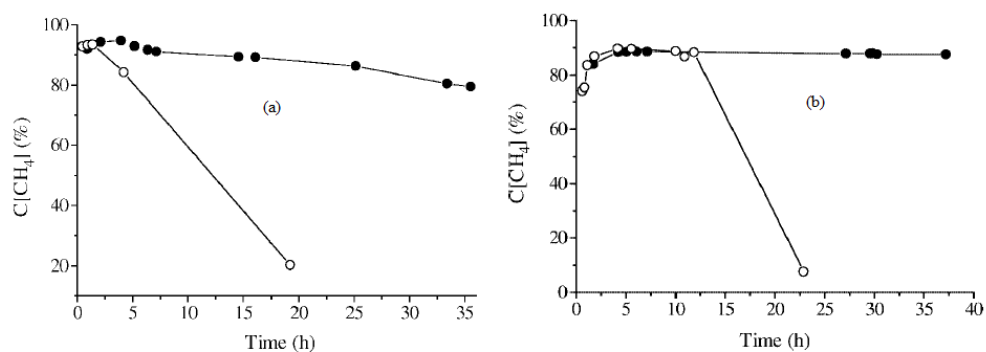


### 2.5.3 Influence of calcination temperature on catalytic activity

Activation methods can influence reactivity and stability of the catalyst (Montero et al., 2009) and it has been reported previously that calcination is a critical step in controlling the size of Ni, which in turn influence catalyst stability and activity (Cesteros et al., 2000; Jiuling Chen et al., 2009; Y. Chen & Zhang, 1992; Shaikhutdinov et al., 1995). Calcination of deposited precursor will be important for the complete decomposition of salts and it is believed that calcination of catalyst creates specific transformations and solid state reactions which include: decomposition of the precursor, solid state reaction of the supported oxide and support and reaction between supported oxide and support (Hagen, 1999; Yan et al., 2003). Calcination of MgO resulted in significant changes arising from the restructuring of the metal oxide, which increased the defect production and were suggested as electron donating ( $O^{2-}$ ) centers. These electrons donating ( $O^{2-}$ ) centers were postulated as super basic sites in solid base catalysis (Montero et al., 2010). A study was reported on effect of calcination temperatures (500 to 800 °C) on MgO and reported that crystallite sites (as a function of calcination temperature) showed no significant increase from 500-700 °C (Mguni et al., 2012). However, a prominent increase in crystallite size (35 nm to 80 nm) occurred due to the sintering of MgO by the calcination of catalyst at higher temperature (800 °C). The smaller particle size achieved by the calcination of catalyst at 500-700 °C showed higher catalytic activities and a decrease in catalytic activity occurred with the further increase of calcination temperature. The relationship between calcination temperature and surface area was also investigated (Jiuling Chen et al., 2009) for Ni/Al<sub>2</sub>O<sub>3</sub> in the range of 300-750 °C. The average NiO crystallite size increased (2.4 nm to 6.3 nm) and surface area decreased from 170 to 105 m<sup>2</sup>/g with the increase of calcination temperature from 300 to 750 °C, which suggested that higher calcination temperatures caused the NiO to coalesce. Moreover, the catalyst calcined at 300 and 450 °C showed higher catalytic activity

compared to the catalyst calcined at 600 and 750 °C and the lower catalytic activity for Ni/Al<sub>2</sub>O<sub>3</sub> could be a result of inactive Ni sites due to the high calcination temperatures.

Metal promoters (K, Ca, Sn, Ga, Ce) played a key role in the hindrance of carbon deposition, increased metal reducibility, enhanced metal-support interaction, increased metal dispersion and suppressed sintering (Castro Luna & Iriarte, 2008). However, the efficiency of these promoters strongly depended on the preparation conditions, calcination temperature and reducing conditions (Al-Zeghayer & Jibril, 2005). The effect of calcination temperatures (400 and 600 °C) and time (2, 8, 24 and 96 h) on the catalytic activity for the hydrodesulfurization (HDS) of dibenzothiophene (DBT) was studied for Co-Mo/Al<sub>2</sub>O<sub>3</sub> (Al-Zeghayer & Jibril, 2005). The global rate constants (g feed/g cat. h) for the catalysts were 7.4 (C400/2), 4.7 (C400/8), 48.1 (C400/24), 37.7 (C400/96) and 31.9 (C600/24), where CXXX/Y notation described the temperature in °C (XXX) at which catalyst was calcined and Y the calcination time (h). Catalyst calcined for shorter time (2 and 8 h) proved to be less active compared to those calcined for longer time (24 and 96 h), and there was no improvement in DBT conversion even when the calcination duration was longer than 24 h or the temperature reached 600 °C. The highest conversion achieved at 400 °C occurred due to better dispersion and increased metal-support interaction. Catalyst calcined at 400 °C (longer treatment duration) exhibited the best performance revealing the importance of careful selection of calcination temperature and treatment duration. However, there is a study reporting the opposite behaviour (Brungs et al., 2000), which observed that the catalyst calcined for shorter durations (4 h) exhibited higher stability compared to the catalyst calcined for longer durations (24 h) (Figure 2.10). The calcination of catalyst at longer duration reported to have deleterious effects on the Mo<sub>2</sub>C catalyst. This study depicts the importance of choosing the suitable calcination durations because catalyst calcined at similar temperature but different time durations will have a negative impact on the stability and lifetime of the catalyst.



**Figure 2.10:** The influence of calcination duration on (a)  $\text{Mo}_2\text{C}/\text{SiO}_2$  and (b)  $\text{Mo}_2\text{C}/\text{Al}_2\text{O}_3$  (•) 4 and (◦) 24 h (Brungs et al., 2000).

The effect of calcination temperatures (350, 450 and 570 °C) on CO oxidation in the presence of 5 wt%  $\text{CoO}_x/\text{TiO}_2$ , and the catalyst calcined at 450 °C showed higher CO conversion (82%) compared to 38% and 2% for 350 and 570 °C, respectively (W.-H. Yang et al., 2007). The main difference was the type of Co species formed at 450 and 570 °C, where 450 °C produced a Type A clean  $\text{Co}_3\text{O}_4$ , the major reason for its higher catalytic activity, while 570 °C produced Type B  $\text{Co}_3\text{O}_4$ , which was covered by  $\text{Co}_n\text{TiO}_{n+2}$  and was the primary reason for the low CO conversion. The study indicates that in some cases, lower calcination temperatures (i.e., 350 °C) will not be sufficient to completely decompose the precursor, which will result in lower catalytic activity.

The influence of calcination temperatures (500–900 °C) on catalyst performance and reducibility for  $\text{Co}/\text{MgO}$  with the different Co loadings (H. Y. Wang & Ruckenstein, 2001). Catalysts with Co loadings between 8 and 36 wt% and calcined at 500 or 800 °C showed higher catalytic activity and stability compared to Co loading between 4 and 48 wt% calcined at 900 °C, while calcination of catalyst with Co (48 wt%) at 500 or 800 °C resulted in deactivation. Formation of  $\text{CoO}/\text{MgO}$  was the primary reason for higher stabilities at 8 and 36 wt% Co loadings and the large metal particle induced by the higher Co loading (48 wt%) calcined at 500 °C or 800 °C was believed to be the major cause of sintering and coke deposition leading to unstable activities. The study leads to conclusion that in some cases, lower calcination temperature and low metal loading were suitable

due to the higher stabilities induced in the catalyst. The influence of calcination temperatures on catalytic activity of various catalysts is shown in Table 2.8.

University of Malaya

**Table 2.8:** Influence of calcination temperature on catalytic activity and stability

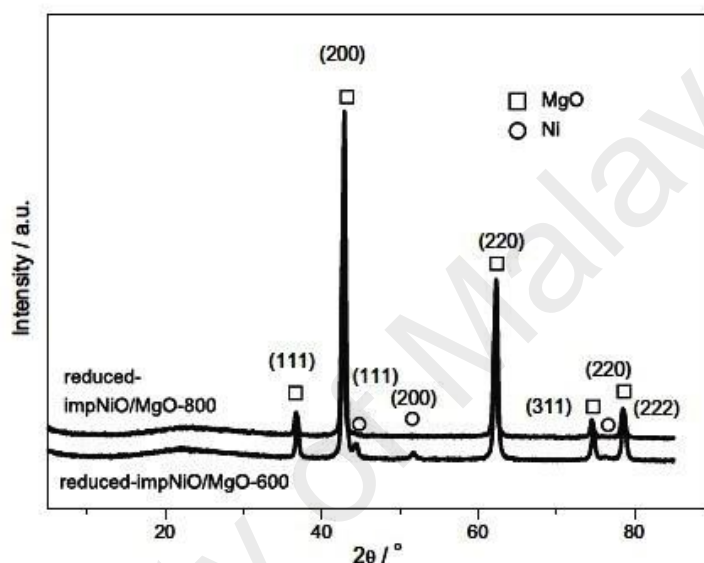
Metal	Support	P	Calc. condition			RC		Conversion <sup>a</sup>		Carbon	Ref.
			T	M	t	T	t	CH <sub>4</sub>	CO <sub>2</sub>		
NiO	MgO	IMP	600	Air	1.5	800	5	82.0	90.0	-	(Feng et al., 2012)
			800					93.0	95.0	-	
Co	MgO	IMP	500	Air	8	900	0.5	95.7	97.4	-	(H. Y. Wang & Ruckenstein, 2001)
			800					91.9	93.9	-	
			900					5.5	11.9	-	
Co	SiO <sub>2</sub>	IMP	*	Air	6	850	25	12	31	-	(S.-H. Song et al., 2014)
			300					22	46	-	
			400					2	8	-	
			500					21	44	-	
			600					16	40	-	
			700					2	9	-	
			900								
Ni	TiO <sub>2</sub> -SiO <sub>2</sub>	IMPCSG	550	Air	5	700	10	57.0	70.0	0.012 <sup>b</sup>	(S. Zhang et al., 2008)
			700				10	65.0	77.0	0.017 <sup>b</sup>	
			800				1.8	60.0	65.0	0.147 <sup>b</sup>	
Ni	Al <sub>2</sub> O <sub>3</sub>	IWIMP	500	Air	3	700	--	63.0	57.0	-	(Therdthianwong et al., 2008)
Ni	Al <sub>2</sub> O <sub>3</sub>	IWIMP	800	Air	4	700	--	91.2	70.6	-	(Sun et al., 2013)
Ni	Al <sub>2</sub> O <sub>3</sub>	SG.	850	Air	10	750	30	84.7	90.8	-	(Castro Luna & Iriarte, 2008)
Ni	Al <sub>2</sub> O <sub>3</sub>	SG.	700	Air	4	800	24	60.0	69.0	19.1 <sup>c</sup>	(Hao, Zhu, Lei, et al., 2008)

**Table 2.8: Continued**

Ni	CaO-Al <sub>2</sub> O <sub>3</sub>	TB.	700 900 1100	Air	48	700	--	17.15 38.84 36.96	21.95 43.59 41.64	2.2 <sup>c</sup> 0.8 <sup>c</sup> 0.4 <sup>c</sup>	(Lemonidou et al., 1998)
Ni	$\gamma$ -Al <sub>2</sub> O <sub>3</sub>	IWIMP	600 900	Air	2	700	9 9	68.0 73.0	66.4 80.1	- -	(Al-Fatesh & Fakeeha, 2012)
Ni-Ce	SiO <sub>2</sub>	IWIMP	800	Ar O <sub>2</sub> CO <sup>2</sup> H <sub>2</sub>	-	800	30	89.3 87.3 85.1 81.4	94.6 92.4 91.4 87.5	- - - -	(Zhu et al., 2013)
La <sub>2</sub> Ni O <sub>4</sub>	$\gamma$ -Al <sub>2</sub> O <sub>3</sub>	SG	500 800	Air	6	700	30	60.0 49.0	49.5 60.0	32.9 <sup>d</sup> 13.8 <sup>d</sup>	(B. S. Liu & Au, 2003)

a: %; b: (g/g<sub>cat</sub>.h); c: wt%; d: (mg/g.h); -: data not available in the original work ; --: initial conversion at time (0 h); P: preparation method; RC: reaction condition; T: temperature (°C); t: time (h); M: medium; IMP: impregnation; SG: sol-gel; ME: microemulsion; IWIMP: incipient wetness impregnation; TB: total blending; IMPCSG: impregnation combined sol-gel.

The higher catalytic activity and stability were reported in a number of studies at calcination temperature of 800 °C (Feng et al., 2012; B. S. Liu & Au, 2003) irrespective of catalyst types. XRD profile (Figure 2.11) revealed the absence of Ni<sup>0</sup> peak for the catalyst calcined at 800 °C pointing towards the existence of strong metal-support interaction, which resulted in the higher reactant conversions for NiO/MgO-800 compared to NiO/MgO-600, which showed the presence of Ni<sup>0</sup> (Feng et al., 2012).



**Figure 2.11:** XRD patterns of impNiO/MgO catalyst (Feng et al., 2012).

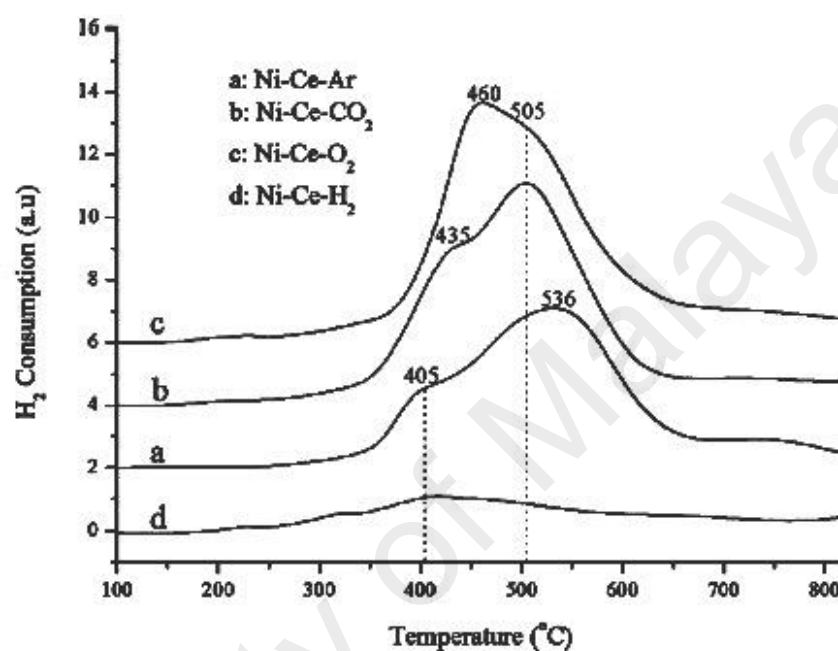
The influence calcination temperatures (500-900 °C) on Pt/ $\gamma$ -Al<sub>2</sub>O<sub>3</sub> and reported that best catalytic activity was observed at 800 °C, while at 900 °C a comparatively lower catalytic activity was recorded and catalyst calcined at 600 °C exhibited worst one (J. Yu et al., 2011). Similar, results were reported by another study (Al-Fatesh & Fakeeha, 2012) that the catalyst calcined at lower temperature exhibited lower catalytic activities compared to catalyst calcined at higher temperature (900 °C). However, there are studies showing that there is a temperature limit as certain higher calcination temperature will not always lead to higher catalytic activity and stability. Another study investigated the wide range of calcination temperatures (700 to 1100 °C) for (Ni/CaO-Al<sub>2</sub>O<sub>3</sub>) and reported that catalyst calcined at 900 °C exhibited higher stability and activity compared to 700

and 1100 °C, which could be attributed to the smaller metal particle size formed at 900 °C (Lemonidou et al., 1998). Moreover, the surface area was decreased (104 to 5.48 m<sup>2</sup>/g), with an increase in calcination temperatures from 700 to 1100 °C (Lemonidou et al., 1998).

Calcination temperature has a major influence on the reactant conversions (comparison of (Therdthianwong et al., 2008) and (Sun et al., 2013)). While the weight percentages of the metal content (15 wt%) and reaction temperatures (700 °C) were the same, the catalyst calcined at a higher temperature (800 °C) resulted in higher methane conversion (91.2%) compared to the catalyst calcined at lower calcination temperature 500 °C (63%). This can be attributed to the smaller particle size formed before (12.1 nm) and after (14.3 nm) the dry reforming of methane and the little change in particles size for used catalyst indicates the higher resistance of catalyst to sintering (Sun et al., 2013). Similar results were obtained for Ni/Al<sub>2</sub>O<sub>3</sub> calcined at 450, 650 and 850 °C for 16 h (Joo & Jung, 2002), where the catalyst calcined at 850 °C showed higher activity and stability compared to the catalyst calcined at 450 °C (Joo & Jung, 2002). The comparison of different studies (Castro Luna & Iriarte, 2008) and (Hao, Zhu, Lei, et al., 2008) showed that catalyst calcined at 700 °C exhibited lower methane (60%) and carbon dioxide (69%) conversions even though the reaction temperature was high (800 °C) (Hao, Zhu, Lei, et al., 2008), while the catalyst calcined at higher calcination temperature (850 °C) showed higher methane conversion (84.7%) even though the reaction temperature was low (750 °C) (Castro Luna & Iriarte, 2008). Thermodynamically, an increase in the reaction temperature would result in increased activity (J. H. Edwards & A. M. Maitra, 1995) while the opposite was observed, indicated the influence of calcination temperature over catalytic activity. A study reported the effect of different calcination mediums (Ar, H<sub>2</sub>, O<sub>2</sub> and CO<sub>2</sub>) on Ni-Ce/SiO<sub>2</sub> and denoted as Ni-Ce-Ar, Ni-Ce-O<sub>2</sub>, Ni-Ce-CO<sub>2</sub>, Ni-Ce-H<sub>2</sub>. Ni-Ce-Ar exhibited higher methane (89.3%) and carbon dioxide (94.6%) conversions



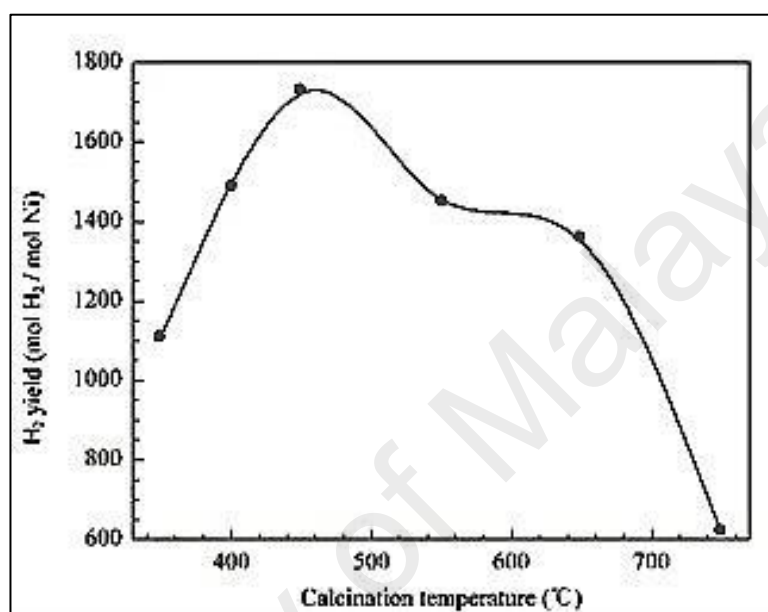
followed by O<sub>2</sub>, CO<sub>2</sub> and H<sub>2</sub> (Zhu et al., 2013). TPR-H<sub>2</sub> profiles showed a higher peak for Ni-Ce-Ar at 536 °C in Figure 2.12, which pointed towards the existence of strong metal-support interaction while the reduction peak at lower temperature (405 °C) was ascribed to the loss of surface oxygen. The study showed that calcination mediums indeed have a certain influence over catalytic activity.



**Figure 2.12:** TPR profiles of fresh Ni-Ce/SiO<sub>2</sub> catalyst (Zhu et al., 2013).

There are various studies reporting better catalytic activities at lower calcination temperature. Ni/TiO<sub>2</sub>-SiO<sub>2</sub> showed lower coke deposition at 700 °C compared to the catalyst calcined 800 °C (S. Zhang et al., 2008), while the better catalytic activity and stability (attributed to the newly formed compound Ni<sub>2.44</sub>Ti<sub>0.72</sub>Si<sub>0.07</sub>O<sub>4</sub>) were due to the synergistic effect between metal and support and the smaller metal particle size (5.7 nm) resisted carbon deposition. Similar trend was noticed for Au/TiO<sub>2</sub> calcined at 200, 300 and 600 °C, where lower temperatures (200 and 300 °C) resulted in the highest catalytic activities (Boccuzzi et al., 2001). Two different studies also reported the presence of certain calcination temperature limits in their investigations for Ni/Al<sub>2</sub>O<sub>3</sub>-SiO<sub>2</sub> (Ashok et al., 2008) and Ni-Mg catalysts, (Moliner et al., 2008). The results implied a certain

temperature limit ( $> 450\text{ }^{\circ}\text{C}$ ) after which a serious decrease in  $\text{H}_2$  yield occurred due to  $\text{NiO}$  formed during pre-treatment (Figure 2.13) (Ashok et al., 2008). Similarly, it was reported that calcination at higher temperatures ( $> 600\text{ }^{\circ}\text{C}$ ) resulted in rapid deactivation due to an increase of  $\text{NiO}$  domain size (from  $31\text{ nm}$  to  $92.7\text{ nm}$  at  $1000\text{ }^{\circ}\text{C}$ ) with a corresponding decrease in BET surface areas (Moliner et al., 2008).



**Figure 2.13:** Effect of calcination temperatures on  $\text{H}_2$  yield (Ashok et al., 2008).

Higher calcination temperature was suggested to affect the morphology of the catalyst as observed for  $\text{Co}/\gamma\text{-Al}_2\text{O}_3$  calcined at  $500\text{ }^{\circ}\text{C}$  and  $1000\text{ }^{\circ}\text{C}$  (E. Ruckenstein & Wang, 2002) and it was reported that surface area would be decreased with the increase of calcination temperature (Moliner et al., 2008; H. Y. Wang & Ruckenstein, 2001; S. Zhang et al., 2008). Different species were generated during calcination, which played a significant role in the enhancement of catalytic activity.  $\text{Co}_3\text{O}_4$  was formed at  $500\text{ }^{\circ}\text{C}$  while at  $1000\text{ }^{\circ}\text{C}$   $\text{Co}_2\text{AlO}_4$  and  $\text{CoAl}_2\text{O}_4$  were observed. The lower Co content (6 wt%) catalyst calcined at  $500\text{ }^{\circ}\text{C}$  showed higher conversion and lower carbon deposition, while the high Co metal content (9 wt%) catalyst calcined at  $1000\text{ }^{\circ}\text{C}$  showed higher conversion and lower carbon deposition (E. Ruckenstein & Wang, 2002). These observations

suggested there may be situations in which one calcination temperature might be working efficiently for a certain metal content while being unsuitable for a different metal content.

The comparison of data from various studies suggested that calcination temperature played a significant role in catalytic activity/stability and indicated the existence of temperature limits above which a certain drop in catalytic activity was observed (Boccuzzi et al., 2001; Moliner et al., 2008; H. Y. Wang & Ruckenstein, 2001; J. Yu et al., 2011; S. Zhang et al., 2008) or below which deactivation occurred (Al-Fatesh & Fakeeha, 2012; Feng et al., 2012; Joo & Jung, 2002; B. S. Liu & Au, 2003). The conclusion from the above studies indicated that although the high calcination temperature leads to the loss of surface area of the catalyst, however, it will produce stable catalyst structure. Hence it will be advisable to calcined the catalysts at high temperatures due to the endothermic nature of dry reforming reaction, which will require higher reaction temperatures to achieve acceptable conversion (Al-Fatesh & Fakeeha, 2012).

## 2.6 Catalyst preparation methods

In the catalysis study, the efficiency of catalytic process is mainly attribute to the expose surface area of active phase due to the fact that majority of reaction occurred at the surface of catalyst (Mul & Moulijn, 2005). Therefore, it is important to express the relationship between the exposed surface area and the particle size of the catalyst. The calculation of surface area can be done by assuming that active phase consists of uniform spherical particles (density,  $\rho$ ).

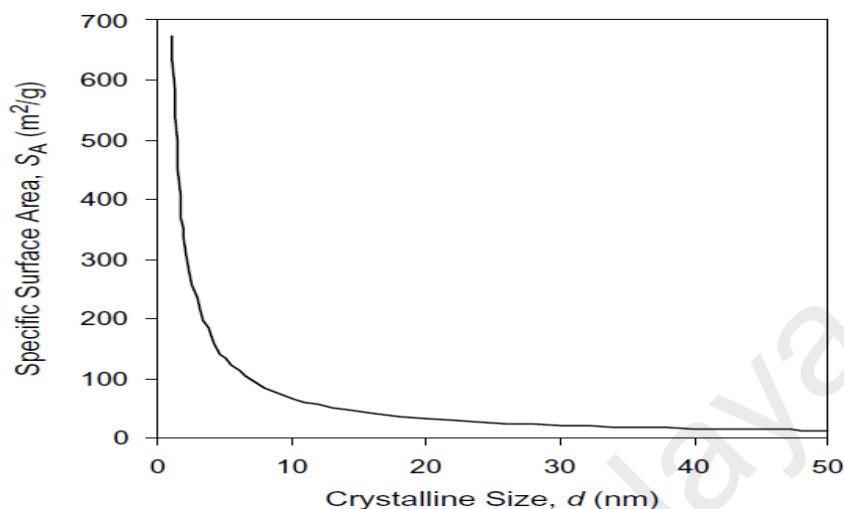
$$\text{Volume of one particle, } V = \frac{1}{6} \pi d^3 \quad (\text{m}^3)$$

$$\text{Weight of one particle, } W = \frac{1}{6} \rho \pi d^3 \quad (\text{kg})$$

$$\text{Surface area of one particle, } S_p = \pi d^2 \quad (\text{m}^2)$$

$$\text{Specific surface area, } SA = S_p/W = \pi d^2 / (\rho \frac{1}{6} \pi d^3) = 6/\rho d \quad (\text{m}^2/\text{kg})$$

The calculation of this plot is shown in Figure 2.14 and it can be seen that only at lower particle size, a significant surface area has been obtained.



**Figure 2.14:** The relationship between particle size and specific surface area for Ni ( $\rho = 8900 \text{ kg/m}^3$ ) (Mul & Moulijn, 2005).

However, the implication of such small size particles in the reactor is difficult; therefore support bodies are required to acquire higher dispersion over support bodies (Mul & Moulijn, 2005). Moreover, the application of the support bodies is important for precious metals based catalyst, which would result in the efficient utilization of precious metals compared to the bulk catalysts. The other purpose of support bodies is to produce catalyst stability and this can be achieved by the higher metal-support interaction. To illustrate the above, take an example of copper oxide which is very efficient oxidation catalyst but exhibits thermal instability. This problem was counteracted by the application of high surface alumina which enhanced its thermal stability and activity (Acres et al., 1981). In this study, we will focus on the preparation methods for supported catalysts: impregnation, co-precipitation, sol-gel, Ion-exchange, deposition (Campanati et al., 2003). The brief description of the methods used previously will be briefly discussed in this section and the microemulsion method will be described in detail.

### **2.6.1 Impregnation**

It is generally described as a preparation method in which the solid is contacted with the liquid phase containing the metal precursor. The two-major type of impregnation are dry or pore volume impregnation and wet or excess solution impregnation. In the dry impregnation, the special care is taken regarding the volume of solution which is chosen equal to or slight less than the pore volume of the support. However, in case of wet impregnation as its name indicates, the excess precursor solution is employed and later on this excess solution is removed with the help of drying (Campanati et al., 2003; Haber et al., 1995). There are two other types of impregnation which depends on the sequence of the introduction of active components: Co-impregnation is regarded as the impregnation in which two or more active components are introduced in a single step and successive impregnation is the type of impregnation in which two or more active components are introduced sequentially (Haber et al., 1995).

### **2.6.2 Co-precipitation**

The catalyst prepared by co-precipitation requires the intimate mixing of metal ions and support (Acres et al., 1981). In the co-precipitation two major stages are included: nucleation and growth. There are several techniques available to synthesize catalyst from co-precipitation, one of them is to add drop wise the solution containing the active metal to the precipitating solution and vice versa (Haber et al., 1995). The process of co-precipitation depends upon the solubility of the components involved in the preparation of catalyst and the chemistry occurring during preparation (Schwarz et al., 1995).

### **2.6.3 Deposition**

This preparation method describes the placement of active metal components on the external surface of the support. Sputtering is described as a technique to achieve this goal, in which the metal vapor is condensed and deposited on the agitated support. However, this process should be done in a high vacuum, which make this technique only useful for model catalysts (Acres et al., 1981).

### **2.6.4 Ion-exchange**

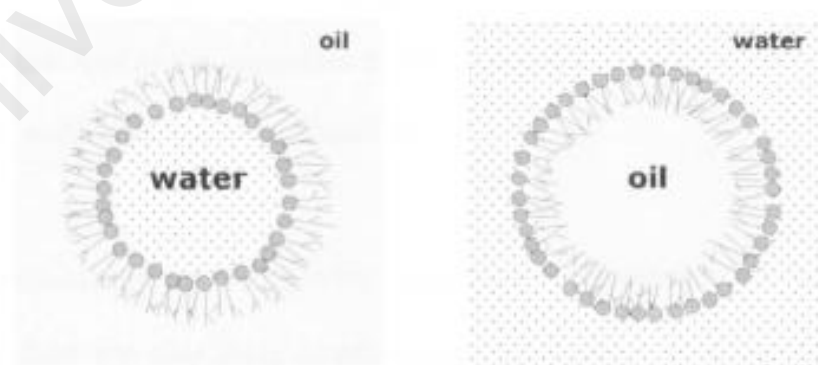
It is described as a method which consists of replacing an ion from the surface of support in an electrostatic interaction with another ion in solution. The ion present in the solution will penetrate into the pore of the solid and the penetrating ion will replace the ion present over target surface. This process will continue until equilibrium is achieved. For example, the surface of support containing ions A is put into excess volume (compared to pore volume) of a solution with ion B. The ions B will penetrate into the solution replacing A over the surface of support and this process will continue until equilibrium is achieved (Campanati et al., 2003).

### **2.6.5 Microemulsion**

The history of microemulsion (ME) dates back to 1940s, when first time it was defined by Schulman and Friend (Schulman & Friend, 1949). The microemulsions have been applied to various industrial process ranging from oil recovery to synthesis of nanoparticles (V Chhabra et al., 1997). However, the synthesis of nanoparticles was reported (Magali Boutonnet et al., 1982) for the first time in 1980s. The literature suggests that for the synthesis of hollow structures, template-assisted approach provides a suitable and versatile procedure, which is divided into two major groups such as: hard templating and soft templating (Q. Zhang et al., 2009). Our focus is on soft template approach, which

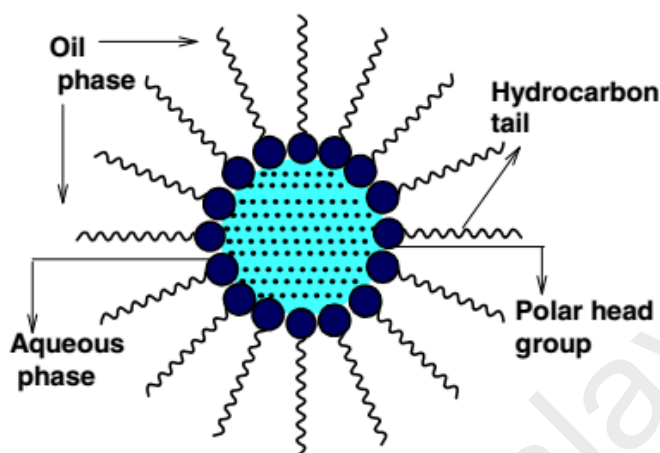
includes surfactants and long chain polymers having the properties of amphiphilic molecules (hydrophilic head and hydrophobic tails) (Fendler, 1987). These materials have the tendency to self-assemble into aggregates in the form of normal and reverse micelles, which restricts the growth of synthesized materials. Both types of emulsions either water-in-oil (W/O) or oil-in-water (O/W) fall in the category of soft templates (Q. Zhang et al., 2009).

Microemulsion is regarded as the mixture of water, oil and surfactant (cationic, anionic, and non-ionic) and its salient features are its transparent nature and thermodynamic stability (Eriksson et al., 2004). Microemulsion exhibits different behaviours at macroscopic and molecular level, in the first case it exhibits homogenous characteristics and in the second case it shows heterogeneous solution (Eriksson et al., 2004). There are two types of microemulsion system based on the dispersed phase and continuous phase. In conventional micelles, the dispersed phase is oil and continuous phase is water as shown in Figure 2.15. The other type is inverse micelle in which dispersed phase is water and continuous phase is oil and normally regarded as water-in-oil (W/O) microemulsion. In W/O microemulsion, the water droplets which are trapped inside are transformed into small droplets ranging from 10-100 nm.



**Figure 2.15:** Microemulsion schematics for water in oil and oil in water.

Water-in-oil microemulsion are defined as the structural setting in which the hydrophilic heads are attracted towards the water and hydrophobic tails are facing towards the non-aqueous phase as shown in Figure 2.16 (Malik et al., 2012).



**Figure 2.16:** Structure of reverse micelles

The distinguished feature of water-in-oil microemulsion synthesis approach is that the water droplets containing metal salt dissolved in it serves as nanoreactors for the synthesis of nanoparticles, when dispersed in continuous oil phase. Thus, the controllability of the nanoparticles size is better based on the water content. These water droplets are stabilized by surfactant and provide a cage effect in the synthesis of nanoparticles via microemulsion, as they will limit the growth and aggregation of particles (Fu & Qutubuddin, 2001; Santra et al., 2001).

The application of microemulsion synthesis approach to synthesize nanoparticles has certain advantages over the previously used preparation methods (impregnation, co-precipitation, sputtering, sol-gel method etc.), as it forms transparent and nano-sized water droplets (dispersed phase) in oil (continuous phase), which are stabilized by the surfactant. This unique type of surfactant covered water droplets create a microenvironment that lead to the formation of monodispersed nanoparticles (D.-H. Chen & Wu, 2000). Another benefit of microemulsion is that it can be synthesize at room temperature which play an important role to produce small size particles, while in case of



conventional preparation methods requires high temperature resulting in larger size particles (Eriksson et al., 2004).

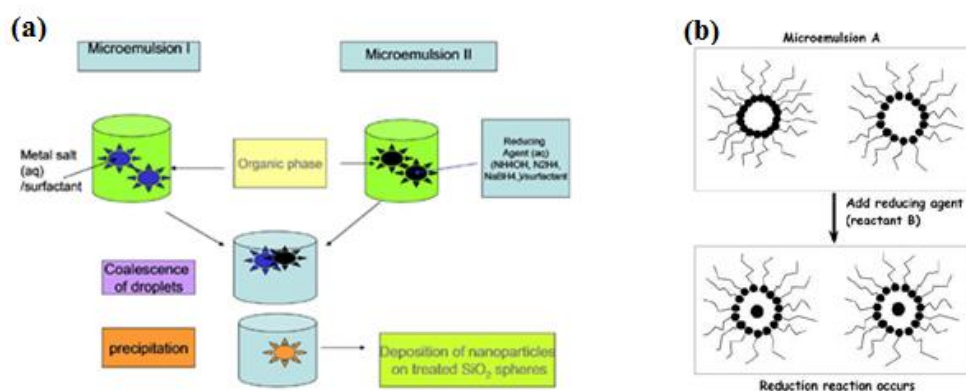
These inverse micelle functioned as a microreactors for processing reactions (D.-H. Chen & Wu, 2000) and also this method allows the formation of nano-sized range metal particles with narrow size distribution which is a very important factor to enhance activity, stability and reduce carbon deposition (Magali Boutonnet et al., 2008). In impregnation, it is quite difficult to control the composition of the bimetallic catalyst, however, the preparation of bimetallic catalyst prepared by microemulsion gives better control over the composition.

## **2.7 Strategy for nanoparticles preparation by microemulsion synthesis**

There are two possible ways to prepare microemulsion depending on the sequence of mixing microemulsion

(a) First route is the preparation of two separate microemulsion, one contained the metal ions and other contained the reducing agent or precipitating agent as shown in Figure 2.17(a). The mixing of both microemulsions lead to the nucleation to occur on the micelle edges.

(b) Another route to prepare is from single microemulsion by adding reagent in one microemulsion and then adding reducing agent in the same microemulsion as shown in Figure 2.17b. This is also a common way to produce metal nanoparticles.



**Figure 2.17:** Description of nanoparticles synthesis from the microemulsion route (Eriksson et al., 2004; Zabidi, 2012)

## 2.8 Influence of various factors on the synthesis of nanoparticles

The major focus in the microemulsion system will be the size of particle formed during the preparation and understanding of the factors affecting the particle size is important to avoid large size particles.

### 2.8.1 Water content

The water content in reverse micelle has an important influence in determining the final size of particles formed. The metal salts are solubilized inside the water pool and provides the space for the reaction to occur. The radius of the reverse micelles for the spherical water droplets formed in microemulsion with the certain water content is calculated by the following expression:  $R^* = 3V/\Sigma$ , in which  $R^*$  denotes the radius,  $V$  denotes the volume and  $\Sigma$  the surface area of the sphere. Thus, it is clear that water content in a reverse micelle is important to control the particle size. The aqueous content present in the emulsion is generally denoted in relation with the surfactant concentration is given by the ratio of water to surfactant ratio  $R = \text{water/surfactant}$  (Eriksson et al., 2004; Ganguli et al., 2010). Previous study reported that the average diameter of Ni particles was decreased (from 14.3 to 4.3 nm) with the increase of water content (from 18wt% to 22wt%) at constant water to surfactant ratio (0.66) (D.-H. Chen & Wu, 2000). As we

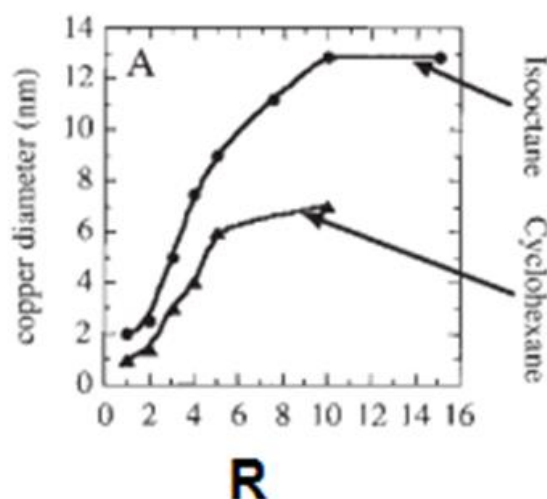
know that microemulsion system consists of water, oil and surfactant, a decrease in the water content will lead to the increase in oil content, which in turn results in the increase of surfactant/oil ratio. The inverse micelle system which consists of oil as continuous phase, the decreased surfactant/oil ratio would mean an unstable interface and lower interaction between the surfactant and oil. This instability of the interface would lead to the larger particle size because the greater mobility of the interface would allow them to rearrange. As the water content was decreased (from 22% to 18%) the surfactant/oil ratio decreased from 0.73 to 0.49, which lead to the formation of larger metal particles (14.3 nm) (D.-H. Chen & Wu, 2000). However, the formation of larger particle size with the decrease of water content does not match with basic microemulsion function and this study contradicts with previous reported studies. Previous studies suggested that lower water content would lead to the decrease in particle size. This phenomenon will be discussed in detail in the following section.

Several authors reported that nanoparticle growth is affected by the change in water to surfactant ratio (Cason et al., 2001; Kitchens et al., 2003). This variation in the particle size with water to surfactant ratio is dedicated to the concept of bound or free water. At low water content, the water inside the polar core is strongly attached to the polar head of the surfactant group and micelle interface is considered to be rigid leading to lower intermicellar exchange and thus growth rates. This can be dedicated to the lower amount of content available to hydrate the polar head group and counter ion (M. Pileni, 1998). The increase of water content makes micelle interface become more fluid leading to the rate of higher growth rate (higher intermicellar exchange), until a point is reached after this extra water added is just added to the bulk water pool. This situation has been reported to occur at water to surfactant ratio of 10 – 15 (M. Pileni, 1993).

Pileni group also investigated the relationship and controllability of the particle size and morphology of nanoparticles by varying water to surfactant ratio (R) (M. Pileni,

2007). The reported that in the synthesis of copper nanoparticles, there was seen an increase in Cu particle size with the increased of water content. Furthermore, the affinity of surfactant towards the metal centre also play an important role to influence the particle size. The lower affinity of the surfactant towards the metal centre leads to the inefficiency to control the growth and an increase in the final particle size was observed (Isabelle Lisiecki, 2005). It is reported that with the increase of water content in the microemulsion system at constant surfactant concentration, an increase in reverse micelle diameter will be observed. The occurrence of this phenomenon will lead to the increase in intermicellar potential and larger particle size will be observed.

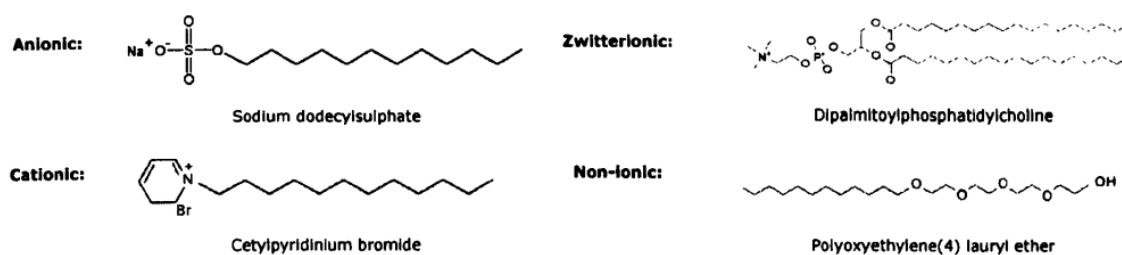
Furthermore, with the increase of water content in microemulsion system, the quantity of tightly bound water decreases and thus lead to lower interaction energy between water and surfactant. The lower interaction energy between water and surfactant will then lead to decrease interfacial rigidity and thus an increase in particle size will be observed (M. Pileni, 1998). As shown in Figure 2.18, an increase in water content in the microemulsion system leads to the increase of copper particle diameter. In this study, two different types of oil such as isooctane and cyclohexane were studied. The study indicates that the application of isooctane (larger solvent molecules) produced larger particles size compared to cyclohexane (smaller solvent molecules). This was attributed to the inability of larger solvent molecules to penetrate into the alkyl chains of surfactant, which favours the occurrence of larger intermicellar exchange and thus larger particle size were formed (M. Pileni, 1998).



**Figure 2.18:** Influence of water content and oil type on copper particle diameter (M. Pileni, 1998)

### 2.8.2 Surfactant types

The source of word surfactant is from “surface active agent” and is extensively used to reduce the interfacial tension between two immiscible phases. Generally, surfactant consist of organic molecules with a polar head group (hydrophilic head) and a long alkyl chain (hydrophobic tail) (Ganguli et al., 2010). The application of surface active agents or surfactants is important as surfactant molecules has the ability to form self-assembles to form aggregates (M. Pileni, 1998). Surfactants are regarded as a kind of amphiphiles having hydrophilicity and hydrophobicity at same time and helps to reduce the interfacial tension. The nature of microemulsion strongly depends on the type of surfactant being used (Lin, 2006). Based on their structure, surfactants are normally divided into ionic, non-ionic and zwitterionic as shown below in Figure 2.19:



**Figure 2.19:** Types of surfactants based on their structure (Lin, 2006)

Similarly, it was reported that increase of surfactant concentration would lead to the smaller particles due to its tendency to enhance the number of droplet. This will eventually lead to the lower metal ions per droplet and in turn smaller size (Eriksson et al., 2004). The formation of microstructure is often linked with the formation of interfacial curvature induced by the balance between surfactant polar head group forces set by electrostatic double layer and by the hydrophobic tails interaction set by the oil (M. Pileni, 1998).

A specific empirical number has been assigned to each surfactant based on the size of two chains, which is known as Hydrophilic-Lipophilic Balance (HLB). It indicates the degree of hydrophilic or lipophilic for specific surfactant. Griffin proposed an HLB scale for the non-ionic surfactants and HLB number 1 was assigned to the most lipophilic molecules while a higher value of 20 was assigned to the most hydrophilic molecules. There are different methods to calculate the HLB number for specific surfactant. For example, HLB values for polyhydric alcohol fatty acid esters can be calculated using the following expression, where  $M_h$  denotes the weight of hydrophobic group and  $M_w$  is the molecular weight (Ganguli et al., 2010).

$$HLB = ( 1 - \frac{M_h}{M_w})$$

The HLB value for fatty acid esters (Tween type) are calculated by the following expression, where E is the weight percentage of oxyethylene and P indicates the weight percentage of polyhydric alcohol.

$$HLB = (E + P)/5$$

HLB values are considered to be dependent on its structure and the application of certain surfactant will be decided based on its HLB number, for example W/O microemulsion type can be formed with the surfactant having low HLB number and O/W microemulsion can be formed with surfactant having a higher HLB number (Ganguli et al., 2010). The addition of surfactant in the microemulsion not only stabilizes the emulsion but also reduced interfacial tension. Furthermore, surfactant wall provides a

spherical module for the synthesis of metal particles (Magali Boutonnet et al., 2008; Eriksson et al., 2004). The miscibility of these surfactants changes with the temperature as suggested in the previous study in which they investigated the application of different ionic and non-ionic surfactants at two different temperatures 25 °C and 60 °C (Lin, 2006). It was reported that ionic surfactant AOT and Tween 85 (non-ionic surfactant), were miscible with all the oil phases studied (isooctane, petroleum ether and cyclohexane). However, Tween 80, Triton X-100, Igepal CO-720 and Brij 97 are not miscible with the above-mentioned oil phases. Moreover, non-ionic surfactants Triton X-114 and Igepal CO-520 dissolved in ether and cyclohexane and remain immiscible with isooctane. The miscibility results for different surfactants are shown in Table 2.9 below for their study (Lin, 2006).

**Table 2.9:** Miscibility data of different surfactant with oil phases at 25 °C.

	Isooctane	Petroleum Ether	Cyclohexane
<b>AOT</b>	✓	✓	✓
<b>Tween 85</b>	✓	✓	✓
<b>Tween 80</b>	☒	☒	☒
<b>Triton X-100</b>	☒	☒	☒
<b>Triton X-114</b>	☒	✓	✓
<b>Igepal CO-520</b>	☒	✓	✓
<b>Igepal CO-720</b>	☒	☒	☒
<b>Brij 97</b>	☒	☒	☒

☒ denotes non-immiscibility, ✓ denotes miscibility.

**Table 2.10:** Miscibility data of different surfactant with oil phases at 60 °C.

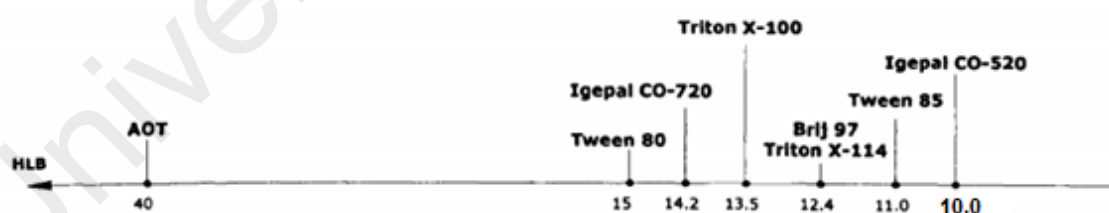
	Isooctane	Petroleum Ether	Cyclohexane
<b>AOT</b>	✓	✓	✓
<b>Tween 85</b>	✓	✓	✓
<b>Tween 80</b>	☒	☒	☒
<b>Triton X-100</b>	☒	☒	☒
<b>Triton X-114</b>	☒	✓	✓
<b>Igepal CO-520</b>	☒	✓	✓
<b>Igepal CO-720</b>	☒	☒	☒
<b>Brij 97</b>	☒	☒	✓

☒ denotes non-immiscibility, ✓ denotes miscibility.

The difference between the miscibility data at 25 °C and 60 °C is that Brij 97 becomes miscible with cyclohexane at 60 °C but still remain immiscible with other two oil phases.

### 2.8.3 Compatibility of surfactant and oil

Another important feature regarding the choice of surfactant in the compatibility (miscibility) of particular surfactant with oil and there is basic strategy to choose proper surfactant for oil, which is the structure similarity. It is suggested that better miscibility exists between surfactant and oil which are having the similar structures, for example, Triton X-100 does not dissolve in cyclohexane due to cyclic structure of oil phase, and can dissolve in isooctane due to its linear structure. However, this does not apply to all the surfactants such as for Tween 85, Triton X-100, Triton X-114, Igepal CO-520 and Igepal CO-720, even though they are having cyclic chain in their structure, however, all of them do not dissolve in cyclohexane (Lin, 2006). Therefore, Hydrophile-Lipophile balance (HLB) values provide a more practical solution to the miscibility and over the formation of different microemulsion either water in oil or oil in water. HLB values for various surfactants are shown in Figure 2.20:



**Figure 2.20:** HLB values of different surfactants

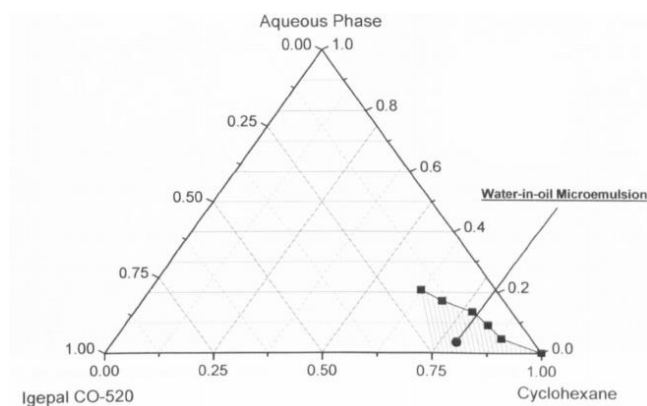
Non-ionic surfactants usually consist of ethylene oxide (EO) units, such as Igepal CO-520 and Triton X series has polyoxyethylenated alkylphenols units, while Tween series has polyoxyethylenated polyols units (Lin, 2006). The hydrophilic nature of non-ionic surfactants depends upon the number of EO units in its structure and an increase in



the number of EO units by applying different non-ionic surfactants gives flexibility to the manufacturer to have different solubility and characteristics of the under investigated system (Schmolka & Shick, 1967). In the solution of non-ionic surfactant with oil, there is tendency that surfactant molecules will aggregate by the intermolecular hydrogen bonding (Kumar & Balasubramanian, 1980) leading to the formation of micelles. The micelles will have the ability to solubilise the aqueous phase by the interaction of EO units present in the polyoxyethylenated (POE) chains (Rosen, 2004). The previous study suggested that cyclohexane is the better choice for all the surfactants being employed in terms of water solubilisation compared to isooctane and petroleum ether. It has been suggested that the water solubilisation in the microemulsion increases with the increase of micelle size and this can be further explained by aggregation number. This aggregation number is the indication of the number of surfactant units forming the micelle. Aggregation number can be calculated by the following formula provided the molecular weight of surfactant used is known:

$$n = M_m/M_o$$

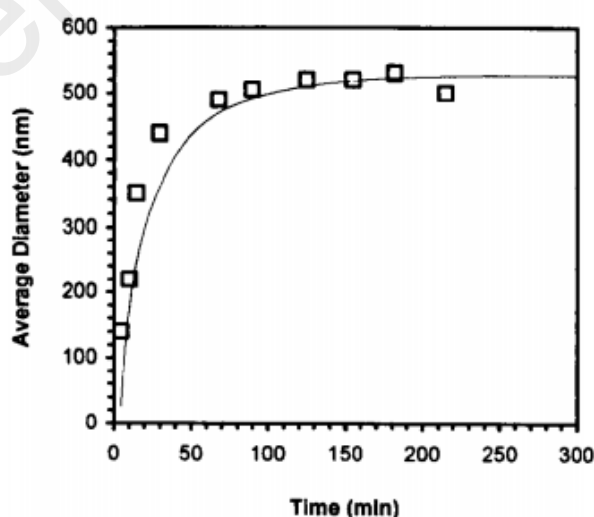
where  $n$  denotes aggregation number,  $M_m$  denotes micelle weight and  $M_o$  molecular weight of surfactant (Rosen, 2004). The above expression suggests that the higher aggregation number indicates the increase in micellar size and better water solubility. Cyclohexane has been found to exhibit better miscibility with surfactants and this leads to the larger aggregation number compared to isooctane and petroleum ether, which is the reason superior water solubility characteristics was observed in water in oil microemulsions (Lin, 2006). The phase diagram for water/Igepal CO-520/cyclohexane microemulsion system is shown in Figure 2.21 and the shaded area indicates the suitable ratio of water, oil and surfactant that should be chosen to form water-in-oil microemulsion (Lin, 2006). Beyond this area, water-in-oil microemulsion will not be observed.



**Figure 2.21:** Phase diagram for water, cyclohexane and Igepal CO-520 system at 25 °C.

#### 2.8.4 Effect of aging time

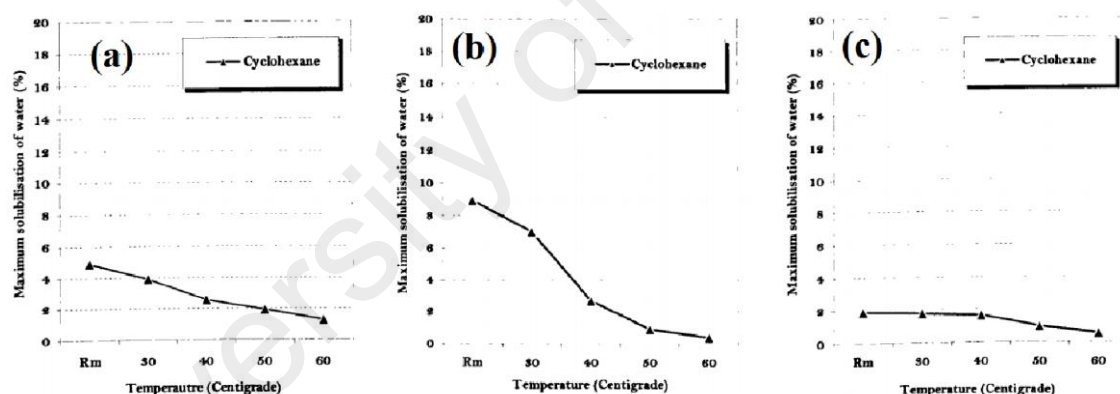
The previous study showed that with the reaction time during the synthesis of nanoparticles can have influence over the average particle size and also on the tetra-ethyl-ortho-silicate (TEOS) hydrolysis via w/o microemulsion. The synthesis of SiO<sub>2</sub> particles studied with the influence of reaction time exhibits that with the increase of time an increase in the average diameter was observed as shown in the below Figure 2.22 (Lin, 2006). Therefore, the choice of proper reaction time is important to have smaller particle size during the nanoparticle synthesis.



**Figure 2.22:** Influence of reaction time on SiO<sub>2</sub> average diameter

## 2.8.5 Effect of temperature

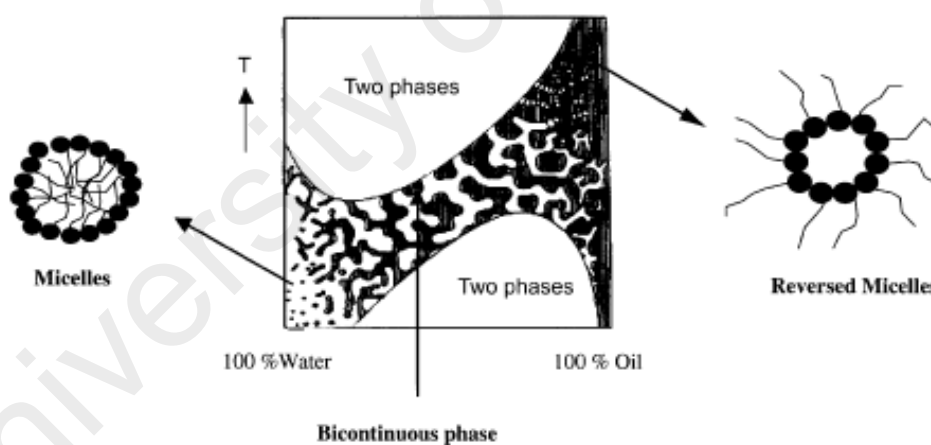
It is suggested that the choice of proper temperature in the microemulsion synthesis approach is critical as it has been found to influence the characteristics of the surfactant aggregates such as: size, shape, ionic nature and also the solubilisation of the surfactant in the system. The shift in temperature from room temperature can have influence over the intermolecular interactions between components (water, oil and surfactant) of microemulsion (Lin, 2006). Furthermore, the proper selection of temperature is important to have maximum solubilisation of water in microemulsion system with non-ionic surfactants (Tween 85, Igepal Co-520 and Triton X-114). It was observed that with the increase of temperature, maximum solubilisation of water decreased for all the surfactants under investigation as shown below in Figure 2.23 (Lin, 2006):



**Figure 2.23:** Maximum solubilisation of (a) Tween 85, (b) Igepal Co-520 (c) Triton X-114 in cyclohexane.

The maximum solubilisation of Igepal CO-520 decreased from 8.9% to 0.4% as the temperature was increased from room temperature 25 °C to 60 °C. The influence of temperature on the solubilisation of water in microemulsion system was more pronounced for Igepal CO-520 compared to Tween 85 and Triton X-114. Therefore, room temperature is better for Igepal CO-520 and cyclohexane based microemulsion system for having maximum solubilisation. Hydrophilicity of surfactant is basically depending

upon the number of EO units present in surfactant chain and it is claimed that the increase of temperature will lead to the dehydration of POE units (Schmolka & Shick, 1967). This will in turn leads to the decrease in the water solubilisation in the micelle core indicating the presence of inverse temperature-solubility behaviour. The dehydration of POE units with the increase of temperature causes structural changes such as in the aggregation number and interfacial tension of surfactant aggregates (Misra, 1991). In a result of decrease in aggregation number, reduction in capacity of micelle occurs and the smaller size of micelle then has lower capacity for water solubilisation (E Ruckenstein & Nagarajan, 1980). The special care should be taken in the choice of temperature in the preparation of inverse micelle as these are temperature sensitive as shown in Figure 2.24. At higher temperature, the structure of oil droplets will be destroyed and at lower temperature water droplets will be affected (Eriksson et al., 2004).



**Figure 2.24:** The effect of temperature and composition of water and oil in the preparation of microemulsion (Schwuger et al., 1995).

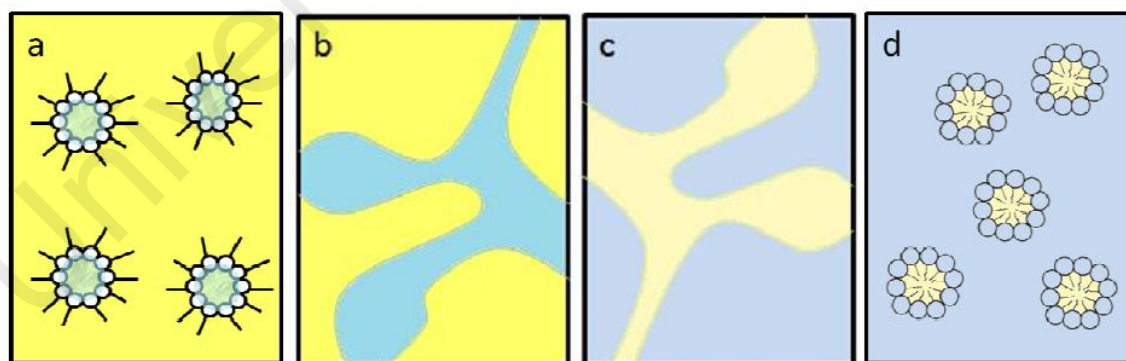
### 2.8.6 Metal salt concentration

Metal salt concentration in the microemulsion system plays a major role in controlling the final metal particles, as higher concentration of salt will result in the increased possibility of having metal precursor or nuclei and will have greater probability of filled-filled micelle exchange upon collision and thus an increase in particle size will

be observed. Therefore, an increase in metal salt concentration will lead to the increase in metal particles, provided that water/surfactant and surfactant/oil ratios are held constant.

## 2.9 Types of microemulsion

The addition of surfactant into the mixture of two immiscible fluids serves as to lower down the interfacial tension, which results in the formation of emulsion or microemulsion. The difference between emulsion and microemulsion lies in their size of droplet and stability of the droplet formed. The former being kinetically stable, while the latter is thermodynamically stable. Basically, there are two types of microemulsion, one is regarded as dispersed and other is bicontinuous. In dispersed microemulsion, droplets formed based on dispersed phase (water or oil) are stabilized by surfactant in continuous phase (water or oil), while in bicontinuous microemulsion, a continuous network of water and oil is separated by the formation of membrane based on surfactant molecules (Hamley, 2007). The description of dispersed and bicontinuous phase are shown below in Figure 2.25 (Savko, 2011):



**Figure 2.25:** Schematics of dispersed and bicontinuous microemulsion a) water in oil dispersed b) water in oil bicontinuous c) oil in water bicontinuous d) oil in water dispersed.

The presence of free water inside the core is called water pool and the structure of interfacial water is different from bulk water. Moreover, in W/O microemulsion, polar

heads of surfactants are directed towards the water core and non-polar tails are directed towards the oil continuum (Magali Boutonnet et al., 1982). Moreover, the water core can be considered bound or unbound based on the water content present in the microemulsion system. Therefore, the situation in which the water content is small, the water molecules will form strong hydrogen bond with the surfactant polar head groups and are said to be bound water. However, as the water content is increased, the chances of the presence of unbound or free water is increased.

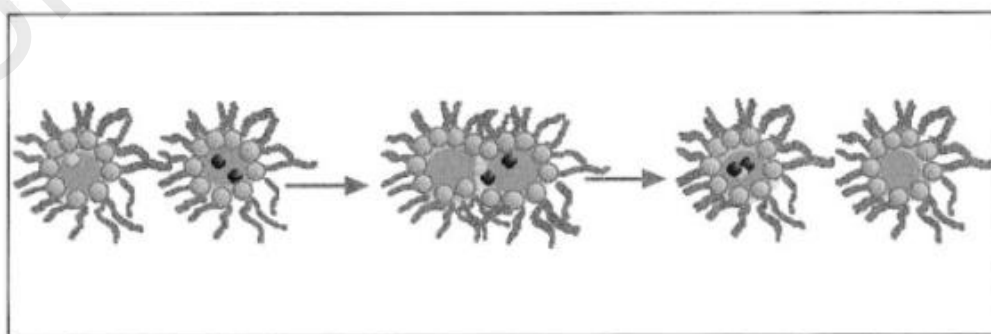
## **2.10 Mechanism**

The micelle formed in the microemulsion system are considered to be of dynamic nature and micelles formed collide with each other via Brownian motion and coalesce to form dimers, which later on exchange contents and break part again (Bommarius et al., 1990). This exchange process and mobile nature of micelles formed lead to the well-mixing of inorganic reagents encapsulated inside the micelles. Furthermore, the exchange process is deemed important for nanoparticle synthesis which are inside reverse micellar templates allowing different reactants to react with each other upon mixing. Micelles in reverse microemulsion are regarded to act as nanoreactors providing a suitable environment for controllable nucleation and growth. The role of surfactant is important that provides protective layer which restricts the nanoparticles from agglomeration (Eastoe et al., 2006; M. Pileni, 1998).

It has been suggested that the final particle is not formed inside the microemulsion droplet but only the nuclei. The microemulsion system is considered as of dynamic nature meaning that during the process of particle formation a number of collisions will occur. The formation of final particles is supposed to be happening in two steps: first is the nucleation process inside the microemulsion droplet and then the growth or aggregation process to form the final particle (Eriksson et al., 2004). The presence of surfactant played

an important role to prevent the occurrence of nucleation too fast. This will result in the nanoparticles which will grow at the same rate favouring the formation of homogenous size distribution. This will form the emulsion system in which small particles stabilized by the surfactant molecules restricting the coalescence phenomenon that otherwise will assist in the occurrence of agglomeration of particles just formed (Eriksson et al., 2004). The size of microemulsion droplet will influence the size of the nuclei but the final size is controlled by the surrounding surfactant molecules (Y. Li & Park, 1999).

Different types of monometallic, bimetallic nanoparticles and semiconducting particles are synthesized by microemulsion synthesis approach. The basic approach in this method is to form a water in oil microemulsion, in which the content of each component is selected from ternary phase diagram for that particular surfactant and oil system. After selecting the suitable amount of water, surfactant and oil, the next step is to prepare metal salt solution in water and then added into the above prepared mixture of surfactant and oil. The aqueous solution of metal salt will then go into the core of micelles forming reverse micelles as the hydrophilic head will be towards the water core and hydrophobic tails will be outward. The addition of reducing or precipitating agent will then form active metal nuclei. Due to their Brownian motion, each micelle will collide each other, which leads to the formation of larger particles as shown in Figure 2.26 for this exchange mechanism.



**Figure 2.26:** Micelle exchange mechanism (M. Pileni, 1998)

The final metal particle size obtained after the synthesis process seems to be the reflection of average number of micelles exchanges, which strongly depend upon the intermicellular potential and also on the rigid nature of the interface. Therefore, as more and more micellar exchange will occur due to more intermicellular potential, it is expected to form larger particle size. Moreover, smaller size particles are expected to form, as a result of lower intermicellular potential. The nature of interface plays an important in controlling the size of metal particles. It is suggested that larger collision energy will be required in order to have successful micelle exchanges for system having rigid interface and in turn leading to the formation of smaller particles (M. Pileni, 1997, 1998). However, many factors are taken into account such as: micelle size, solvent molar volume, which can have influence over intermicellular potential. In the next section, we will discuss the catalyst prepared by microemulsion synthesis approach and applied for dry reforming of methane.

## **2.11 Preparation of catalysts via microemulsion synthesis**

In recent studies on dry reforming of methane, the supported Ni-catalysts exhibited better catalytic activities due to the advanced preparation techniques and preparation methods (Kang et al., 2012). One way to tackle the issue of carbon deposition is to encapsulate metallic nanoparticles in silica ( $\text{SiO}_2$ ) porous shell. It was reported that the isolation of nanoparticles by porous shell will not only enhance the excess of reactant to active metal core but will also reduce the chances of sintering during the reaction (Y. Li et al., 2014). The preparation of these porous shell can be executed by microemulsion technique (Y. Li et al., 2014).

A new class of catalyst has been emerged by the combination of core-shell and hollow structures named as yolk-shell or nano-rattles structure (core@void@shell) and denoted as A@B (J. Liu et al., 2011). These coated catalysts have higher resistance for



sintering and surface area loss compared to conventional supported catalysts (Dahlberg & Schwank, 2012). Moreover, the internal void can be regarded as reaction chamber or nanoreactor in which chemical reaction will occur in a different manner especially from macro-scale reactions due to the confinement effects of the active metal inside a shell (Q. Yang et al., 2008). The synthesis of Ni@SiO<sub>2</sub> core@shell structure was executed by W/O microemulsion synthesis approach (Dahlberg & Schwank, 2012). They reported the formation of cylindrical nanotube cavities in which the movement of Ni particles inside the cavity results in greater accessibility of metal surfaces. Such type of catalysts in which metal particles are covered with oxide layers exhibited strong resistance against sintering and occurrence of single-atom migration such as Ostwald ripening or leaching (Dahlberg & Schwank, 2012). Another study also reported the preparation of Ni@SiO<sub>2</sub> yolk-shell structure (Park et al., 2010) and investigated for steam reforming of methane. The higher sintering and coking resistance of Ni@SiO<sub>2</sub> catalyst was attributed to the confinement effect of Ni particles inside silica shell. There are number of papers discussing the application of yolk shell catalysts for partial oxidation of methane (L. Li, He, et al., 2012; L. Li, Lu, et al., 2012; Takenaka et al., 2007) and steam reforming of methane (Park et al., 2010; Takenaka et al., 2008), however, there was little fewer studied reporting their application on dry reforming reaction. A study reported the preparation of Ni@SiO<sub>2</sub> by microemulsion and reported 60% CH<sub>4</sub> and 73.5% CO<sub>2</sub> conversion and higher stability (90 h) for dry forming of methane (Z. Li et al., 2014). It was reported that although the carbon deposition was little high 29.4% for Ni@SiO<sub>2</sub>, it showed excellent stability within 20 h of the reaction period. It was ascribed to the formation of active type of carbon C<sub>α</sub> during the reaction period instead of inactive type C<sub>β</sub>. Another recent study reported the formation of yolk-shell bimetallic catalyst (Cu-Ni@SiO<sub>2</sub>) by microemulsion synthesis approach and compared the catalytic activity of yolk-shell catalyst for dry reforming of methane with impregnated catalyst (T. Wu et al., 2013). The higher catalytic activity and

stability of yolk-shell catalyst was attributed to the isolation effect of core particles from each other and resulted in enhanced sintering resistance. The lower catalytic activity of the impregnated catalyst was attributing to the weak metal-support interactions, which leads to the poor sintering resistance and in turn lower catalytic activities and stability. A study investigated a Ni/CZ catalyst prepared by W/O microemulsion exhibited 6.1% methane conversion while Ni/MgO-SiO<sub>2</sub> catalyst prepared by similar method produced a nano-sized catalyst in the range of 3-7 nm, though conversion rates were not reported (Makhum, 2006). Another study reported the preparation of LaNiO<sub>3</sub> nanoparticles covered by SiO<sub>2</sub> shell (LaNiO<sub>3</sub>@SiO<sub>2</sub>) and compared the activity and stability of the catalyst with conventionally prepared impregnated catalysts (Ni/SiO<sub>2</sub> and LaNiO<sub>3</sub>/SiO<sub>2</sub>) for dry reforming of methane (Zheng et al., 2014). The study reported higher catalytic activity and stability of yolk shell catalyst prepared by microemulsion compared to impregnated catalysts. This was attributed to smaller Ni particles, resistance to agglomeration and carbon deposition provided by protective shell of metal oxide (SiO<sub>2</sub>) to LaNiO<sub>3</sub> nanoparticles. TGA analysis of the various catalysts verified the higher carbon deposition resistance for yolk shell catalyst (LaNiO<sub>3</sub>@SiO<sub>2</sub>) compared to impregnated catalysts.

However, it was suggested that the application of inert support material (SiO<sub>2</sub>) will lead to monofunctional mechanism such that both methane and carbon dioxide will be activated by metal alone. In this pathway, the methane decomposition will first produce H<sub>2</sub> and carbon, while in the second important step gasification of produced C with CO<sub>2</sub> will have limited opportunity to occur. This will lead to the deactivation of the catalyst. Therefore, the application of MgO and CeO<sub>2</sub> exhibiting bifunctional mechanism will play an important role in the enhancement of catalyst performance, where both metal and support have their own separate role of activating methane and carbon dioxide, respectively (Theofanidis et al., 2015).

There were few studies reported on the formation of MgO supported with different active metals by microemulsion synthesis. A study was reported on the microemulsion synthesis of MgO supported  $\text{LaMnO}_3$  nanoparticles, however their application studies were focused on methane combustion (Svensson et al., 2006). Another study also reported the preparation of Ni/MgO core/shell nanoparticles by a special experimental setup in which beam of Ni nanocluster was co-deposited with evaporated MgO in controlled  $\text{O}_2$  environment, however, no specific application studies were reported (D'Addato et al., 2011). Another study reported the preparation of  $\text{SnO}_2$  nanoparticles by microemulsion synthesis approach supported over basic metal oxide (MgO and CaO). Their study focused on the catalytic oxidation of dimethyl ether and reported that both catalyst exhibited acceptable activity for dimethyl conversion (L. Yu et al., 2007). Another study reported the synthesis of NiO-MgO nanoparticle encapsulated by silica shell, however, their application study was focused on  $\text{CO}_2$  methanation only and was prepared by modified stöber method (Y. Li et al., 2014). A study reported the preparation of  $\text{MgAl}_2\text{O}_4$  by microemulsion synthesis approach (water/ Igepal CO-520/cyclohexane), however, the application of this catalyst was not discussed (Chandradass et al., 2010). Ni/MgO- $\text{SiO}_2$  catalyst was prepared by microemulsion synthesis approach by applying Igepal CO-520, cyclohexane and water, however, the catalytic activity of the catalyst for dry reforming of methane was not reported (Bae, 2013). Several studies were also found on the preparation of MgO nanoparticles alone through microemulsion synthesis applying different surfactant, co-surfactant and oil types (Ganguly et al., 2011; Han et al., 2005; Wen et al., 2010).

Number of studies reported on the synthesis of Ni/ $\text{CeO}_2$  catalyst by various preparation methods (impregnation, hard template method and solvothermal approach) as described in sub-section 2.5.2., however there were no studies reported on the application of microemulsion synthesis (water/Igepal CO-520/cyclohexane) approach for the

preparation of Ni@CeO<sub>2</sub> core-shell like structures and applied for dry reforming of methane. A study reported the synthesis of CeO<sub>2</sub> yolk for the stabilization of Au nanoparticles synthesized by solvothermal approach and their application was on the reduction of p-nitrophenol. A detailed review was published recently on the encapsulation of noble metals (Pt, Au, Pd, Rh and Ru) by CeO<sub>2</sub> core and yolk shell catalysts, however it was mainly focused on noble metal catalysts and none of the studies were presented for non-noble metals (Ni and Co) (S. Song et al., 2015). Another study reported the synthesis of Ce<sub>1-x</sub>Ni<sub>x</sub>O<sub>2-y</sub> by reverse microemulsion method, however, the application of the catalyst was on water gas shift reaction (Barrio et al., 2010). Another study reported the synthesis of Ni-based catalyst supported on cerium-lanthanum oxide by microemulsion synthesis approach, however they studied this catalyst for the selective oxidation of ammonia (Nassos et al., 2006) . Different types of catalysts prepared by different types of surfactants and oil are described in Table 2.11 along with their application.

**Table 2.11:** Different catalysts prepared by microemulsion synthesis approach

Catalyst	Application	Microemulsion	Ref
Pt/Al <sub>2</sub> O <sub>3</sub> , pumice	Hydrogenation	PEGDE/hexadecane /water	(M Boutonnet et al., 1980)
Pt, Pd, Rh/pumice	Hydrogenation	PEGDE/hexadecane or hexane/water	(M. Boutonnet et al., 1987)
Pt/TiO <sub>2</sub>	Selective hydrogenation	PEGDE/ <i>n</i> -octane/ water	(Boutonnet Kizling et al., 1996)
Pd, Rh particles	Hydrogenation	AOT + PFPE-PO <sub>4</sub> / water/supercritical CO <sub>2</sub>	(H. Ohde et al., 2002; M. Ohde et al., 2002)
CeO <sub>2</sub> /Al <sub>2</sub> O <sub>3</sub>	CO oxidation	OP-10/cyclohexane / <i>n</i> -hexyl alcohol/ water	(Masui et al., 1997)
Pt/Al <sub>2</sub> O <sub>3</sub>	Combustion of methane	Tween 80/ cyclohexane or heptane/ cyclohexanol/ water	(Rymeš et al., 2002)
BaAl <sub>19</sub> O <sub>11</sub>	Combustion of methane	Neodol 91-6/1- pentanol/ <i>iso</i> -octane/ water	(Zarur & Ying, 2000)
Pd/Al <sub>2</sub> O <sub>3</sub>	Combustion of methane	Berol 02/ cyclohexane/water	(Pocoroba et al., 2001)

**Table 2.11: Continued**

Pd/ZrO <sub>2</sub> , TiO <sub>2</sub> , Al <sub>2</sub> O <sub>3</sub>	Methanol synthesis	NP-5/ cyclohexane/water	(Kim et al., 1998)
Cu/ZnO	H <sub>2</sub> production	Berol 02 /cyclohexane /water	(Agrell et al., 2001)
Rh/SiO <sub>2</sub>	CO <sub>2</sub> hydrogenation	NP-5/cyclohexane / water	(Kishida et al., 1996)
Rh/SiO <sub>2</sub>	CO <sub>2</sub> hydrogenation	NP-5/cyclohexane / water	(Kishida et al., 1995)
Rh/SiO <sub>2</sub>	CO hydrogenation	CTAB/hexanol/ water	(Kishida et al., 1998)
Rh/SiO <sub>2</sub>	CO hydrogenation	CTAB/hexanol/ water	(Hanaoka et al., 1997)
Rh/SiO <sub>2</sub>	CO hydrogenation	CTAC/hexanol/ water	(Tago et al., 2000)
Pd/ZrO <sub>2</sub>	CO hydrogenation	CTAB/hexanol/ water	(Kim et al., 1997)
Fe/SiO <sub>2</sub>	CO hydrogenation	NP-5 or NP-10 or NP-20/hexanol or butanol/ water	(Hayashi et al., 2002)
2Li <sub>2</sub> O/MgO	Oxidative coupling of methane reaction	Span-83/kerosene/ propanol /water	(Fallah & Falamaki, 2010)

## 2.12 Summary

This chapter summarizes all the literature present on dry reforming of methane with various catalysts studied at different reaction conditions. The influence of metal, support and calcination temperature over catalytic activity was discussed in detail. Microemulsion synthesis approach has been discussed in details along with its significant parameters influencing the morphology and structure of synthesized nanoparticles.

## CHAPTER 3: MATERIALS AND METHODS

### 3.1 Introduction

Water-in-oil microemulsion synthesis method consists of two steps operation, first the synthesis of active metal nanoparticles at desired parameters and later on the addition of support materials to the microemulsion system. In this section, the methodology of the preparation of MgO and CeO<sub>2</sub> based catalysts and their activity studies at desired condition are described;

➤ **Part 1:**

Synthesis of Ni nanoparticles and 20%Ni/MgO at different preparation parameters (water/surfactant ratio, aging time, calcination temperature, molar concentration) and investigating their catalytic activity and characterization.

➤ **Part 2:**

An investigation on the influence of catalyst composition, calcination and reduction temperatures on Ni/MgO catalyst for dry reforming of methane.

➤ **Part 3:**

Water-in-oil microemulsion synthesis of Ni@CeO<sub>2</sub> core-shell like structures for dry reforming of methane

### **3.2 Part 1: Synthesis of Ni nanoparticles and 20%Ni/MgO at different preparation parameters (water/surfactant ratio, aging time, calcination temperature, molar concentration) and investigating their catalytic activity and characterization.**

In this section, the influence of different synthesis parameters on the Ni nanoparticle was investigated and later on synthesize Ni/MgO catalyst at these optimized parameters.

#### **3.2.1 Materials and chemicals**

Nickel (II) nitrate hexahydrate  $\text{Ni}(\text{NO}_3)_2 \cdot 6\text{H}_2\text{O}$  and magnesium nitrate hexahydrate ( $\text{Mg}(\text{NO}_3)_2 \cdot 6\text{H}_2\text{O}$ ) were procured from Acros Organics. Ammonium hydroxide (28 wt %) and ethanol was purchased from R&M solutions. Non-anionic surfactant Igepal CO-520 (Polyoxyethylene (5) nonylphenylether) was acquired from Sigma-Aldrich. A number of gases used in our study such as:  $\text{H}_2$  (99.999%),  $\text{CH}_4$  (99.995%)  $\text{CO}_2$  (99.995%) and  $\text{N}_2$  (99.99%) were procured from Linde Malaysia.

#### **3.2.2 Preparation of Ni nanoparticles**

The microemulsion compositions investigated in this study were chosen according to the ternary phase diagram for water/Igepal co-520/ cyclohexane system (Figure 2.21). Microemulsion system having different compositions of surfactant, water and oil were prepared as mentioned in Table 4.1 and method described here is for microemulsion system A2 (water/ surfactant/ oil; 6/9/85). First of all, 9 ml of Igepal CO-520 were added to 85 ml of cyclohexane and stirred for around 15 min. Later on, 2 M  $\text{Ni}(\text{NO}_3)_2$  solution was prepared according to the aqueous phase (water%) deemed suitable for each microemulsion system. Nickel solution was added dropwise to

microemulsion system by keeping in view the transparency of ME system as shown in Figure 3.1.



Figure 3.1: (a,b) Microemulsion system containing Igepal CO-520, cyclohexane and Ni metal solution, (c) After addition of  $\text{NH}_4\text{OH}$  in the microemulsion solution.

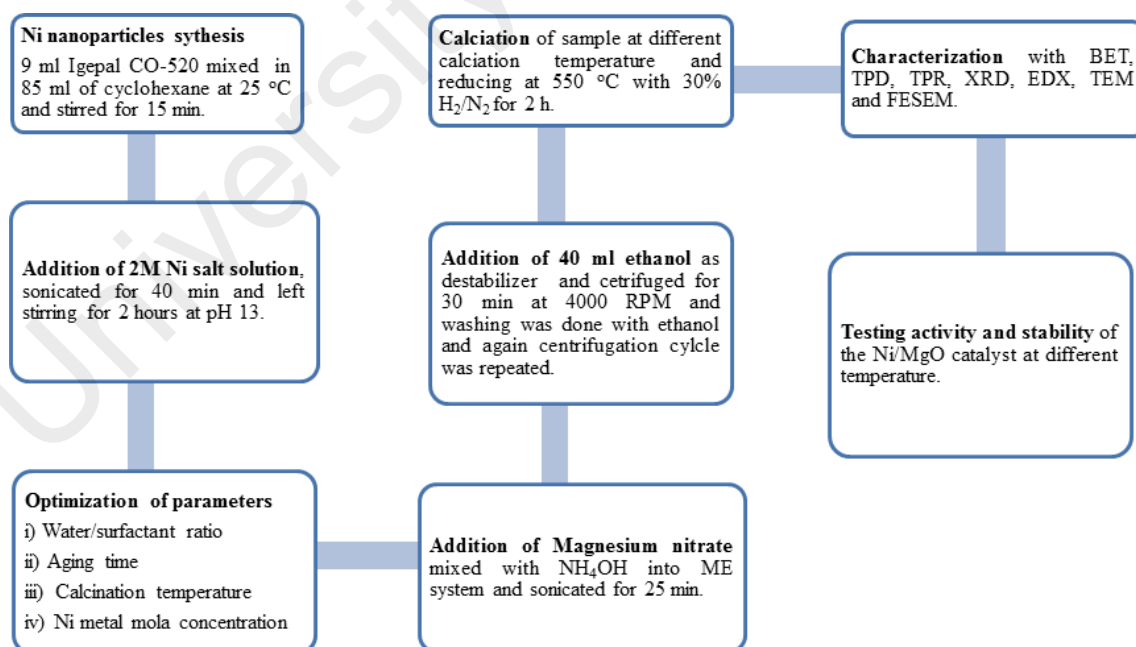
The migration of transparent region to translucent indicates the ending signal for the addition of aqueous phase Ni solution. The pH of the microemulsion was adjusted at 13 with the aid of ammonium solution (28 wt%). The microemulsion solution was then put on sonication for 40 min. The temperature was continuously monitored and controlled at room temperature with the assistance of cold water. After sonication, the sample was left for stirring for 2 h at 650 rpm. The sample was removed from stirrer and ethanol (40 ml) was added as a destabilizer for microemulsion system. The sample was then centrifuged at 4000 rpm for 30 min and another cycle of washing and centrifugation was repeated with ethanol. The sample was then dried at 100 °C for overnight and then calcined at 450 °C for 2h. Similar procedure was repeated to investigate the influence of aging time (0.5 to 24 h), calcination temperature (450 to 100 °C) and metal molar concentration (2 M to 7 M). Different microemulsion systems were denoted with A1, A2, A3, A4, A5 and A6 for different water to surfactant ratios.

### 3.2.3 Preparation of Ni/MgO catalyst

To prepare 20% (wt) Ni/MgO, desired quantity of  $\text{Mg}(\text{NO}_3)_2 \cdot 6\text{H}_2\text{O}$  was first added in suitable amount of water enough to dissolve complete salt and then ammonium



hydroxide (28 wt%) was added to convert it to magnesium hydroxide. For supported catalyst preparation, the prepared magnesium solution was added into the microemulsion system of metal solution after the sonication of 15 min. Then, the solution was stirred for 30 min and later on sonicated for 25 minutes. The solution was then put on stirrer for 2 hours at 650 rpm. The sample was removed from stirrer and ethanol (40 ml) was added as a destabilizer for microemulsion system. The sample was then centrifuged at 4000 rpm for 30 min and another cycle of washing and centrifugation was repeated with ethanol. The sample was then dried at 100 °C for overnight. The produced nanocatalysts was calcined at 450 °C for 2 h and then reduced at 550 °C with 30% H<sub>2</sub>/N<sub>2</sub> mixture prior to activity and stability test. To investigate the influence of calcination temperature on the supported catalysts, the prepared samples were calcined at 600 and 800 °C for 2 h and then reduced at same conditions. Catalysts calcined at different calcination temperatures (450, 600 and 800 °C) was expressed as Cat1, Cat2 and Cat3, respectively. The detailed methodology of the experiments is described in Figure 3.2.



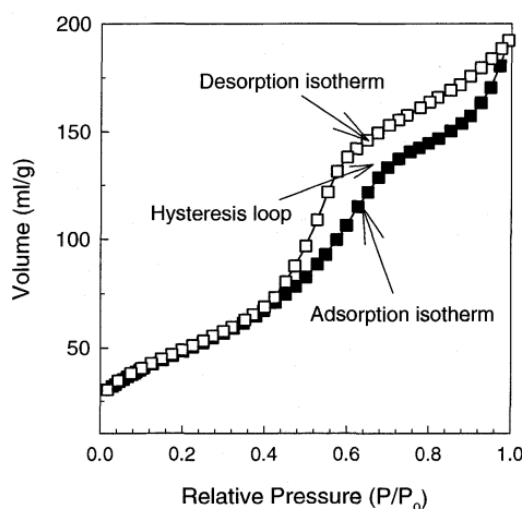
**Figure 3.2:** Experimental methodology flow chart

### 3.2.4 Catalyst characterization

The catalysts were characterized with different characterization techniques at conditions described below in detail;

#### 3.2.4.1 Surface area and pore volume

The convenient way to measure the surface area, pore volume and surface properties is  $N_2$  physisorption. The adsorption of nitrogen on solid surface is not selective at boiling point of nitrogen ( $-196\text{ }^{\circ}\text{C}$ ). For the measurement of surface area, first  $N_2$  is adsorbed on the solid surface until relative pressure ( $P/P_0$ ) equal to 1, where  $P$  denotes the  $N_2$  equilibrium pressure in the system and  $P_0$  expresses the saturated pressure of  $N_2$ . The reverse process of  $N_2$  adsorption, can be studied by lowering the relative pressure ( $P/P_0$ ) from 1 to zero and regarded as  $N_2$  desorption. The desorption will result in the release of adsorbed  $N_2$  from the surface of solid or evaporates from the pores. Adsorption/desorption isotherms can be obtained by simply plotting the nitrogen adsorption/desorption volumes versus relative pressure and these isotherms can be classified on the basis of IUPAC system explain the surface properties, average diameter of pores and pore size distribution. A hysteresis loop will be formed provided that desorption of  $N_2$  does not take the similar path as  $N_2$  adsorption as shown in Figure 3.3.

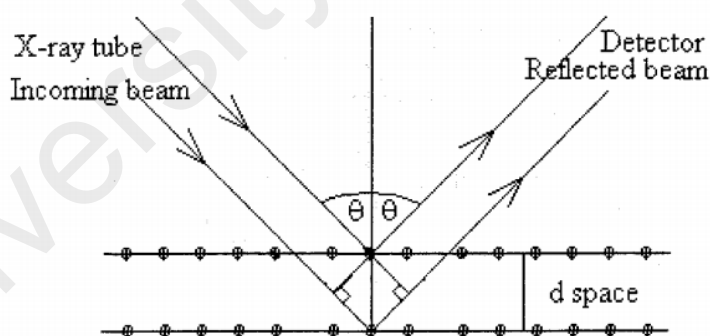


**Figure 3.3:** Adsorption/desorption isotherms for  $N_2$  molecules

Therefore, in this study specific surface area (BET), pore size distribution, pore volume and mean particle size was estimated from N<sub>2</sub> adsorption-desorption isotherms at liquid nitrogen temperature (-196 °C) with an Autosorb BET apparatus (Micromeritics ASAP 2020). Prior to each measurement, the sample was first degassed at 90 °C for 1 h and then at 300 °C for 4 h. The pore size distribution curve was obtained by Barrett, Joyner & Halenda (BJH) method.

### 3.2.4.2 X-Ray diffraction

X-ray diffraction (XRD) technique is regarded as an important non-destructive tool to determine the crystallite size and structure of the metal oxides. The basic principle of this technique is that the constructive and destructive interference will occur provided that the atoms are organized regularly in crystals and the distance between them is of same magnitude as shown in Figure 3.4. This will result in the X-rays emitted at certain angles based on the space between atoms called planes.



**Figure 3.4:** X-ray diffraction principal

XRD patterns of the fresh and spent catalyst were obtained in a PANalytical diffractometer to determine the crystallite size and structure of the metal oxides. The evaluation of the diffractograms was made by X'pert High score software. Diffraction patterns of the samples were recorded with a Rigaku miniflex Cu-K $\alpha$  radiation with a

generator voltage of 45 kV and current of 40 mA. The intensity was measured by step scanning in the  $2\theta$  range of  $5-80^\circ$  with a step of  $0.026^\circ$  and a scan rate of  $0.0445^\circ \text{ s}^{-1}$ . The scherrer equation was used to obtain average crystallite size of different Ni nanoparticles produced as shown below:

$$D_{avg} = \frac{0.9\lambda}{\beta \cos \theta} \left( \frac{180}{\pi} \right) \quad (3.1)$$

Where K denotes shape factor with a value of 0.9,  $\lambda$  denotes wavelength (0.154 nm),  $\beta$  is the width of the peak at half height and  $\theta$  is Bragg angle.

### 3.2.4.3 Temperature-programmed reduction

The reducibility characteristics of metal oxides can be investigated by temperature-programmed reduction in the presence of reducing agents such as:  $\text{H}_2$ , CO and  $\text{CH}_4$ . The reduction properties of metal oxides for example nickel oxide (NiO) changes with the addition of support materials indicating the strong or weak interaction between metal and support materials. The reduction of NiO with  $\text{H}_2$  as reducing agent is explained by following simple reaction shown below in equation 3.2:



The theoretical consumption of  $\text{H}_2$  can be estimated by the stoichiometry of the above reaction and extent of reduction can then be calculated by the ratio of theoretical and actual  $\text{H}_2$  consumption. In this study, temperature-programmed reduction was conducted with hydrogen ( $\text{H}_2$ ). Temperature-programmed reduction  $\text{H}_2$  (TPR- $\text{H}_2$ ) was performed with Micromeritics TPx 2720 analyzer by placing 0.03 g of sample at the bottom of the U-shaped quartz tube. The sample was first purged with He at  $130^\circ \text{C}$  for 60 min at a flow rate of 20 ml/min. After the cleaning process, the sample was reduced by 5%  $\text{H}_2/\text{N}_2$  at a flow rate of 20 ml/min and the temperature was ramped at  $10^\circ \text{C}/\text{min}$

from 100 °C to 900 °C. H<sub>2</sub> consumption during the reduction process was recorded by thermal conductivity detector (TCD).

#### **3.2.4.4 Temperature-programmed desorption**

Temperature programmed desorption (TPD) technique is used to determine the intensity of acidic and basic active sites on the surface of catalysts by measuring the desorption of probe molecules (CO<sub>2</sub> and NH<sub>3</sub>). The catalyst placed inside the quartz tube will be first saturated with probe molecules and then the excess gas will be flushed with inert gas i.e., helium. Later on, the catalyst saturated with probe molecules will be heated in presence of inert atmosphere at certain temperature ramp, which will lead to the desorption of molecules by breaking the bonds between solid and molecules. In this study, the basicity of Ni/MgO catalyst was investigated by CO<sub>2</sub> desorption.

Temperature-programmed desorption-CO<sub>2</sub> (TPD) was performed to identify the strength of basic active sites of catalysts in Micromeritics TPx 2720 analyzer. In this technique, 0.03 g of sample was first heated to 800 °C (ramp 10 °C/min) with helium flow (20 ml/min) passing through quartz tube for 60 min. Then, the catalyst bed temperature was brought about to 25 °C with helium flow and the flow was switched to 10% CO<sub>2</sub>/He mixture with flow rate of 20 ml/min for 30 min to have significant adsorption on the catalyst surface. Thereafter, the sample was purged with helium for 30 min to remove physisorbed elements from the sample. Then the sample was heated to 900 °C from room temperature at a rate of 10 °C/min.

#### **3.2.4.5 Transmission electron microscopy**

This technique allows the micro-structural examination of catalysts at high-magnification imaging and also give detailed information about the crystal structure, orientation. Furthermore, the produced carbon during the reaction studies examined by

transmission electron microscopy (TEM) analysis gives insight into the structure of carbon either open mouth, closed mouth, shell-like or in the form of nanotubes. TEM is regarded as an electron-optical microscope, which employs electromagnetic lenses to focus and direct electron beam and data will be collected once the beam passed through the sample. TEM images of fresh and spent catalysts were performed by using FEI Tecnai<sup>TM</sup> controlled at an accelerating rate of 200 keV.

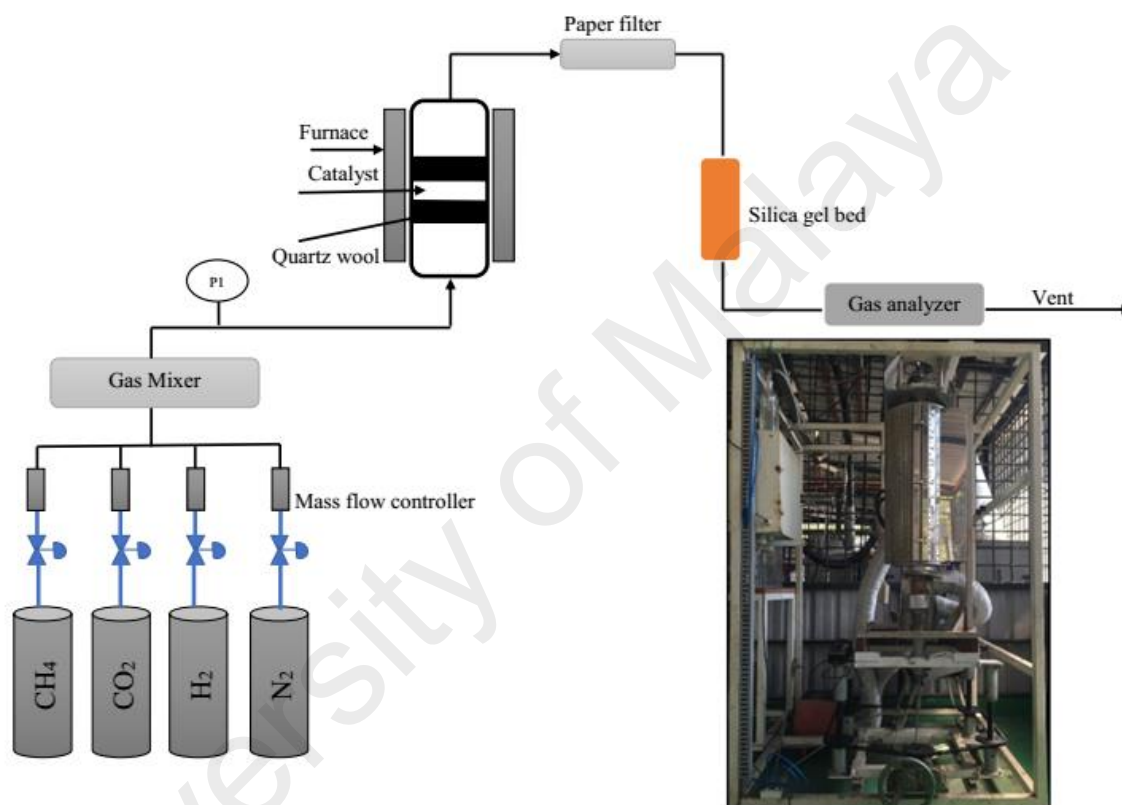
#### **3.2.4.6 Scanning electron microscopy**

Scanning electron microscopy (SEM) provides information regarding the morphology of solids in the form of images formed by the electron emitted by the surface of the solid. Moreover, 3-dimensional images of the object under investigation are obtained due to the longer depth of field. The principal theory of this technique is that field emission source provides electron, which are accelerate by electrical field gradient and due to the high vacuum, these electrons are deflected by electronic lenses to form a narrow scan beam. With the assistance of electron detector, the image formation electrons are capture and electronic signals are produced. These electron signals are then amplified and later can be seen on monitor in the form of video-scan image. Surface morphology of the spent catalyst was studied by field emission scanning electron microscopy (FESEM) images and elemental composition of pure catalyst was performed by FEG Quanta 450, EDX-OXFORD.

### **3.3 Catalytic activity test**

Activity tests were carried out in a fixed-bed reactor made of stainless steel having 6.03 cm outer diameter, 0.87 cm wall thickens and 120 cm length. To avoid the interaction of feed gas with stainless steel, a quartz tube with 3.56 cm internal diameter, 4 cm outer diameter and 120 cm length was placed inside the reactor obtained from Technical Glass

Products (Painesville, USA). For each run, 0.5 g of catalyst was immobilized between two quartz wool plugs to serve as catalyst bed. Reactant gases (methane and carbon dioxide) were fed into the reactor at a total flow rate of 1.4 L/min ( $\text{CH}_4$ :  $\text{CO}_2$  = 1:1) and weight hourly space velocity (WHSV) of  $1.68 \times 10^5 \text{ ml g}^{-1} \text{ h}^{-1}$  or  $168 \text{ L h}^{-1} \text{ g}^{-1}$ . Before activity tests, the reduction of catalysts was done with 30%  $\text{H}_2/\text{N}_2$  at 550 °C for 2 h. Schematic diagram for the reactor used in dry reforming reaction is shown in Figure 3.5.



**Figure 3.5:** Schematic diagram of experimental setup and dry reforming of methane unit.

Thereafter, the mixture of reactant gases consisting of methane and carbon dioxide ( $\text{CH}_4$ :  $\text{CO}_2$  = 1:1) was introduced and the activity test was conducted at different temperatures ranging from 550 °C to 850 °C. The stability of the catalysts was investigated at the same reaction conditions but at three different temperatures (750 °C, 800 °C and 850 °C). The flow rate of reactant gases was controlled by mass flow controllers purchased from Dwyer, USA, in the range of 0 - 2 L/min. The mole percentage of hydrogen produced and unreacted methane was detected by calibrated Rosemount

Analytical X-STREAM (UK) on-line analyzer. The composition of carbon monoxide and carbon dioxide in the outlet gases were measured by GAURDIAN NG EDINBURGH SENSORR (UK). The conversion and yields of both reactants and products are calculated as follows:

$$\text{CH}_4 \text{ conversion (\%)} = \frac{\text{moles of CH}_4 \text{ converted}}{\text{moles of CH}_4 \text{ in feed}} \times 100$$

$$\text{CO}_2 \text{ conversion (\%)} = \frac{\text{moles of CO}_2 \text{ converted}}{\text{moles of CO}_2 \text{ in feed}} \times 100$$

$$\text{H}_2 \text{ yield (\%)} = \frac{\text{moles of H}_2 \text{ produced}}{2 \text{ moles of CH}_4 \text{ in feed}} \times 100$$

$$\text{CO yield (\%)} = \frac{\text{moles of CO produced}}{(\text{moles of CH}_4 \text{ in feed} + \text{moles of CO}_2 \text{ in feed})} \times 100$$

$$\text{H}_2/\text{CO} = \text{moles of H}_2 \text{ produced} / \text{moles of CO produced}$$

$$\text{Weight hourly space velocity (WHSV) ml/h.g} = \frac{\text{Feed flow rate } F_{\text{feed}}(\text{ml/h})}{\text{weight of catalyst (g)}}$$

$$\text{Carbon deposition (g}_c/\text{g}_{\text{cat}}) = \frac{\text{Weight of deposited carbon on the catalyst (g}_c)}{\text{total weight of catalyst (g}_{\text{cat}})}$$

### **3.4 Part 2: An investigation on the influence of catalyst composition, calcination and reduction temperatures on Ni/MgO catalyst for dry reforming of methane.**

In this section, the influence of different Ni metal content (20, 40 and 80 wt%), calcination temperatures (450, 600 and 800 °C) and reduction temperatures (550 and 800 °C) over the catalytic activity and catalyst performance was investigated. The materials mentioned in sec 3.2.1 are same for this study and also the characterization techniques are same also.



### 3.4.1 Catalyst preparation

In this study, microemulsion system based on water/Igepal CO-520/ cyclohexane was chosen and their ratio (water/surfactant/oil = 6/9/85) was selected from the ternary phase diagram. In the first step, 9 ml of Igepal was added into cyclohexane (85 ml) and left under stirring for 15 min. To synthesize, Ni/MgO catalyst having different weight percentage of Ni (20 wt%, 40 wt% and 80 wt%), desirable amount of  $\text{Ni}(\text{NO}_3)_2$  was dissolved in 6 ml of water to prepare 2 M Ni metal solution and then added dropwise to the mixture of surfactant and oil. The solution was put on stirrer for 15 min and then sonicated for 15 min. The pH of the microemulsion was adjusted at 13 with the addition of ammonium hydroxide. Thereafter, the  $\text{Mg}(\text{NO}_3)_2$  solution was prepared separately, in which desirable amount of magnesium nitrate was dissolved in a suitable amount of water to dissolve all salt and then ammonium hydroxide was added to convert it to magnesium hydroxide. The prepared solution was then added to the microemulsion system containing Ni metal solution and then sonicated for 25 min. The temperature was continuously monitored and controlled at room temperature by using ice cold water. After sonication, the sample was put on stirrer for 2 h at 650 rpm and then ethanol (40 ml) was added as a destabilizer. Later on, centrifugation was done at 4000 rpm for 30 min and then washing was done with ethanol. After washing, another cycle of centrifugation was repeated. The sample was dried for overnight at 100 °C and calcined at 450 °C for 2h. Ni/MgO catalysts with different weight percentages of Ni (20 wt%, 40 wt% and 80 wt%) are denoted as CS1, CS2 and CS3, respectively. To investigate the influence of calcination temperatures on the supported catalyst (CS3 (80wt%)-450 °C), same preparation procedure was repeated and the catalysts were calcined at 600 °C and 800 °C for 2 h, denoted as CS4 and CS5, respectively.

### 3.4.2 Experimental setup

In this study, all the reaction conditions were similar to previously explained activity assessment test in sec 3.3. However, in this study, the catalysts were reduced at two different reduction temperatures (550 °C and 800 °C) to investigate the influence of reduction temperatures.

### 3.5 Part 3: Water-in-oil microemulsion synthesis of Ni@CeO<sub>2</sub> core-shell like structures for dry reforming of methane.

In this study, microemulsion approach was used to synthesize Ni@CeO<sub>2</sub> core-shell like structures at the optimum condition used to prepare Ni nanoparticles and later on cerium(III) nitrate hexahydrate was added into the emulsion.

#### 3.5.1 Material and chemicals

Nickel (II) nitrate hexahydrate (Ni(NO<sub>3</sub>)<sub>2</sub>·6H<sub>2</sub>O) and cerium(III) nitrate hexahydrate (Ce(NO<sub>3</sub>)<sub>3</sub>·6H<sub>2</sub>O) were obtained from Acros Organics. Ammonium hydroxide (28 wt%) and ethanol was purchased from R&M solutions. Non-anionic surfactant Igepal CO-520 (Polyoxyethylene (5) nonylphenylether) was acquired from Sigma-Aldrich. Gases used in our study, such as: H<sub>2</sub> (99.999%), CH<sub>4</sub> (99.995%) CO<sub>2</sub> (99.995%) and N<sub>2</sub> (99.99%) were acquired from Linde Malaysia.

#### 3.5.2 Catalyst preparation

In this study, water/Igepal CO-520/cyclohexane were chosen to form water-in-oil (W/O) microemulsion system and the ratio of constituents (water/surfactant/oil = 6/9/85) were selected from the ternary phase diagram. In the first step, 9 ml of Igepal CO-520 was added into cyclohexane (85 ml) and left under stirring for 15 min. To prepare Ni@CeO<sub>2</sub> catalyst, having different weight percentage of Ni (20 wt%, 40 wt% and 80

wt%), desirable amount of  $\text{Ni}(\text{NO}_3)_2$  was dissolved in 6 ml of water to prepare 2 M Ni metal solution and then added dropwise to the mixture of surfactant and oil. The solution was put on stirrer for 15 min and then sonicated for 15 min. The pH of the microemulsion was adjusted at 13 with the addition of ammonium hydroxide. Thereafter, solution was prepared separately by dissolving a desirable amount of cerium (III) nitrate and the quantity was chosen according to the required weight percentage of  $\text{CeO}_2$  in total catalyst weight. pH of the solution was adjusted at 13 by the addition of  $\text{NH}_4\text{OH}$  and left for stirring for 1 hour. Later on, the prepared yellowish like precipitate was added to the above microemulsion system and sonicated for 25 min. The temperature was continuously monitored and controlled at room temperature by using ice cold water. After sonication, the sample was put on stirrer for 2 h at 650 rpm then ethanol (40 ml) was added as a destabilizer. Later on, centrifugation was done at 4000 rpm for 30 min and washing was done with ethanol. After washing, another cycle of centrifugation was repeated. The sample was dried for overnight at 80 °C and calcined at 450 °C for 2h. Ni@ $\text{CeO}_2$  catalysts prepared with different weight percentages of Ni (20 wt%, 40 wt% and 80 wt%) are denoted as NC1, NC2 and NC3, respectively.

### 3.5.3 Catalytic activity

Activity tests were carried out in a fixed-bed reactor made of stainless steel having 6.03 cm outer diameter, 0.87 cm wall thickness and 120 cm length. To avoid the interaction of feed gas with stainless steel, a quartz tube with 3.56 cm internal diameter, 4 cm outer diameter and 120 cm length was placed inside the reactor obtained from Technical Glass Products (Painesville, USA). In this study, 0.5 g of catalyst was immobilized between two quartz wool plugs to serve as catalyst bed. The feeding gases (methane and carbon dioxide) flow rate was set at 1.0 L/min ( $\text{CH}_4$ :  $\text{CO}_2$  = 1:1) and weight hourly space velocity (WHSV) of  $1.2 \times 10^5 \text{ ml g}^{-1} \text{ h}^{-1}$  or  $120 \text{ L h}^{-1} \text{ g}^{-1}$ . The reduction of catalysts before each

activity run was performed with 30% H<sub>2</sub>/N<sub>2</sub> at 550 °C for 2 h. Thereafter, the activity tests were conducted at different temperatures ranging from 550 °C to 800 °C at a temperature ramp of 5 °C/min. The stability of the catalysts was studied under the equimolar concentration of feed gas (CH<sub>4</sub>/CO<sub>2</sub> = 1) and at reaction temperature of 800 °C. Mass flow controllers (0 - 2 L/min) were used to control the flow of feed gas purchased from Dwyer, USA. Rosemount Analytical X-STREAM on-line analyzer was used to measure the mole percentage of unreacted methane and H<sub>2</sub> produced, while Guardian NG gas monitor supplied by Edinburgh Sensors (UK) was used to measure the composition of carbon dioxide and carbon monoxide at the outlet.

## CHAPTER 4: RESULTS AND DISCUSSION

**Part 1: Synthesis of Ni nanoparticles and 20%Ni/MgO at different preparation parameters (surfactant ratio, aging time, calcination temperature, molar concentration) and investigating their catalytic activity and characterization.**

### **4.1 Characterization of fresh catalyst**

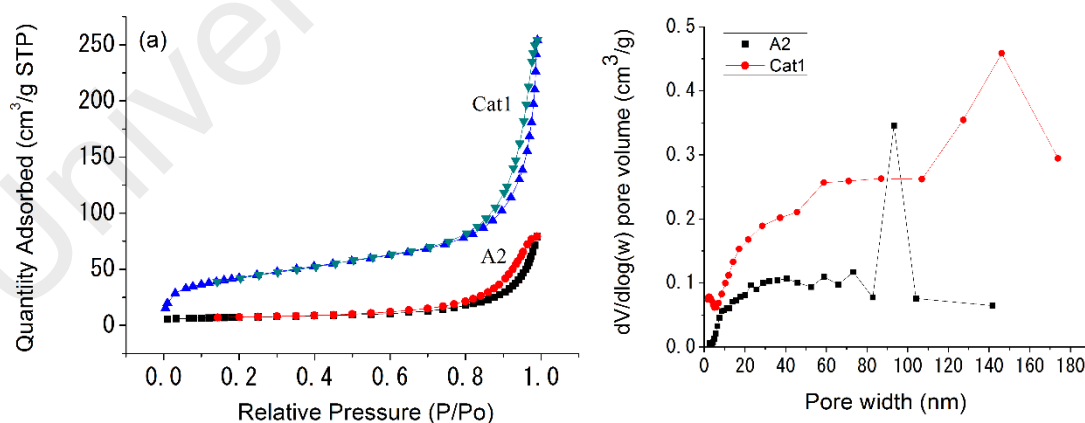
#### **4.1.1 Surface area and pore volume**

The investigation on the porous nature of NiO nanoparticle and NiO/MgO catalysts prepared was executed by N<sub>2</sub> adsorption-desorption measurements. In this study, pure magnesium oxide (MgO) exhibited 34.69 m<sup>2</sup>/g surface area and bare NiO nanoparticles exhibited surface area around 23.87 m<sup>2</sup>/g. The addition of MgO in microemulsion system depicted quite high surface area around 153.22 m<sup>2</sup>/g, which indicated the porous nature of MgO support. BET surface areas for the pure NiO nanoparticles prepared at different water to surfactant ratios are described in Table 4.1. According to the IUPAC classification, N<sub>2</sub> adsorption/desorption isotherms for A2 (pure NiO) and Cat1 (NiO/MgO) exhibit a type III isotherm with a large type H3 hysteresis loop as shown in Figure 4.1(a). The formation of this type of hysteresis loop at relatively high pressure indicates the formation of large pore volume in the samples.

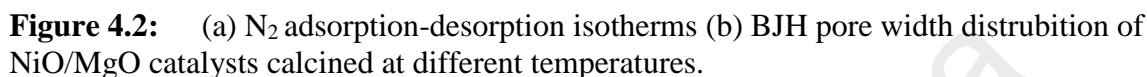
The study of isotherms for supported catalysts (Cat1, Cat2 and Cat3) indicate that the increase of calcination temperature leads to the decrease in surface area and mesoporous volume as mentioned in Table 4.2 and Figure 4.2(a). The catalyst calcined at lower temperature (Cat1-450 °C) exhibited higher surface area, smaller BET pore size and higher mesoporous volume. It was suggested that the lower calcination temperature is more favourable to form smaller pores with greater surface area in the structure of NiO/MgO solid solution (Feng et al., 2012). The results indicate that the calcination temperature has strong influence over the surface area and pore size distribution. Similar,

type of decrease in surface area from 38.0 m<sup>2</sup>/g to 27.4 m<sup>2</sup>/g was reported with the increase of calcination temperature from 600 °C to 800 °C, respectively for impregnated NiO/MgO catalysts (Feng et al., 2012). Another study also reported that the increase of calcination temperature from 600 °C to 900 °C lead to the decrease in surface area from 89 to 30 m<sup>2</sup>/g for 2(Ni<sub>0.1</sub>Mg<sub>0.9</sub>)/Al catalyst (Djaidja et al., 2006).

The pore distribution of prepared catalysts was obtained from the analysis of adsorption branch of N<sub>2</sub> isotherm by the Barret-Joyner-Halenda (BJH) method as depicted in Figure 4.1(b) and Figure 4.2 (b). It can be seen from the BJH pore size distribution plot that the majority of pore size culminates around 0 - 50 nm, however, the formation of fewer pores with higher size (50 nm to 150 nm) maybe be linked with the formation of voids due to inter-nanoparticles in contact. Furthermore, BJH average pore width for A2, Cat1, Cat2 and Cat3 was calculated to be around 22.56 nm, 15.06 nm, 24.88 nm and 20.27 nm, respectively. The higher surface area and smaller particle size for supported catalyst indicates the excellent ability of MgO coating to resist agglomeration of NiO nanoparticles.



**Figure 4.1:** (a) N<sub>2</sub> adsorption-desorption isotherms (b) BJH pore width distribution of A2 and Cat1.



Sample ID	ME system (W/S/O)	W/S	S/O	BET SA m <sup>2</sup> /g	Mesoporous volume cm <sup>3</sup> /g	BET pore size (nm)	XRD crystallite size (nm)
A1	12/18/70	0.66	0.257	5.19	0.0344	30.34	39.09
A2	6/9/85	0.66	0.105	23.87	0.1151	20.36	27.58
A3	9/18/73	0.5	0.246	3.86	0.0325	36.85	32.08
A4	6/12/82	0.5	0.146	9.28	0.0681	31.44	26.40
A5	7/21/72	0.33	0.291	3.65	0.0349	39.62	31.36
A6	4/12/84	0.33	0.142	9.97	0.0865	37.39	24.55

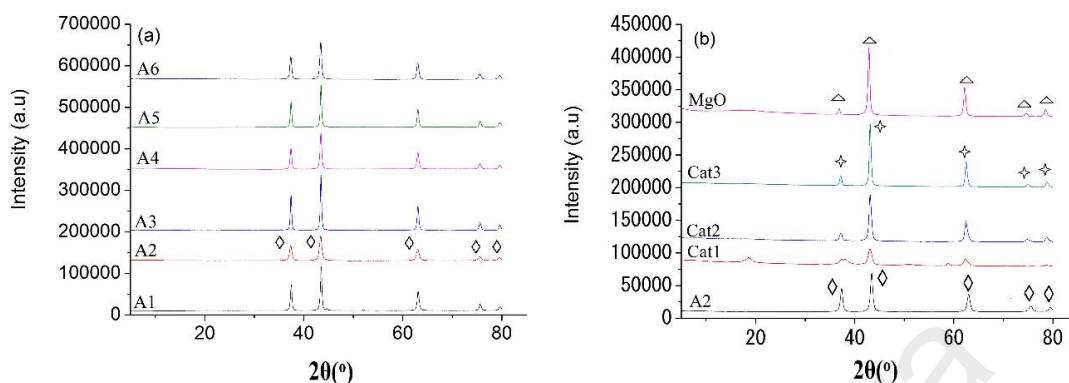
Catalyst	BET SA m <sup>2</sup> /g	Calcination temperature (°C)	Mesoporous volume cm <sup>3</sup> /g	BET pore size (nm)	XRD crystallite size (nm)
A2	23.87	450	0.1151	20.36	27.58
MgO	34.69	450	0.8326	9.643	25.69
Cat1	153.22	450	0.3856	10.26	18.81
Cat2	63.45	600	0.3483	22.37	21.29
Cat3	34.72	800	0.1264	15.14	22.21

The study of the crystalline structure and size for pure NiO nanoparticles prepared by microemulsion system was identified by X-ray diffraction (XRD) patterns. Figure 4.3(a) shows the XRD patterns for all the unreduced pure NiO nanoparticles obtained by calcining at 450 °C for 2 h. Pure NiO exhibits sharp peaks at  $2\theta$  values of 37.28°, 43.44°,

63.01°, 75.55° and 79.40° corresponding to respective crystallite phase of (111), (200), (220), (311), and (222). The peaks observed in this study for NiO are in good agreement with standard card of cubic NiO with JCPDS no. 01-073-1519. Figure 4.3(b) exhibits the XRD patterns for pure NiO (JCPDS no. 01-073-1519), pure MgO (JCPDS no. 01-079-0612) and NiO/MgO (JCPDS no. 00-024-0712) catalyst. XRD patterns of MgO are quite similar to those of NiO patterns.  $2\theta$  values of MgO values are matched at 62.23°, 74.63° and 78.52° for their respective crystal phase of (220), (311), and (222), respectively. However, same crystalline phase was observed for NiO at  $2\theta$  values but were greater by values of 0.78°, 0.92° and 0.88° than MgO. The similar results were reported by another study for the preparation of NiO/MgO catalyst (Feng et al., 2012). The formation of NiO-MgO solid solution will be identified using the three diffraction lines at  $2\theta$  values of 62.37°, 74.80° and 78.54°. These diffraction peaks are present in all the prepared catalysts and can be dedicated to the presence of NiO-MgO solid solution or MgO. Similar type of diffraction lines was reported by another study at same  $2\theta$  values (62.32°, 74.72° and 78.66°). However, it is difficult to distinguish between the diffraction peaks of NiO, MgO and NiO-MgO solid solution (Hua et al., 2010). This has been dedicated to the similarity in their oxides structure (NiO and MgO) both having face-centered-cubic structures with very similar lattice parameters (4.1946 and 4.2112 Å, respectively) and quite matching bond distance at 2.10 and 2.11 Å for both NiO and magnesium oxides, respectively (Y. J. Asencios et al., 2011). Figure 4.3(b) clearly indicates the diffraction peaks observed near the above  $2\theta$  values indicating the formation of NiO-MgO solid solution. The  $2\theta$  values of Cat1 at 43.02° and 62.37° become weaker and broad compared to pure Cat2 and Cat3 at similar diffraction lines. Thus, indicating the higher dispersion of Ni particle and smaller particle size as confirmed by BET results also (Hua et al., 2010). Furthermore, even though XRD indicates the formation of NiO-MgO solid solution but the strength of



solid solution formation ranging from mild to very strong metal-support interaction will be investigated by TPR studies.

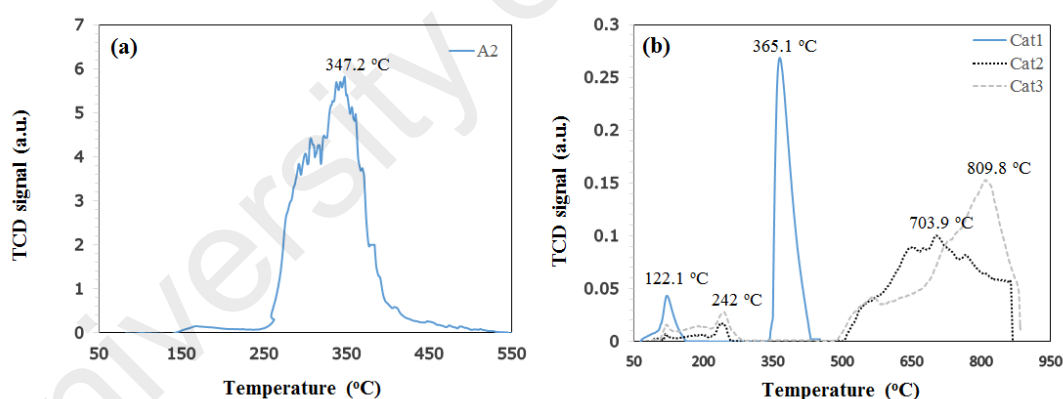


**Figure 4.3:** (a) XRD patterns for pure NiO particle, (b) XRD patterns of NiO/MgO catalysts prepared at different calcination temperatures. Where ( $\times$ ) presents NiO-MgO solid solution, ( $\diamond$ ) presents NiO crystallite peaks and ( $\Delta$ ) presents MgO crystallite peaks.

#### 4.1.3 Temperature-programmed reduction

The reducibility characteristics of the catalysts has been studied widely by temperature-programmed reduction- $H_2$  (TPR- $H_2$ ) and is an established technique to distinguish between various species in solid solution. Two peaks were observed for Cat1, one at very low temperature 122.1 °C and other at quite high temperature 365.1 °C (Figure 4.4(b)). The lower temperature peaks can be ascribed to the reduction of bulk NiO and higher reduction peak can be ascribed to the reduction of  $Ni^{3+}$  surface species located at surface sites for NiO/MgO catalyst. However, for Cat1 the higher reduction peaks ( $> 500$  °C), which are the indication of strong metal-support interaction were not observed because of the lower calcination temperature used. The indication of strong metal-support interaction was exhibited at quite higher reduction temperature peaks greater than 500 °C as reported in many studies (Feng et al., 2012; M. Yu et al., 2014). The higher  $H_2$  uptake capacity for pure NiO indicates the higher reducibility referring to its higher NiO content (Figure 4.4(a)). Furthermore, the addition of MgO leads to the lower  $H_2$  uptake capacity for NiO/MgO catalysts and reduction temperature was shifted to slightly higher temperature from 347.2 to 365.1 °C. It has been strongly agreed that the extent of NiO

incorporation into NiO-MgO solution depends strongly on the calcination temperature. Therefore, the application of higher calcination temperature in Cat2 and Cat3 indicated the higher reduction peak temperatures 703.9 °C and 809.8 °C, respectively (Figure 4.4(b)). The higher temperature reduction peak (703.9 °C) for Cat2 indicates the reduction of  $\text{Ni}^{2+}$  ions in the outermost and sub-surface layers of the MgO lattice. While, for Ni/MgO catalyst calcined at 800 °C, the higher reduction peak temperature indicates the reduction of lattice  $\text{Ni}^{2+}$  ions in the MgO matrix. Both peaks of Cat2 and Cat3 at higher reduction temperature are the indication of the formation of strong NiO-MgO solid solution. It can be concluded from the results that the NiO was completely diffused into the MgO to form strong NiO-MgO solid solution. This behaviour indicates the presence of strong metal-support interaction which restricts the reduction of NiO, owing to the formation of solid solution of NiO-MgO (Y. J. Asencios et al., 2011).

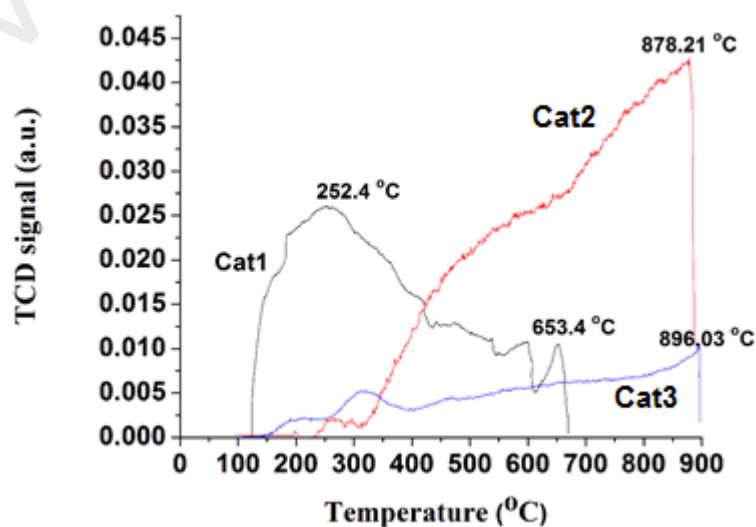


**Figure 4.4:** (a) TPR profiles of pure Ni particles and (b) Ni/MgO catalyst calcined at different temperatures

#### 4.1.4 Temperature-programmed desorption

The basicity of the catalysts was investigated by temperature-programmed desorption  $\text{CO}_2$  (TPD- $\text{CO}_2$ ). The strength of basic sites is described as the temperature where the chemisorbed  $\text{CO}_2$  on the basic sites is desorbed. Therefore, the desorption of  $\text{CO}_2$  occurring at lower temperature indicates the presence of weak basic sites and

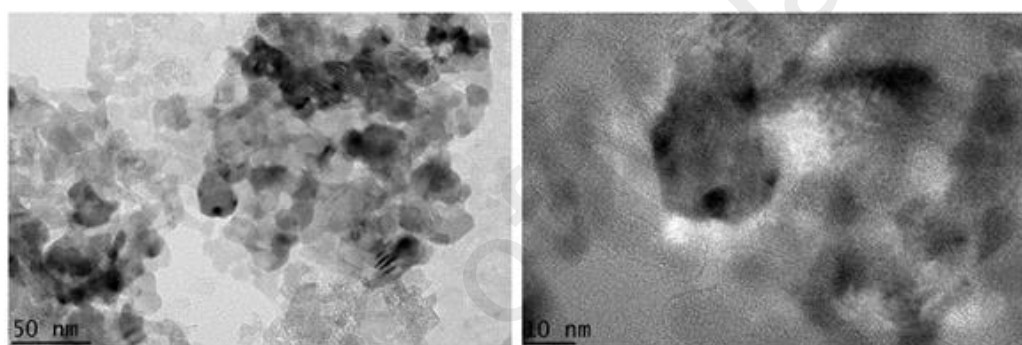
similarly strong basic sites are linked with the CO<sub>2</sub> desorption peaks at higher temperature. TPD profiles for the catalysts calcined at lower calcination temperature (Cat1) indicates the presence of two major peaks, one being at lower temperature 252.4 °C and other at higher temperature (653.4 °C). The desorption peaks of CO<sub>2</sub> at lower temperature indicates the presence of weak basic sites, while the higher temperature peaks exhibit the existence of strong basic sites. TPD- CO<sub>2</sub> profiles in Figure 4.5 indicates that the calcination temperature has strong influence over the enhancement of strong basic actives. The increase of calcination temperature (450 to 800 °C) shifts the CO<sub>2</sub> desorption peaks to the higher temperature indicating that higher calcination has a strong influence on the formation of strong basic sites. Moreover, the desorption peak temperature at higher temperature can be dedicated to the decomposition of carbonate formed earlier from the interaction between catalyst and CO<sub>2</sub>. The increase in calcination temperature from 450 °C to 800 °C leads to the conclusion that Cat3 has desorbed CO<sub>2</sub> very small compared to Cat1 and Cat2. The increase in calcination temperature (450 to 800 °C) shifts the CO<sub>2</sub> desorption peak temperature from 653.4 °C to 896.03 °C indicates the existence of strong basic sites and all the NiO has incorporated in MgO phase to form NiO-MgO solid solution as described by the higher reduction peaks in TPR profiles.



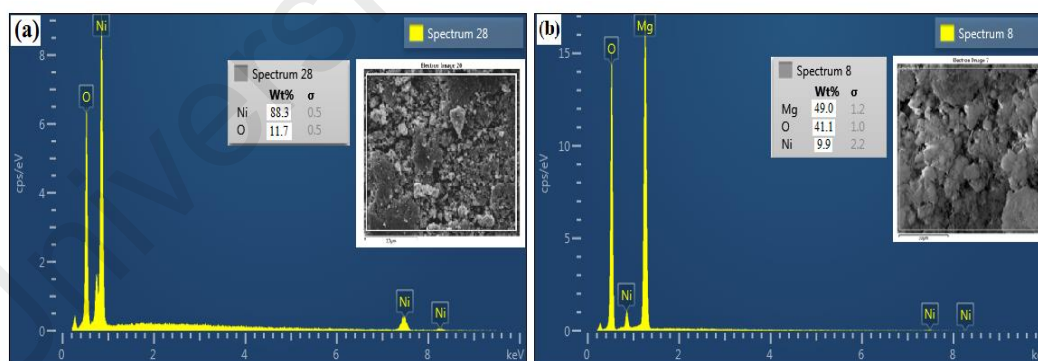
**Figure 4.5:** TPD-CO<sub>2</sub> profiles of Ni/MgO catalyst calcined at different temperatures

#### 4.1.5 TEM and EDX analysis

TEM analysis depicts the morphology and structural characteristics of Ni/MgO catalyst (Cat1) exhibited that the addition of coating material (MgO) leads to the better nanoparticle distribution and also restricts the agglomeration of Ni nanoparticles (Figure 4.6). This leads to higher surface area and smaller particle size for supported Ni/MgO catalysts as evident in BET results. Furthermore, EDX analysis indicates the weight percentages of A2 (pure NiO) and Cat1 (NiO/MgO) before reduction in Figure 4.7(a) and Figure 4.7(b), respectively.



**Figure 4.6:** TEM images of the fresh Cat1



**Figure 4.7:** EDX analysis of fresh A2 (a) and Cat1(b) before reduction.

## 4.2 Influence of different microemulsion parameters

### 4.2.1 Effect of surfactant, water and oil composition

In the synthesis of nanoparticles by microemulsion system, the concept of the size of microemulsion droplet is very important, which depends solely on the solution

composition. The role of surfactant is not only to serve as a protective agent but also to restrict the agglomeration of nanoparticles. Therefore, the choice of microemulsion composition is critical steps in the synthesis of nanoparticles because it will not only affect the stability of microemulsion system but will play a major role to alternate the particle size. In this study, several microemulsion composition were chosen according to ternary phase diagram of water/Igepal CO-520/cyclohexane.

In this set of experiments, the microemulsion system with lower water content for each water/surfactant ratio (0.33, 0.5, 0.66) exhibited higher surface area and smaller particles size. The detail of water to surfactant, surfactant to oil ratios (A1, A2, A3, A4, A5 and A6) along with different characteristics of nanoparticles such as: BET surface area, mesoporous volume, pore size and crystallite size are listed in Table 4.1. N<sub>2</sub> adsorption-desorption isotherms for these six samples are shown in Appendix A. A closer look at individual water/surfactant ratio (e.g., 0.66) leads to the conclusion that the results are consistent with basic microemulsion function that the microemulsion system with lower water content produced higher surface area and smaller particle sizes. Furthermore, it also describes that smaller microemulsion droplet formation plays more critical role in this scheme of experiments rather than surfactant/oil ratio.

The microemulsion system, dynamics, nanoparticle synthesis has been extensively reviewed previously and reached different conclusion (Eriksson et al., 2004; Lopez-Quintela, 2003; López-Quintela et al., 2004; M.-P. Pileni, 2003; M. Pileni, 1997). Water content in microemulsion system is described mostly by the water-to-surfactant ratio, however, it is important to recognize that water content can be increased not only by increasing water to surfactant ratio but also by increasing surfactant concentration in the microemulsion system (Eastoe et al., 2006). The similar trend has been depicted in Table 4.1 that at constant water to surfactant ratio (e.g., 0.66) the increase of surfactant weight ratio from 9 wt% to 18 wt% results in the increase of water content from 6 wt%

to 12 wt%, respectively. Previous study showed that final particle size will be dependent on initial water to surfactant ratio and have better control over the nanoparticle synthesis by merely changing water to surfactant ratio (Berkovich et al., 2002; I Lisiecki & Pileni, 1993, 1995; Natarajan et al., 1996; M. Pileni, 1997).

Another study exhibited the similar trend that the increase of water content induces a slight increase in droplet diameter  $D_h$  (from 24 to 32 nm) leads an increase in equivalent spherical diameter  $D$  (from 7.5 to 8.2) of the  $\gamma$ -Fe<sub>2</sub>O<sub>3</sub> particles synthesized. Hence, leading to the conclusion that microemulsion droplet diameter played an important role in the control of average size of synthesized nanoparticles (Vishal Chhabra et al., 1996). The results from our study also matched with another study in which they reported that the increase of water content at constant water to surfactant ratio induces an increase in microemulsion droplet size due to the increase of water content in the microemulsion system and produced larger particle size of the synthesized nanoparticles (Chandradass et al., 2010; Chandradass & Kim, 2009). The increase of water content has been ascribed to the increase of droplet size which leads to the surfactant films becomes thinner and enhancing the exchange process. This would give rise to larger particle size (López-Quintela et al., 2004). The size of microemulsion water core is tuneable with the adjustment of water/surfactant ratio and assist in the control of the diameter of the nanoparticle in the ME. Therefore, the nucleation and growth of Ni nanoparticles is suggested to be diffusion-controlled process through interaction between micelles, however, other factors such as phase behaviour, solubility, dynamic behaviour of microemulsion, the reagent concentration in the water core also play important role in the synthesis of nanoparticles and affecting the morphology (Chandradass et al., 2010; Chandradass & Kim, 2009).

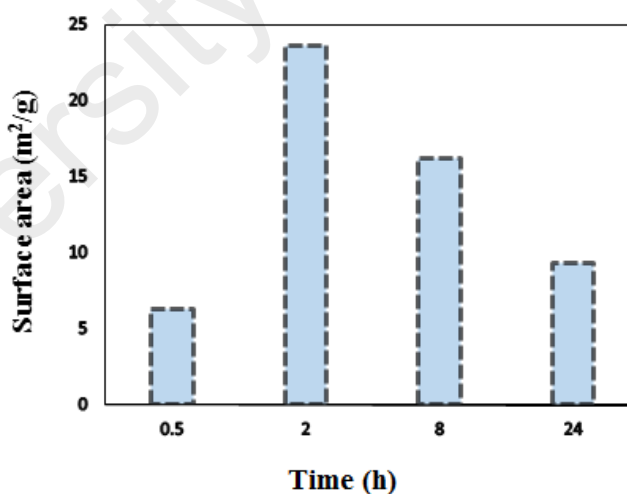
In the above section, the influence of water/surfactant ratio was discussed in detail with respect to water content, however, the final particle size of the nanoparticles depends

also on the average number of micelle exchange. In Table 4.1, the study exhibited that at constant water to surfactant ratio the microemulsion system with lower water content leads to the continuous decrease in the particle size and respective increase in the surface area. This can be described by the concept of free and bound water which has considerable influence over the particle synthesis and morphology. The microemulsion system with lower water content is considered to be bound and the micelle interface is said to be rigid having insufficient water available to solvate both polar head group of surfactant and counter ion. Thus, the rigid nature of micelle interface leads to the lower rates of intermicellar exchange and in turn lower growth rates (Eastoe et al., 2006).

The rate of micellar exchange depends upon the intermicellar potential and the rigidity of the surface. The higher net intermicellar potential will tend to favour growth interactions forming larger particles. On the other hand, the less intermicellar interaction will result in few micellar exchanges favouring smaller particles. The higher surface area in the lower water content microemulsion system is related to the rigid interface, which limits the rate of micellar exchange collisions and resulting in smaller particle size. A more rigid interface favours requires a large collision energy to effect a successful micelle exchange (M. Pileni, 1993, 1997, 1998). This intermicellar potential depends upon many factors such as micelle size, solvent molar volume, salinity and electrostatic charge. The increase of water content at constant water/surfactant ratio, the reverse micelle size increases. The increase of micelle size leads to two different phenomena: a) The intermicellar attraction potential increases and produced larger particle size. b) The increase of water content would lead to the lower rigidity due to the hydration of surfactant polar head group and lower interaction energy between water and the surfactant. This in turn leads to lower interfacial rigidity and an increase in particle size will be observed (M. Pileni, 1998).

#### 4.2.2 Effect of aging time

The selection of proper aging time plays an important role in the synthesis of nanoparticles via microemulsion synthesis. The effect of different aging times (0.5 h (T1), 2 h (T2), 8 h (T3) and 24 h (T4)) were studied for their influence on surface area as depicted in Figure 4.8. The influence of different aging time (1.5, 3, 6, 24) for the preparation of Ni@SiO<sub>2</sub> reported better morphology with narrow size distribution and have better cavity length distribution at base case for 3h (Dahlberg & Schwank, 2012). The further increase in aging time lead to the increase in the cavity length formation and produce longer nanotube instead of more organize spherical shapes. An investigation on the influence of aging time over the synthesis of SiO<sub>2</sub> nanoparticle via microemulsion system reveals that with the increase of aging time, there was seen an increase in SiO<sub>2</sub> particle size (Lin, 2006). Therefore, in our study aging time of 2 h for chosen as a base case for the preparation of Ni nanoparticles. N<sub>2</sub> adsorption-desorption isotherms for the influence of different aging times (T1, T2, T3 and T4) are shown in Appendix B.



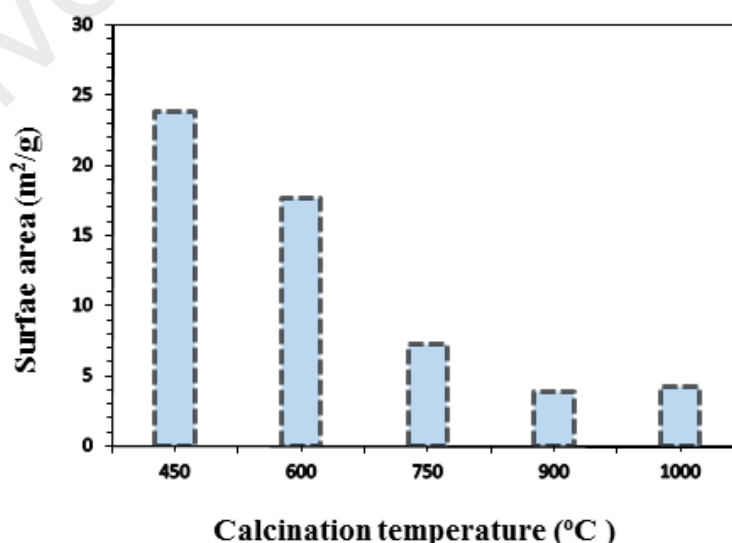
**Figure 4.8:** BET surface area for NiO particles at different aging times.

#### 4.2.3 Effect of calcination temperature:

Activation methods has been considered to play an important role in the reactivity and stability of catalysts and it has been reported that calcination is a critical step in



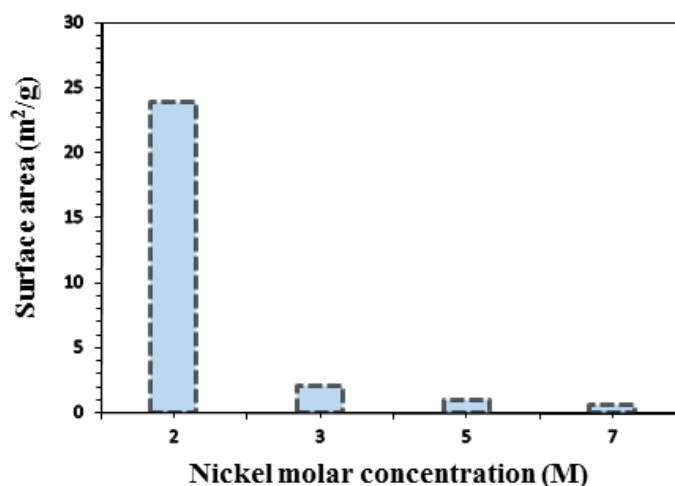
controlling the size of Ni nanoparticles which in turn influence the activity and stability. The influence of calcination temperature for Ni/Al<sub>2</sub>O<sub>3</sub> catalysts exhibited that the increase of calcination temperature from 300 to 750 °C lead to the decrease in surface area from 170 to 105 m<sup>2</sup>/g (Jiuling Chen et al., 2009). This decrease in surface area was dedicated to the coalescence of NiO particles. It was reported that not only the surface area was decreased with the increase of calcination temperature but also the catalytic activity was decreased for the catalysts calcined at higher calcination temperature. A similar type of decrease in the surface area and increase in NiO domain size (from 31 nm to 92.7 nm) was reported with the increase of calcination temperature (from 600 to 1000 °C) for Ni-Mg catalysts (Moliner et al., 2008). Therefore, in this study the influence of different calcination temperatures (450 °C (C1), 600 °C (C2), 750 °C (C3), 900 °C (C4) and 1000 °C (C5)) was investigated over Ni nanoparticles formed by microemulsion system. The study exhibited that with the rise of calcination temperature, a decrease in surface area was noticed as shown in Figure 4.9. It can be concluded that the lower calcination temperature was suitable for the synthesis of higher surface area, smaller particle size and smaller crystallite size. N<sub>2</sub> adsorption-desorption isotherms for the influence of different calcination temperatures (C1, C2, C3, C4 and C5) are shown in Appendix C.



**Figure 4.9:** BET surface area for NiO particles at different calcination temperature.

#### 4.2.4 Effect of molar concentration

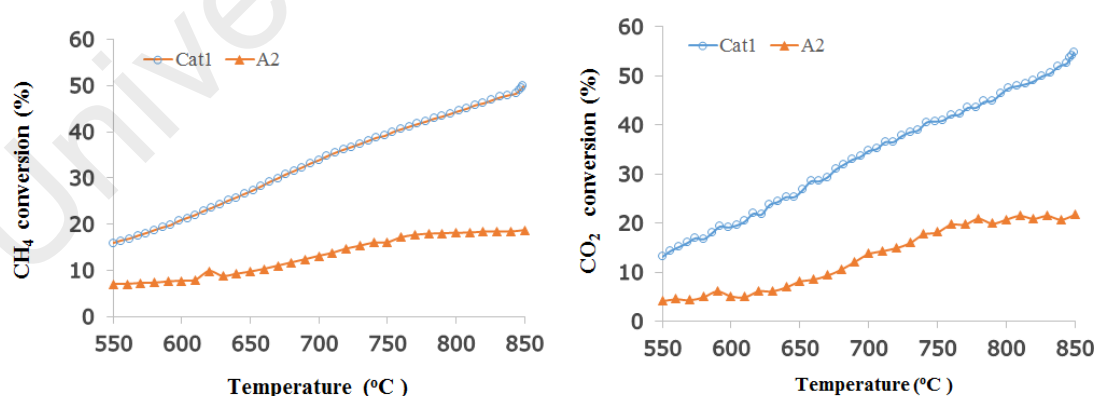
The choice of Ni metal concentration in the microemulsion system not only influences the final metal size but also plays an important role in the stability of the reverse micelle. The increase in precursor molar concentration would decrease the stability of reverse micelle which results in the occurrence of coalescence of metal particles and in turn produce higher metal particle size. Therefore, it is important to select suitable Ni molar concentration in microemulsion system. In this study, we have investigated different Ni metal concentrations such as: 2M (M1), 3M (M2), 5M (M3) and 7M (M4). BET analysis of different prepared samples indicate that the higher surface area for the samples having lower metal concentration as depicted in Figure 4.10. (T. Wu et al., 2013) reported that the different copper ( $\text{Cu}^{2+}$ ) concentration (0.07, 0.1 and 0.15M) in Cu-Ni@SiO<sub>2</sub> catalysts lead to the different particle size and depicted different crystal growth kinetics. The study reported that higher metal concentration (0.15 M) lead to the formation of unstable microemulsion and fast growth of crystals. The fast growth of nanoparticles would lead to the aggregation of water droplets producing larger size of particles. Another study also reported similar type of results for cobalt concentration in the microemulsion system. The study suggested that the increase in metal concentration would lead to the higher fraction of micelles containing nuclei and therefore it is highly probable that the interaction of micelle having metal particles increase and will produce larger particle size (Barber, 2005). Therefore, in this study the increase in metal concentration from 2M to 7M lead to the severe decrease in surface area from 23.87 to 0.5640 m<sup>2</sup>/g. N<sub>2</sub> adsorption-desorption isotherms for the influence of different calcination temperatures (M1, M2, M3 and M4) are shown in Appendix D.



**Figure 4.10:** BET surface area for NiO particles at different Ni molar concentration.

### 4.3 Activity and stability test

The study of catalytic activity with respect to temperature for Cat1 and A2 was seen to increase with the rise of temperature, which was attributed to the thermodynamic nature of dry reforming reaction. Figure 4.11 exhibits the methane and carbon dioxide conversion for A2 and Cat1 with temperature ranging from 550 to 850 °C. Higher methane (49.93%) and carbon dioxide (54.80%) conversion was observed for Cat1 compared to pure Ni nanoparticles (18.72% CH<sub>4</sub> and 21.80% CO<sub>2</sub>).



**Figure 4.11:** Methane and carbon dioxide conversion with respect to temperature for pure Ni and Ni/MgO catalyst.

The higher catalytic activity of supported catalysts can be dedicated to its higher surface area, smaller particle size and also the strong metal-support interaction compared

to pure Ni nanoparticles as described by BET and TPR results. The investigation on the stability of Cat1 at different temperature (750 °C, 800 °C and 850 °C) indicates that among these three temperatures, 750 °C was suitable for dry reforming of methane. The application of higher temperature lead to the lower reactants conversion at the end of reaction time (140 min) as indicated in Table 4.3. However, Cat1 exhibited the higher stability despite the fact it has higher carbon deposition compared to the reaction studied at 800 °C and 850 °C. Thus, exhibiting the fact that carbon deposition does not lead to the severe deactivation and the occurrence of coke deposition are not affecting the stability of the catalysts.

Furthermore, the stability test of the A2 and Cat1 indicates the higher stability for Ni/MgO catalysts compared to bare Ni nanoparticles (A2), which deactivated within 20 min of the reaction time. This led to the conclusion that the addition of MgO in the microemulsion system has significant effect on the reactivity and stability of catalysts but also resist towards the sintering of the catalyst. The stability study of different catalysts (Cat1, Cat2 and Cat3) calcined at different temperatures (Table 4.3) indicates that the catalyst calcined at lower calcination temperature (Cat1) depicted higher stability compared to the catalysts calcined at higher calcination temperatures (Cat2 and Cat3) as shown in Figure 4.12. The results from the stability study of the catalysts calcined at different temperatures are interesting and vary from the general trend, which suggest that the formation of strong NiO-MgO solid solution is favourable for dry reforming of methane and will exhibits higher activities. However, there are studies reporting otherwise and suggests that not all the times the increase of calcination temperature for Ni/MgO and strong solid solution formation leads to the higher activities and stabilities. Two set of catalysts  $\text{Ni}_{0.05}\text{Mg}_{0.95}$  (solid solution) and 5%Ni/MgO were prepared by co-precipitation and impregnation, respectively (Djaidja et al., 2006).  $\text{Ni}_{0.05}\text{Mg}_{0.95}$  catalysts exhibited very low catalytic activity only 1%  $\text{CH}_4$  conversion and 1.4%  $\text{CO}_2$  conversion.

On the other hand, 5%Ni/MgO exhibited higher initial methane and carbon dioxide conversion ( $> 80\%$ ). The comparison of the activity of two catalysts having same weight percentages of Ni suggests that this rapid increase was due to the higher surface area of 5%Ni/MgO ( $46 \text{ m}^2/\text{g}$ ) compared to  $\text{Ni}_{0.05}\text{Mg}_{0.95}$ . Moreover, the increase in conversion was dedicated to the easier accessibility of the Ni active sites in 5%Ni/MgO, which seems difficult on Ni-Mg solid solution for  $\text{Ni}_{0.05}\text{Mg}_{0.95}$ .

NiO/MgO catalyst prepared at three different calcination temperatures denoted as MPF12-Std (calcined at  $400^\circ\text{C}$ ), MPF12-6 (calcined at  $600^\circ\text{C}$ ), MPF12-8 (calcined at  $800^\circ\text{C}$ ) was applied to steam reforming of methane (Parmaliana et al., 1993). The study reported that the MPF12-std exhibited higher catalytic activities compared to other catalysts calcined at higher temperature (MPF12-6, MPF12-8). The study also reported that MPF12-Std exhibited higher stability, while MPF12-6 exhibited the second highest and MPF12-8 exhibited a strong decrease in the catalytic activity. They also suggested that the catalyst calcined at lower temperature MPF12-Std may not form complete solid solution but MPF12-8 certainly formed a solid solution. The similar trend is observed in our study that the catalysts calcined at lower temperature exhibited higher stability followed by the Cat2 and Cat3 exhibited the lower reactivity. This can be attributed to the higher surface area, smaller particle size and easier accessibility of Ni active sites compared to Cat2 and Cat3.

The lower catalyst performance of Cat2 and Cat3 can be described by the TPR results, which depicts that the formation of strong solid solution leads to the reduction of rare NiO species. Thus, the smaller number of active sites describe the lower reactants conversion as mentioned in Table 4.3 and Figure 4.12. However, for the same weight percentage of Ni in Cat1, TPR results depicts the number of reduced active sites increases, which arises due to the comparatively weak metal support interaction and thus increase in active sites leads to the increase in conversion. XRD analysis of spent catalyst (Cat1)

also indicates the presence of more intense Ni<sup>o</sup> diffraction peaks compared to Cat2 and Cat3 leading to the fact that it has more active sites and thus higher conversion was observed (Figure 4.12). Furthermore, the study exhibited the reduction of surface area with the increase of calcination temperature as described in Table 4.2. The higher BET surface area observed for Cat1 provides a larger contact area for the reactants that lead to the higher catalytic performance. However, for the catalysts calcined at higher temperature there was seen a significant decrease in surface area and mesoporous volume, which describes well the lower reactivity and stability of the catalysts.

Moreover, the decrease in surface area decreases the number of active sites exposed to the chemical atmosphere or reactant gases. It can be deduced from the reactivity tests that the catalysts calcined at higher temperature has lower methane and carbon dioxide conversion, lower BET surface area and consequently the amount of carbon on the catalysts was low too. The catalytic activity and stability of the catalysts follows the same trend as their surface area and the mesoporous volume such as: Cat1 > Cat2 > Cat3 > A2. The correlation of the catalyst stability and carbon deposition indicates the fact that the catalyst stability and carbon deposition are not correlated. The study indicates that Cat2 and Cat3 has lower carbon deposition compared to Cat1, even then Cat1 exhibits the better stability after reaction period. The occurrence of carbon deposition has led to some extent of catalyst deactivation but our study indicates that it should not be the deciding factor that the catalyst having higher carbon deposition will always exhibit poor stability. The simultaneous occurrence of higher activity and carbon deposition leads to the conclusion that both the reforming and carbon formation may occur over the catalyst surface active sites (D. Liu, Lau, et al., 2009). Table 4.3 indicates that the catalysts with higher calcination temperature (Cat2 and Cat3) exhibited lower reactants conversion and consequently lower carbon deposition rates. This indicates the fact that even though the higher carbon resistance of the catalysts maybe attributed to the

very strong NiO-MgO solid solution but the lower decomposition rates of the reactants also contributed to the lower carbon deposition. Similar types of results were reported for NiO-MgO-ZrO<sub>2</sub> catalysts applied for reforming of model biogas (Y. J. Asencios et al., 2011). The catalysts (NiZ, Ni4MZ) having lower decomposition rates exhibited the lower carbon deposition (10 and 23 mmol h<sup>-1</sup>) compared to the catalysts Ni20MZ and NiM, which exhibited higher decomposition rates accompanied with higher carbon deposition of 26 and 46 mmol h<sup>-1</sup>, respectively. The impregnation of noble metal (Rh) into Ni-MCM-41 catalyst for dry reforming of methane and reported that Rh@Ni-MCM-41-V exhibited stable and high activities (Arbag et al., 2010).

Although XRD results indicated the presence of intense peaks for graphitic carbon (26.0°) for this catalyst and the study concluded that coke formation on the surface did not cause major deactivation. Furthermore, the better performance of Rh@Ni-MCM-41-V catalysts maybe attributed to the porous nature of coke formed allowing the transport of reacting gases to the active sites. Furthermore, all the tested catalysts in the stability and activity tests exhibited higher CO<sub>2</sub> conversion compared to CH<sub>4</sub> conversion and the detection of traceable amount of water at the outlet indicates the occurrence of another important reaction called as reverse water gas shift reaction (RWGS) as described in equation 4.1 (Meshkani & Rezaei, 2011; Zanganeh et al., 2013). The lower H<sub>2</sub> production compared to CO in this study can be dedicated to its consumption in RWGS reaction and results in higher CO<sub>2</sub> conversion and CO production.

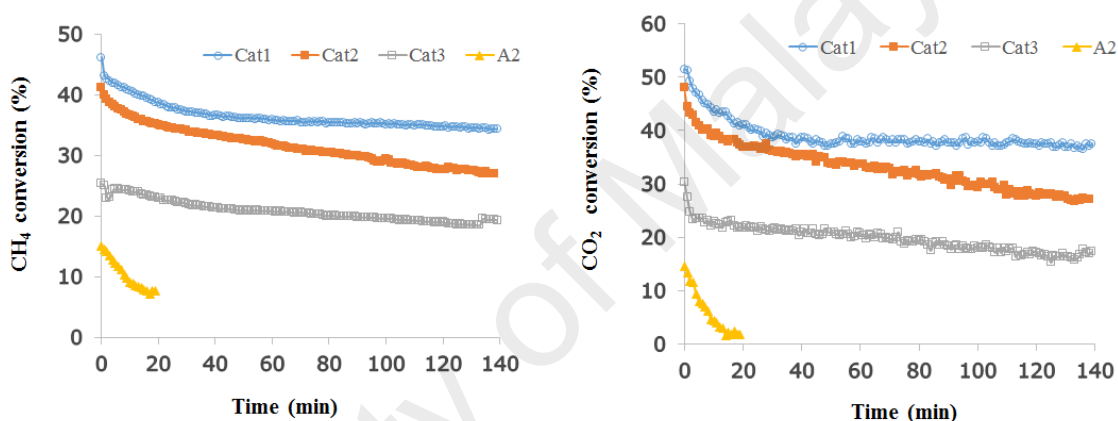


The catalytic activity and stability indicates that the lower calcination temperature is suitable for dry reforming of methane for the catalysts prepared by microemulsion system for this MgO rich solid solution.

**Table 4.3:** Initial and final reactants conversion along with their carbon deposition at different calcination and reaction temperatures.

Sample ID	Tc (°C)	Tr (°C)	Initial % Conv.		Final % Conv. (after 140 min)		Carbon deposition (g <sub>c</sub> /g <sub>cat</sub> )
			CH <sub>4</sub>	CO <sub>2</sub>	CH <sub>4</sub>	CO <sub>2</sub>	
Cat1	450	750	46.13	51.40	34.30	37.60	2.648
Cat1	450	800	45.43	50.80	24.83	22.40	0.820
Cat1	450	850	46.44	55.20	27.98	27.00	0.122
Cat2	600	750	41.26	48.00	26.95	27.20	0.244
Cat3	800	750	25.39	30.40	19.29	17.40	0.034
A2 <sup>a</sup>	450	750	15.06	14.60	7.69	1.80	0.016

a: stability of pure Ni at initial and after 20 min, Tc: calcination temperature; Tr: Reaction temperature.



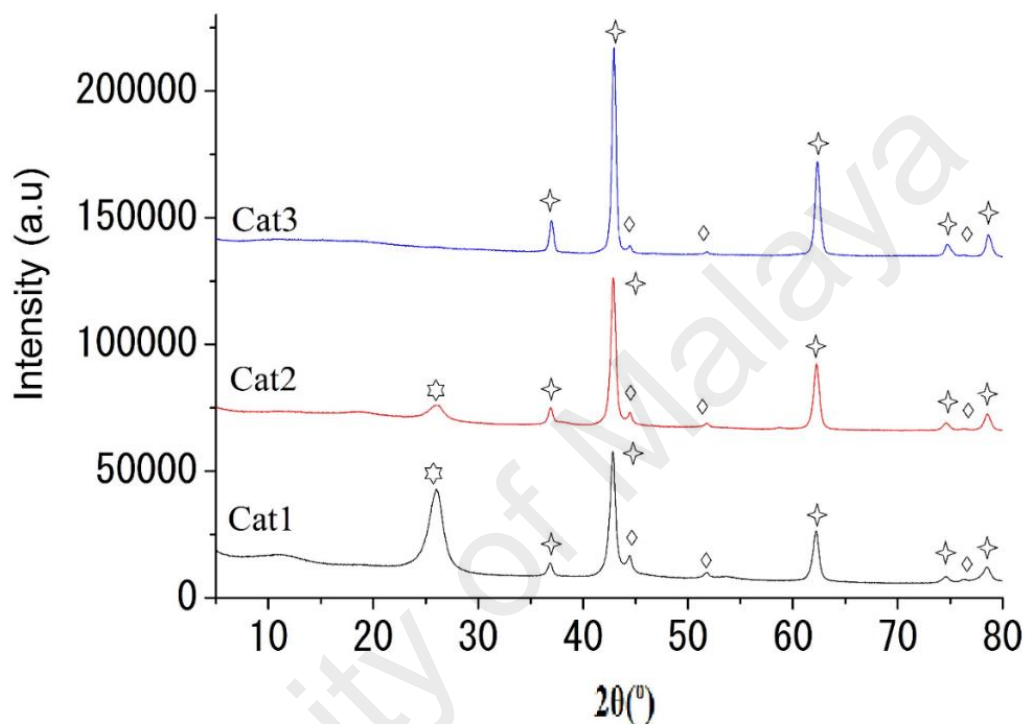
**Figure 4.12:** Methane and carbon dioxide conversion with respect to time at 750 °C for pure Ni and Ni/MgO catalysts calcined at different temperatures.

#### 4.4 Characterization of spent catalyst

XRD patterns of the spent catalysts (Cat1 and Cat2) indicate the characteristics of graphite peak (002) around 26° indicating the crystalline phase of CNTs matching with JCPDS no. 01-075-1621 (Figure 4.13). However, no such peaks related to graphite carbon was observed for Cat3 and matched well with the reported coke deposition in Table 4.3. XRD analysis of the spent catalyst (Cat1, Cat2 and Cat3) indicates the presence of Ni<sup>0</sup> peaks (at 44.48°, 51.83° and 76.35°) matching with JCPDS no. 01-070-1849. The intensity of these peaks was strong for Cat1 compared to Cat2 and Cat3, which exhibits weak diffraction peak related to Ni<sup>0</sup> indicating the fact that not all NiO present in NiO-MgO is reduced and still have intact strong NiO-MgO solid solution. XRD analysis also



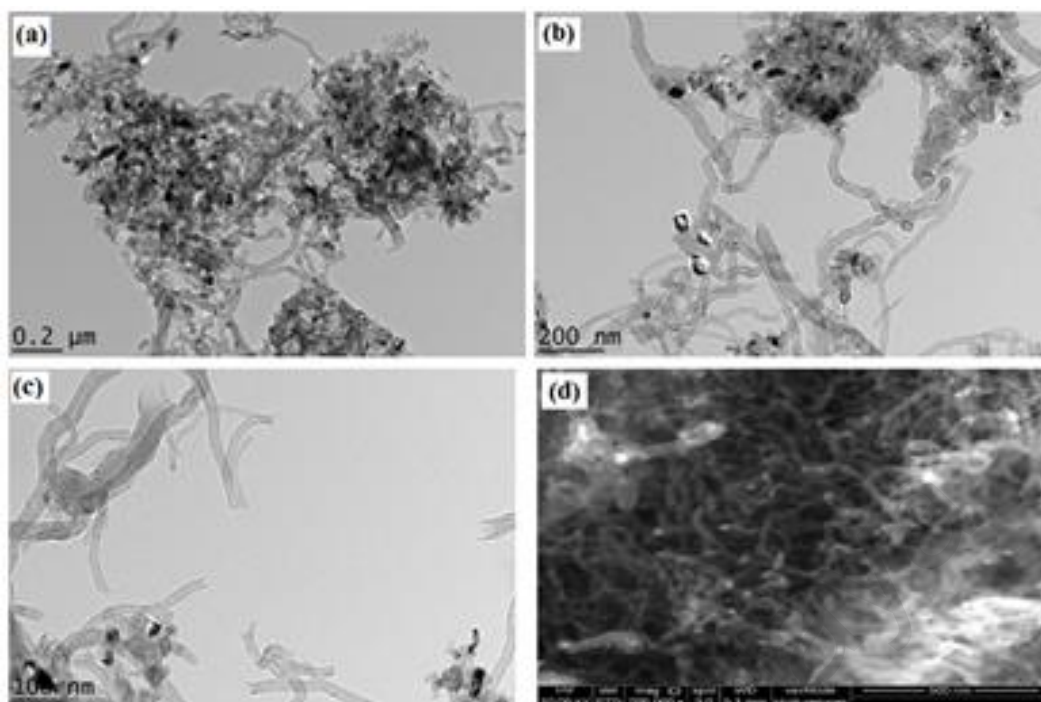
indicated the broad and strong  $\text{Ni}^0$  peaks, which suggests that these samples have more active sites on  $\text{Ni}^0$  under these reaction conditions and matches well with the higher conversion rates. However, Cat2 and Cat3 exhibited less intense peaks related to  $\text{Ni}^0$  species and the presence of strong NiO-MgO solid solution peaks exhibits the fact that there are less accessible active  $\text{Ni}^0$  sites.



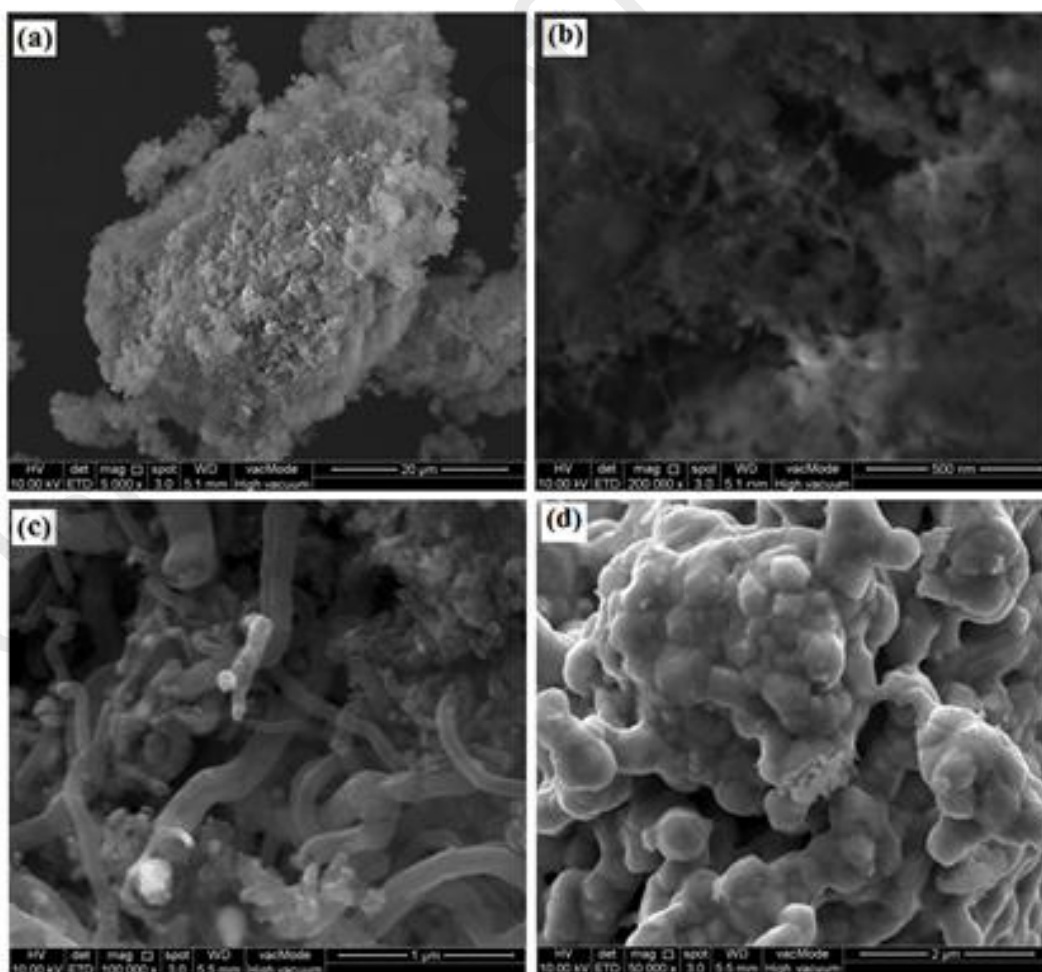
**Figure 4.13:** XRD analysis of spent catalysts where (✧) presents NiO-MgO solid solution, (◇) presents Ni crystallite peaks and (☆) presents graphite crystallite peaks.

The characterization of spent catalysts (Cat1, Cat2, Cat3, A2) by TEM and FESEM analysis exhibits the coke formation in different quantities and matches well with the reported Table 4.3 and XRD analysis. TEM images of Cat1 indicates the presence of homogenous distribution of CNTs covering MgO-based catalysts. The catalysts surface seems to completely cover by filamentous carbon. Moreover, TEM images of Cat1 (Figure 4.14(a-c)) indicates the formation of majority whisker carbon species with a hollow internal channel having the open-end structure and no Ni particles found at the tip of CNTs. TEM images of Cat1 indicated that the carbon deposited was majority filamentous type (whisker-like), however, the presence of encapsulating like carbon,

which have a shell-like structure was not seen. This whisker like carbon deposits does not cause catalyst deactivation as described by the stability test and matches well with the studies reported previously (Arbag et al., 2010; D. Chen et al., 2001; Montoya et al., 2000; Tomishige et al., 1999; Tomishige et al., 1998). The study suggests that only shell-like carbon have the deactivation behaviour. Similar results were reported by Kroll and swan for their study on the deactivation behaviour of Ni-based catalysts for dry reforming of methane (Kroll, Swaan, et al., 1996b; Swaan et al., 1994). They reported that whisker like carbon have very little toxicity but shell-like carbon deposits has higher toxicity and has tendency to encapsulate Ni particles hindering the access of reacting sites to active surface. Furthermore, TEM images indicates that the filamentous carbon was of different diameters indicating the presence of a distribution of Ni crystallite sites. The difference between the catalytic activity and stability of Cat1 and A2 can be linked with the type of carbon deposits as depicted by TEM and FESEM images in Figure 4.14(a-c) and Figure 4.15(c,d). FESEM images of pure Ni indicates the formation of globular carbon and also strong agglomeration of Ni particles can be seen in the spent catalyst depicting its lower catalytic activity and strong deactivation. FESEM images of Cat2 (Figure 4.14(d)) and Cat3 (Figure 4.15(a,b)) indicates the lower quantities of carbon deposition and matches well with the XRD analysis. FESEM images of Cat3 indicates the agglomeration of supported catalysts and thus lead to the lower conversion rates.



**Figure 4.14:** TEM images of spent Cat1 (a,b,c) and FESEM images of Cat2 (d) after stability test.



**Figure 4.15:** FESEM images of spent Cat3 (a,b) and pure Ni (c,d) after stability test.

## 4.5 Summary

The synthesis of pure Ni nanoparticles by microemulsion synthesis approach indicates that water content plays an important role on the surface area of Ni particles. The increased water content at constant water-to-surfactant ratio leads to the higher intermicellar attraction potential and also the lower rigidity of the micelles, which in turn produced larger particle size or lower surface area. Furthermore, higher calcination temperature (800 °C) exhibited a decrease in catalytic activity compared to the catalysts, which were calcined at lower calcination temperature (450 °C).

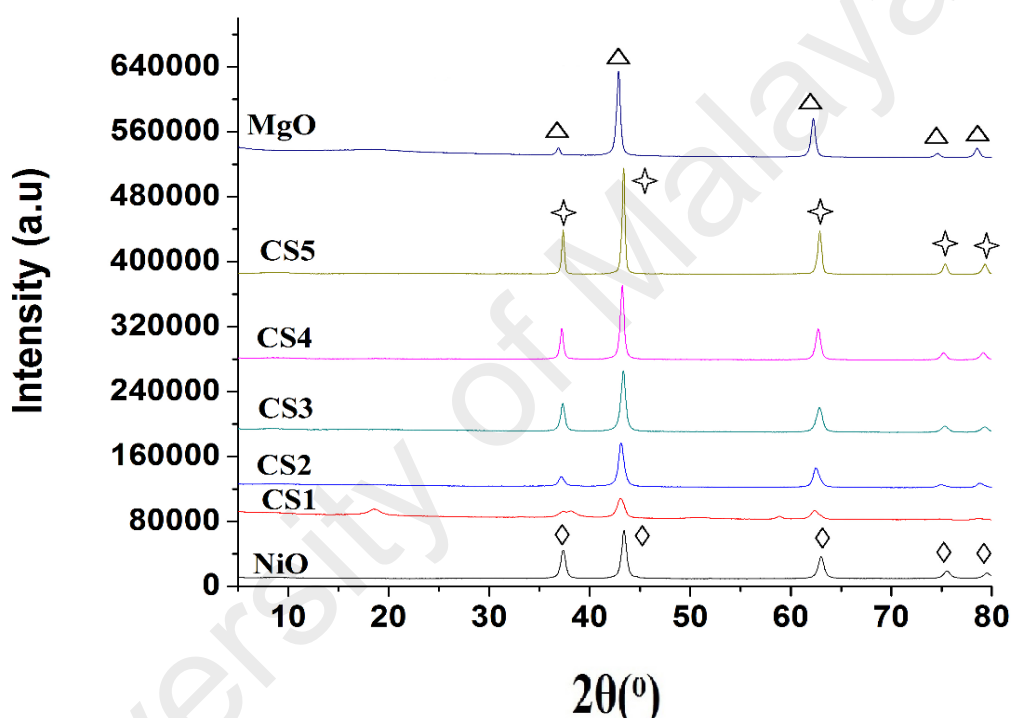
**Part 2: An investigation on the influence of catalyst composition, calcination and reduction temperatures on Ni/MgO catalyst for dry reforming of methane.**

## 4.6. Characterization of fresh catalyst

### 4.6.1 X-Ray diffraction

X-ray diffraction (XRD) patterns of NiO, MgO and NiO/MgO catalyst gave insight into the crystallite size as shown in Figure 4.16. Pure NiO exhibits sharp peaks at  $2\theta$  values of  $37.28^\circ$ ,  $43.44^\circ$ ,  $63.01^\circ$ ,  $75.55^\circ$  and  $79.40^\circ$  corresponding to the respective crystallite phase of (111), (200), (220), (311), and (222), which matches well with standard card of cubic NiO with JCPDS no. 01-073-1519. Furthermore, pure MgO and NiO/MgO catalyst matched well with the standard card of cubic JCPDS no. 01-079-0612 and JCPDS no. 00-024-0712, respectively. The presence of diffraction lines at  $2\theta$  values of  $62.37^\circ$ ,  $74.80^\circ$  and  $78.54^\circ$  are attributed to the formation of NiO-MgO solid solution and in the present study for all the catalysts (CS1 to CS5), these diffraction lines are present indicating the formation of NiO-MgO solid solution. Another study also reported the formation of NiO-MgO solid solution at similar  $2\theta$  values ( $62.32^\circ$ ,  $74.72^\circ$  and  $78.66^\circ$ ) (Hua et al., 2010). However, the close similarity of NiO and MgO in their oxides structure

both having face-centered-cubic structures and also having similar lattice parameters (4.1946 and 4.2112 Å) makes it quite difficult to distinguish between the diffraction peaks of NiO, MgO and NiO/MgO (Y. J. Asencios et al., 2011). Furthermore, Figure 4.16 clearly indicates that with the increase of Ni content (20% to 80%) diffraction peaks become narrow indicating the increase of crystallite size (Table 4.4). The broad diffraction peaks for CS1 indicates the presence of small crystallite size, which matches well with the BET results for CS1 exhibiting larger surface area (Table 4.4).

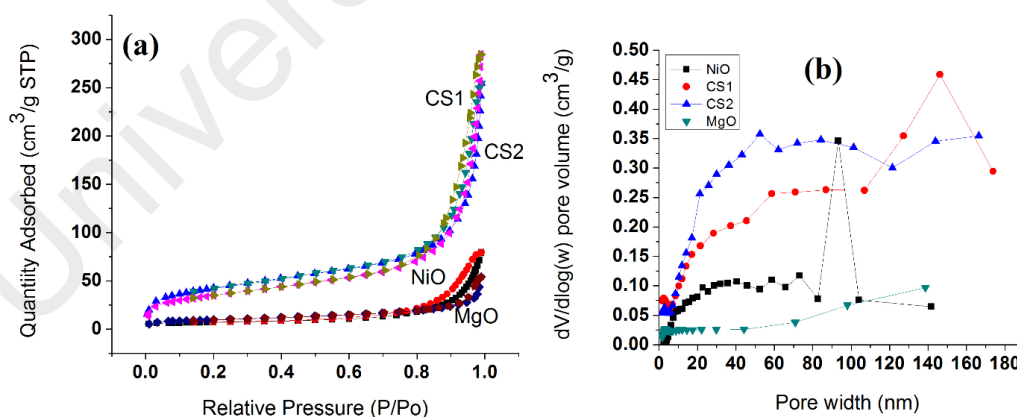


**Figure 4.16:** XRD patterns of calcined catalysts, where (✦), (◇), and (Δ) presents NiO-MgO solid solution peaks, NiO crystallite peaks and MgO crystallite peaks, respectively.

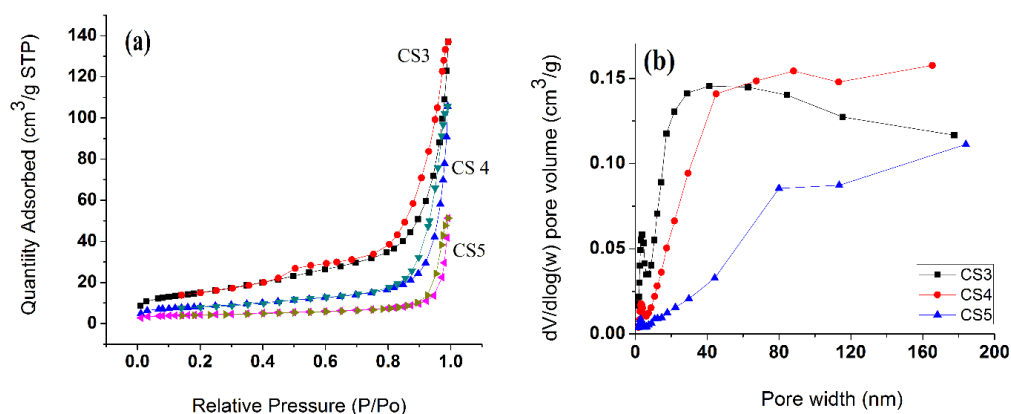
#### 4.6.2 Surface area and pore volume

BET surface area and pore size distribution of the catalysts were measured by N<sub>2</sub>-physisorption. The isotherms of nitrogen adsorption and desorption for these catalysts were found to be type III isotherm with a large type H3 hysteresis loop according to the IUPAC classification. The formation of type H3 hysteresis loop at relatively high pressure indicates the formation of large pore volumes in the samples. N<sub>2</sub> adsorption/desorption isotherms for NiO, MgO, CS1 and CS2 are depicted in Figure 4.17(a). N<sub>2</sub> isotherms for

catalysts (CS3, CS4 and CS5) having higher Ni weight percentage (80%) and calcined at different temperatures are exhibited in Figure 4.18(a). The surface area of pure NiO nanoparticles and MgO was 23.87 m<sup>2</sup>/g and 34.69 m<sup>2</sup>/g, respectively. An increase in surface area was observed for the supported catalysts (CS1, CS2, CS3) calcined at 450 °C with the addition of MgO support as depicted in Figure 4.17(a), Figure 4.18(a) and Table 4.4. However, with the increase of Ni content (CS1 to CS3), there was seen a decrease in surface area from 153.22 to 54.01 m<sup>2</sup>/g. The decrease of surface area with the increase of Ni content can be attributed to the deposition of Ni onto smaller pore of support. A further decrease in the surface area from 54.01 m<sup>2</sup>/g to 15.19 m<sup>2</sup>/g was observed with the increase of calcination temperature from 450 °C (CS3) to 800 °C (CS5), respectively as depicted in Table 4.4 and Figure 4.18(a). Pore size distribution of catalysts was determined by Barret-Joyner-Halenda (BJH) method based on adsorption branch of N<sub>2</sub> isotherm as shown in Figure 4.17(b) and Figure 4.18(b). Furthermore, BJH average pore width sizes for NiO, MgO, CS1, CS2, CS3, CS4 and CS5 were calculated to be around 22.56 nm, 12.41 nm, 15.06 nm, 18.04 nm, 15.34 nm, 27.04 nm and 30.85 nm, respectively.



**Figure 4.17:** (a) N<sub>2</sub> adsorption-desorption isotherms and (b) BJH pore width distribution of calcined catalysts.



**Figure 4.18:** (a) N<sub>2</sub> adsorption-desorption isotherms and (b) BJH pore width distribution of calcined catalysts.

**Table 4.4:** BET surface area, total pore volume and XRD crystallite size of calcined catalysts.

Catalyst	BET SA m <sup>2</sup> /g	Pore volume cm <sup>3</sup> /g	BET pore size (nm)	Average crystallite size (nm)	Average Ni <sup>o</sup> size (nm) <sup>d</sup>	
					spent catalyst reduced at 550 °C	spent catalyst reduced at 800 °C
NiO	23.87	0.1215	20.36	27.58 <sup>a</sup>	-	-
MgO	34.69	0.0836	9.643	25.69 <sup>b</sup>	-	-
CS1	153.22	0.3932	10.26	18.81 <sup>c</sup>	50.82	-
CS2	125.82	0.4401	13.92	26.69	56.71	-
CS3	54.01	0.2121	15.70	27.09	30.98	32.63
CS4	29.11	0.1634	22.46	28.56	44.07	47.63
CS5	15.19	0.0794	20.91	33.90	27.22	32.54

<sup>a</sup>Based on all NiO peaks in JCPDS no. 01-073-1519; <sup>b</sup>Based on all MgO peaks in JCPDS no. 01-079-0612; <sup>c</sup>Based on all NiO-MgO peaks in JCPDS no. 00-024-0712; <sup>d</sup>Based on Ni<sup>o</sup> peaks located at 44.48° and 51.83°.

#### 4.6.3 Temperature-programmed reduction

Surface reducibility of the catalysts were examined by TPR-H<sub>2</sub>, which has been recognized as a technique to discriminate various species in solid solutions. TPR profiles of the Pure NiO and Ni/MgO catalysts are exhibited in Figure 4.19. The higher reducibility of pure NiO exhibited by higher H<sub>2</sub> uptake refers to the reduction of bulk NiO as shown in Figure 4.19(a). TPR profiles of supported catalysts (CS1, CS2 and CS3) exhibited two peaks one at very low temperature (T<sub>L</sub>) and second peak at quite higher temperature (T<sub>H</sub>) except for CS1 for which the second peak also appear at medium temperature (T<sub>M</sub>) around 365.1 °C. The presence of temperature peaks (< 400 °C) can

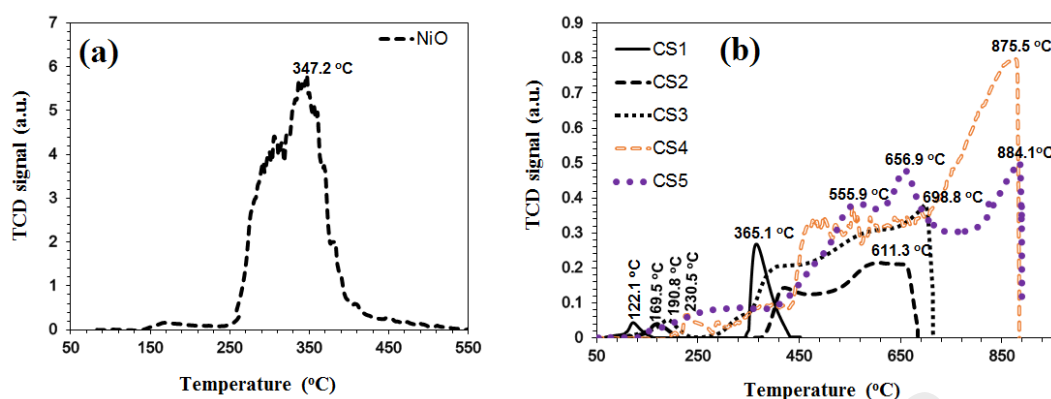
either be attributed to the reduction of  $\text{Ni}^{3+}$  surface species located at surface sites for Ni/MgO catalyst or to the reduction of NiO which was uninfluenced by the MgO support. The presence of higher reduction peaks temperature in the range of 500-700 °C for supported catalysts indicates the reduction of  $\text{Ni}^{2+}$  ions in the outermost and sub-surface layers of the MgO lattice, which is in accordance with the literature cited (Feng et al., 2012; Y.-H. Wang et al., 2009; M. Yu et al., 2014).

Previous studies suggested that calcination temperature has a strong influence on the incorporation of NiO into NiO-MgO solid solution (Feng et al., 2012; Y.-H. Wang et al., 2009). This is the reason that for CS4 and CS5, application of higher calcination temperature (600 °C and 800 °C, respectively) shifts the reduction peak temperature from 698.8 °C (CS3-450 °C) to 875.5 °C and 884.1 °C, respectively as shown in Figure 4.19(b). The shift of reduction peak to higher temperature (> 800 °C) indicates the reduction of lattice  $\text{Ni}^{2+}$  ions in the MgO matrix, which indicates the formation of strong NiO-MgO solid solution. Furthermore, the increase of calcination temperature from 600 °C to 800 °C, shifted the medium reduction peak at 555.9 °C to 656.9 °C, which indicates the presence of strong metal-support interaction for CS5. The detail of the reduction peaks temperature along with their reducibility extent are mentioned in Table 4.5. Similar type of shift in reduction peaks to higher temperature was reported for Ni/MgO catalyst (Feng et al., 2012) as the calcination temperature was increased from 600 °C to 800 °C. Figure 4.19(a,b) also showed that the addition of MgO leads to the shift of reduction peaks to higher temperature and also the interaction between NiO and MgO probably hindered the reduction of NiO owing to the formation of NiO-MgO solid solution.

**Table 4.5:** Reduction peaks temperatures and reducibility of Ni/MgO catalysts

Catalyst	$T_L$ (°C)	$T_M$ (°C)	$T_H$ (°C)	Reducibility (%)
NiO	-	347.2	-	-
CS1	122.1	365.1	-	11.26
CS2	169.5	-	611.3	20.96
CS3	190.8	-	698.8	31.42
CS4	230.5	555.9	875.5	46.55
CS5	-	656.9	884.1	45.63



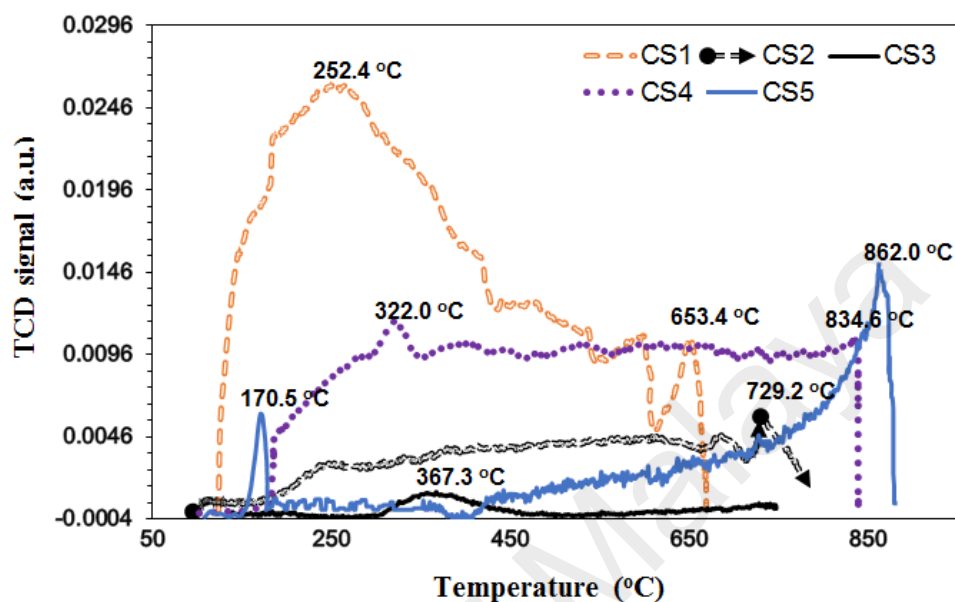


**Figure 4.19:** TPR-H<sub>2</sub> profiles of (a) NiO and (b) Ni/MgO catalysts.

#### 4.6.4 Temperature-programmed desorption

The application of basic support (MgO) will have a strong influence on the strength of basic sites in Ni/MgO catalyst. Temperature programmed desorption of CO<sub>2</sub> (TPD-CO<sub>2</sub>) was performed in order to investigate the strength of basic sites in Ni/MgO catalyst. The temperature at which chemisorbed CO<sub>2</sub> on the basic sites is desorbed, indicates the strength of basic sites. Weak basic sites are said to be formed in Ni/MgO catalyst, when CO<sub>2</sub> desorption peaks occur at lower temperature, whereas strong basic sites exhibit an opposite trend (Bhavani et al., 2012). TPD-CO<sub>2</sub> profiles for the catalysts having higher MgO content (CS1 and CS2) exhibited higher peak temperature at 653.4 °C and 729.2 °C, respectively, which indicates the presence of strong basic active sites. The lower peak temperature for CS1 at 252.4 °C indicates the presence of weak basic sites. TPD-CO<sub>2</sub> profiles for the catalyst having lower MgO content (CS3) exhibited the peak temperature at 367.1 °C, which indicates the presence of medium strength basic sites. The investigation on the influence of calcination temperature over the strength of basic sites indicated that CO<sub>2</sub> desorption peaks were shifted to the higher temperature as the calcination temperature increased from 450 °C to 600 °C and 800 °C for CS4 and CS5, respectively. For CS4, the peak temperature shifted from 367.3 °C to 834.6 °C as depicted

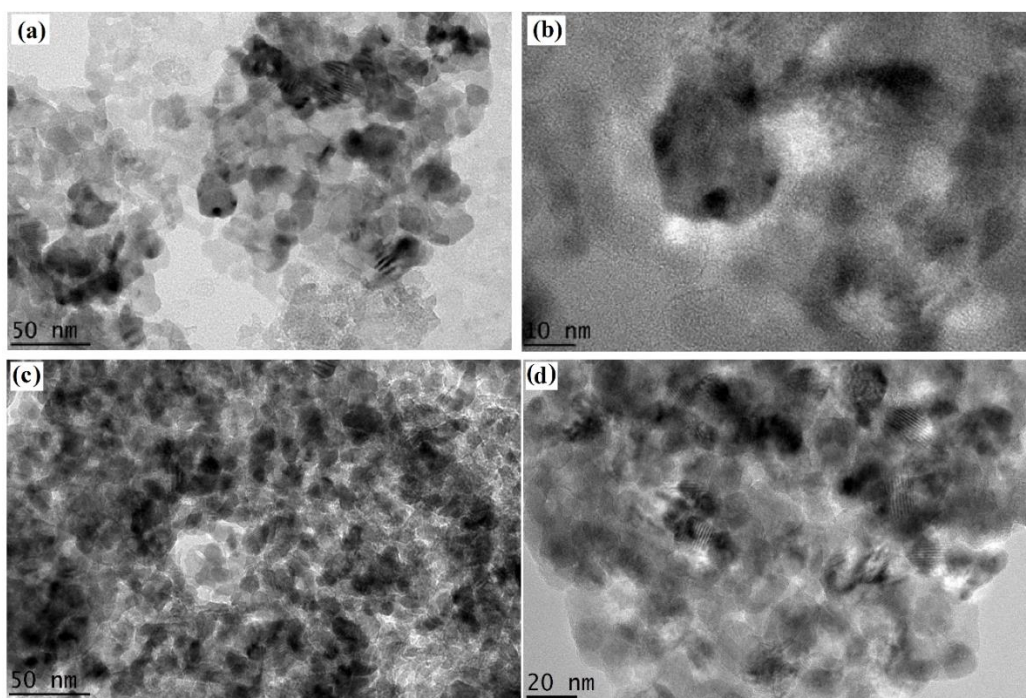
in Figure 4.20, whilst for CS5 the peak temperature shifted to further higher temperature (862.0 °C). TPD-CO<sub>2</sub> profiles for CS4 and CS5 indicates the existence of very strong basic sites, which indicates the interaction of metal sites with basic sites.



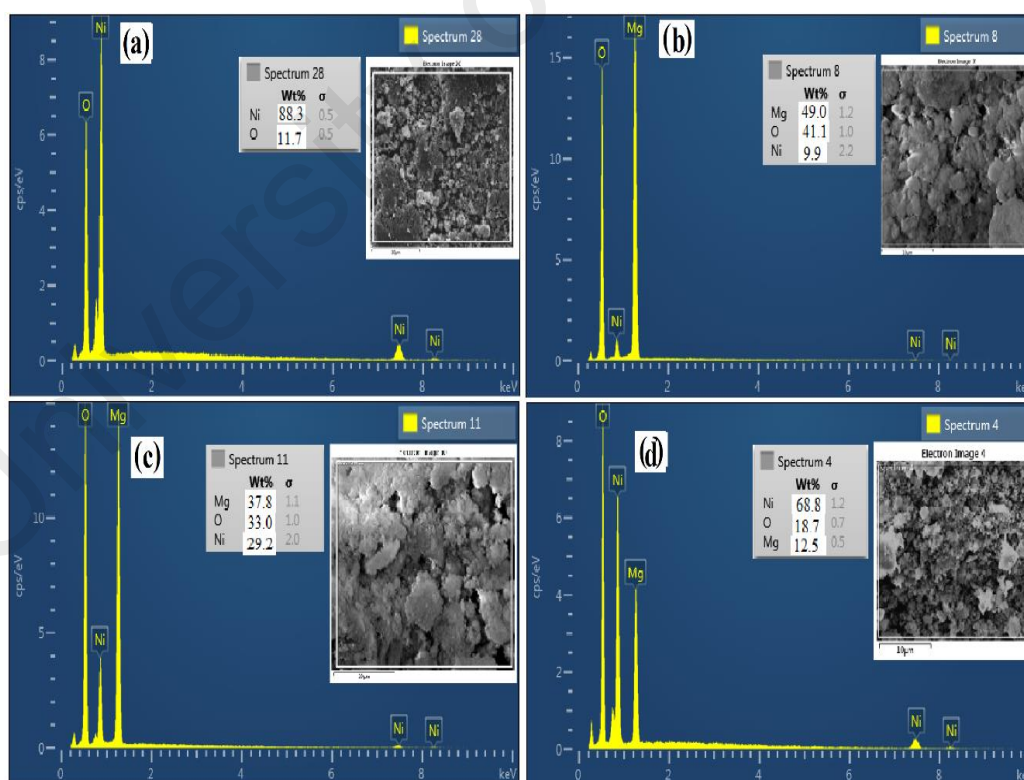
**Figure 4.20:** TPD-CO<sub>2</sub> profiles for Ni/MgO catalysts.

#### 4.6.5 TEM and EDX analysis

TEM images of Ni/MgO catalyst having higher MgO content (CS1, Figure 4.21 (a,b)) and lower MgO content (CS3, Figure 4.21(c,d)) exhibited that the addition of MgO in the microemulsion system leads to the better nanoparticle distribution, however, the influence of the addition of MgO to resist agglomeration was more pronounced in CS1 compared to CS3, as depicted by its higher surface area in BET results (Table 4.4). Furthermore, EDX analysis of NiO, CS1, CS2 and CS3 indicates the weight percentages of Ni and Mg before the reduction are shown in Figure 4.22.



**Figure 4.21:** TEM images of freshly calcined catalysts (a,b) CS1 and (c,d) CS3.

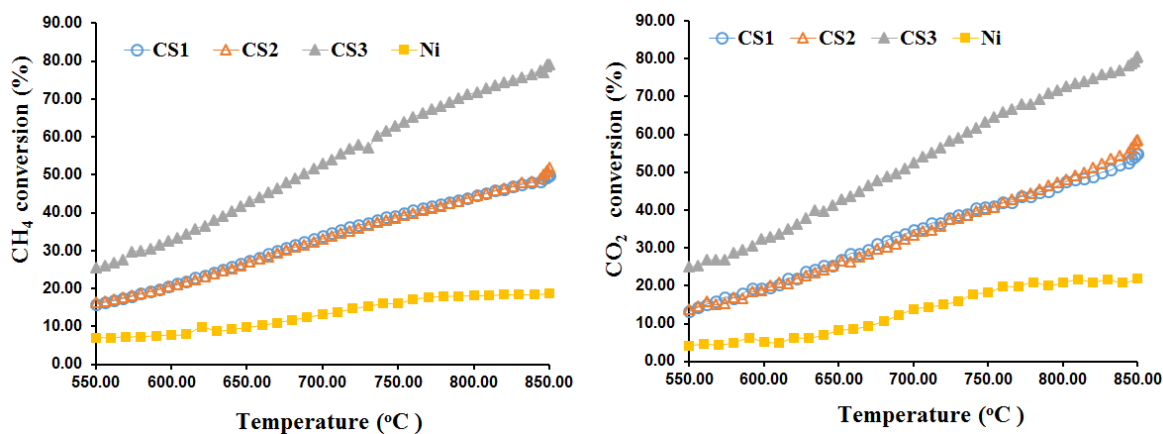


**Figure 4.22:** EDX analysis of (a) NiO, (b) CS1, (c) CS2 and (d) CS3 catalysts.

#### 4.7. Activity and stability test

The study of catalytic activity of catalysts (CS1, CS2, CS3, Ni) indicates that there was seen an increase in CH<sub>4</sub> and CO<sub>2</sub> conversions with the increase of temperature, which was attributed to the thermodynamic nature of the dry reforming reaction. Figure 4.23 indicates that the catalyst having higher Ni content (CS3) exhibited higher catalytic activity among all the catalysts tested (CS1, CS2 and Ni). However, both CS1, CS2 exhibited comparable activity, while CS2 being slightly higher. Ni nanoparticles exhibited the lower methane (18.72%) and carbon dioxide (21.80%) conversion at final temperature 850 °C.

The stability test of different catalysts (CS1, CS2 and CS3) at different reaction temperatures (700 °C, 800 °C and 850 °C) exhibited that CS3 has the higher catalytic activity and stability at 750 °C compared to CS1 and CS2 as shown in Figure 4.24(a,b) and Table 4.6. The stability study of catalysts at higher reaction temperatures (800 °C and 850 °C), exhibited a severe decrease in the catalytic activity. However, with the rise of reaction temperature, a significant decrease in carbon deposition was observed as mentioned in Table 4.6. This can be attributed to the presence of more reactive carbon species produced by methane decomposition at these higher reaction temperatures, which are easily gasified by CO<sub>2</sub> (Kathiraser et al., 2015). The catalytic activity of both CS1 and CS2 were comparable to each other with respect to reaction temperature (Figure 4.23), however, the stability of both catalysts exhibited a different trend as mentioned in Table 4.6. CS1 exhibited higher initial catalytic activity than CS2 at 750 °C, however, CS2 exhibited higher initial and final conversions at higher reaction temperatures (800 and 850 °C). Ni nanoparticles exhibited severe decrease in catalytic activity within 20 min of reaction period as shown in Figure 4.24(a,b), which was attributed the agglomeration of Ni particles.



**Figure 4.23:** Conversion-temperature relationship of different catalysts (Reaction conditions: CH<sub>4</sub>/CO<sub>2</sub> = 1/1 and WHSV =  $1.68 \times 10^5 \text{ ml g}^{-1} \text{ h}^{-1}$ ).

The study exhibited the fact that Ni content in Ni/MgO catalyst has an important role in catalytic activity and stability of catalysts. TPR-H<sub>2</sub> results suggested that with the increase of Ni content (20 wt% to 80 wt%) an increase in hydrogen consumption was observed, which indicates the reduction of more NiO to Ni<sup>0</sup>. The higher Ni content in Ni/MgO catalyst will produce more Ni active sites upon reduction, which would be easily accessible by the reactants and thus exhibited higher catalytic activity as shown in Table 4.6. This can be justified on the basis of XRD analysis of spent catalysts (Figure 4.26), which indicates the presence of more intense peak related to Ni<sup>0</sup> for CS3. Thus, it can be concluded that the activity of the catalysts was related to the quantity of Ni<sup>0</sup> present in the catalyst, which was obviously higher for the catalyst having higher Ni content. The surface area was decreased from 153.22 to 54.01 m<sup>2</sup>/g with the increase of Ni content from 20% to 80%, however, the methane and carbon dioxide conversion were increased from 46.13% to 49.76% and from 51.40% to 63.80%, respectively at 750 °C. Similar type of results was reported for Ni/Al<sub>2</sub>O<sub>3</sub> catalyst, when the Ni content was increase from 5% to 25%, the BET surface was decreased from 212.4 to 164.8 m<sup>2</sup>/g, respectively (Therdthianwong et al., 2008). However, both methane and carbon dioxide conversions were seen to increase with Ni content. For 5% Ni/Al<sub>2</sub>O<sub>3</sub>, CH<sub>4</sub> and CO<sub>2</sub> conversions were

only 7.0% and 19.5% and increased to 63.4% and 66.9%, respectively for 25% Ni/Al<sub>2</sub>O<sub>3</sub> at 700 °C.

The carbon deposition on CS3 was comparatively high (6.684 g<sub>c</sub>/g<sub>cat</sub>) compared to CS1 (2.648 g<sub>c</sub>/g<sub>cat</sub>) and CS2 (3.700 g<sub>c</sub>/g<sub>cat</sub>). However, when one correlates the amount of carbon deposition and catalyst stability, it can be found that larger amount of carbon deposition does not always lead to the severe decrease in activity. A closer look at Figure 4.24(a,b) and Table 4.6, indicates even though carbon deposition was high for CS3 but it exhibited better catalyst stability. Similar type of results was reported for Ni catalysts supported on mesoporous material MCM-41 having different (gel Si/Ni ratio) (D. Liu, Lau, et al., 2009). They reported that Ni-MCM-41(B) and Ni-MCM-41(C) show poor stability, even though they have lower carbon deposition compared to Ni-MCM-41(D), which exhibited highest catalyst stability. The higher carbon deposition on CS3 can be attributed to the larger particle size, which leads to the production of higher carbon deposition (Hu & Ruckenstein, 2002).

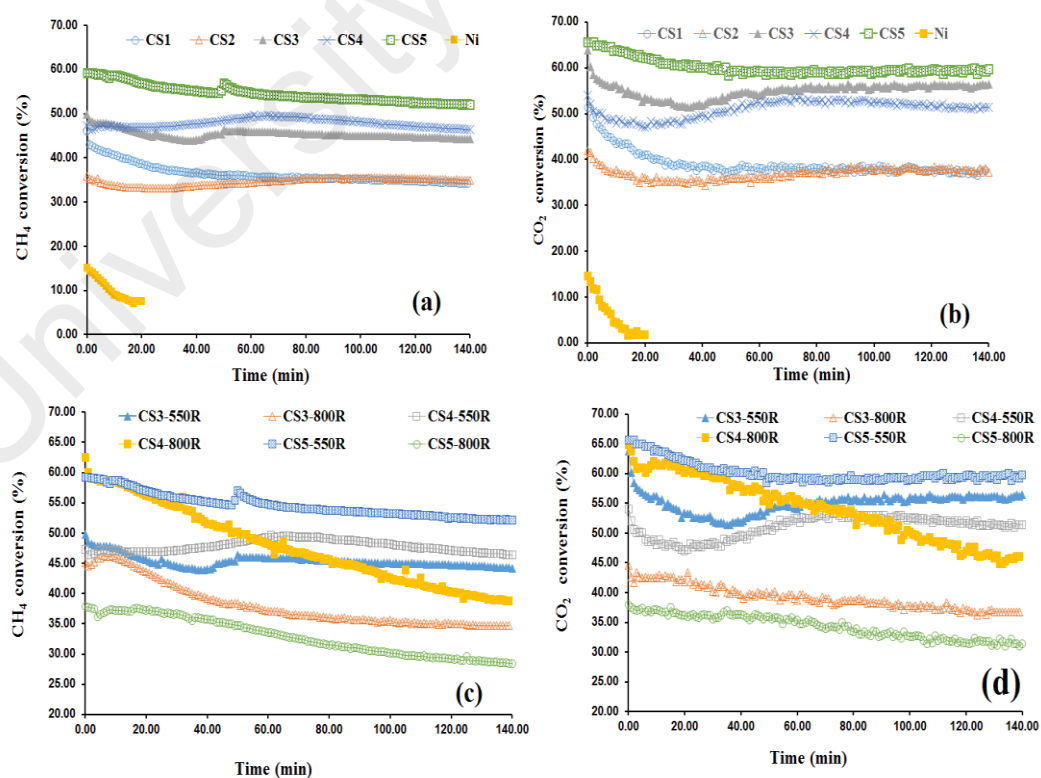
The influence of calcination temperature over catalyst stability was studied at 750 °C, by calcining the catalyst CS3-450 °C at higher calcination temperatures, 600 °C (CS4) and 800 °C (CS5). The study showed that CS5 exhibited the higher stability and both initial (59.22% CH<sub>4</sub> and 65.60% CO<sub>2</sub>) and final (52.09% CH<sub>4</sub> and 59.80% CO<sub>2</sub>) conversions were high compared to CS3 and CS4. Even though, with the increase of calcination temperature (450 to 800 °C), there was seen a further decrease in BET surface area from 54.01 to 15.19 m<sup>2</sup>/g. The stability of the catalyst was uninfluenced with the decrease of BET surface area (larger particle size), which showed that the catalyst particle size did not play major role in the catalytic activity and stability. Furthermore, the carbon deposition was low for CS5 (3.580 g<sub>c</sub>/g<sub>cat</sub>) compared to CS3 (6.684 g<sub>c</sub>/g<sub>cat</sub>) and CS4 (4.782 g<sub>c</sub>/g<sub>cat</sub>), which can be attributed to the strong NiO-MgO solid solution. BET analysis indicates that CS5 has the largest particle size among all the catalyst test, still it

exhibited the better stability and activity. Similar results was reported for another study in which active metal Ni, NiCo or NiRh supported on CeZr-mixed oxide exhibited stable activity for the samples containing larger particles size and suggested that larger particle size was also responsible for long term stability (Horváth et al., 2011).

It has been suggested that reduction temperature plays an important role in catalytic activity and stability of the catalyst. The investigation on the influence of reduction temperature was done in order to optimize the activation conditions. Therefore, the influence of reduction temperatures (550 °C and 800 °C) on the catalytic stability of catalysts (CS3, CS4 and CS5) was investigated and the results are shown in Figure 4.24(c,d). The study shows that the catalysts reduced at higher reduction temperature (800 °C) exhibited severe catalyst deactivation. The results indicated that the catalyst (CS5) calcined at higher temperature (800 °C) and reduced at lower temperature (550 °C) exhibited the better stability and activity of the catalyst compared to CS3 and CS4 as mentioned in Figure 4.24(c,d) and Table 4.6. The catalysts (CS3 and CS5) reduced at higher temperature (800 °C), even lead to the lower initial reactants conversions, while, CS4 exhibited higher initial catalytic activity at 800 °C compared to the same catalysts reduced at 550 °C (Table 4.6). The influence of reduction temperature (700 °C, 750 °C, 800 °C and 850 °C, 900 °C and 950 °C) on the catalytic behaviour of Co/TiO<sub>2</sub> catalyst was investigated for dry reforming of methane (Takanabe et al., 2005a). The study showed that the catalyst Co/TiO<sub>2</sub> exhibited higher methane (65.5%) and carbon dioxide (71.7%) conversion at lower reduction temperature (700 °C). Both methane and carbon dioxide conversions were decreased with the increase of reduction temperature such as: that at 750 °C it exhibited 55.7% CH<sub>4</sub> and 64.3% CO<sub>2</sub> conversion, at 800 °C exhibited 39.0% CH<sub>4</sub> and 51.2% CO<sub>2</sub> conversion, at 850 °C exhibited 5.6% CH<sub>4</sub> and 9.2% CO<sub>2</sub> conversion. Furthermore, at higher reduction temperatures of 900 °C and 950 °C, methane and carbon dioxide conversion become negligible. They suggested that catalyst



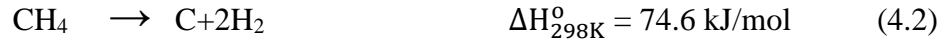
deactivation of Co/TiO<sub>2</sub> catalysts with the increase of reduction temperature was attributed to the metal sintering. The study of the influence of reduction temperature (400 °C, 500 °C, 600 °C and 700 °C and 900 °C) on cobalt catalyst supported on SiO<sub>2</sub> applied for Fischer-Tropsch catalysis exhibited that the catalysts reduced at higher reduction temperature were more prone to sintering and exhibited lower catalyst performance compared to the catalyst reduced at lower reduction temperature (Bezemer et al., 2006). Similar results were reported for Ni-MCM-41 in which the increase of reduction temperature from 550 to 750 °C leads to the decrease in methane conversion from 80% to 73% and carbon dioxide from 83% to 74% (D. Liu, Lau, et al., 2009). The study leads to the conclusion that the reduction of catalysts at higher reduction temperature makes the catalysts more prone to sintering, which in turn reduces the number of available active sites and thus leads to the lower catalytic activities and deactivation. Therefore, it seems that the proper choice of reduction temperature is critical and should be investigated properly for each of the preparation method.



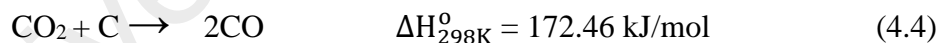
**Figure 4.24:** Conversion-time relationship of different catalysts (Reaction conditions: 750 °C CH<sub>4</sub>/CO<sub>2</sub> =1/1, WHSV= 1.68 x 10<sup>5</sup> ml g<sup>-1</sup> h<sup>-1</sup>).



Carbon formation during the dry reforming reaction is suggested to be produced by two major reactions: methane decomposition (equation 4.2) and Boudouard reaction (equation 4.3) being endothermic and exothermic, respectively (Guczi et al., 2010; M. Yu et al., 2014; J. Zhang et al., 2008).



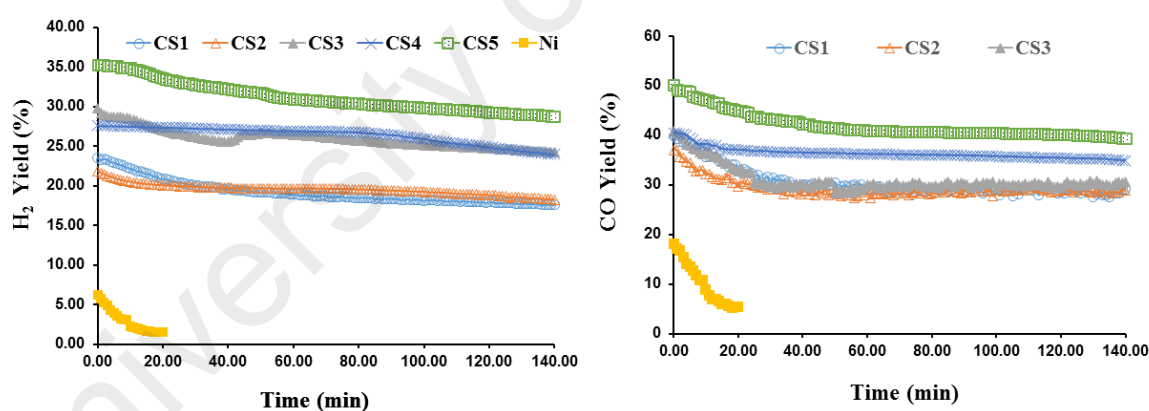
Thermodynamic analysis of dry reforming reaction suggests that this reaction becomes spontaneous at higher reaction temperature ( $> 640^{\circ}\text{C}$ ) (S. Wang et al., 1996; J. Zhang et al., 2007). Furthermore, previous studies suggested that methane decomposition is favourable at higher reaction temperatures ( $> 700^{\circ}\text{C}$ ) due to its endothermic nature (P Frontera et al., 2013; M. Yu et al., 2014), while, Boudouard reaction is not thermodynamically favourable at higher reaction temperatures ( $> 700^{\circ}\text{C}$ ) and above  $700^{\circ}\text{C}$  becomes non-spontaneous (P Frontera et al., 2013; S. Wang et al., 1996; J. Zhang et al., 2008). Therefore, the application of higher reaction temperature not only eliminates the influence of Boudouard reaction (J. Zhang et al., 2007) but also will shift the equilibrium to the left side and will favour the occurrence of reverse of Boudouard reaction as shown in equation 4.4 (Özdemir, Öksüzömer, & Gürkaynak, 2010).



Furthermore, the spontaneous reaction temperature for reverse Boudouard reaction is  $719^{\circ}\text{C}$  (Long Xu et al., 2014). Therefore, dry reforming of methane at higher reaction temperature ( $750^{\circ}\text{C}$ ) can be regarded as a combination of one carbon formation reaction (equation 4.2) and one carbon elimination reaction (equation 4.4) (J. Zhang et al., 2008). The occurrence of reverse Boudouard reaction will assist in the removal of carbon produced by reacting with chemisorbed  $\text{CO}_2$  (Meshkani & Rezaei, 2011; J. Zhang et al., 2008). However, the occurrence of carbon deposition at  $750^{\circ}\text{C}$  (Table 4.6) during this study indicates the existence of following conditions such as: the rate of methane

decomposition (equation 4.2) was high compared to carbon removal reaction (equation 4.4) and reverse Boudouard reaction seems to be the limiting step as suggested by various studies (Y. J. Asencios et al., 2011; J. Zhang et al., 2008).

Higher CO<sub>2</sub> conversion was exhibited by Ni/MgO catalyst compared to methane during the activity and stability tests. Furthermore, the presence of water at outlet indicates the occurrence of reverse water gas shift reaction (RWGS) as shown in equation 4.5 (Meshkani & Rezaei, 2011; Zanganeh et al., 2013). The study also indicated that during the reaction time CO yield was always higher than H<sub>2</sub> yield for all the catalysts as shown in Figure 4.25, which is attributed to the RWGS reaction. The utilization of produced H<sub>2</sub> in the RWGS reaction (equation 4.5) by CO<sub>2</sub> leads to the production of higher CO and in turn higher CO<sub>2</sub> conversions are observed.



**Figure 4.25:** H<sub>2</sub> and CO yield of different catalysts (Reaction conditions: 750 °C CH<sub>4</sub>/CO<sub>2</sub> = 1/1, WHSV = 1.68 x 10<sup>5</sup> ml g<sup>-1</sup> h<sup>-1</sup>).

Thus, the study leads to the conclusion that the better catalytic activity and stability of the Ni/MgO catalyst was exhibited by the formation of strong “NiO rich” solid solution and obviously will be present in the catalyst having higher Ni content. For the catalysts having higher MgO content (CS1 and CS2), NiO would diffuse from the outermost layer into a deeper layer to form a more stable type of “MgO rich” solid solution. However, for catalytic reactions, a surface “NiO rich” solid solution will be

more beneficial as it will produce more Ni<sup>o</sup> active sites compared to the “MgO rich” solid solution (Y. Li et al., 2014). That is the reason, that catalysts having higher Ni content (CS3, CS4 and CS5) exhibited higher catalytic activity, which are having “NiO rich” solid solution. Furthermore, with the increase of Ni content an increase in the reducibility of NiO in calcined NiO/MgO was observed (Figure 4.19). Hu and Ruckenstein (Hu & Ruckenstein, 2002) suggested that the occurrence of such type of phenomenon would lead to the formation of large Ni particle size in Ni/MgO catalyst similar to that observed in this study by BET results (Table 4.4), which will be eventually more prone to the sintering and coking at high Ni loading. Hence, larger Ni particles in Ni/MgO catalyst would lead to severe deactivation of the catalytic activity during the reaction time (Hu & Ruckenstein, 2002).

However, according to the present data for activity (Table 4.6 and Figure 4.23 and Figure 4.24(a,b)) and surface area of different catalysts (Table 4.4), particle size of Ni was not having a major influence over the stability of the reduced Ni/MgO catalyst. Similar type of results were reported (Y.-H. Wang et al., 2009) for Ni/MgO catalyst in which the larger Ni particle size (20.0 nm) was observed on reduced Ni<sub>30</sub>Mg-6 compared to the smaller particle sizes (16.7 and 10.0 nm) observed for reduced Ni<sub>8</sub>Mg-4 and Ni<sub>8</sub>Mg-5, respectively. However, Ni<sub>30</sub>Mg-6 exhibited very stable activity, but both Ni<sub>8</sub>Mg-4 and Ni<sub>8</sub>Mg-5 catalysts were deactivated rapidly during the reaction time. These results lead to an important conclusion that not only the Ni loading and Ni particle size in the reduced catalyst, but also physicochemical state of NiO in the oxidized sample plays a major role in affecting the stability of the catalyst. Previous study suggested that for Ni/MgO catalyst it is important to have NiO entities that belong to NiO-MgO solid solution, otherwise it would not be possible to have stable Ni sites (Y.-H. Wang et al., 2009). Therefore, the key to form stable Ni sites in Ni/MgO catalyst, it is necessary to have a complete reaction of the NiO component with the MgO support during the

calcination step to form NiO-MgO solid solution. Therefore, in this study the catalyst calcined at higher temperature (800 °C) exhibited better stability due to the formation of strong NiO-MgO solid solution compared to the catalysts calcined at a lower calcination temperature (CS3-450 °C and CS4-600 °C) having similar Ni content. Previous study suggested that calcination temperature has significant influence on the diffusion of Ni<sup>2+</sup> ions into the MgO lattice and strong metal-support interaction was observed (Feng et al., 2012).

The comparison of different catalysts applied to dry reforming of methane with the present study indicates that Ni/MgO catalyst prepared by microemulsion synthesis exhibited better performance compared to the previous studies (Arbag et al., 2010; X. Chen et al., 2005b; Hua et al., 2010; M Rezaei et al., 2008; Tomishige et al., 2002; Zanganeh et al., 2013) as mentioned in Table 4.7. Previous studies reported that the catalysts at low WHSVs exhibited higher reactants (CH<sub>4</sub> and CO<sub>2</sub>) conversion and opposite trend will be observed at high WHSVs. The lower reactants conversion at higher WHSV values, was attributed to the fact that the residence or contact time will be lower, moreover, larger amounts of reactants will be flowing into the reactor and reactants will have limited opportunity to adsorb on active sites (Newnham et al., 2012; Rahemi et al., 2013; San José-Alonso et al., 2013; Leilei Xu et al., 2012). However, the comparison of Ni/MgO catalyst (present work) with previous studies exhibited that even though the WHSV was quite higher ( $1.68 \times 10^5 \text{ ml h}^{-1} \text{ g}^{-1}$ ), it exhibited higher reactants conversion indicating its better performance even under severe reaction conditions. Moreover, the study suggests that the preparation conditions, Ni metal content, calcination temperatures and reduction temperatures has much strong influence over this unique system of NiO-MgO solid solution prepared by microemulsion synthesis. Therefore, we can conclude that the influence of MgO addition was prominent not only on the activity of Ni/MgO catalyst, but also provide resistance towards the agglomeration of Ni particles.

Furthermore, the stability tests of CS1, CS2 and CS3 at 800 °C and 850 °C are shown in Appendix E and Appendix F.

**Table 4.6:** Activity and stability of Ni/MgO catalysts at CH<sub>4</sub>/CO<sub>2</sub> = 1/1 and WHSV = 1.68 x 10<sup>5</sup> ml g<sup>-1</sup> h<sup>-1</sup>

Sample ID	T <sub>c</sub> (°C)	T <sub>red</sub> (°C)	T <sub>reac</sub> (°C)	Initial % Conv.		Final % Conv. (after 140 min)		Carbon (g <sub>c</sub> /g <sub>cat</sub> )
				CH <sub>4</sub>	CO <sub>2</sub>	CH <sub>4</sub>	CO <sub>2</sub>	
CS1	450	550	750	46.13	51.40	34.30	37.60	2.648
			800	45.43	50.80	24.83	22.40	0.820
			850	46.44	55.20	27.98	27.00	0.122
CS2	450	550	750	35.87	41.80	34.90	37.20	3.700
			800	53.05	60.40	37.40	44.60	2.892
			850	63.72	70.20	42.16	48.60	0.806
CS3	450	550	750	49.76	63.80	44.21	56.40	6.684
			800	62.09	69.00	44.01	49.80	3.380
			850	73.84	79.40	43.89	53.20	2.680
			800 750	45.03	44.60	34.72	36.80	3.760
CS4	600	550	750	47.29	54.00	46.37	51.40	4.782
			800	62.48	64.80	38.82	46.00	3.884
CS5	800	550	750	59.22	65.60	52.09	59.80	3.580
			800	37.84	38.00	28.46	31.40	3.030
Ni <sup>a</sup>	450	550	750	15.06	14.60	7.69	1.80	0.016

a: final conversions of pure Ni after 20 min; T<sub>c</sub>: calcination temperature; T<sub>red</sub>: reduction temperature, T<sub>reac</sub>: reaction temperature.

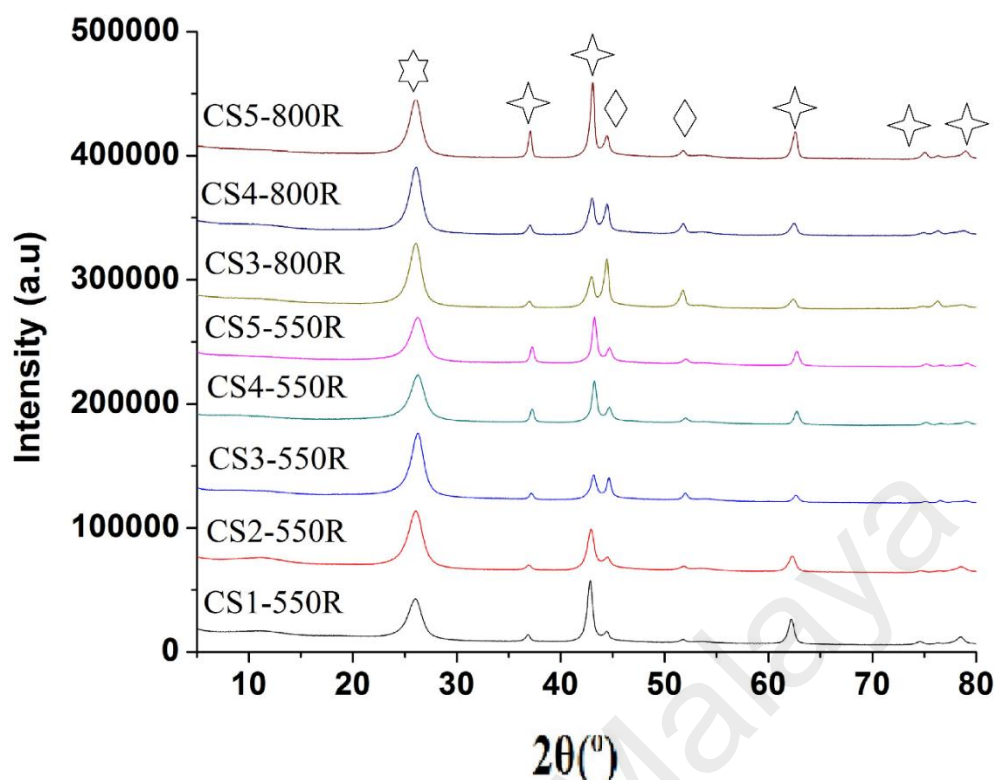
**Table 4.7:** Comparison of catalytic activity of previous studies with Ni/MgO catalysts.

Catalyst	RC		Final conversion (%)			Ref.
	T	WHSV	T	CH <sub>4</sub>	CO <sub>2</sub>	
Ni <sub>0.10</sub> Mg <sub>0.90</sub> O	600	1.4 x 10 <sup>4</sup>	300	25.0	30.0	(Zanganeh et al., 2013)
Ni-MCM-41	600	3.6 x 10 <sup>4</sup>	240	28.0	38.0	(Arbag et al., 2010)
Rh-MCM-41-V				32.0	39.0	
5%Ni/ZrO <sub>2</sub>	700	1.5 x 10 <sup>4</sup>	300	54.0	59.0	(M Rezaei et al., 2008)
PT-Ni/MgO	700	9.6 x 10 <sup>4</sup>	240	49.0	54.0	(Hua et al., 2010)
C-Ni/MgO				20.0	30.0	
NiO/Al <sub>2</sub> O <sub>3</sub>	800	9.37 x 10 <sup>4</sup>	300	52.5	-	(X. Chen et al., 2005b)
3 mol% Ni/MgO	850	5.6 x 10 <sup>4</sup>	240	50.0	62.0	(Tomishige et al., 2002)
3 mol% Pt/MgO				40.0	50.0	
Ni/MgO (CS5)	750	1.68 x 10 <sup>5</sup>	140	52.09	59.80	This study
Ni/MgO (CS4)				46.37	51.40	
Ni/MgO (CS3)				44.21	56.40	

T: temperature °C; WHSV: weight hourly space velocity ml h<sup>-1</sup> g<sup>-1</sup>; t: min; PT: plasma treated catalyst; C: conventional impregnated catalyst.

#### 4.8 Characterization of spent catalyst

The characterization of spent catalysts (CS1-CS5) by XRD analysis indicates the presence of graphite peak (002) around  $26^{\circ}$ , which was attributed to the crystalline phase of CNTs matching with JCPDS no. 01-075-1621 (Figure 4.26). Furthermore, XRD analysis of all the spent catalysts exhibited  $\text{Ni}^0$  peaks at  $44.48^{\circ}$  and  $51.83^{\circ}$ , which matched with JCPDS no. 01-070-1849. XRD analysis of spent catalyst (CS3) indicates the presence of broad and strong  $\text{Ni}^0$  peaks compared to CS1 and CS2, which suggests that CS3 have more  $\text{Ni}^0$  active sites at these reaction conditions and this can be attributed to the higher Ni content. Therefore, the catalyst having higher Ni content (CS3) exhibited higher catalytic activity compared to the catalysts having lower Ni content (CS1 and CS2). XRD analysis of spent catalysts reduced at higher reduction temperature ( $800^{\circ}\text{C}$ ) are also shown in Figure 4.26 and the average crystallite sizes of spent catalysts (reduced at  $550^{\circ}\text{C}$  and  $800^{\circ}\text{C}$ ) are mentioned in Table 4.4. An increase in the crystallite sizes was observed for the catalysts reduced at  $800^{\circ}\text{C}$  compared to the catalysts reduced at lower reduction temperature ( $550^{\circ}\text{C}$ ) indicating the occurrence of Ni metal sintering, which matches well with the previous studies that the higher reduction temperature makes the catalyst prone to sintering (Bezemer et al., 2006; Takanabe et al., 2005a).

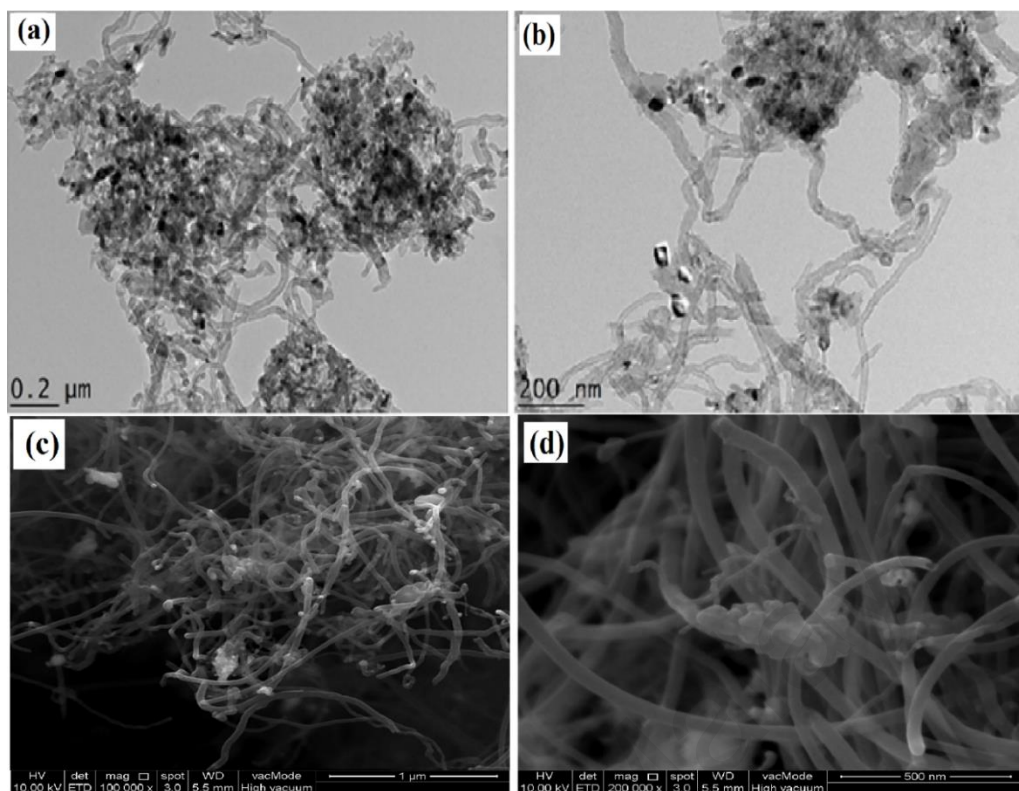


**Figure 4.26:** XRD analysis of spent catalysts, where (☆), (◇) and (☆) presents NiO-MgO solid solution peaks, Ni crystallite peaks and graphite peaks, respectively.

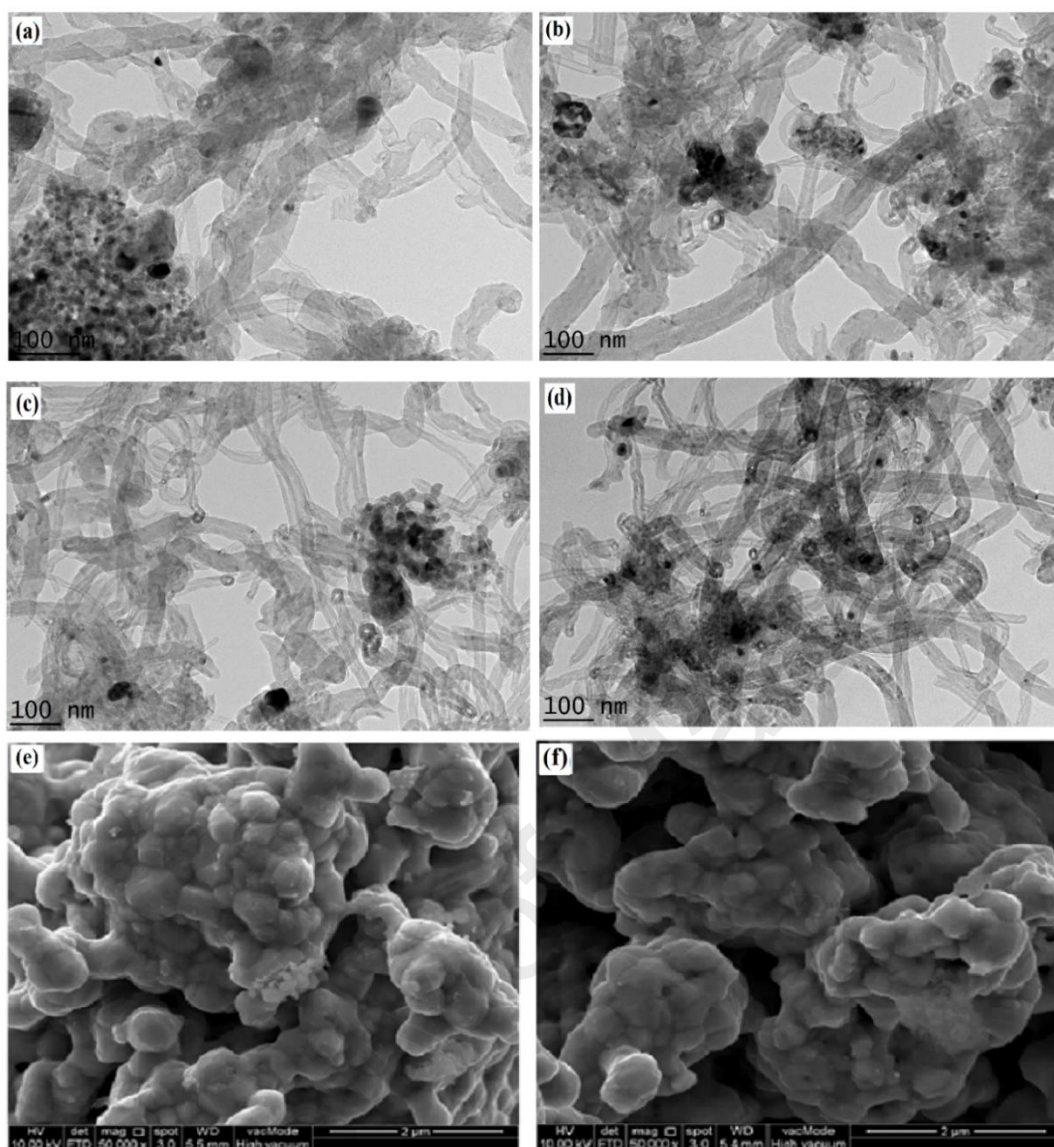
Carbon accumulation on spent catalysts can be observed by TEM and FESEM images, indicating the presence of carbon species having different morphologies. The analysis of spent catalysts (CS1, CS2, CS3 and CS5) indicates that the majority of the accumulated carbon were in the form of carbon nanotubes (whisker-like carbon species). Moreover, TEM and FESEM images (Figure 4.27 and Figure 4.28) indicate the presence of different types of carbon nanotubes (CNTs) such as: CNTs with Ni particle at the tip, CNTs with closed end but without the presence of Ni particle on the tip, CNTs with different diameters and CNTs with hollow internal channel having open end structure and no Ni particles at the tip. Previous studies suggested that the formation of single wall and multiwall carbon nanotubes either follow tip-growth or base-growth mechanism (Amelinckx et al., 1994; S. Fan et al., 1999). Moreover, the intensity of metal-support interaction plays a decisive role in the formation of carbon nanotubes mechanism either by tip-growth or base-growth mode. Tip-growth mode will be more pronounced for

catalysts having weak metal support interaction and metal particles will be lifted up by the growing carbon nanotubes. On the other hands, for the catalysts having strong metal-support interaction, base-growth mode will be more pronounced in the formation of carbon nanotubes (Saraswat & Pant, 2011). Therefore, CNTs with hollow internal channel having open end structure and no Ni particles at the tip are more prominent for CS5 (Figure 4.28(c,d)), which can be attributed to its strong metal-support interaction as discussed in TPR-H<sub>2</sub> results. Thus, indicates that base-growth mechanism was more pronounced for CS5 instead of tip growth model. Furthermore, previous studies suggested that the cracking of hydrocarbon on Ni based catalysts will lead to the production of filamentous (whisker-like) and encapsulating (shell-like) carbon species. However, it was reported that in terms of degree of toxicity, the former is considered less toxic from the point of view of deactivation process (D. Chen et al., 2001; Frusteri et al., 2002; Tsang et al., 1995), while the latter has serious influence on the deactivation of the catalysts by decreasing the total number of active sites. In the present study, all of the spent catalysts indicate the presence of filamentous type of carbon rather than encapsulating carbon species and previous studies suggested that this type of carbon does not cause major deactivation (Arbag et al., 2010; D. Chen et al., 2001; Montoya et al., 2000; Tomishige et al., 1999; Tomishige et al., 1998). This conclusion matches well with the present study that the catalysts indicating the presence of whisker-like carbon species does not exhibited deactivation and were quite stable during the reaction period. Furthermore, severe deactivation exhibited by pure Ni nanoparticles can be attributed to the existence of strong agglomeration of Ni particles as described in the FESEM images (Figure 4.28(e,f)).





**Figure 4.27:** TEM and FESEM images of spent catalysts (a,b) CS1 and (c,d) CS2 after the dry reforming reaction at 750 °C.



**Figure 4.28:** TEM images of spent catalysts (a,b) CS3, (c,d) CS5 and FESEM images of Ni (e,f) after the dry reforming reaction at 750 °C.

## 4.9 Summary

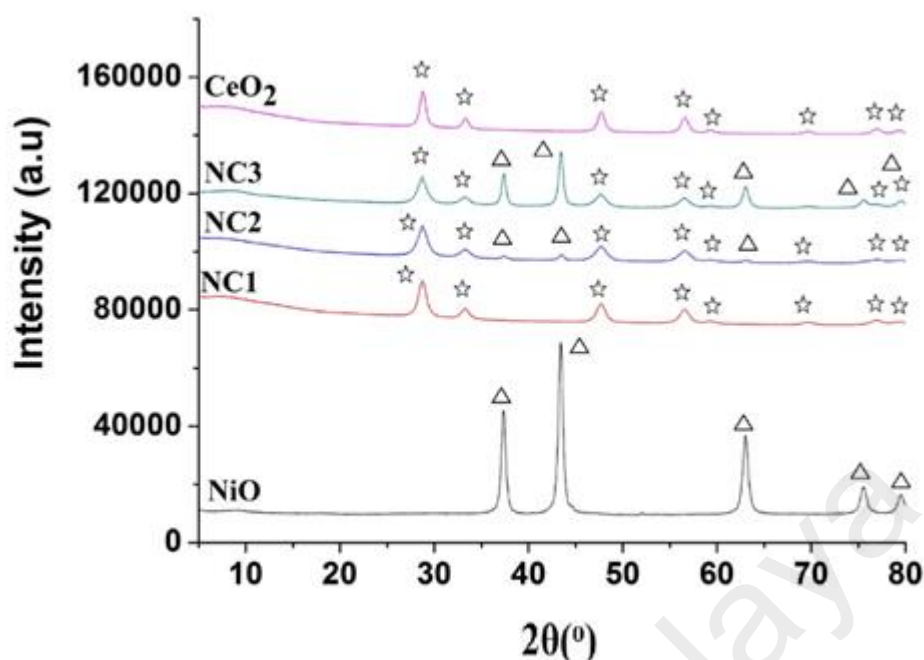
The increase of calcination temperature increased the strength of NiO-MgO solid solution and also the higher Ni content played an important role in the higher performance of catalyst. Moreover, the application of higher reduction temperature leads to the lower catalytic activity as the catalyst more prone to sintering.

### **Part 3: Water-in-oil microemulsion synthesis of Ni@CeO<sub>2</sub> core-shell like structures for dry reforming of methane.**

#### **4.10 Characterization of fresh catalyst**

##### **4.10.1 X-ray diffraction**

The powder X-ray diffraction of the prepared catalysts are shown in Figure 4.29. Pure NiO nanoparticles exhibited reflections at  $2\theta$  values of  $37.28^\circ$ ,  $43.44^\circ$ ,  $63.01^\circ$ ,  $75.55^\circ$  and  $79.40^\circ$  corresponding to the crystallite phases of (111), (200), (220), (311) and (222), respectively matching with standard card of cubic NiO with JCPDS no. 01-073-1519. XRD patterns of pure CeO<sub>2</sub> and the supported catalysts (NC1, NC2 and NC3) exhibited reflections at  $28.72^\circ$ ,  $33.40^\circ$ ,  $47.65^\circ$ ,  $56.67^\circ$ ,  $59.28^\circ$ ,  $69.64^\circ$ ,  $76.98^\circ$  and  $79.1^\circ$  corresponding to (111), (200), (220), (311) (222), (400), (331) and (420) phases matching with distinct fluorite type oxide structure of CeO<sub>2</sub> (JCPDS no. 34-0394). Moreover, for NC2 and NC3 catalyst, peaks observed at  $2\theta$  values of  $37.42^\circ$ ,  $43.46^\circ$ ,  $62.95^\circ$  and  $75.51^\circ$  were assigned to NiO phases. With the increase of metal content for the supported catalysts, an increase in the crystallite size occurred, which matches well with the BET results as decrease in surface area was also observed (Table 4.8). For NC1, no NiO peaks were observed, however, for NC2 three small blunt peaks were observed at  $2\theta$  values of  $37.28^\circ$ ,  $43.44^\circ$  and  $63.01^\circ$  indicating that almost all the NiO is dissolved in CeO<sub>2</sub>. Similar type of results was reported for Ni/CeO<sub>2</sub> catalyst prepared by impregnation that only small intensity peaks were observed at  $2\theta$  values of  $37.25^\circ$ ,  $43.28^\circ$  and  $62.88^\circ$  corresponding to (111), (200) and (220) reflections indicating that NiO dissolved in CeO<sub>2</sub> (M. Yu et al., 2015). However, in case of NC3 the presence of strong NiO peaks indicates that not all the NiO particles are dissolved by CeO<sub>2</sub> in NC3 catalyst and still free NiO particle exist in the catalyst.



**Figure 4.29:** XRD patterns of calcined catalysts, where (☆), and (Δ) presents  $\text{CeO}_2$  peaks and NiO crystallite peaks, respectively.

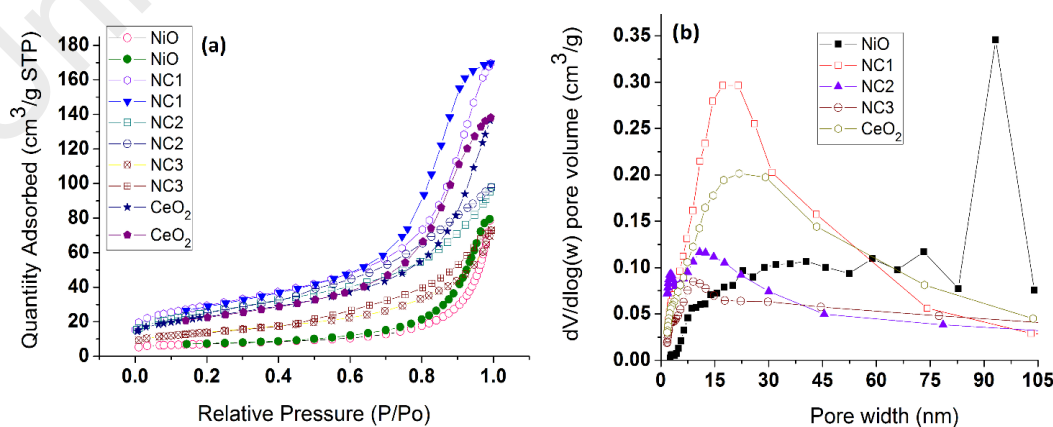
#### 4.10.2 Surface area and pore volume

The evolution of the pore structure of the catalysts were investigated by  $\text{N}_2$  adsorption-desorption measurements at 77K. The supported catalysts (NC1, NC2 and NC3) having different Ni metal content exhibited a type IV adsorption isotherm typical for mesoporous materials with type H3 hysteresis loop at the higher relative pressure indicates the formation of large pore volumes as shown in Figure 4.30(a). (Zanganeh et al., 2013). The encapsulation of Ni nanoparticles by the addition of  $\text{CeO}_2$  shell promotes the diffusion of feed gas ( $\text{CH}_4$  and  $\text{CO}_2$ ) molecules to Ni core and also  $\text{N}_2$  molecules diffusion. Previous studies suggested that surface area of core-shell like structures were influenced by both core particle size as well as the shell characteristics (thickens and porosity) (Yao et al., 2010; Zheng et al., 2014). There was seen a decrease in surface area and total pore volume from  $104.26 \text{ m}^2/\text{g}$  and  $0.263 \text{ cm}^3/\text{g}$  to  $49.36 \text{ m}^2/\text{g}$  and  $0.112 \text{ cm}^3/\text{g}$  with the increase of Ni content from 20 wt% to 80 wt%, respectively. Large surface area of NC1 can be attributed to the thicker  $\text{CeO}_2$  shell due to the higher cerium content (80 wt%). Similar types of results were reported for core-shell catalysts in which nano- $\text{Fe}_2\text{O}_3$ ,

nano-NiO, nano-RuO<sub>2</sub> were encapsulated by SiO<sub>2</sub> and nano-Fe<sub>2</sub>O<sub>3</sub> by Al<sub>2</sub>O<sub>3</sub> shell also (Yao et al., 2010). Nano-NiO@SiO<sub>2</sub>, nano-Fe<sub>2</sub>O<sub>3</sub>@SiO<sub>2</sub>, nano-RuO<sub>2</sub>@SiO<sub>2</sub> and nano-Fe<sub>2</sub>O<sub>3</sub>@Al<sub>2</sub>O<sub>3</sub> exhibited BET surface area of 112 m<sup>2</sup>/g, 34 m<sup>2</sup>/g, 42 m<sup>2</sup>/g and 38 m<sup>2</sup>/g. The higher surface area for Nano-NiO@SiO<sub>2</sub> was attributed to the thicker SiO<sub>2</sub> shell. BJH pore size distribution curve confirm the uniform pore size distribution centered around 22 nm, 13 nm and 8 nm for NC1, NC2 and NC3, respectively. The pore size distribution centered at 20 nm for NC1 is attributed to the mesopores between interparticles. Furthermore, NC2 exhibited peak at lower pore width centered at 2.5 nm, which are considered as inner pore and larger pore size (13 nm) correspond to mesopores between interparticles (J. Liu et al., 2010; Ma et al., 2012). Pore size distribution of catalysts was determined by Barret-Joyner-Halenda (BJH) method based on adsorption branch of N<sub>2</sub> isotherm as shown in Figure 4.30(b).

**Table 4.8:** BET surface area, total pore volume and average XRD crystallite size of catalysts.

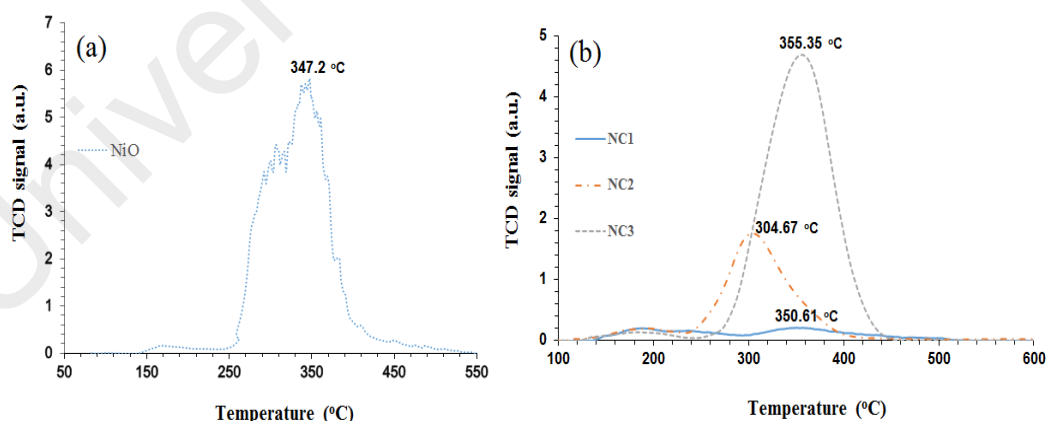
Catalyst	BET SA m <sup>2</sup> /g	Pore volume cm <sup>3</sup> /g	BET pore size (nm)	Average crystallite size (nm)
NiO	23.87	0.121	20.36	27.58
CeO <sub>2</sub>	81.50	0.213	10.48	34.53
NC1	104.63	0.263	10.02	27.14
NC2	91.48	0.151	6.60	30.52
NC3	49.36	0.112	9.14	31.88



**Figure 4.30:** (a) N<sub>2</sub> adsorption-desorption isotherms and (b) BJH pore width distribution of calcined catalysts.

#### 4.10.3 Temperature-programmed reduction

In order to understand the reducibility characteristics of catalysts, temperature-programmed reduction studies (TPR-H<sub>2</sub>) were performed. TPR-H<sub>2</sub> profiles for all catalysts exhibited two reduction peaks: one at low temperature in the range of 180-195 °C and other at quite high temperature in the range of 300-360 °C. Previous studies suggested that the peaks observed at lower reduction temperature (180-195 °C) indicates the reduction of adsorbed oxygen, which is susceptible to reduction by H<sub>2</sub> at these temperature ranges (Ay & Üner, 2015; Italiano et al., 2015). Pure NiO nanoparticles exhibited higher H<sub>2</sub> uptake indicating the higher reducibility of bulk NiO as shown in Figure 4.31(a). However, the presence of higher reduction temperature peaks (300-360 °C) can be attributed to the reduction of strongly interacting NiO species with CeO<sub>2</sub> support as shown in Figure 4.31(b). The presence of higher reduction peak at 355.35 °C for NC3 is the indication of strong metal-support interaction compared to NC1 and NC2 (Du et al., 2012). Moreover, higher H<sub>2</sub> consumption refers to the availability of higher NiO species for reduction, which can be attributed to the higher NiO content (80 wt%).

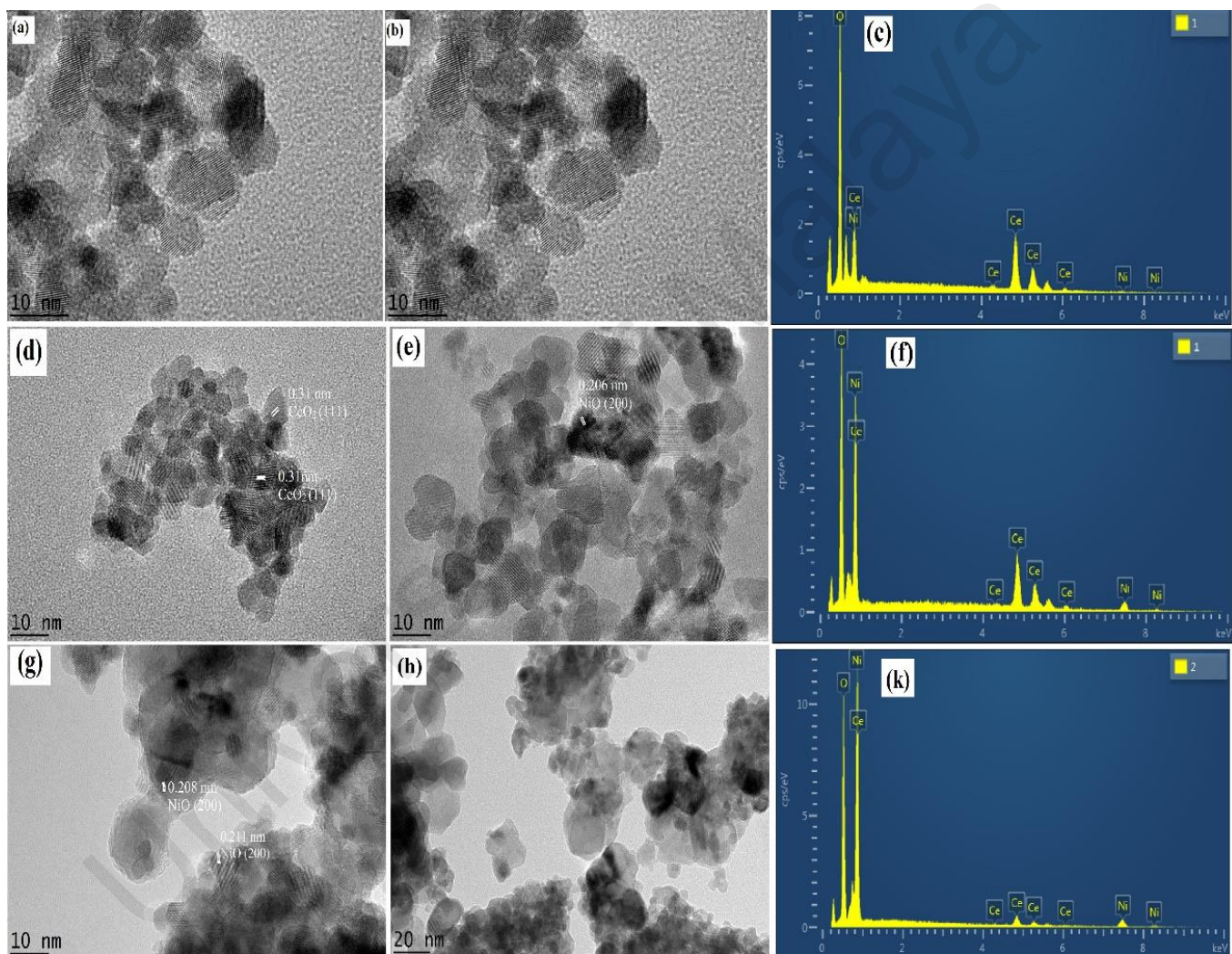


**Figure 4.31:** TPR-H<sub>2</sub> profiles of (a) NiO and (b) Ni@CeO<sub>2</sub> catalysts.

#### 4.10.4 Transmission electron microscopy

TEM images for NC1, NC2 and NC3 catalysts clearly indicates the formation of core-shell like structures in which Ni nanoparticles are encapsulated in a CeO<sub>2</sub> shell. The literature suggests that morphology of these encapsulated catalysts not only depend on core nature (size and dispersion of cores), but also on the shell thickness used to encapsulate cores. Therefore, the accessibility of core increases with the decrease of shell thickness such as in case of NC2 and NC3 having lower CeO<sub>2</sub> compared to NC1. However, as the Ni content increases, the chances of agglomeration and sintering also increases. Therefore, the proper balance between core metal and metal oxide content employed to encapsulate is important for better catalyst performance as the catalyst should have higher accessibility and lower agglomeration. For NC2 and NC3, Ni cores were prominent and visible in the form of dark spots covered by CeO<sub>2</sub> shell as confirmed by the TEM images and evident by lattice fringe spacing of 0.206 and 0.208 corresponding to the 200 facet of NiO species as shown in Figure 4.32(e, g, h). Furthermore, NiO species were also present on the edges (0.211 nm corresponds to 200 facet) suggesting that not all NiO species were dissolved by CeO<sub>2</sub>, which matches well with XRD results.



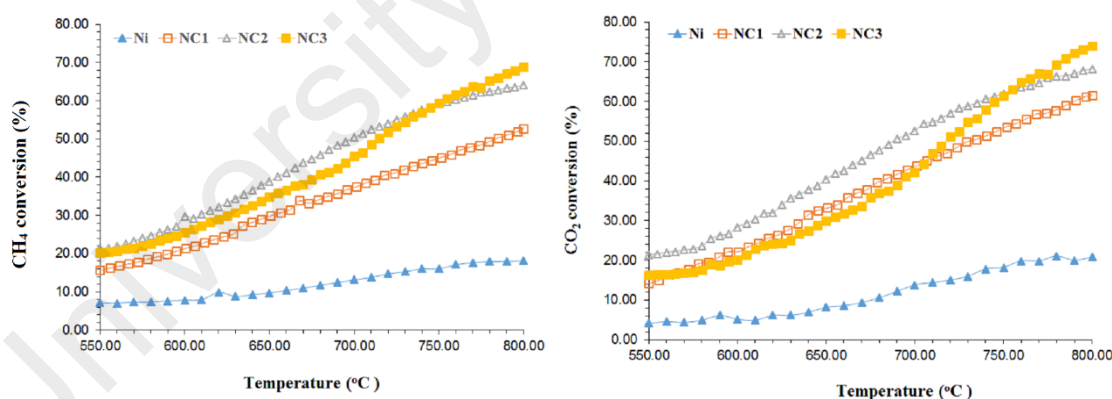


**Figure 4.32:** TEM images of freshly calcined catalysts (a,b,c) NC1 and (d,e,f) NC2, (g,h,k) NC3.



#### 4.11 Activity and stability test

Methane and carbon dioxide conversions for the supported catalysts (NC1, NC2 and NC3) and pure Ni is shown in Figure 4.33. The study exhibited that the increase of reaction temperature leads to the increase in reactants conversion ( $\text{CH}_4$  and  $\text{CO}_2$ ) due to the endothermic nature of dry reforming reaction. Catalytic activity of both NC2 and NC3 increased with temperature; with NC1 exhibited 52.71% and 61.60%, NC2 exhibited 64.12% and 68.20%, while NC3 exhibited 68.85% and 74.00% methane and carbon dioxide conversion at 800 °C, respectively. NC2 (40% Ni@CeO<sub>2</sub>) exhibited higher reactants conversion compared to NC1 and NC3 until 750 °C as shown in Figure 4.33. However, with the further increase of temperature (> 750 °C) an increase in  $\text{CH}_4$  and  $\text{CO}_2$  conversion was observed. Moreover,  $\text{CO}_2$  conversion for NC3 was lower than NC1 until 700 °C, even though it has higher Ni<sup>0</sup> active sites compared to NC1 and after 700 °C, the carbon dioxide conversion increased. Ni nanoparticles exhibited 18.13%  $\text{CH}_4$  and 20.80%  $\text{CO}_2$  conversion at 800 °C reaction temperature.



**Figure 4.33:** Conversion-temperature relationship of different catalysts (Reaction conditions:  $\text{CH}_4/\text{CO}_2 = 1/1$  and  $\text{WHSV} = 1.20 \times 10^5 \text{ ml g}^{-1} \text{ h}^{-1}$ ).

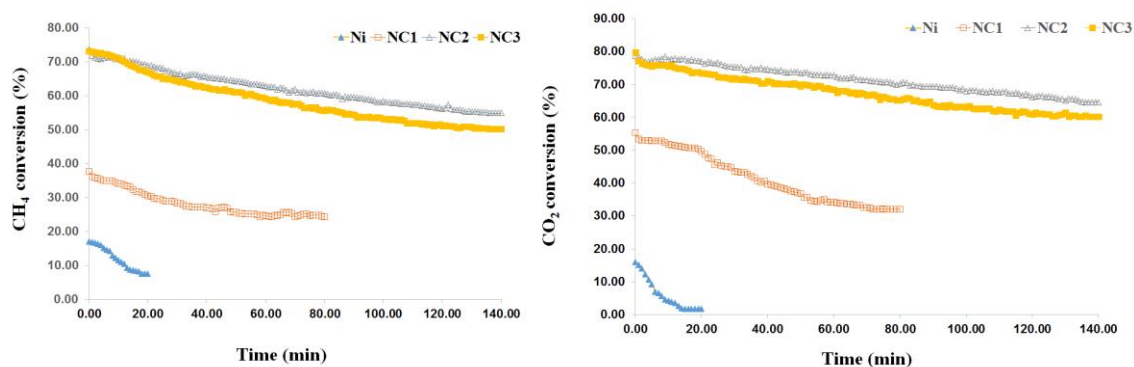
The stability of supported catalysts was studied at 800 °C, 1 atm, WHSV of  $1.2 \times 10^5 \text{ ml h}^{-1} \text{ g}^{-1}$  and at stoichiometric ratio of reactants ( $\text{CH}_4/\text{CO}_2 = 1/1$ ). The study exhibited that NC2 has higher stability and catalytic activity compared to NC1 and NC3 as shown in Figure 4.34. NC2 exhibited 54.92%  $\text{CH}_4$  and 64.60%  $\text{CO}_2$  final conversion after 140

min of reaction time, which was higher than NC1 (24.29% CH<sub>4</sub> and 32.00% CO<sub>2</sub>) and NC3 (50.31% CH<sub>4</sub> and 60.20% CO<sub>2</sub>) as mentioned in Table 4.9. Moreover, NC1 exhibited rapid decrease in both methane and carbon dioxide conversion within 80 min of reaction time. Moreover, the carbon deposition after the stability test at 800 °C was 1.00 g<sub>c</sub>/g<sub>cat</sub> for NC2, which was lower than NC3 exhibiting 1.480 g<sub>c</sub>/g<sub>cat</sub>. However, NC1 exhibited much lower carbon deposition (0.100 g<sub>c</sub>/g<sub>cat</sub>) but the deactivation was much faster and lower catalytic activity was observed. The highest catalytic activity and stability of NC2 can be attributed to its lower carbon deposition and better coverage of CeO<sub>2</sub> shell to resist agglomeration and sintering of Ni core particles. However, as discussed previously in XRD result of fresh NC3 catalyst indicated the presence of free NiO species not dissolved in CeO<sub>2</sub> due to its high Ni content (80%). Therefore, the presence of free NiO species will increase the chances of sintering and coalescence as the reforming reaction will take place. This will lead to the lower accessibility of Ni active sites (Abasaeed et al., 2015) and in turn lower catalytic activity and stability was observed together with higher carbon deposition.

**Table 4.9:** Activity and stability of Ni@CeO<sub>2</sub> catalysts at CH<sub>4</sub>/CO<sub>2</sub> =1/1 and WHSV= 1.20 x 10<sup>5</sup> ml g<sup>-1</sup> h<sup>-1</sup>

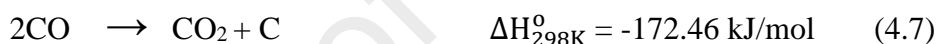
Catalyst	Treac(°C)	Initial % Conv.		Final % Conv.		Carbon (g <sub>c</sub> /g <sub>cat</sub> )
		CH <sub>4</sub>	CO <sub>2</sub>	CH <sub>4</sub>	CO <sub>2</sub>	
NC1	800	37.74	55.26	24.29	32.00	0.100
NC2	750	72.09	76.60	48.89	56.40	1.472
	800	73.59	78.80	54.92	64.60	1.00
NC3	750	72.00	70.40	47.18	54.40	2.840
	800	73.22	79.80	50.31	60.20	1.480
Ni <sup>a</sup>	800	17.10	16.04	7.49	1.72	0.026

a: final methane and carbon conversion after 20 min; Treac: reaction temperature.



**Figure 4.34:** Conversion-time relationship of different catalysts (Reaction conditions: 800 °C, CH<sub>4</sub>/CO<sub>2</sub> = 1/1, WHSV = 1.20 x 10<sup>5</sup> ml g<sup>-1</sup> h<sup>-1</sup>).

Carbon deposition in dry reforming reaction is attributed to the occurrence of methane decomposition and CO disproportionation (Khajenoori et al., 2014) reactions as described in equations 4.6 and 4.7:



It is suggested that with the rise of temperature, equilibrium constant of CO disproportionation reaction exponentially decreases, which in turn suggest that carbon deposition from this source is increasing unlikely at this higher reaction temperatures (800 °C) (Djinović et al., 2011; P Frontera et al., 2013; S. Wang et al., 1996; J. Zhang et al., 2008). However, equilibrium constant for methane decomposition was seen to increase with the rise of temperature, making this source a major reason for carbon deposition (Djinović et al., 2011; J. Zhang et al., 2008).

Ceria is believed to prevent the catalyst from deactivating as it has higher thermal stability, oxygen storage capacity and oxygen transfer ability (Rad et al., 2016). Therefore, during the reforming reaction, ceria goes through continuous Ce<sup>4+</sup>/Ce<sup>3+</sup> redox cycle supplying mobile surface oxygen (Djinović, Batista, et al., 2012; Özkara-Aydınoglu et al., 2009), which enhances the catalyst cleaning ability of surface from carbon deposited on Ni by methane decomposition (Djinović, Batista, et al., 2012; Özkara-



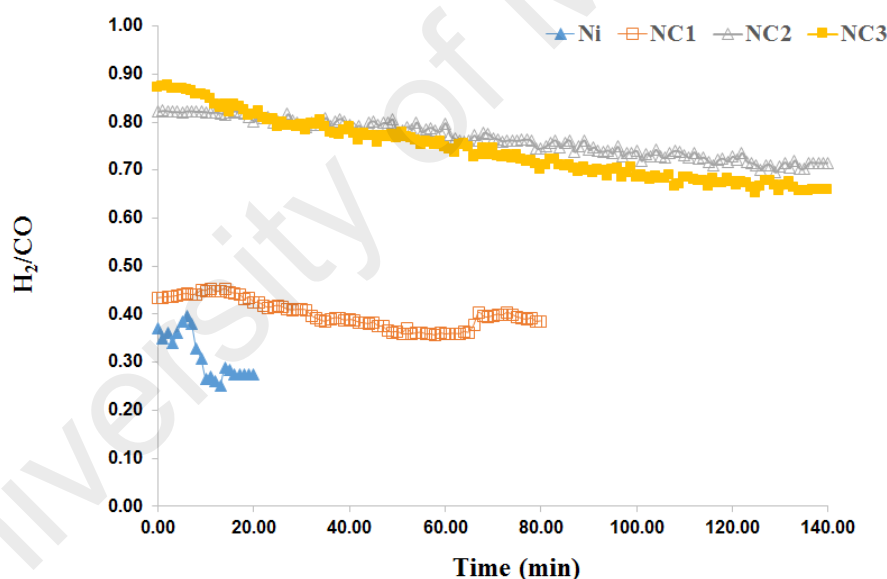
It is reported that with the rise of reaction temperature oxygen-ion conductivity (i.e., mobility of lattice oxygen) increases leading to higher catalytic activities. Similar type of results was reported for CO<sub>2</sub> dissociation over Ni supported over SDC and GDC (Huang & Yu, 2005). They reported that oxygen-ion conductivity increased with the rise of reaction temperature from 450 °C to 500 °C, promoting the mobility of lattice oxygen, therefore, the oxygen vacancies become available for O species produced during reaction. Similarly, in this study, the rise of reaction temperature (750 °C to 800 °C) for NC2 and NC3 catalyst, a significant decrease in carbon deposition was observed, which can be attributed to the increase mobility of lattice oxygen. Thus, leads to the increased oxidation of produced carbon species. Deactivation of catalysts occurs, provided that the rate of oxygen transfer from support to the Ni metal is less than the rate of carbon formation (Özkara-Aydinoğlu et al., 2009). Therefore, the occurrence of carbon deposition (Table 4.9) indicates that the rate of methane decomposition was higher compared to the rate of oxygen transfer to Ni surface as the oxygen transfer rate was not fast enough to oxidize the deposited carbon.

The lower catalytic activity at 800 °C for NC1 can be attributed to the lower number of Ni<sup>0</sup> active sites, as they will have limited active sites for the reactants feed gas molecules to adsorb and react. With the decrease of ceria content in NC3 catalyst, the oxygen storage capacity and oxygen transfer ability of catalyst decreased and lead to the higher carbon deposition. Therefore, the higher number of mobile surface oxygen will enhance the catalyst performance by inhibiting carbon deposition on the Ni metal surface during the reforming reaction as exhibited by NC2. Therefore, NC2 exhibited better catalyst performance having lower carbon deposition due to its unique balance between Ni active sites and CeO<sub>2</sub> quantity as both are critical components to achieve higher catalyst performance.

CO<sub>2</sub> conversions for all the catalysts during stability test were higher than methane conversion, which is attributed to the occurrence of inevitable reverse water gas shift (RWGS) reaction, a well-established primary causes for this phenomenon as shown in equation 4.9 (Djinović et al., 2011; Zanganeh et al., 2013).



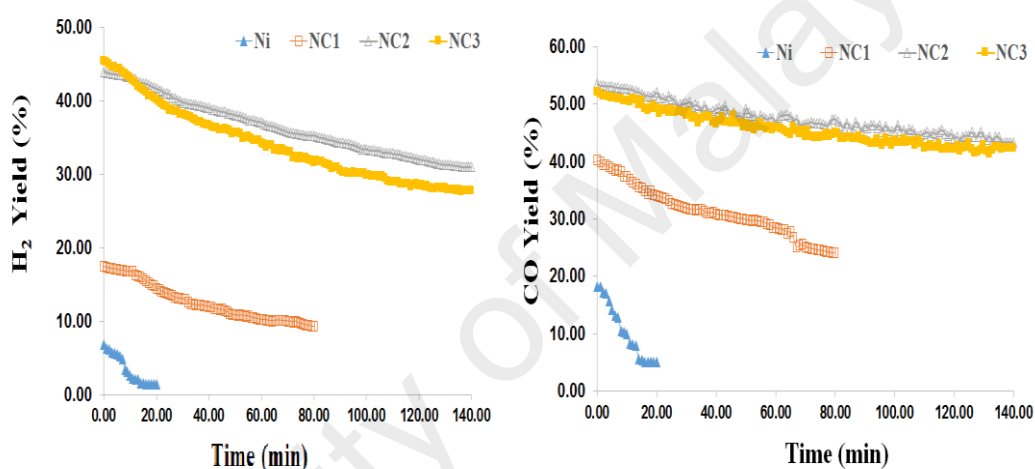
The occurrence of RWGS reaction influences the quality of produced syn-gas by lowering the H<sub>2</sub>/CO ratio below the theoretical value of unity (Djinović et al., 2011). Higher syn-gas ratio was observed for NC2 (H<sub>2</sub>/CO = 0.72) compared to NC1 (H<sub>2</sub>/CO = 0.39) and NC3 (H<sub>2</sub>/CO = 0.66) after 140 min of reaction time as shown in Figure 4.36. H<sub>2</sub>/CO ratio decreased from initial 0.43 to 0.39 for NC1, 0.82 to 0.72 for NC2 and 0.87 to 0.66 for NC3, indicating the influence of RWGS reaction.



**Figure 4.36:** H<sub>2</sub>/CO ratio of different catalysts (Reaction conditions: 800 °C, CH<sub>4</sub>/CO<sub>2</sub> =1/1, WHSV= 1.20 x 10<sup>5</sup> ml g<sup>-1</sup> h<sup>-1</sup>).

Furthermore, CO yield was always higher than H<sub>2</sub> yield as shown in Figure 4.37 for all the catalysts, due to the occurrence of RWGS reaction. The utilization of produced H<sub>2</sub> in the RWGS reaction by CO<sub>2</sub> leads to the production of higher CO and in turn higher CO<sub>2</sub> conversions are observed. The core-shell like structures performed much better than naked Ni nanoparticles. The result suggests that these encapsulated catalysts may provide

a unique core environment beneficial for the reaction. Based on the catalytic activity and stability results, we can conclude that both core properties (particle size, quantity), and shell properties (shell thickness, quantity) and also the interactions between them dictates the performance of core-shell like structures. The study indicates that in NC2 an optimal ratio of core and shell content exists, which is critical to have better coke resistance and also better catalyst performance. Therefore, it can be concluded that the excellent catalytic activity and the high coke resistance can be attributed to the high oxygen mobility and reduced sintering of Ni metal particles due to the protective CeO<sub>2</sub> shell.

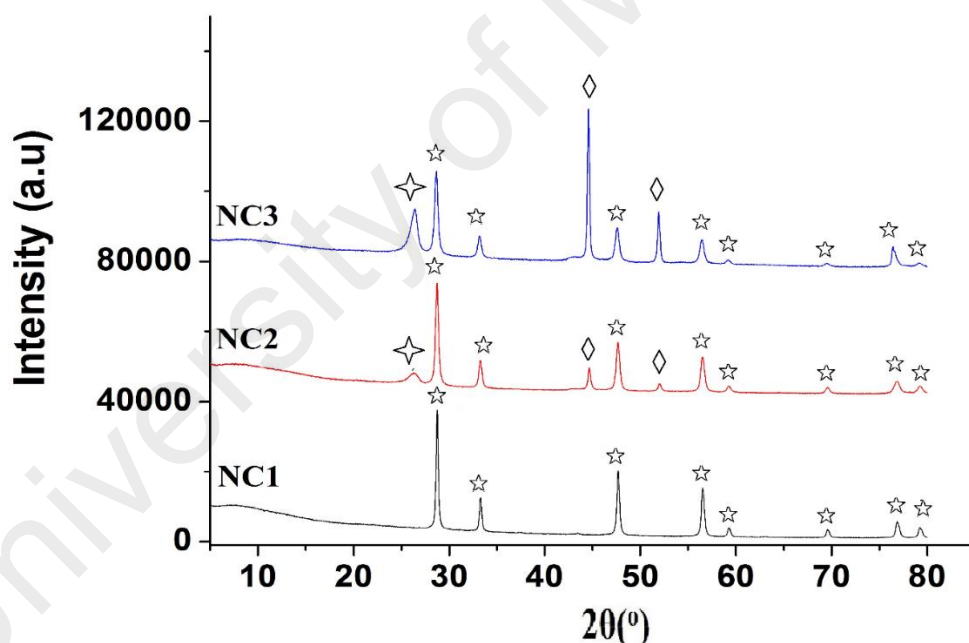


**Figure 4.37:** H<sub>2</sub> and CO yield of different catalysts (Reaction conditions: 800 °C, CH<sub>4</sub>/CO<sub>2</sub> = 1/1, WHSV = 1.20 × 10<sup>5</sup> ml g<sup>-1</sup> h<sup>-1</sup>).

#### 4.12. Characterization of spent catalyst

XRD patterns of the spent catalysts (NC2 and NC3) indicate the presence of diffraction peaks around 26°, which are attributed to the crystalline phase of CNTs matching with JCPDS no. 01-075-1621. The intensity of graphite peak was weak for NC2 compared to NC3 indicating very sharp diffraction peaks. However, no such graphite peaks were observed for NC1 as shown in Figure 4.38, which matches well with TEM results exhibiting the absence of formation of CNTs. XRD analysis of spent catalysts (NC2 and NC3) indicate the presence of Ni<sup>0</sup> peaks at 2θ values of 44.63° and 51.9° matching with JCPDS no. 01-070-1849. The intensity of Ni<sup>0</sup> peaks was strong for NC3

compared to NC2 and can be said that Ni particles were dislodged from shell, which can be seen in TEM images of spent catalysts. However, for NC1, the peaks related to  $\text{Ni}^0$  peaks were absent and Ni core particles were covered by encapsulated carbon, therefore, no Ni particles were seen. Moreover, the diffraction peaks belonging to  $\text{Ni}^0$  for the spent NC3 catalyst are sharper and narrower, which suggest occurrence of the sintering of Ni particles. The literature suggests that the sintering of metal particles during the reaction plays an important role in the decrease of catalytic activity as it reduces the number of active sites in the catalysts (Abasaheed et al., 2015). However,  $\text{Ni}^0$  peaks appear for spent NC2 catalyst are broader indicating the lower intensity of sintering. Therefore, NC2 present better stability and catalytic activity as discussed earlier compared to NC3, as it has better resistance to sintering and also has better oxygen mobility.



**Figure 4.38:** XRD analysis of spent catalysts, where (✱), (◆) and (☆) presents graphite peaks, Ni crystallite peaks,  $\text{CeO}_2$  peaks, respectively.

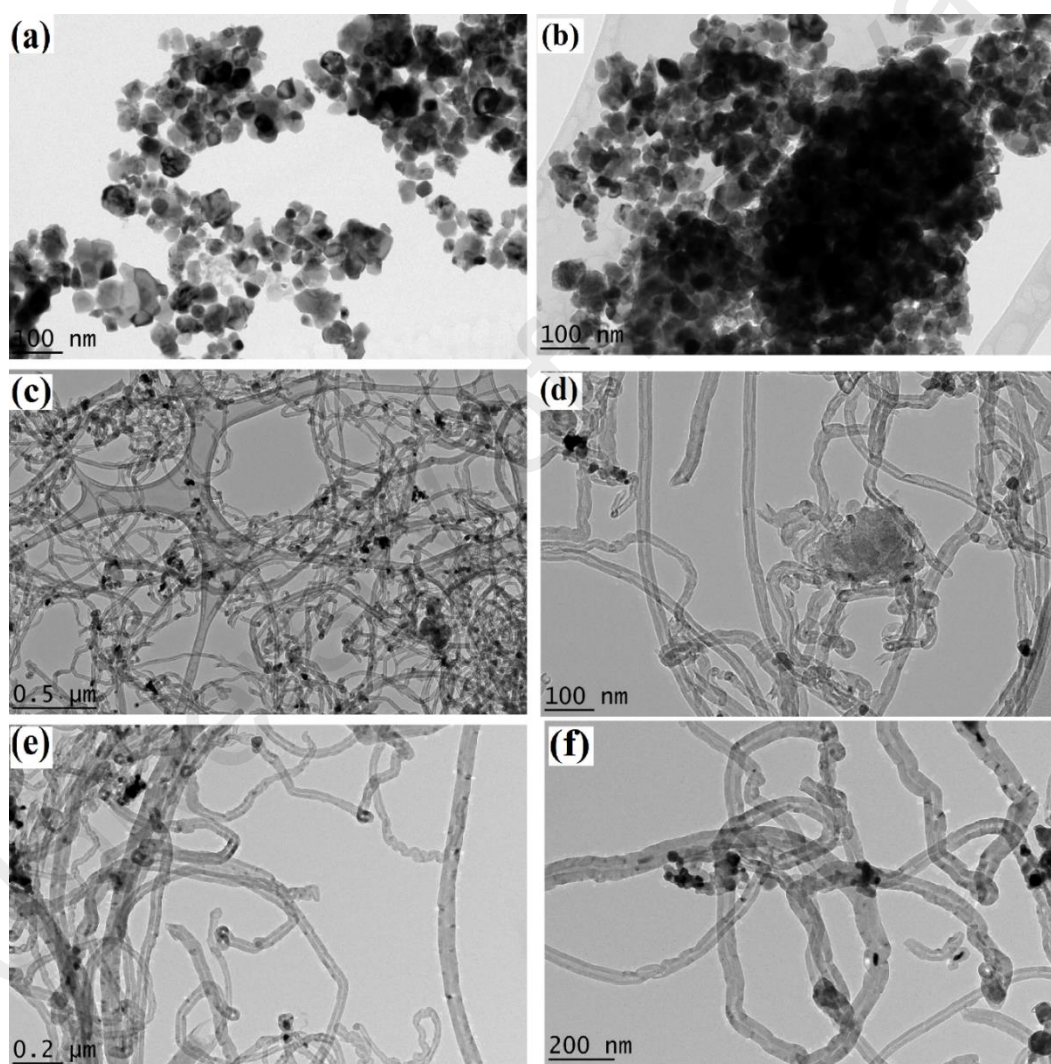
Deactivation of catalyst in dry reforming reaction is attributed to several factors such as: carbon deposition, sintering of metal particles and oxidation of metallic active sites (Ay & Üner, 2015). It has been reported that the reforming of hydrocarbons on Ni-based catalysts produces carbon deposits in the form of whisker (carbon nanotubes) and



shell-like (encapsulating) carbon species (Kroll, Swaan, et al., 1996a). TEM and FESEM images of spent catalysts (NC1, NC2, NC3 and pure Ni) after stability test indicates the presence of different type of morphology and structure of deposited carbon as exhibited in Figure 4.39 and Figure 4.40. TEM images of spent catalysts indicates the presence of very thin graphitic shell-like coke deposits encapsulating the metal particles for NC1, while for NC2 and NC3 extensive formation of filamentous coke was observed as shown in Figure 4.39.

Different morphologies of carbon nanotubes (CNTs) such as: CNTs with Ni particle at the tip, CNTs with closed end but without the presence of Ni particle on the tip, CNTs with different diameters and CNTs with hollow internal channel having open end structure and no Ni particles at the tip were observed for NC2 and NC3 catalysts. For NC1, shell-like (encapsulating) carbon species were formed and severe deactivation exhibited by NC1 can be attributed to the formation of encapsulating carbon. The shell-like carbon deposits occur due to the reason that part of the carbon formed during the early period of reforming reaction was unable to transfer in the bulk of Ni metal particles due to the relatively low diffusion rate of carbon (P. Chen et al., 1997). This leads to the blockage of Ni active sites and lower accessibility of active sites, thus severe deactivation and lower catalytic activity was observed for NC1 catalyst. Moreover, filamentous type of carbon deposits deactivates the catalyst by dislodgment of metal particles from the support to the tip of the filament (Ay & Üner, 2015). The position of metal particle in the CNTs is important for the stability of the catalyst. In this study, some of the metal particles were seen at the tip of the filaments and some were embedded in the carbon nanotubes. The previous study suggests that the condition in which metal particles are at the top of the filament, the reactants will have access to the active sites and may preserve the activity for some time. However, the situation in which the metal particles are embedded in the carbon, catalytic activity of the catalysts is seen to decrease as the reactant have lower

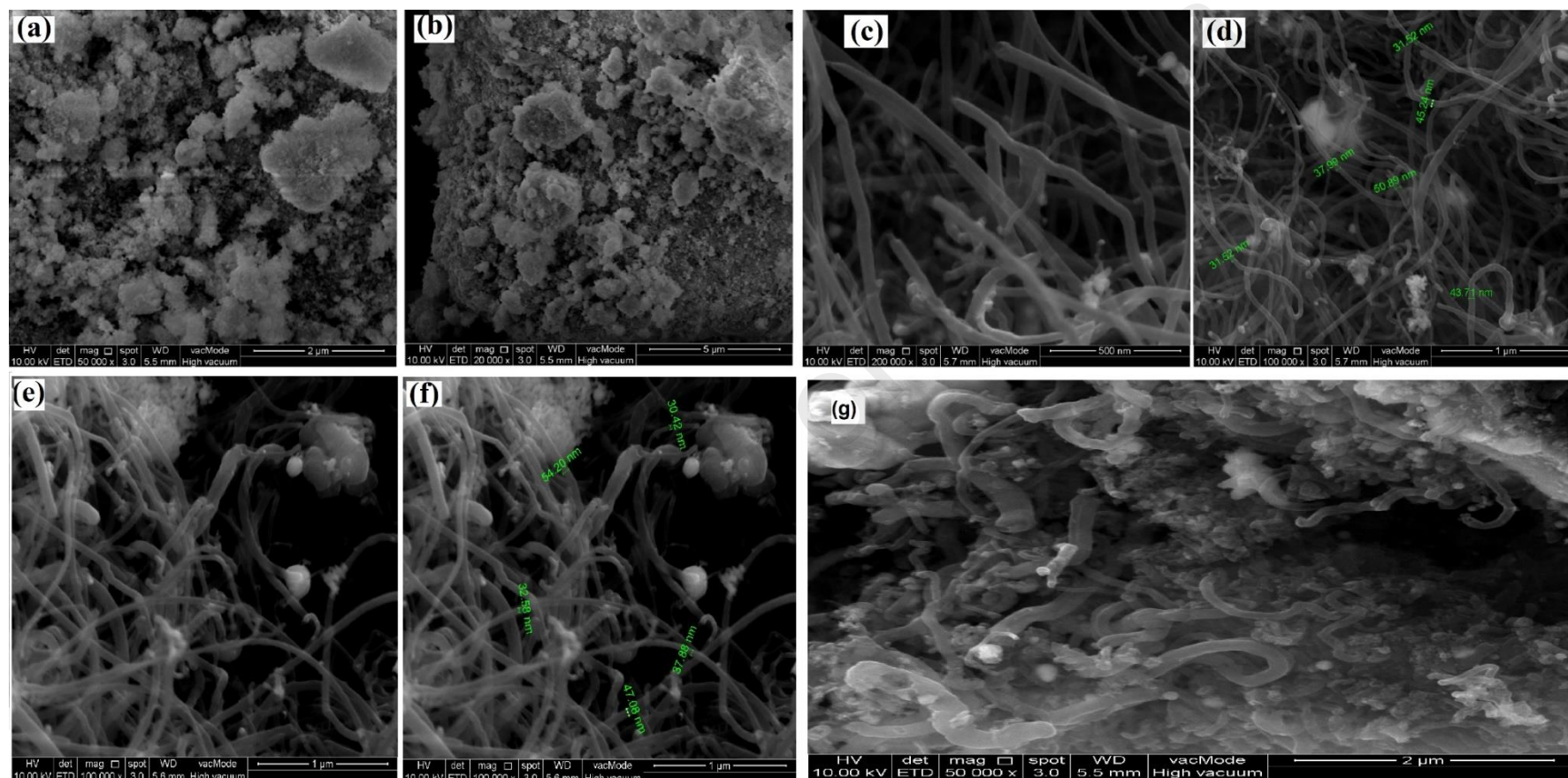
accessibility of the metal particles (San-José-Alonso et al., 2009). That is the reason, deactivation was observed for the NC2 and NC3 catalysts, however, the deactivation was not severe as in the case of encapsulating carbon. Similar type of results was reported by previous studies (D. Chen et al., 2001; Frusteri et al., 2002; Kroll, Swaan, et al., 1996a; Tsang et al., 1995), that whisker-like carbon species are less toxic compared to the shell-like carbon species, as latter has the tendency to encapsulate the Ni particles and render the active sites inaccessible for reactants.



**Figure 4.39:** TEM images of spent catalysts (a,b) NC1, (c,d) NC2 and (e,f) NC3 after stability test for 140 min at 800 °C.

TEM images indicates the homogenous distribution of carbon nanotubes having coil structure with different diameters as can be seen in FESEM images (Figure 4.40) for NC2 and NC3 catalysts. Furthermore, FESEM images of spent Ni catalyst exhibit the strong agglomeration of Ni particles and that is the reason very low catalytic activity and severe deactivation was observed.

University of Malaya



**Figure 4.40:** FESEM images of spent catalysts (a,b) NC1 and (c,d) NC2, (e,f) NC3 and (g) Ni catalysts after stability test

#### 4.13 Summary

The application of Ni@CeO<sub>2</sub> for dry reforming of methane exhibited that balance between Ni active sites (Ni content) and CeO<sub>2</sub> content played an important role on the performance of catalyst, as the presence of suitable CeO<sub>2</sub> content will lead to lower carbon deposition. It was observed that shell like carbon deposits covers the Ni active sites and makes them inaccessible for the reactants and exhibited severe deactivation as exhibited for 20% Ni@CeO<sub>2</sub>. However, the catalysts which produced whisker like carbon deposits during the catalytic activity exhibited the fact that it does not deactivates the catalyst severely.

The comparison of the catalysts (Ni/MgO (CS5) and Ni@CeO<sub>2</sub> (NC2)) exhibiting best stability among all the series of catalysts prepared as mentioned in Table 4.6 and Table 4.9 indicated that Ni@CeO<sub>2</sub> exhibited lower carbon deposition (1.00 g<sub>c</sub>/g<sub>cat</sub>) compared to MgO based catalyst (3.580 g<sub>c</sub>/g<sub>cat</sub>), also the final (CH<sub>4</sub> and CO<sub>2</sub>) conversions after 140 min was high for Ni@CeO<sub>2</sub> catalyst. However, Ni/MgO catalysts were studied at much higher WHSV (1.68 x 10<sup>5</sup> ml g<sup>-1</sup> h<sup>-1</sup>) and lower reaction temperature (750 °C) compared to Ni@CeO<sub>2</sub> studied at comparatively low WHSV (1.20 x 10<sup>5</sup> ml g<sup>-1</sup> h<sup>-1</sup>) and higher reaction temperature (800 °C). However, the fact that the carbon deposition was 3 times lower for Ni@CeO<sub>2</sub> catalyst in important factor and has more significance in dry reforming reaction. Therefore, it has better edge over Ni/MgO catalyst in the present reaction conditions.

## CHAPTER 5: CONCLUSIONS AND RECOMMENDATIONS FOR FUTURE WORK

### 5.1 Conclusions

The conclusions drawn on the basis of this study are mentioned below:

#### 5.1.1 Part 1: Synthesis of Ni nanoparticles and 20%Ni/MgO at different preparation parameters (surfactant ratio, aging time, calcination temperature, molar concentration) and investigating their catalytic activity and characterization

The investigation on the synthesis of Ni nanoparticles by microemulsion synthesis approach leads to the conclusion this synthesis approach gave better control on the particle size and morphology of Ni nanoparticles by varying the surfactant, water and oil ratios at room temperature. Lower calcination temperature, moderate aging time and lower Ni molar concentration are suitable for the achievement of higher surface area and smaller particle size. The addition of MgO in the microemulsion system for Ni/MgO catalyst exhibited higher catalytic activity compared to Ni alone, which was attributed to higher surface area, smaller particle size and lesser agglomeration of Ni particles. The investigation on the influence of calcination temperature over 20%Ni/MgO catalysts lead to the conclusion that even though strong NiO-MgO solid solution was formed at higher calcination temperature, the activity and stability of the catalysts was not enhanced. The catalyst calcined at lower temperature performed well in the activity and stability tests. The better performance was attributed to the higher surface area and higher accessibility of Ni active sites. The study suggests that the formation of strong NiO-MgO solid solution is not favourable from the perspective of catalytic activity at these synthesis conditions (20 wt% Ni). Furthermore, the study suggests that the formation of filamentous carbon on Cat1 did not cause major deactivation and the catalysts maintains its stability during the reaction time.

However, as the Ni content in Ni/MgO catalyst was increased, influence of calcination temperature on the catalytic activity was different as it was for lower Ni content (20% Ni).

### **5.1.2 Part 2: An investigation on the influence of catalyst composition, calcination and reduction temperatures on Ni/MgO catalyst for dry reforming of methane.**

In this section, the influence of Ni metal content, calcination temperature and reduction temperature was studied for dry reforming reaction. Ni/MgO catalyst (CS3) having higher Ni content (80%) exhibited better catalytic activity compared to 20%Ni/MgO (CS1) and 40%Ni/MgO (CS2) catalyst, even though it exhibited higher carbon deposition. This can be attributed to the higher number of Ni<sup>0</sup> active sites crucial for the reactants to be adsorbed and react. Even though BET results indicated that CS3 has the lower surface area (larger particle size) compared to CS1 and CS2 but this did not influence the activity and stability of the catalyst. The increase of calcination temperature from 450 °C to 800 °C for the catalyst having higher Ni content (80%) not only enhanced metal-support interaction but also lower carbon deposition was observed compared to the catalyst calcined at lower calcination temperature (450 °C). The increase of catalytic activity for the catalyst (80%Ni/MgO) calcined at higher temperature (800 °C) can be attributed to the increased number of Ni<sup>2+</sup> ions having strong interaction with MgO support and also better resistance towards sintering. The reduction of catalyst (80%Ni/MgO) at higher reduction temperature (800 °C) exhibited severe catalyst deactivation and this can be attributed to the more susceptibility of catalyst towards sintering. To sum up all the results, the key to form stable Ni/MgO catalyst prepared by microemulsion synthesis is the application of higher Ni content, higher calcination temperature and lower reduction temperature.

### **5.1.3 Part 3: Water-in-oil microemulsion synthesis of Ni@CeO<sub>2</sub> core-shell like structures for dry reforming of methane.**

In the present study, catalytic performance of Ni@CeO<sub>2</sub> catalyst were thoroughly investigated for dry reforming of methane. Two types of carbon deposits were observed such as: encapsulated or shell-like carbon deposits for 20%Ni@CeO<sub>2</sub> and whisker-like carbon species for 40%Ni@CeO<sub>2</sub> and 80%Ni@CeO<sub>2</sub>. The lower catalytic activity and deactivation of 20%Ni@CeO<sub>2</sub> was dedicated to the shell-like carbon deposits which decreases the access of reactants to active sites. The presence of higher Ni content for 40%Ni@CeO<sub>2</sub> and 80%Ni@CeO<sub>2</sub> leads to the increase of catalytic activity, however, 40%Ni@CeO<sub>2</sub> exhibited better catalyst performance due to the high CeO<sub>2</sub> content compared to 80%Ni@CeO<sub>2</sub>. The lower carbon deposition for 40%Ni@CeO<sub>2</sub> was dedicated to the increase of oxygen mobility and also CeO<sub>2</sub> provides more oxygen to Ni surface to oxidize the deposited carbon. This indicates the importance of proper choice of both Ni and CeO<sub>2</sub> content in Ni@CeO<sub>2</sub> core-shell like structures. However, the occurrence of carbon deposition indicated that the rate of methane decomposition was high compared to the rate of transfer of oxygen to Ni surface to oxidize the deposited carbon.

## **5.2 Recommendations for future work**

This project has demonstrated performance of Ni-based catalysts supported on MgO and CeO<sub>2</sub> for dry reforming reaction utilizing landfill gas (CH<sub>4</sub> and CO<sub>2</sub>) in stoichiometric ratio. However, these catalysts need more rigorous testing in the presence of impurities present in the biogas such as: chlorocarbons (chloromethane, CH<sub>3</sub>Cl) and hydrogen sulphide (H<sub>2</sub>S). The prospect of the application of small amount of noble metals (Rh, Ru, Pt or Pd) in Ni-based catalysts will be interesting and bimetallic catalysts can exhibit better performance. Furthermore, the addition of non-noble metals such as: cobalt



(Co) and iron (Fe) can be investigated in future work for the catalysts prepared via microemulsion synthesis approach. The future work can also be focused on the combination of both supports (MgO and CeO<sub>2</sub>) applied for Ni-based catalysts and also with the addition of noble metals. Thus, it will be interesting to investigate the influence of both basicity and oxygen mobility on catalytic activity of these combined catalysts.

University of Malaya

## REFERENCES

- Abasaheed, A. E., Al-Fatesh, A. S., Naeem, M. A., Ibrahim, A. A., & Fakeeha, A. H. (2015). Catalytic performance of CeO<sub>2</sub> and ZrO<sub>2</sub> supported Co catalysts for hydrogen production via dry reforming of methane. *International Journal of Hydrogen Energy*, 40(21), 6818-6826.
- Abd Kadir, S. A. S., Yin, C.-Y., Rosli Sulaiman, M., Chen, X., & El-Harbawi, M. (2013). Incineration of municipal solid waste in Malaysia: Salient issues, policies and waste-to-energy initiatives. *Renewable and Sustainable Energy Reviews*, 24(0), 181-186. doi:http://dx.doi.org/10.1016/j.rser.2013.03.041
- Abushammala, M. F., Basri, N. E. A., Basri, H., El-Shafie, A. H., & Kadhum, A. A. H. (2011). Regional landfills methane emission inventory in Malaysia. *Waste Management & Research*, 29(8), 863-873.
- Acres, K., Bird, A., Jenkins, J., & King, F. (1981). The design and preparation of supported catalysts. *Spec. Period. Rep. Catal*, 4, 1-30.
- Agrell, J., Hasselbo, K., Jansson, K., Järås, S. G., & Boutonnet, M. (2001). Production of hydrogen by partial oxidation of methanol over Cu/ZnO catalysts prepared by microemulsion technique. *Applied Catalysis A: General*, 211(2), 239-250.
- Akpan, E., Sun, Y., Kumar, P., Ibrahim, H., Aboudheir, A., & Idem, R. (2007). Kinetics, experimental and reactor modeling studies of the carbon dioxide reforming of methane (CDRM) over a new Ni/CeO<sub>2</sub>-ZrO<sub>2</sub> catalyst in a packed bed tubular reactor. *Chemical Engineering Science*, 62(15), 4012-4024.
- Al-Fatesh, A. S. A., & Fakeeha, A. H. (2012). Effects of calcination and activation temperature on dry reforming catalysts. *Journal of Saudi Chemical Society*, 16(1), 55-61. doi:http://dx.doi.org/10.1016/j.jscs.2010.10.020
- Al-Zeghayer, Y. S., & Jibril, B. (2005). On the effects of calcination conditions on the surface and catalytic properties of  $\gamma$ -Al<sub>2</sub>O<sub>3</sub>-supported CoMo hydrodesulfurization catalysts. *Applied Catalysis A: General*, 292, 287-294.
- Al-Fatish, A. S. A., Ibrahim, A. A., Fakeeha, A. H., Soliman, M. A., Siddiqui, M. R. H., & Abasaheed, A. E. (2009). Coke formation during CO<sub>2</sub> reforming of CH<sub>4</sub> over alumina-supported nickel catalysts. *Applied Catalysis A: General*, 364(1-2), 150-155. doi:10.1016/j.apcata.2009.05.043
- Amelinckx, S., Zhang, X., Bernaerts, D., Zhang, X., Ivanov, V., & Nagy, J. (1994). A formation mechanism for catalytically grown helix-shaped graphite nanotubes. *Science*, 265(5172), 635-639.

- Arbag, H., Yasyerli, S., Yasyerli, N., & Dogu, G. (2010). Activity and stability enhancement of Ni-MCM-41 catalysts by Rh incorporation for hydrogen from dry reforming of methane. *International Journal of Hydrogen Energy*, 35(6), 2296-2304. doi:10.1016/j.ijhydene.2009.12.109
- Asencios, Y. J., Bellido, J. D., & Assaf, E. M. (2011). Synthesis of NiO–MgO–ZrO<sub>2</sub> catalysts and their performance in reforming of model biogas. *Applied Catalysis A: General*, 397(1), 138-144.
- Asencios, Y. J. O., & Assaf, E. M. (2013). Combination of dry reforming and partial oxidation of methane on NiO–MgO–ZrO<sub>2</sub> catalyst: Effect of nickel content. *Fuel Processing Technology*, 106, 247-252. doi:10.1016/j.fuproc.2012.08.004
- Ashok, J., Raju, G., Reddy, P. S., Subrahmanyam, M., & Venugopal, A. (2008). Catalytic decomposition of CH<sub>4</sub> over Ni-Al<sub>2</sub>O<sub>3</sub>-SiO<sub>2</sub> catalysts: Influence of pretreatment conditions for the production of H<sub>2</sub>. *Journal of Natural Gas Chemistry*, 17(2), 113-119. doi:http://dx.doi.org/10.1016/S1003-9953(08)60036-5
- Ay, H., & Üner, D. (2015). Dry reforming of methane over CeO<sub>2</sub> supported Ni, Co and Ni–Co catalysts. *Applied Catalysis B: Environmental*, 179, 128-138.
- Bae, D. S. (2013). *Synthesis and Characterization of Ni/MgO-SiO<sub>2</sub> Catalysts for Carbon Dioxide Reforming of Methane*. Paper presented at the 9th International Conference on Fracture & Strength of Solids, Korea.
- Ballarini, A. D., de Miguel, S. R., Jablonski, E. L., Scelza, O. A., & Castro, A. A. (2005). Reforming of CH<sub>4</sub> with CO<sub>2</sub> on Pt-supported catalysts. *Catalysis Today*, 107-108, 481-486. doi:10.1016/j.cattod.2005.07.058
- Barber, K. N. (2005). Size controlled reverse micelle synthesis of metallic cobalt nanoparticles. (Master of Science), University of Oklahoma, United states. Retrieved from <http://hdl.handle.net/11244/9620>
- Barrio, L., Kubacka, A., Zhou, G., Estrella, M., Martínez-Arias, A., Hanson, J. C., . . . Rodriguez, J. A. (2010). Unusual Physical and Chemical Properties of Ni in Ce<sub>1-x</sub>Ni<sub>x</sub>O<sub>2-y</sub> Oxides: Structural Characterization and Catalytic Activity for the Water Gas Shift Reaction. *The Journal of Physical Chemistry C*, 114(29), 12689-12697. doi:10.1021/jp103958u
- Barroso-Quiroga, M. M., & Castro-Luna, A. E. (2010). Catalytic activity and effect of modifiers on Ni-based catalysts for the dry reforming of methane. *International Journal of Hydrogen Energy*, 35(11), 6052- 6056. doi: 10.1016/j.ijhydene. 2009. 12.073

- Berkovich, Y., Aserin, A., Wachtel, E., & Garti, N. (2002). Preparation of amorphous aluminum oxide-hydroxide nanoparticles in amphiphilic silicone-based copolymer microemulsions. *Journal of Colloid and Interface Science*, 245(1), 58-67.
- Bezemer, G. L., Radstake, P., Koot, V., Van Dillen, A., Geus, J., & De Jong, K. (2006). Preparation of Fischer–Tropsch cobalt catalysts supported on carbon nanofibers and silica using homogeneous deposition-precipitation. *Journal of Catalysis*, 237(2), 291-302.
- Bhavani, A. G., Kim, W. Y., Kim, J. Y., & Lee, J. S. (2012). Improved activity and coke resistance by promoters of nanosized trimetallic catalysts for autothermal carbon dioxide reforming of methane. *Applied Catalysis A: General*, 450, 63-72.
- Bobin, A., Sadykov, V., Rogov, V., Mezentseva, N., Alikina, G., Sadovskaya, E., . . . Veniaminov, S. (2013). Mechanism of CH<sub>4</sub> dry reforming on nanocrystalline doped ceria-zirconia with supported Pt, Ru, Ni, and Ni–Ru. *Topics in Catalysis*, 56(11), 958-968.
- Boccuzzi, F., Chiorino, A., Manzoli, M., Lu, P., Akita, T., Ichikawa, S., & Haruta, M. (2001). Au/TiO<sub>2</sub> nanosized samples: A catalytic, TEM, and FTIR study of the effect of calcination temperature on the CO oxidation. *Journal of Catalysis*, 202(2), 256-267. doi:http://dx.doi.org/10.1006/jcat.2001.3290
- Bommarius, A. S., Holzwarth, J. F., Wang, D. I., & Hatton, T. A. (1990). Coalescence and solubilize exchange in a cationic four-component reversed micellar system. *Journal of Physical Chemistry*, 94(18), 7232-7239.
- Boutonnet Kizling, M., Bigey, C., & Touroude, R. (1996). Novel method of catalyst preparation for selective hydrogenation of unsaturated aldehydes. *Applied Catalysis A: General*, 135(1), L13-L17. doi:http://dx.doi.org/10.1016/0926-860X(95)00278-2
- Boutonnet, M., Andersson, C., & Larsson, R. (1980). Liquid-phase hydrogenation of 1-hexene and 2-hexene with 30 Å platinum particles on alumina support. *Acta chemica scandinavica series A-physical and inorganic chemistry*, 34(9), 639-644.
- Boutonnet, M., Kizling, J., Mints-Eya, V., Choplin, A., Touroude, R., Maire, G., & Stenius, P. (1987). Monodisperse colloidal metal particles from nonaqueous solutions: Catalytic behavior in hydrogenation of but-1-ene of platinum, palladium, and rhodium particles supported on pumice. *Journal of Catalysis*, 103(1), 95-104. doi:http://dx.doi.org/10.1016/0021-9517(87)90096-0
- Boutonnet, M., Kizling, J., Stenius, P., & Maire, G. (1982). The preparation of monodisperse colloidal metal particles from microemulsions. *Colloids and surfaces*, 5(3), 209-225.

- Boutonnet, M., Lögdberg, S., & Elm Svensson, E. (2008). Recent developments in the application of nanoparticles prepared from w/o microemulsions in heterogeneous catalysis. *Current Opinion in Colloid & Interface Science*, 13(4), 270-286. doi:http://dx.doi.org/10.1016/j.cocis.2007.10.001
- Bradford, M. C. J., & Albert Vannice, M. (1999). The role of metal–support interactions in CO<sub>2</sub> reforming of CH<sub>4</sub>. *Catalysis Today*, 50(1), 87-96. doi:http://dx.doi.org/10.1016/S0920-5861(98)00465-9
- Bradford, M. C. J., & Vannice, M. A. (1999). CO<sub>2</sub> reforming of CH<sub>4</sub>. *Catalysis Reviews*, 41(1), 1-42. doi:10.1081/cr-100101948
- Brungs, A., York, A. E., Claridge, J., Márquez-Alvarez, C., & Green, M. H. (2000). Dry reforming of methane to synthesis gas over supported molybdenum carbide catalysts. *Catalysis Letters*, 70(3-4), 117-122. doi:10.1023/A:1018829116093
- Campanati, M., Fornasari, G., & Vaccari, A. (2003). Fundamentals in the preparation of heterogeneous catalysts. *Catalysis Today*, 77(4), 299-314.
- Carvalho, L. S., Martins, A. R., Reyes, P., Oportus, M., Albonoz, A., Vicentini, V., & Rangel, M. d. C. (2009). Preparation and characterization of Ru/MgO-Al<sub>2</sub>O<sub>3</sub> catalysts for methane steam reforming. *Catalysis Today*, 142(1–2), 52-60. doi:http://dx.doi.org/10.1016/j.cattod.2009.01.010
- Cason, J. P., Miller, M. E., Thompson, J. B., & Roberts, C. B. (2001). Solvent effects on copper nanoparticle growth behavior in AOT reverse micelle systems. *The Journal of Physical Chemistry B*, 105(12), 2297-2302.
- Castro Luna, A. E., & Iriarte, M. E. (2008). Carbon dioxide reforming of methane over a metal modified Ni-Al<sub>2</sub>O<sub>3</sub> catalyst. *Applied Catalysis A: General*, 343(1-2), 10-15. doi:10.1016/j.apcata.2007.11.041
- Cesteros, Y., Salagre, P., Medina, F., & Sueiras, J. E. (2000). Preparation and characterization of several high-area NiAl<sub>2</sub>O<sub>4</sub> spinels. Study of their reducibility. *Chemistry of Materials*, 12(2), 331-335.
- Chandradass, J., & Bae, D.-S. (2008). Synthesis and characterization of alumina nanoparticles by igepal CO-520 stabilized reverse micelle and sol-gel processing. *Materials and Manufacturing Processes*, 23(5), 494-498.
- Chandradass, J., Balasubramanian, M., Bae, D. S., Kim, J., & Kim, K. H. (2010). Effect of water to surfactant ratio (R) on the particle size of MgAl<sub>2</sub>O<sub>4</sub> nanoparticle prepared via reverse micelle process. *Journal of Alloys and Compounds*, 491(1), L25-L28.

- Chandradass, J., & Kim, K. H. (2009). Size-controlled synthesis of  $\text{LaAlO}_3$  by reverse micelle method: Investigation of the effect of water-to-surfactant ratio on the particle size. *Journal of Crystal Growth*, 311(14), 3631-3635.
- Chang, J.-S., Hong, D.-Y., Li, X., & Park, S.-E. (2006). Thermogravimetric analyses and catalytic behaviors of zirconia-supported nickel catalysts for carbon dioxide reforming of methane. *Catalysis Today*, 115(1-4), 186-190. doi:10.1016/j.cattod.2006.02.052
- Chen, D.-H., & Wu, S.-H. (2000). Synthesis of nickel nanoparticles in water-in-oil microemulsions. *Chemistry of Materials*, 12(5), 1354-1360. doi:10.1021/cm991167y
- Chen, D., Lødeng, R., Omdahl, K., Anundskås, A., Olsvik, O., & Holmen, A. (2001). A model for reforming on Ni catalyst with carbon formation and deactivation. *Studies in Surface Science and Catalysis*, 139, 93-100.
- Chen, J., Ma, Q., Rufford, T. E., Li, Y., & Zhu, Z. (2009). Influence of calcination temperatures of Feitknecht compound precursor on the structure of  $\text{Ni-Al}_2\text{O}_3$  catalyst and the corresponding catalytic activity in methane decomposition to hydrogen and carbon nanofibers. *Applied Catalysis A: General*, 362(1-2), 1-7. doi:http://dx.doi.org/10.1016/j.apcata.2009.04.025
- Chen, J., Wu, Q., Zhang, J., & Zhang, J. (2008). Effect of preparation methods on structure and performance of  $\text{Ni/Ce}_{0.75}\text{Zr}_{0.25}\text{O}_2$  catalysts for  $\text{CH}_4\text{-CO}_2$  reforming. *Fuel*, 87(13-14), 2901-2907. doi:10.1016/j.fuel.2008.04.015
- Chen, P., Zhang, H.-B., Lin, G.-D., Hong, Q., & Tsai, K. (1997). Growth of carbon nanotubes by catalytic decomposition of  $\text{CH}_4$  or  $\text{CO}$  on a  $\text{Ni-MgO}$  catalyst. *Carbon*, 35(10), 1495-1501.
- Chen, W., Zhao, G. F., Xue, Q. S., Chen, L., & Lu, Y. (2013). High carbon-resistance  $\text{Ni/CeAlO}_3\text{-Al}_2\text{O}_3$  catalyst for  $\text{CH}_4/\text{CO}_2$  reforming. *Applied Catalysis B: Environmental*, 136, 260-268. doi:DOI 10.1016/j.apcatb.2013.01.044
- Chen, X., Honda, K., & Zhang, Z.-G. (2005a). A comprehensive comparison of  $\text{CH}_4\text{-CO}_2$  reforming activities of  $\text{NiO/Al}_2\text{O}_3$  catalysts under fixed- and fluidized-bed operations. *Applied Catalysis A: General*, 288(1-2), 86-97. doi:10.1016/j.apcata.2005.04.037
- Chen, X., Honda, K., & Zhang, Z.-G. (2005b). A comprehensive comparison of  $\text{CH}_4\text{-CO}_2$  reforming activities of  $\text{NiO/Al}_2\text{O}_3$  catalysts under fixed-and fluidized-bed operations. *Applied Catalysis A: General*, 288(1), 86-97.

- Chen, Y.-G., Tomishige, K., & Fujimoto, K. (1997). Formation and characteristic properties of carbonaceous species on nickel-magnesia solid solution catalysts during CH<sub>4</sub>-CO<sub>2</sub> reforming reaction. *Applied Catalysis A: General*, 161(1–2), L11-L17. doi:http://dx.doi.org/10.1016/S0926-860X(97)00106-3
- Chen, Y., & Zhang, L. (1992). Surface interaction model of  $\gamma$ -alumina-supported metal oxides. *Catalysis Letters*, 12(1-3), 51-62.
- Chhabra, V., Ayyub, P., Chattopadhyay, S., & Maitra, A. (1996). Preparation of acicular  $\gamma$ -Fe<sub>2</sub>O<sub>3</sub> particles from a microemulsion-mediated reaction. *Materials Letters*, 26(1), 21-26.
- Chhabra, V., Free, M., Kang, P., Truesdail, S., & Shah, D. (1997). Microemulsions as all emerging technology: From petroleum recovery to nanoparticle synthesis of magnetic materials and superconductors. *Tenside, surfactants, detergents*, 34(3), 156-168.
- Chubb, T. A. (1980). Characteristics of CO<sub>2</sub>/CH<sub>4</sub> reforming-methanation cycle relevant to the solchem thermochemical power system. *Solar Energy*, 24(4), 341-345.
- Crisafulli, C., Scirè, S., Minicò, S., & Solarino, L. (2002). Ni–Ru bimetallic catalysts for the CO<sub>2</sub> reforming of methane. *Applied Catalysis A: General*, 225(1–2), 1-9. doi:http://dx.doi.org/10.1016/S0926-860X(01)00585-3
- D’Addato, S., Grillo, V., Altieri, S., Frabboni, S., Rossi, F., & Valeri, S. (2011). Assembly and fine analysis of Ni/MgO core/shell nanoparticles. *The Journal of Physical Chemistry C*, 115(29), 14044-14049.
- Dahlberg, K. A., & Schwank, J. W. (2012). Synthesis of Ni@SiO<sub>2</sub> nanotube particles in a water-in-oil microemulsion template. *Chemistry of Materials*, 24(14), 2635-2644. doi:10.1021/cm203779v
- de Leitenburg, C., Trovarelli, A., & Kašpar, J. (1997). A temperature-programmed and transient kinetic study of CO<sub>2</sub> activation and methanation over CeO<sub>2</sub> supported noble metals. *Journal of Catalysis*, 166(1), 98-107.
- Djaidja, A., Libs, S., Kiennemann, A., & Barama, A. (2006). Characterization and activity in dry reforming of methane on NiMg/Al and Ni/MgO catalysts. *Catalysis Today*, 113(3–4), 194-200. doi:http://dx.doi.org/10.1016/j.cattod.2005.11.066
- Djinović, P., Batista, J., & Pintar, A. (2012). Efficient catalytic abatement of greenhouse gases: Methane reforming with CO<sub>2</sub> using a novel and thermally stable Rh–CeO<sub>2</sub> catalyst. *International Journal of Hydrogen Energy*, 37(3), 2699-2707.

- Djinović, P., Črnivec, I. G. O., Batista, J., Levec, J., & Pintar, A. (2011). Catalytic syngas production from greenhouse gasses: Performance comparison of Ru-Al<sub>2</sub>O<sub>3</sub> and Rh-CeO<sub>2</sub> catalysts. *Chemical Engineering and Processing: Process Intensification*, 50(10), 1054-1062. doi:http://dx.doi.org/10.1016/j.cep. 2011. 05. 018
- Djinović, P., Osojnik Črnivec, I. G., Erjavec, B., & Pintar, A. (2012). Influence of active metal loading and oxygen mobility on coke-free dry reforming of Ni–Co bimetallic catalysts. *Applied Catalysis B: Environmental*, 125(0), 259-270. doi:http://dx.doi.org/10.1016/j.apcatb.2012.05.049
- Dowden, D., Schnell, C., & Walker, G. (1968). *The design of complex catalysts*. Paper presented at the Proceedings of the 4th International Congress on Catalysts (Moscow)(1968) 201.
- Du, X., Zhang, D., Shi, L., Gao, R., & Zhang, J. (2012). Morphology dependence of catalytic properties of Ni/CeO<sub>2</sub> nanostructures for carbon dioxide reforming of methane. *The Journal of Physical Chemistry C*, 116(18), 10009-10016.
- Eastoe, J., Hollamby, M. J., & Hudson, L. (2006). Recent advances in nanoparticle synthesis with reversed micelles. *Advances in Colloid and Interface Science*, 128, 5-15.
- Edwards, J., & Maitra, A. (1995). The chemistry of methane reforming with carbon dioxide and its current and potential applications. *Fuel Processing Technology*, 42(2), 269-289.
- Edwards, J. H., & Maitra, A. M. (1995). The chemistry of methane reforming with carbon dioxide and its current and potential applications. *Fuel Processing Technology*, 42(2–3), 269-289. doi:http://dx.doi.org/10.1016/0378-3820(94)00105-3
- Effendi, A., Hellgardt, K., Zhang, Z. G., & Yoshida, T. (2003). Characterisation of carbon deposits on Ni/SiO<sub>2</sub> in the reforming of CH<sub>4</sub>–CO<sub>2</sub> using fixed- and fluidised-bed reactors. *Catalysis Communications*, 4(4), 203-207. doi:10.1016/s1566-7367(03) 00034-7
- Eriksson, S., Nylén, U., Rojas, S., & Boutonnet, M. (2004). Preparation of catalysts from microemulsions and their applications in heterogeneous catalysis. *Applied Catalysis A: General*, 265(2), 207-219. doi:http://dx.doi.org/ 10.1016/j.apcata. 2004.01.014
- Fallah, B., & Falamaki, C. (2010). A new nano-(2Li<sub>2</sub>O/MgO) catalyst/porous alpha-alumina composite for the oxidative coupling of methane reaction. *AIChE Journal*, 56(3), 717-728.



- Fan, M.-S., Abdullah, A. Z., & Bhatia, S. (2010). Utilization of greenhouse gases through carbon dioxide reforming of methane over Ni–Co/MgO–ZrO<sub>2</sub>: Preparation, characterization and activity studies. *Applied Catalysis B: Environmental*, 100(1-2), 365-377. doi:10.1016/j.apcatb.2010.08.013
- Fan, S., Chapline, M. G., Franklin, N. R., Tombler, T. W., Cassell, A. M., & Dai, H. (1999). Self-oriented regular arrays of carbon nanotubes and their field emission properties. *Science*, 283(5401), 512-514.
- Fendler, J. H. (1987). Atomic and molecular clusters in membrane mimetic chemistry. *Chemical Reviews*, 87(5), 877-899.
- Feng, J., Ding, Y., Guo, Y., Li, X., & Li, W. (2012). Calcination temperature effect on the adsorption and hydrogenated dissociation of CO<sub>2</sub> over the NiO/MgO catalyst. *Fuel*, 109, 110-115. doi:http://dx.doi.org/10.1016/j.fuel.2012.08.028
- Fogler, H. S. (1986). *Elements of chemical reaction engineering*. Englewood Cliffs, New Jersey: Prentice-Hall.
- Fraenkel, D., Levitan, R., & Levy, M. (1986). A solar thermochemical pipe based on the CO<sub>2</sub>/ CH<sub>4</sub> (1: 1) system. *International Journal of Hydrogen Energy*, 11(4), 267-277.
- Frontera, P., Aloise, A., Macario, A., Antonucci, P. L., Crea, F., Giordano, G., & Nagy, J. B. (2010). Bimetallic zeolite catalyst for CO<sub>2</sub> reforming of methane. *Topics in Catalysis*, 53(3-4), 265-272. doi:10.1007/s11244-009-9409-8
- Frontera, P., Macario, A., Aloise, A., Antonucci, P., Giordano, G., & Nagy, J. (2013). Effect of support surface on methane dry-reforming catalyst preparation. *Catalysis Today*, 218, 18-29.
- Frusteri, F., Spadaro, L., Arena, F., & Chuvilin, A. (2002). TEM evidence for factors affecting the genesis of carbon species on bare and K-promoted Ni/MgO catalysts during the dry reforming of methane. *Carbon*, 40(7), 1063-1070.
- Fu, X., & Qutubuddin, S. (2001). Polymer–clay nanocomposites: exfoliation of organophilic montmorillonite nanolayers in polystyrene. *Polymer*, 42(2), 807-813.
- Gadalla, A. M., & Bower, B. (1988). The role of catalyst support on the activity of nickel for reforming methane with CO<sub>2</sub>. *Chemical Engineering Science*, 43(11), 3049-3062.

- Gangadharan, P., Kanchi, K. C., & Lou, H. H. (2012). Evaluation of the economic and environmental impact of combining dry reforming with steam reforming of methane. *Chemical Engineering Research and Design*, 90(11), 1956-1968. doi:http://dx.doi.org/10.1016/j.cherd.2012.04.008
- Ganguli, A. K., Ganguly, A., & Vaidya, S. (2010). Microemulsion-based synthesis of nanocrystalline materials. *Chemical Society Reviews*, 39(2), 474-485.
- Ganguly, A., Trinh, P., Ramanujachary, K., Ahmad, T., Mugweru, A., & Ganguli, A. K. (2011). Reverse micellar based synthesis of ultrafine MgO nanoparticles (8–10nm): Characterization and catalytic properties. *Journal of Colloid and Interface Science*, 353(1), 137-142.
- García-Diéguez, M., Finocchio, E., Larrubia, M. Á., Alemany, L. J., & Busca, G. (2010). Characterization of alumina-supported Pt, Ni and PtNi alloy catalysts for the dry reforming of methane. *Journal of Catalysis*, 274(1), 11-20. doi:10.1016/j.jcat.2010.05.020
- García, V., Fernández, J. J., Ruíz, W., Mondragón, F., & Moreno, A. (2009). Effect of MgO addition on the basicity of Ni/ZrO<sub>2</sub> and on its catalytic activity in carbon dioxide reforming of methane. *Catalysis Communications*, 11(4), 240-246.
- Guczi, L., Stefler, G., Geszti, O., Sajó, I., Pászti, Z., Tompos, A., & Schay, Z. (2010). Methane dry reforming with CO<sub>2</sub>: A study on surface carbon species. *Applied Catalysis A: General*, 375(2), 236-246.
- Guo, J., Lou, H., & Zheng, X. (2007). The deposition of coke from methane on a Ni/MgAl<sub>2</sub>O<sub>4</sub> catalyst. *Carbon*, 45(6), 1314-1321.
- Haber, J., Block, J., & Delmon, B. (1995). Manual of methods and procedures for catalyst characterization. *Pure and Applied Chemistry*, 67, 1257-1257.
- Hagen, J. (1999). Heterogeneous catalysis: Fundamentals. *Industrial Catalysis: A Practical Approach, Second Edition*, 99-222.
- Hamley, I. W. (2007). Amphiphiles *Introduction to Soft Matter* (pp. 161-220): John Wiley & Sons, Ltd.
- Han, D., Yang, H. Y., & Shen, C. (2005). Preparation of size controllable MgO nanoparticles via reverse microemulsion method. Paper presented at the Materials Science Forum.

- Hanaoka, T., Kim, W.-Y., Kishida, M., Nagata, H., & Wakabayashi, K. (1997). Enhancement of CO hydrogenation activity of Rh/SiO<sub>2</sub> with low rhodium content. *Chemistry Letters*(7), 645-646.
- Hao, Z., Zhu, Q., Jiang, Z., Hou, B., & Li, H. (2009). Characterization of aerogel Ni/Al<sub>2</sub>O<sub>3</sub> catalysts and investigation on their stability for CH<sub>4</sub>-CO<sub>2</sub> reforming in a fluidized bed. *Fuel Processing Technology*, 90(1), 113-121. doi:10.1016/j.fuproc. 2008. 08. 004
- Hao, Z., Zhu, Q., Jiang, Z., & Li, H. (2008). Fluidization characteristics of aerogel Co/Al<sub>2</sub>O<sub>3</sub> catalyst in a magnetic fluidized bed and its application to CH<sub>4</sub>-CO<sub>2</sub> reforming. *Powder Technology*, 183(1), 46-52. doi:10.1016/j.powtec.2007.11. 015
- Hao, Z., Zhu, Q., Lei, Z., & Li, H. (2008). CH<sub>4</sub>-CO<sub>2</sub> reforming over Ni/Al<sub>2</sub>O<sub>3</sub> aerogel catalysts in a fluidized bed reactor. *Powder Technology*, 182(3), 474-479. doi:10.1016/j.powtec.2007.05.024
- Hayashi, H., Chen, L. Z., Tago, T., Kishida, M., & Wakabayashi, K. (2002). Catalytic properties of Fe/SiO<sub>2</sub> catalysts prepared using microemulsion for CO hydrogenation. *Applied Catalysis A: General*, 231(1), 81-89.
- Helveg, S., Sehested, J., & Rostrup-Nielsen, J. (2011). Whisker carbon in perspective. *Catalysis Today*, 178(1), 42-46.
- Horváth, A., Stefler, G., Geszti, O., Kienneman, A., Pietraszek, A., & Guczi, L. (2011). Methane dry reforming with CO<sub>2</sub> on CeZr-oxide supported Ni, NiRh and NiCo catalysts prepared by sol-gel technique: Relationship between activity and coke formation. *Catalysis Today*, 169(1), 102-111.
- Hou, Z., Chen, P., Fang, H., Zheng, X., & Yashima, T. (2006). Production of synthesis gas via methane reforming with CO on noble metals and small amount of noble-(Rh-) promoted Ni catalysts. *International Journal of Hydrogen Energy*, 31(5), 555-561. doi:http://dx.doi.org/10.1016/j.ijhydene.2005.06.010
- Hu, Y. H., & Ruckenstein, E. (2002). Binary MgO-based solid solution catalysts for methane conversion to syngas. *Catalysis Reviews*, 44(3), 423-453. doi:10.1081 /cr-120005742
- Hua, W., Jin, L., He, X., Liu, J., & Hu, H. (2010). Preparation of Ni/MgO catalyst for CO<sub>2</sub> reforming of methane by dielectric-barrier discharge plasma. *Catalysis Communications*, 11(11), 968-972. doi:10.1016/j.catcom.2010.04.007
- Huang, J., Ma, R., Huang, T., Zhang, A., & Huang, W. (2011). Carbon dioxide reforming of methane over Ni/Mo/SBA-15-La<sub>2</sub>O<sub>3</sub> catalyst: Its characterization and catalytic

performance. *Journal of Natural Gas Chemistry*, 20(5), 465-470. doi:10.1016/s1003-9953(10)60226-5

Huang, T.-J., Lin, H.-J., & Yu, T.-C. (2005). A comparison of oxygen-vacancy effect on activity behaviors of carbon dioxide and steam reforming of methane over supported nickel catalysts. *Catalysis Letters*, 105(3-4), 239-247. doi:10.1007/s10562-005-8697-2

Huang, T.-J., & Yu, T.-C. (2005). Effect of steam and carbon dioxide pretreatments on methane decomposition and carbon gasification over doped-ceria supported nickel catalyst. *Catalysis Letters*, 102(3-4), 175-181.

Huang, T., Huang, W., Huang, J., & Ji, P. (2011). Methane reforming reaction with carbon dioxide over SBA-15 supported Ni–Mo bimetallic catalysts. *Fuel Processing Technology*, 92(10), 1868-1875. doi:10.1016/j.fuproc.2011.05.002

Hussain, A., Nasir Ani, F., Sulaiman, N., & Fadzil Adnan, M. (2006). Combustion modelling of an industrial municipal waste combustor in Malaysia. *International Journal of Environmental Studies*, 63(3), 313-329.

Italiano, C., Vita, A., Fabiano, C., Laganà, M., & Pino, L. (2015). Bio-hydrogen production by oxidative steam reforming of biogas over nanocrystalline Ni/CeO<sub>2</sub> catalysts. *International Journal of Hydrogen Energy*, 40(35), 11823-11830.

Jang, W.-J., Jeong, D.-W., Shim, J.-O., Roh, H.-S., Son, I. H., & Lee, S. J. (2013). H<sub>2</sub> and CO production over a stable Ni–MgO–Ce<sub>0.8</sub>Zr<sub>0.2</sub>O<sub>2</sub> catalyst from CO<sub>2</sub> reforming of CH<sub>4</sub>. *International Journal of Hydrogen Energy*, 38, 4508-4512. doi:10.1016/j.ijhydene.2013.01.196

Jing, Q. S., Fei, J. H., Lou, H., Mo, L. Y., & Zheng, X. M. (2004). Effective reforming of methane with CO<sub>2</sub> and O<sub>2</sub> to low H<sub>2</sub>/CO ratio syngas over Ni/MgO–SiO<sub>2</sub> using fluidized bed reactor. *Energy Conversion and Management*, 45(20), 3127-3137. doi:10.1016/j.enconman.2004.02.002

Johari, A., Ahmed, S. I., Hashim, H., Alkali, H., & Ramli, M. (2012). Economic and environmental benefits of landfill gas from municipal solid waste in Malaysia. *Renewable and Sustainable Energy Reviews*, 16(5), 2907-2912.

Joo, O.-S., & Jung, K.-D. (2002). CH<sub>4</sub> dry reforming on alumina-supported nickel catalyst. *Bulletin-korean chemical society*, 23(8), 1149-1153.

Jóźwiak, W. K., Nowosielska, M., & Rynkowski, J. (2005). Reforming of methane with carbon dioxide over supported bimetallic catalysts containing Ni and noble metal: I. Characterization and activity of SiO<sub>2</sub> supported Ni–Rh catalysts. *Applied*

*Catalysis A: General*, 280(2), 233-244. doi:<http://dx.doi.org/10.1016/j.apcata.2004.11.003>

Kambolis, A., Matralis, H., Trovarelli, A., & Papadopoulou, C. (2010). Ni/CeO<sub>2</sub>-ZrO<sub>2</sub> catalysts for the dry reforming of methane. *Applied Catalysis A: General*, 377(1-2), 16-26. doi:<http://dx.doi.org/10.1016/j.apcata.2010.01.013>

Kambolis, A., Matralis, H., Trovarelli, A., & Papadopoulou, C. (2010). Ni/CeO<sub>2</sub>-ZrO<sub>2</sub> catalysts for the dry reforming of methane. *Applied Catalysis A: General*, 377(1), 16-26.

Kang, K.-M., Shim, I.-W., & Kwak, H.-Y. (2012). Mixed and autothermal reforming of methane with supported Ni catalysts with a core/shell structure. *Fuel Processing Technology*, 93(1), 105-114.

Kathiraser, Y., Oemar, U., Saw, E. T., Li, Z., & Kawi, S. (2015). Kinetic and mechanistic aspects for CO<sub>2</sub> reforming of methane over Ni based catalysts. *Chemical Engineering Journal*, 278, 62-78.

Kathirvale, S., Yunus, M. N. M., Sopian, K., & Samsuddin, A. H. (2004). Energy potential from municipal solid waste in Malaysia. *Renewable energy*, 29(4), 559-567.

Khajenoori, M., Rezaei, M., & Meshkani, F. (2014). Characterization of CeO<sub>2</sub> promoter of a nanocrystalline Ni/MgO catalyst in dry reforming of methane. *Chemical engineering & technology*, 37(6), 957-963.

Kim, W.-Y., Hanaoka, T., Kishida, M., & Wakabayashi, K. (1997). Hydrogenation of carbon monoxide over zirconia-supported palladium catalysts prepared using water-in-oil microemulsion. *Applied Catalysis A: General*, 155(2), 283-289.

Kim, W.-Y., Hayashi, H., Kishida, M., Nagata, H., & Wakabayashi, K. (1998). Methanol synthesis from syngas over supported palladium catalysts prepared using water-in-oil microemulsion. *Applied Catalysis A: General*, 169(1), 157-164.

Kishida, M., Fujita, T., Umakoshi, K., Ishiyama, J., Nagata, H., & Wakabayashi, K. (1995). Novel preparation of metal-supported catalysts by colloidal microparticles in a water-in-oil microemulsion; catalytic hydrogenation of carbon dioxide. *Journal of the Chemical Society, Chemical Communications*(7), 763-764.

Kishida, M., Ichiki, K.-i., Hanaoka, T., Nagata, H., & Wakabayashi, K. (1998). Preparation method for supported metal catalysts using w/o microemulsion: Study on immobilization conditions of metal particles by hydrolysis of alkoxide. *Catalysis Today*, 45(1), 203-208.

- Kishida, M., Umakoshi, K., Ishiyama, J.-i., Nagata, H., & Wakabayashi, K. (1996). Hydrogenation of carbon dioxide over metal catalysts prepared using microemulsion. *Catalysis Today*, 29(1), 355-359.
- Kitchens, C. L., McLeod, M. C., & Roberts, C. B. (2003). Solvent effects on the growth and steric stabilization of copper metallic nanoparticles in AOT reverse micelle systems. *The Journal of Physical Chemistry B*, 107(41), 11331-11338.
- Kohn, M. P., Castaldi, M. J., & Farrauto, R. J. (2014). Biogas reforming for syngas production: The effect of methyl chloride. *Applied catalysis. B, Environmental*, 144, 353-361.
- Kohn, M. P., Lee, J., Basinger, M. L., & Castaldi, M. J. (2011). Performance of an internal combustion engine operating on landfill gas and the effect of syngas addition. *Industrial & engineering chemistry research*, 50(6), 3570-3579.
- Kroll, V., Swaan, H., Lacombe, S., & Mirodatos, C. (1996). Methane reforming reaction with carbon dioxide over Ni/SiO<sub>2</sub> catalyst: II. A mechanistic study. *Journal of Catalysis*, 164(2), 387-398.
- Kroll, V., Swaan, H., & Mirodatos, C. (1996a). Methane reforming reaction with carbon dioxide over Ni/SiO<sub>2</sub> Catalyst: I. Deactivation Studies. *Journal of Catalysis*, 161(1), 409-422.
- Kroll, V., Swaan, H., & Mirodatos, C. (1996b). Methane reforming reaction with carbon dioxide over Ni/SiO<sub>2</sub> catalyst: I. Deactivation studies. *Journal of Catalysis*, 161(1), 409-422.
- Kumar, C., & Balasubramanian, D. (1980). Spectroscopic studies on the microemulsions and lamellar phases of the system triton X-100: hexanol: water in cyclohexane. *Journal of Colloid and Interface Science*, 74(1), 64-70.
- Larimi, A. S., & Alavi, S. M. (2012). Ceria-Zirconia supported Ni catalysts for partial oxidation of methane to synthesis gas. *Fuel*, 102(0), 366-371. doi:http://dx.doi.org/10.1016/j.fuel.2012.06.050
- Lemonidou, A. A., Goula, M. A., & Vasalos, I. A. (1998). Carbon dioxide reforming of methane over 5wt.% nickel calcium aluminate catalysts – effect of preparation method. *Catalysis Today*, 46(2–3), 175-183. doi:http://dx.doi.org/10.1016/S0920-5861(98)00339-3
- Levy, M., Levitan, R., Meirovitch, E., Segal, A., Rosin, H., & Rubin, R. (1992). Chemical reactions in a solar furnace 2: Direct heating of a vertical reactor in an insulated receiver. Experiments and computer simulations. *Solar Energy*, 48(6), 395-402.

- Li, D., Nakagawa, Y., & Tomishige, K. (2011). Methane reforming to synthesis gas over Ni catalysts modified with noble metals. *Applied Catalysis A: General*, 408(1–2), 1-24. doi:http://dx.doi.org/10.1016/j.apcata.2011.09.018
- Li, L., He, S., Song, Y., Zhao, J., Ji, W., & Au, C.-T. (2012). Fine-tunable Ni@porous silica core-shell nanocatalysts: Synthesis, characterization, and catalytic properties in partial oxidation of methane to syngas. *Journal of Catalysis*, 288(0), 54-64. doi:http://dx.doi.org/10.1016/j.jcat.2012.01.004
- Li, L., Lu, P., Yao, Y., & Ji, W. (2012). Silica-encapsulated bimetallic Co–Ni nanoparticles as novel catalysts for partial oxidation of methane to syngas. *Catalysis Communications*, 26(0), 72-77. doi:http://dx.doi.org/10.1016/j.catcom.2012.05.005
- Li, Y., Lu, G., & Ma, J. (2014). Highly active and stable nano NiO–MgO catalyst encapsulated by silica with a core-shell structure for CO<sub>2</sub> methanation. *RSC Advances*, 4(34), 17420-17428.
- Li, Y., & Park, C.-W. (1999). Particle size distribution in the synthesis of nanoparticles using microemulsions. *Langmuir*, 15(4), 952-956.
- Li, Z., Mo, L., Kathiraser, Y., & Kawi, S. (2014). Yolk–Satellite–Shell Structured Ni–Yolk@Ni@SiO<sub>2</sub> Nanocomposite: Superb Catalyst toward Methane CO<sub>2</sub> Reforming Reaction. *ACS Catalysis*, 4(5), 1526-1536. doi:10.1021/cs401027p
- Lin, M. (2006). *Synthesis of magnetic nanoparticles and nanocomposites via water-in-oil microemulsions*. Loughborough University, UK. Retrieved from https://dspace.lboro.ac.uk/2134/7817
- Lisiecki, I. (2005). Size, shape, and structural control of metallic nanocrystals. *The Journal of Physical Chemistry B*, 109(25), 12231-12244.
- Lisiecki, I., & Pileni, M. (1993). Spin crossover compound in nano-confined reversed micelle system. *J. Am. Chem. Soc*, 115, 3887-3896.
- Lisiecki, I., & Pileni, M. (1995). Copper metallic particles synthesized "in situ" in reverse micelles: influence of various parameters on the size of the particles. *The Journal of Physical Chemistry*, 99(14), 5077-5082.
- Liu, B. S., & Au, C. T. (2003). Carbon deposition and catalyst stability over La<sub>2</sub>NiO<sub>4</sub>/γ-Al<sub>2</sub>O<sub>3</sub> during CO<sub>2</sub> reforming of methane to syngas. *Applied Catalysis A: General*, 244(1), 181-195. doi:http://dx.doi.org/10.1016/S0926-860X(02)00591-4

- Liu, D., Cheo, W. N. E., Lim, Y. W. Y., Borgna, A., Lau, R., & Yang, Y. (2010). A comparative study on catalyst deactivation of nickel and cobalt incorporated MCM-41 catalysts modified by platinum in methane reforming with carbon dioxide. *Catalysis Today*, 154(3-4), 229-236. doi:10.1016/j.cattod.2010.03.054
- Liu, D., Lau, R., Borgna, A., & Yang, Y. (2009). Carbon dioxide reforming of methane to synthesis gas over Ni-MCM-41 catalysts. *Applied Catalysis A: General*, 358(2), 110-118. doi:10.1016/j.apcata.2008.12.044
- Liu, D., Quek, X. Y., Cheo, W. N. E., Lau, R., Borgna, A., & Yang, Y. (2009). MCM-41 supported nickel-based bimetallic catalysts with superior stability during carbon dioxide reforming of methane: Effect of strong metal-support interaction. *Journal of Catalysis*, 266(2), 380-390. doi:10.1016/j.jcat.2009.07.004
- Liu, J., Qiao, S. Z., Budi Hartono, S., & Lu, G. Q. M. (2010). Monodisperse yolk-shell nanoparticles with a hierarchical porous structure for delivery vehicles and nanoreactors. *Angewandte Chemie*, 122(29), 5101-5105.
- Liu, J., Qiao, S. Z., Chen, J. S., Lou, X. W. D., Xing, X., & Lu, G. Q. M. (2011). Yolk/shell nanoparticles: new platforms for nanoreactors, drug delivery and lithium-ion batteries. *Chemical Communications*, 47(47), 12578-12591.
- Liu, S., Guan, L., Li, J., Zhao, N., Wei, W., & Sun, Y. (2008). CO<sub>2</sub> reforming of CH<sub>4</sub> over stabilized mesoporous Ni-CaO-ZrO<sub>2</sub> composites. *Fuel*, 87(12), 2477-2481. doi:10.1016/j.fuel.2008.02.009
- Lopez-Quintela, M. A. (2003). Synthesis of nanomaterials in microemulsions: formation mechanisms and growth control. *Current Opinion in Colloid & Interface Science*, 8(2), 137-144.
- López-Quintela, M. A., Tojo, C., Blanco, M., Rio, L. G., & Leis, J. (2004). Microemulsion dynamics and reactions in microemulsions. *Current Opinion in Colloid & Interface Science*, 9(3), 264-278.
- Lucredio, A. F., Assaf, J. M., & Assaf, E. M. (2012). Reforming of a model biogas on Ni and Rh-Ni catalysts: Effect of adding La. *Fuel Processing Technology*, 102, 124-131.
- Lucrédio, A. F., Assaf, J. M., & Assaf, E. M. (2011). Methane conversion reactions on Ni catalysts promoted with Rh: Influence of support. *Applied Catalysis A: General*, 400(1-2), 156-165. doi:10.1016/j.apcata.2011.04.035
- Lunsford, J. H. (2000). Catalytic conversion of methane to more useful chemicals and fuels: a challenge for the 21st century. *Catalysis Today*, 63(2-4), 165-174. doi:http://dx.doi.org/10.1016/S0920-5861(00)00456-9



- Ma, Q., Wang, D., Wu, M., Zhao, T., Yoneyama, Y., & Tsubaki, N. (2012). Effect of catalytic site position: Nickel nanocatalyst selectively loaded inside or outside carbon nanotubes for methane dry reforming. *Fuel*, 108, 430-438. doi:10.1016/j.fuel.2012.12.028
- Makhum, Y. (2006). Ni-Rh catalysts on cerium zirconyl oxide for dry reforming of methane. (Master of Science), Chulalongkorn University, Thailand.
- Malik, M. A., Wani, M. Y., & Hashim, M. A. (2012). Microemulsion method: a novel route to synthesize organic and inorganic nanomaterials. *Arabian Journal of Chemistry*, 5(4), 397-417.
- Manaf, L. A., Samah, M. A. A., & Zukki, N. I. M. (2009). Municipal solid waste management in Malaysia: Practices and challenges. *Waste Management*, 29(11), 2902-2906.
- Mark, M. F., Maier, W. F., & Mark, F. (1997). Reaction kinetics of the CO<sub>2</sub> reforming of methane. *Chemical engineering & technology*, 20(6), 361-370.
- Masui, T., Fujiwara, K., Machida, K.-i., Adachi, G.-y., Sakata, T., & Mori, H. (1997). Characterization of cerium (IV) oxide ultrafine particles prepared using reversed micelles. *Chemistry of Materials*, 9(10), 2197-2204.
- McCarthy, J. J., Canziani, O. F., Leary, N. A., Dokken, D. J., & White, K. S. (2001). *Climate change 2001: impacts, adaptation, and vulnerability: contribution of working Group II to the third assessment report of the intergovernmental panel on climate change*. UK: Cambridge University Press.
- Meshkani, F., & Rezaei, M. (2011). Nickel catalyst supported on magnesium oxide with high surface area and plate-like shape: A highly stable and active catalyst in methane reforming with carbon dioxide. *Catalysis Communications*, 12(11), 1046-1050.
- Mguni, L. L., Meijboom, R., & Jalama, K. (2012). Effect of calcination temperature and mgo crystallite size on MgO/TiO<sub>2</sub> catalyst system for soybean transesterification. *World Academy of Science, Engineering and Technology*, 64, 889-893.
- Misra, D. (1991). Adsorption of low molecular weight poly (acrylic acid) on hydroxyapatite: role of molecular association and apatite dissolution. *Langmuir*, 7(11), 2422-2424.
- Moliner, R., Echegoyen, Y., Suelves, I., Lázaro, M. J., & Palacios, J. M. (2008). Ni-Mg and Ni-Cu-Mg catalysts for simultaneous production of hydrogen and carbon nanofibers: The effect of calcination temperature. *International Journal of*

*Hydrogen Energy*, 33(6), 1719-1728. doi:<http://dx.doi.org/10.1016/j.ijhydene.2008.01.005>

- Montagnini, F., & Nair, P. (2004). Carbon sequestration: an underexploited environmental benefit of agroforestry systems *New Vistas in Agroforestry* (pp. 281-295): Springer.
- Montero, J. M., Brown, D. R., Gai, P. L., Lee, A. F., & Wilson, K. (2010). In situ studies of structure–reactivity relations in biodiesel synthesis over nanocrystalline MgO. *Chemical Engineering Journal*, 161(3), 332-339.
- Montero, J. M., Gai, P., Wilson, K., & Lee, A. F. (2009). Structure-sensitive biodiesel synthesis over MgO nanocrystals. *Green chemistry*, 11(2), 265-268.
- Montoya, J. A., Romero-Pascual, E., Gimón, C., Del Angel, P., & Monzon, A. (2000). Methane reforming with CO<sub>2</sub> over Ni/ZrO<sub>2</sub>–CeO<sub>2</sub> catalysts prepared by sol–gel. *Catalysis Today*, 63(1), 71-85.
- Mul, G., & Moulijn, J. A. (2005). Preparation of supported metal catalysts. *Catal. Sci. Series*, 5, 1-32.
- Nagaoka, K., Seshan, K., Aika, K.-i., & Lercher, J. A. (2001). Carbon deposition during carbon dioxide reforming of methane—comparison between Pt/Al<sub>2</sub>O<sub>3</sub> and Pt/ZrO<sub>2</sub>. *Journal of Catalysis*, 197(1), 34-42. doi:<http://dx.doi.org/10.1006/jcat.2000.3062>
- Nagaraja, B. M., Bulushev, D. A., Beloshapkin, S., & Ross, J. R. (2011). The effect of potassium on the activity and stability of Ni–MgO–ZrO<sub>2</sub> catalysts for the dry reforming of methane to give synthesis gas. *Catalysis Today*, 178(1), 132-136.
- Nassos, S., Svensson, E. E., Nilsson, M., Boutonnet, M., & Järås, S. (2006). Microemulsion-prepared Ni catalysts supported on cerium-lanthanum oxide for the selective catalytic oxidation of ammonia in gasified biomass. *Applied Catalysis B: Environmental*, 64(1), 96-102.
- Natarajan, U., Handique, K., Mehra, A., Bellare, J. R., & Khilar, K. C. (1996). Ultrafine metal particle formation in reverse micellar systems: effects of intermicellar exchange on the formation of particles. *Langmuir*, 12(11), 2670-2678.
- Newnham, J., Mantri, K., Amin, M. H., Tardio, J., & Bhargava, S. K. (2012). Highly stable and active Ni-mesoporous alumina catalysts for dry reforming of methane. *International Journal of Hydrogen Energy*, 37(2), 1454-1464. doi:10.1016/j.ijhydene.2011.10.036

- Nieva, M. A., Villaverde, M. M., Monzón, A., Garetto, T. F., & Marchi, A. J. (2014). Steam-methane reforming at low temperature on nickel-based catalysts. *Chemical Engineering Journal*, 235(0), 158-166. doi:http://dx.doi.org/10.1016/j.cej.2013.09.030
- Noor, Z. Z., Yusuf, R. O., Abba, A. H., Abu Hassan, M. A., & Mohd Din, M. F. (2013). An overview for energy recovery from municipal solid wastes (MSW) in Malaysia scenario. *Renewable and Sustainable Energy Reviews*, 20(0), 378-384. doi:http://dx.doi.org/10.1016/j.rser.2012.11.050
- Ocsachoque, M., Pompeo, F., & Gonzalez, G. (2011). Rh–Ni/CeO<sub>2</sub>–Al<sub>2</sub>O<sub>3</sub> catalysts for methane dry reforming. *Catalysis Today*, 172(1), 226-231. doi:http://dx.doi.org/10.1016/j.cattod.2011.02.057
- Odedairo, T., Chen, J., & Zhu, Z. (2013). Metal–support interface of a novel Ni–CeO<sub>2</sub> catalyst for dry reforming of methane. *Catalysis Communications*, 31, 25-31. doi:10.1016/j.catcom.2012.11.008
- Ohde, H., Wai, C. M., Kim, H., Kim, J., & Ohde, M. (2002). Hydrogenation of olefins in supercritical CO<sub>2</sub> catalyzed by palladium nanoparticles in a water-in-CO<sub>2</sub> microemulsion. *Journal of the American Chemical Society*, 124(17), 4540-4541.
- Ohde, M., Ohde, H., & Wai, C. M. (2002). Catalytic hydrogenation of arenes with rhodium nanoparticles in a water-in-supercritical CO<sub>2</sub> microemulsion. *Chemical Communications*(20), 2388-2389.
- Olah, G. A., Goeppert, A., Czaun, M., & Prakash, G. S. (2012). Bi-reforming of methane from any source with steam and carbon dioxide exclusively to metgas (CO–2H<sub>2</sub>) for methanol and hydrocarbon synthesis. *Journal of the American Chemical Society*, 135(2), 648-650.
- Osojnik Črnivec, I. G., Djinović, P., Erjavec, B., & Pintar, A. (2012). Effect of synthesis parameters on morphology and activity of bimetallic catalysts in CO<sub>2</sub>–CH<sub>4</sub> reforming. *Chemical Engineering Journal*, 207-208, 299-307. doi: 10.1016/j.cej.2012.06.107
- Oyama, S. T., Hacıoğlu, P., Gu, Y., & Lee, D. (2012). Dry reforming of methane has no future for hydrogen production: Comparison with steam reforming at high pressure in standard and membrane reactors. *International Journal of Hydrogen Energy*, 37(13), 10444-10450. doi:http://dx.doi.org/10.1016/j.ijhydene. 2011. 09.149
- Özdemir, H., Öksüzömer, F., & Ali Gürkaynak, M. (2010). Preparation and characterization of Ni based catalysts for the catalytic partial oxidation of methane: Effect of support basicity on H<sub>2</sub>/CO ratio and carbon deposition. *International Journal of Hydrogen Energy*, 35(22), 12147-12160.

- Özdemir, H., Öksüzömer, M. F., & Gürkaynak, M. A. (2010). Preparation and characterization of Ni based catalysts for the catalytic partial oxidation of methane: Effect of support basicity on H<sub>2</sub>/CO ratio and carbon deposition. *International Journal of Hydrogen Energy*, 35(22), 12147-12160.
- Özkara-Aydınoğlu, Ş., Özensoy, E., & Aksoylu, A. E. (2009). The effect of impregnation strategy on methane dry reforming activity of Ce promoted Pt/ZrO<sub>2</sub>. *International Journal of Hydrogen Energy*, 34(24), 9711-9722.
- Park, J. C., Bang, J. U., Lee, J., Ko, C. H., & Song, H. (2010). Ni@SiO<sub>2</sub> yolk-shell nanoreactor catalysts: High temperature stability and recyclability. *Journal of Materials Chemistry*, 20(7), 1239-1246.
- Parmaliana, A., Arena, F., Frusteri, F., Coluccia, S., Marchese, L., Martra, G., & Chuvilin, A. (1993). Magnesia-supported nickel catalysts: ii. surface properties and reactivity in methane steam reforming. *Journal of Catalysis*, 141(1), 34-47.
- Parry, M. L. (2007). *Climate change 2007: Impacts, adaptation and vulnerability: Working group I contribution to the fourth assessment report of the IPCC* (Vol. 4): Cambridge University Press.
- Pawelec, B., Damyanova, S., Arishtirova, K., Fierro, J. L. G., & Petrov, L. (2007). Structural and surface features of PtNi catalysts for reforming of methane with CO<sub>2</sub>. *Applied Catalysis A: General*, 323(0), 188-201. doi:http://dx.doi.org/10.1016/j.apcata.2007.02.017
- Pena, M. A., Gómez, J. P., & Fierro, J. L. G. (1996). New catalytic routes for syngas and hydrogen production. *Applied Catalysis A: General*, 144(1-2), 7-57. doi:http://dx.doi.org/10.1016/0926-860X(96)00108-1
- Pietraszek, A., Koubaisy, B., Roger, A.-C., & Kiennemann, A. (2011). The influence of the support modification over Ni-based catalysts for dry reforming of methane reaction. *Catalysis Today*, 176(1), 267-271.
- Pileni, M.-P. (2003). The role of soft colloidal templates in controlling the size and shape of inorganic nanocrystals. *Nature materials*, 2(3), 145-150.
- Pileni, M. (1993). Reverse micelles as microreactors. *The Journal of Physical Chemistry*, 97(27), 6961-6973.
- Pileni, M. (1997). Nanosized particles made in colloidal assemblies. *Langmuir*, 13(13), 3266-3276.

- Pileni, M. (1998). Fabrication and properties of nanosized material made by using colloidal assemblies as templates. *Crystal Research and Technology*, 33(7-8), 1155-1186.
- Pileni, M. (2007). Control of the size and shape of inorganic nanocrystals at various scales from nano to macrodomains. *The Journal of Physical Chemistry C*, 111(26), 9019-9038.
- Pino, L., Vita, A., Cipitì, F., Laganà, M., & Recupero, V. (2011). Hydrogen production by methane tri-reforming process over Ni–ceria catalysts: Effect of La-doping. *Applied Catalysis B: Environmental*, 104(1–2), 64-73. doi:http://dx.doi.org/10.1016/j.apcatb.2011.02.027
- Pocoroba, E., Pettersson, L. J., Agrell, J., Boutonnet, M., & Jansson, K. (2001). Exhaust gas catalysts for heavy-duty applications: influence of the Pd particle size and particle size distribution on the combustion of natural gas and biogas. *Topics in Catalysis*, 16(1-4), 407-412.
- Pompeo, F., Nichio, N. N., Souza, M. M. V. M., Cesar, D. V., Ferretti, O. A., & Schmal, M. (2007). Study of Ni and Pt catalysts supported on  $\alpha$ -Al<sub>2</sub>O<sub>3</sub> and ZrO<sub>2</sub> applied in methane reforming with CO<sub>2</sub>. *Applied Catalysis A: General*, 316(2), 175-183. doi:10.1016/j.apcata.2006.09.007
- Raco, B., Battaglini, R., & Lelli, M. (2010). Gas emission into the atmosphere from controlled landfills: an example from Legoli landfill (Tuscany, Italy). *Environmental Science and Pollution Research*, 17(6), 1197-1206.
- Rad, S. J. H., Haghighi, M., Eslami, A. A., Rahmani, F., & Rahemi, N. (2016). Sol–gel vs. impregnation preparation of MgO and CeO<sub>2</sub> doped Ni/Al<sub>2</sub>O<sub>3</sub> nanocatalysts used in dry reforming of methane: Effect of process conditions, synthesis method and support composition. *International Journal of Hydrogen Energy*, 41(11), 5335-5350.
- Rahemi, N., Haghighi, M., Babaluo, A. A., Jafari, M. F., & Estifae, P. (2013). Synthesis and physicochemical characterizations of Ni/Al<sub>2</sub>O<sub>3</sub>–ZrO<sub>2</sub> nanocatalyst prepared via impregnation method and treated with non-thermal plasma for CO<sub>2</sub> reforming of CH<sub>4</sub>. *Journal of Industrial and Engineering Chemistry*, 19(5), 1566-1576. doi:10.1016/j.jiec.2013.01.024
- Ranjbar, A., & Rezaei, M. (2012). Dry reforming reaction over nickel catalysts supported on nanocrystalline calcium aluminates with different CaO/Al<sub>2</sub>O<sub>3</sub> ratios. *Journal of Natural Gas Chemistry*, 21(2), 178-183. doi:http://dx.doi.org/10.1016/S1003-9953(11)60351-4

- Rezaei, M., Alavi, S., Sahebdehfar, S., Bai, P., Liu, X., & Yan, Z.-F. (2008). CO<sub>2</sub> reforming of CH<sub>4</sub> over nanocrystalline zirconia-supported nickel catalysts. *Applied Catalysis B: Environmental*, 77(3), 346-354.
- Rezaei, M., Alavi, S. M., Sahebdehfar, S., & Yan, Z.-F. (2009). A highly stable catalyst in methane reforming with carbon dioxide. *Scripta Materialia*, 61(2), 173-176. doi:10.1016/j.scriptamat.2009.03.033
- Richardson, J. T. (1989). Catalyst development *Principles of Catalyst Development* (pp. 41-48): Springer.
- Rosen, M. J. (2004). Micelle formation by surfactants. *Surfactants and Interfacial Phenomena, Third Edition*, 105-177.
- Rostrup-Nielsen, J. R. (1993). Production of synthesis gas. *Catalysis Today*, 18(4), 305-324.
- Ruckenstein, E., & Hang Hu, Y. (1999). Methane partial oxidation over NiO/MgO solid solution catalysts. *Applied Catalysis A: General*, 183(1), 85-92. doi:http://dx.doi.org/10.1016/S0926-860X(99)00047-2
- Ruckenstein, E., & Nagarajan, R. (1980). Aggregation of amphiphiles in nonaqueous media. *The Journal of Physical Chemistry*, 84(11), 1349-1358.
- Ruckenstein, E., & Wang, H. Y. (2002). Carbon deposition and catalytic deactivation during CO<sub>2</sub> reforming of CH<sub>4</sub> over Co/ $\gamma$ -Al<sub>2</sub>O<sub>3</sub> Catalysts. *Journal of Catalysis*, 205(2), 289-293. doi:http://dx.doi.org/10.1006/jcat.2001.3458
- Rymeš, J., Ehret, G., Hilaire, L., Boutonnet, M., & Jiráťová, K. (2002). Microemulsions in the preparation of highly active combustion catalysts. *Catalysis Today*, 75(1), 297-303.
- Saeed, M. O., Hassan, M. N., & Mujeebu, M. A. (2009). Assessment of municipal solid waste generation and recyclable materials potential in Kuala Lumpur, Malaysia. *Waste Management*, 29(7), 2209-2213.
- Safariamin, M., Tidahy, L. H., Abi-Aad, E., Siffert, S., & Aboukaïs, A. (2009). Dry reforming of methane in the presence of ruthenium-based catalysts. *Comptes Rendus Chimie*, 12(6), 748-753.
- San-José-Alonso, D., Juan-Juan, J., Illán-Gómez, M., & Román-Martínez, M. (2009). Ni, Co and bimetallic Ni-Co catalysts for the dry reforming of methane. *Applied Catalysis A: General*, 371(1), 54-59.

- San José-Alonso, D., Illán-Gómez, M. J., & Román-Martínez, M. C. (2013). Low metal content Co and Ni alumina supported catalysts for the CO<sub>2</sub> reforming of methane. *International Journal of Hydrogen Energy*, 38(5), 2230-2239. doi:10. 1016/j.ijhydene.2012.11.080
- Santos, A., Damyanova, S., Teixeira, G., Mattos, L. V., Noronha, F. B., Passos, F. B., & Bueno, J. (2005). The effect of ceria content on the performance of Pt/CeO<sub>2</sub>/Al<sub>2</sub>O<sub>3</sub> catalysts in the partial oxidation of methane. *Applied Catalysis A: General*, 290(1), 123-132.
- Santra, S., Tapeç, R., Theodoropoulou, N., Dobson, J., Hebard, A., & Tan, W. (2001). Synthesis and characterization of silica-coated iron oxide nanoparticles in microemulsion: the effect of nonionic surfactants. *Langmuir*, 17(10), 2900-2906.
- Saraswat, S. K., & Pant, K. K. (2011). Ni–Cu–Zn/MCM-22 catalysts for simultaneous production of hydrogen and multiwall carbon nanotubes via thermo-catalytic decomposition of methane. *International Journal of Hydrogen Energy*, 36(21), 13352-13360. doi:10.1016/j.ijhydene.2011.07.102
- Savko, N. (2011). *The role of inverse nonionic microemulsion in the synthesis of SiO<sub>2</sub> nanoparticles*. (PhD), Università degli studi di Trieste, Italy.
- Schmolka, I., & Shick, M. (1967). Nonionic surfactants. *Surfactant Science Series*, Marcel Dekker, New York.
- Schulman, J., & Friend, J. (1949). Light scattering investigation of the structure of transparent oil-water disperse systems. II. *Journal of Colloid Science*, 4(5), 497-509.
- Schwarz, J. A., Contescu, C., & Contescu, A. (1995). Methods for preparation of catalytic materials. *Chemical Reviews*, 95(3), 477-510.
- Schwuger, M.-J., Stickdorn, K., & Schomaecker, R. (1995). Microemulsions in technical processes. *Chemical Reviews*, 95(4), 849-864.
- Shaikhutdinov, S. K., Avdeeva, L., Goncharova, O., Kochubey, D., Novgorodov, B., & Plyasova, L. (1995). Coprecipitated Ni-Al and Ni-Cu-Al catalysts for methane decomposition and carbon deposition I. Genesis of calcined and reduced catalysts. *Applied Catalysis A: General*, 126(1), 125-139.
- Sharma, S., Hilaire, S., Vohs, J., Gorte, R., & Jen, H.-W. (2000). Evidence for oxidation of ceria by CO<sub>2</sub>. *Journal of Catalysis*, 190(1), 199-204.

- Shin, H.-C., Park, J.-W., Kim, H.-S., & Shin, E.-S. (2005). Environmental and economic assessment of landfill gas electricity generation in Korea using LEAP model. *Energy Policy*, 33(10), 1261-1270.
- Shiraz, M. H. A., Rezaei, M., & Meshkani, F. (2016). Microemulsion synthesis method for preparation of mesoporous nanocrystalline  $\gamma$ -Al<sub>2</sub>O<sub>3</sub> powders as catalyst carrier for nickel catalyst in dry reforming reaction. *International Journal of Hydrogen Energy*, 41(15), 6353-6361.
- Song, S.-H., Son, J.-H., Budiman, A. W., Choi, M.-J., Chang, T.-S., & Shin, C.-H. (2014). The influence of calcination temperature on catalytic activities in a Co based catalyst for CO<sub>2</sub> dry reforming. *Korean Journal of Chemical Engineering*, 1-6.
- Song, S., Wang, X., & Zhang, H. (2015). CeO<sub>2</sub>-encapsulated noble metal nanocatalysts: enhanced activity and stability for catalytic application. *NPG Asia Materials*, 7(5), e179.
- Steinhauer, B., Kasireddy, M. R., Radnik, J., & Martin, A. (2009). Development of Ni-Pd bimetallic catalysts for the utilization of carbon dioxide and methane by dry reforming. *Applied Catalysis A: General*, 366(2), 333-341. doi:http://dx.doi.org/10.1016/j.apcata.2009.07.021
- Sun, L., Tan, Y., Zhang, Q., Xie, H., Song, F., & Han, Y. (2013). Effects of Y<sub>2</sub>O<sub>3</sub>-modification to Ni/ $\gamma$ -Al<sub>2</sub>O<sub>3</sub> catalysts on autothermal reforming of methane with CO<sub>2</sub> to syngas. *International Journal of Hydrogen Energy*, 38(4), 1892-1900. doi:10.1016/j.ijhydene.2012.11.114
- Svensson, E. E., Nassos, S., Boutonnet, M., & Järås, S. G. (2006). Microemulsion synthesis of MgO-supported LaMnO<sub>3</sub> for catalytic combustion of methane. *Catalysis Today*, 117(4), 484-490.
- Swaan, H., Kroll, V., Martin, G., & Mirodatos, C. (1994). Deactivation of supported nickel catalysts during the reforming of methane by carbon dioxide. *Catalysis Today*, 21(2), 571-578.
- Tada, S., Shimizu, T., Kameyama, H., Haneda, T., & Kikuchi, R. (2012). Ni/CeO<sub>2</sub> catalysts with high CO<sub>2</sub> methanation activity and high CH<sub>4</sub> selectivity at low temperatures. *International Journal of Hydrogen Energy*, 37(7), 5527-5531.
- Tago, T., Hanaoka, T., Dhupatemiya, P., Hayashi, H., Kishida, M., & Wakabayashi, K. (2000). Effects of Rh content on catalytic behavior in CO hydrogenation with Rh-silica catalysts prepared using microemulsion. *Catalysis Letters*, 64(1), 27-31.
- Takanabe, K., Nagaoka, K., Nariai, K., & Aika, K.-i. (2005a). Influence of reduction temperature on the catalytic behavior of Co/TiO<sub>2</sub> catalysts for CH<sub>4</sub>/CO<sub>2</sub> reforming



and its relation with titania bulk crystal structure. *Journal of Catalysis*, 230(1), 75-85.

Takanabe, K., Nagaoka, K., Nariai, K., & Aika, K.-i. (2005b). Titania-supported cobalt and nickel bimetallic catalysts for carbon dioxide reforming of methane. *Journal of Catalysis*, 232(2), 268-275.

Takenaka, S., Orita, Y., Umebayashi, H., Matsune, H., & Kishida, M. (2008). High resistance to carbon deposition of silica-coated Ni catalysts in propane stream reforming. *Applied Catalysis A: General*, 351(2), 189-194. doi:http://dx.doi.org/10.1016/j.apcata.2008.09.017

Takenaka, S., Umebayashi, H., Tanabe, E., Matsune, H., & Kishida, M. (2007). Specific performance of silica-coated Ni catalysts for the partial oxidation of methane to synthesis gas. *Journal of Catalysis*, 245(2), 392-400.

Tchobanoglous, G., Theisen, H., & Vigil, S. (1993). *Integrated solid waste management: engineering principles and management issues*: McGraw-Hill, Inc.

Theofanidis, S. A., Galvita, V. V., Poelman, H., & Marin, G. B. (2015). Enhanced carbon-resistant dry reforming Fe-Ni catalyst: role of Fe. *ACS Catalysis*, 5(5), 3028-3039.

Therdthianwong, S., Siangchin, C., & Therdthianwong, A. (2008). Improvement of coke resistance of Ni/Al<sub>2</sub>O<sub>3</sub> catalyst in CH<sub>4</sub>/CO<sub>2</sub> reforming by ZrO<sub>2</sub> addition. *Fuel Processing Technology*, 89(2), 160-168. doi:10.1016/j.fuproc.2007.09.003

Tomishige, K., Chen, Y.-g., & Fujimoto, K. (1999). Studies on carbon deposition in CO<sub>2</sub> reforming of CH<sub>4</sub> over nickel–magnesia solid solution catalysts. *Journal of Catalysis*, 181(1), 91-103.

Tomishige, K., Matsuo, Y., Yoshinaga, Y., Sekine, Y., Asadullah, M., & Fujimoto, K. (2002). Comparative study between fluidized bed and fixed bed reactors in methane reforming combined with methane combustion for the internal heat supply under pressurized condition. *Applied Catalysis A: General*, 223(1–2), 225-238. doi:http://dx.doi.org/10.1016/S0926-860X(01)00757-8

Tomishige, K., Yamazaki, O., Chen, Y., Yokoyama, K., Li, X., & Fujimoto, K. (1998). Development of ultra-stable Ni catalysts for CO<sub>2</sub> reforming of methane. *Catalysis Today*, 45(1), 35-39.

Trakarnpruk, W., & Sukkaew, C. (2008). Preparation of Ni/MgOZrO<sub>2</sub> nanocrystals by citrate sol–gel method. *Journal of Alloys and Compounds*, 460(1–2), 565-569. doi:http://dx.doi.org/10.1016/j.jallcom.2007.06.018

- Tsang, S., Claridge, J., & Green, M. (1995). Recent advances in the conversion of methane to synthesis gas. *Catalysis Today*, 23(1), 3-15.
- Tsipouriari, V., Efstathiou, A., & Verykios, X. (1996). Transient kinetic study of the oxidation and hydrogenation of carbon species formed during CH<sub>4</sub>/He, CO<sub>2</sub>/He, and CH<sub>4</sub>/CO<sub>2</sub> reactions over Rh/Al<sub>2</sub>O<sub>3</sub> catalyst. *Journal of Catalysis*, 161(1), 31-42.
- Tsyganok, A. I., Inaba, M., Tsunoda, T., Hamakawa, S., Suzuki, K., & Hayakawa, T. (2003). Dry reforming of methane over supported noble metals: a novel approach to preparing catalysts. *Catalysis Communications*, 4(9), 493-498. doi:http://dx.doi.org/10.1016/S1566-7367(03)00130-4
- Usman, M., Daud, W. W., & Abbas, H. F. (2015). Dry reforming of methane: Influence of process parameters—A review. *Renewable and Sustainable Energy Reviews*, 45, 710-744.
- Wang-Yao, K., Towprayoon, S., Chiemchaisri, C., Gheewala, S. H., & Nopharatana, A. (2006). *Seasonal variation of landfill methane emission from seven solid waste disposal sites in central Thailand*. Paper presented at the The 2<sup>nd</sup> Joint International Conference on "Sustainable Energy and Environment (SEE 2006)", Thailand.
- Wang, H. Y., & Ruckenstein, E. (2000). Carbon dioxide reforming of methane to synthesis gas over supported rhodium catalysts: the effect of support. *Applied Catalysis A: General*, 204(1), 143-152. doi:http://dx.doi.org/10.1016/S0926-860X(00)00547-0
- Wang, H. Y., & Ruckenstein, E. (2001). CO<sub>2</sub> reforming of CH<sub>4</sub> over Co/MgO solid solution catalysts — effect of calcination temperature and Co loading. *Applied Catalysis A: General*, 209(1-2), 207-215. doi:http://dx.doi.org/10.1016/S0926-860X(00)00753-5
- Wang, S., Lu, G. Q., & Millar, G. J. (1996). Carbon dioxide reforming of methane to produce synthesis gas over metal-supported catalysts: State of the art. *Energy & Fuels*, 10(4), 896-904. doi:10.1021/ef950227t
- Wang, S., Murata, K., Hayakawa, T., Hamakawa, S., & Suzuki, K. (2001). Selective oxidation of ethane and propane over sulfated zirconia-supported nickel oxide catalysts. *Journal of Chemical Technology & Biotechnology*, 76(3), 265-272. doi:10.1002/jctb.373
- Wang, Y.-H., Liu, H.-M., & Xu, B.-Q. (2009). Durable Ni/MgO catalysts for CO<sub>2</sub> reforming of methane: Activity and metal-support interaction. *Journal of Molecular Catalysis A: Chemical*, 299(1), 44-52.

- Wen, X., Shi-an, Z., & Bang, F. (2010). A study on preparation of MgO nanoparticles by reverse microemulsion and formation mechanisms. *Modern Chemical Industry*, 30(3), 61-63.
- Wilhelm, D. J., Simbeck, D. R., Karp, A. D., & Dickenson, R. L. (2001). Syngas production for gas-to-liquids applications: technologies, issues and outlook. *Fuel Processing Technology*, 71(1-3), 139-148. doi:http://dx.doi.org/10.1016/S0378-3820(01)00140-0
- Wu, J. C. S., & Chou, H.-C. (2009). Bimetallic Rh-Ni/BN catalyst for methane reforming with CO<sub>2</sub>. *Chemical Engineering Journal*, 148(2-3), 539-545. doi:http://dx.doi.org/10.1016/j.cej.2009.01.011
- Wu, T., Cai, W., Zhang, P., Song, X., & Gao, L. (2013). Cu-Ni@SiO<sub>2</sub> alloy nanocomposites for methane dry reforming catalysis. *RSC Advances*, 3(46), 23976-23979. doi:10.1039/C3RA43203C
- Wurzel, T., Malcus, S., & Mleczko, L. (2000). Reaction engineering investigations of CO<sub>2</sub> reforming in a fluidized-bed reactor. *Chemical Engineering Science*, 55(18), 3955-3966. doi:http://dx.doi.org/10.1016/S0009-2509(99)00444-3
- Xu, J., Zhou, W., Li, Z., Wang, J., & Ma, J. (2009). Biogas reforming for hydrogen production over nickel and cobalt bimetallic catalysts. *International Journal of Hydrogen Energy*, 34(16), 6646-6654. doi:http://dx.doi.org/10.1016/j.ijhydene.2009.06.038
- Xu, L., Liu, Y., Li, Y., Lin, Z., Ma, X., Zhang, Y., . . . Fan, M. (2014). Catalytic CH<sub>4</sub> reforming with CO<sub>2</sub> over activated carbon based catalysts. *Applied Catalysis A: General*, 469(0), 387-397. doi:http://dx.doi.org/10.1016/j.apcata.2013.10.022
- Xu, L., Zhao, H., Song, H., & Chou, L. (2012). Ordered mesoporous alumina supported nickel based catalysts for carbon dioxide reforming of methane. *International Journal of Hydrogen Energy*, 37(9), 7497-7511.
- Yan, Q., Weng, W., Wan, H., Toghiani, H., Toghiani, R., & Pittman Jr, C. (2003). Activation of methane to syngas over a Ni/TiO<sub>2</sub> catalyst. *Applied Catalysis A: General*, 239(1), 43-58.
- Yang, M., Guo, H., Li, Y., & Dang, Q. (2012). CH<sub>4</sub>-CO<sub>2</sub> reforming to syngas over Pt-CeO<sub>2</sub>-ZrO<sub>2</sub>/MgO catalysts: Modification of support using ion exchange resin method. *Journal of Natural Gas Chemistry*, 21(1), 76-82. doi:10.1016/s1003-9953(11)60336-8

- Yang, Q., Han, D., Yang, H., & Li, C. (2008). Asymmetric Catalysis with Metal Complexes in Nanoreactors. *Chemistry – An Asian Journal*, 3(8-9), 1214-1229. doi:10.1002/asia.200800110
- Yang, W.-H., Kim, M. H., & Ham, S.-W. (2007). Effect of calcination temperature on the low-temperature oxidation of CO over CoOx/TiO<sub>2</sub> catalysts. *Catalysis Today*, 123(1-4), 94-103. doi:http://dx.doi.org/10.1016/j.cattod.2007.01.048
- Yao, L., Li, Y., Zhao, J., Ji, W., & Au, C. (2010). Core-shell structured nanoparticles (M@ SiO<sub>2</sub>, Al<sub>2</sub>O<sub>3</sub>, MgO; M= Fe, Co, Ni, Ru) and their application in COx-free H<sub>2</sub> production via NH<sub>3</sub> decomposition. *Catalysis Today*, 158(3), 401-408.
- Yasyerli, S., Filizgok, S., Arbag, H., Yasyerli, N., & Dogu, G. (2011). Ru incorporated Ni-MCM-41 mesoporous catalysts for dry reforming of methane: Effects of Mg addition, feed composition and temperature. *International Journal of Hydrogen Energy*, 36(8), 4863-4874. doi:10.1016/j.ijhydene.2011.01.120
- Yu, J., Ge, Q., Fang, W., & Xu, H. (2011). Influences of calcination temperature on the efficiency of CaO promotion over CaO modified Pt/ $\gamma$ -Al<sub>2</sub>O<sub>3</sub> catalyst. *Applied Catalysis A: General*, 395(1-2), 114-119. doi:http://dx.doi.org/ 10.1016/j.apcata.2011.01.031
- Yu, L., Xu, J., Sun, M., & Wang, X. (2007). Catalytic Oxidation of Dimethyl Ether to Hydrocarbons over SnO<sub>2</sub>/MgO and SnO<sub>2</sub>/CaO Catalysts. *Journal of Natural Gas Chemistry*, 16(2), 200-203.
- Yu, M., Zhu, K., Liu, Z., Xiao, H., Deng, W., & Zhou, X. (2014). Carbon dioxide reforming of methane over promoted Ni<sub>x</sub>/Mg<sub>1-x</sub>O (111) platelet catalyst derived from solvothermal synthesis. *Applied Catalysis B: Environmental*, 148, 177-190.
- Yu, M., Zhu, Y.-A., Lu, Y., Tong, G., Zhu, K., & Zhou, X. (2015). The promoting role of Ag in Ni-CeO<sub>2</sub> catalyzed CH<sub>4</sub>-CO<sub>2</sub> dry reforming reaction. *Applied Catalysis B: Environmental*, 165, 43-56.
- Zabidi, N. M. (2012). Synthesis of nanocatalysts via reverse microemulsion route for Fischer-Tropsch reactions. In R. Najjar (Ed.), *Microemulsions - An Introduction to Properties and Applications* (pp. 262). Malaysia: Intech Open Access Publisher.
- Zanganeh, R., Rezaei, M., & Zamaniyan, A. (2013). Dry reforming of methane to synthesis gas on NiO-MgO nanocrystalline solid solution catalysts. *International Journal of Hydrogen Energy*, 38(7), 3012-3018. doi:10.1016/j.ijhydene.2012.12.089

- Zarur, A. J., & Ying, J. Y. (2000). Reverse microemulsion synthesis of nanostructured complex oxides for catalytic combustion. *Nature*, 403(6765), 65-67.
- Zhang, J., Wang, H., & Dalai, A. K. (2007). Development of stable bimetallic catalysts for carbon dioxide reforming of methane. *Journal of Catalysis*, 249(2), 300-310.
- Zhang, J., Wang, H., & Dalai, A. K. (2008). Effects of metal content on activity and stability of Ni-Co bimetallic catalysts for CO<sub>2</sub> reforming of CH<sub>4</sub>. *Applied Catalysis A: General*, 339(2), 121-129. doi:10.1016/j.apcata.2008.01.027
- Zhang, M., Ji, S., Hu, L., Yin, F., Li, C., & Liu, H. (2006). Structural characterization of highly stable Ni/SBA-15 catalyst and its catalytic performance for methane reforming with CO<sub>2</sub>. *Chinese Journal of Catalysis*, 27(9), 777-781. doi:10.1016/s1872-2067(06)60043-0
- Zhang, Q., Wang, W., Goebel, J., & Yin, Y. (2009). Self-templated synthesis of hollow nanostructures. *Nano Today*, 4(6), 494-507.
- Zhang, S., Wang, J., & Wang, X. (2008). Effect of calcination temperature on structure and performance of Ni/TiO<sub>2</sub>-SiO<sub>2</sub> catalyst for CO<sub>2</sub> reforming of methane. *Journal of Natural Gas Chemistry*, 17(2), 179-183. doi:http://dx.doi.org/10.1016/S1003-9953(08)60048-1
- Zhang, W. D., Liu, B. S., & Tian, Y. L. (2007). CO<sub>2</sub> reforming of methane over Ni/Sm<sub>2</sub>O<sub>3</sub>-CaO catalyst prepared by a sol-gel technique. *Catalysis Communications*, 8(4), 661-667. doi:10.1016/j.catcom.2006.08.020
- Zhang, Z. L., & Verykios, X. E. (1994). Carbon dioxide reforming of methane to synthesis gas over supported Ni catalysts. *Catalysis Today*, 21(2-3), 589-595. doi:http://dx.doi.org/10.1016/0920-5861(94)80183-5
- Zheng, X., Tan, S., Dong, L., Li, S., & Chen, H. (2014). LaNiO<sub>3</sub>@SiO<sub>2</sub> core-shell nanoparticles for the dry reforming of CH<sub>4</sub> in the dielectric barrier discharge plasma. *International Journal of Hydrogen Energy*, 39(22), 11360-11367. doi:http://dx.doi.org/10.1016/j.ijhydene.2014.05.083
- Zhu, J., Peng, X., Yao, L., Deng, X., Dong, H., Tong, D., & Hu, C. (2013). Synthesis gas production from CO<sub>2</sub> reforming of methane over Ni-Ce/SiO<sub>2</sub> catalyst: The effect of calcination ambience. *International Journal of Hydrogen Energy*, 38(1), 117-126. doi:http://dx.doi.org/10.1016/j.ijhydene.2012.07.136
- Zhu, J., Peng, X., Yao, L., Tong, D., & Hu, C. (2012). CO<sub>2</sub> reforming of methane over Mg-promoted Ni/SiO<sub>2</sub> catalysts: the influence of Mg precursors and impregnation sequences. *Catalysis Science & Technology*, 2(3), 529-537.